University of Southampton
FACULTY OF ENGINEERING AND PHYSICAL SCIENCES
SCHOOL OF CHEMISTRY

Molecular Dynamics Simulations of Complex Bacterial Membranes

by
Eilish McBurnie

Thesis for the degree of Doctor of Philosophy

October 2020

University of Southampton

ABSTRACT

FACULTY OF ENGINEERING AND PHYSICAL SCIENCES
SCHOOL OF CHEMISTRY

Thesis for the degree of Doctor of Philosophy

Molecular Dynamics Simulations of Complex Bacterial Membranes

by Eilish McBurnie

Bacterial envelopes are a frontier that must be faced by all products that come into contact with them, including antibiotics, antiseptics and host defences. Many antimicrobials exploit features of the bacterial envelope in order to inhibit bacterial growth or cause cell death whilst the immune system recognises bacterial cell envelope patterns in order to mount an appropriate response. Given this, and the ever-growing concerns around antimicrobial resistance, it is vital that the mechanisms involved are well understood. This work used atomistic and coarse-grained molecular dynamics simulations to better understand the relationship between bacterial membranes and antimicrobials. The first chapter explored many of the aspects of the mode of action of membrane penetrating antibiotic, daptomycin. This investigated the relationship between daptomycin and calcium ions in addition to its dependence on phosphatidylglycerol. The second chapter of this work aimed to understand the mode of action of the membrane active antiseptic, chlorhexidine, on the *Staphylococcus aureus* membrane. The third chapter aimed to compare the differences of simulating chlorhexidine with the *S. aureus* membrane using different force fields. The final chapter focused on coarse-grain simulations of thrombin-derived C-terminal peptides (TCPs) with bacterial envelope products. This work aimed to support experimental work that had showed the co-aggregation of TCPs in the presence of bacterial envelope products as a mechanism to avoid host immune overreaction.

Contents

List of Figures vi
List of Tables xviii
List of Accompanying Materials xix
Research Thesis: Declaration of Authorship xx
Acknowledgements xxi
Definitions and Abbreviations xxii
Chapter 1 - Introduction 24
1.1 Bacterial Cells 24
1.2 Bacterial Cell Envelopes 25
1.2.1 Gram-negative Bacterial Cell Envelopes 25
1.2.2 Gram-positive Bacterial Cell Envelopes 26
1.3 *Staphylococcus aureus* 27
1.4 Antibiotics 29
1.4.1 Inhibitors of Protein Biosynthesis 29
1.4.2 Inhibitors of DNA/RNA Replication 30
1.4.3 Antibiotics Targeting Cell Walls 30
1.4.4 Antibiotics Targeting Phospholipid Membranes 31
1.5 Antiseptics 32
1.6 Mechanisms of Bacterial Resistance to Antibiotics 35
1.6.1 Efflux Pumps 35
1.6.2 Modification of Target Molecules 35
1.6.3 Antibiotic Inactivation 36
1.7 Aims 36
Chapter 2 - Computational Methods 38
2.1 Molecular Dynamics 38
2.2 The Integrator 41
2.2.1 Leap-frog Algorithm 41
2.2.3 The Time-step 42
2.3 Energy Minimisation 42
2.4 Thermodynamic Ensembles 43
2.4.1 Temperature & Pressure Coupling 43
2.4.2 Thermostats 43
2.4.3 Barostats 43
2.5 Periodic Boundary Conditions 43
2.6 Force fields 44
2.6.1 Bonded Interactions 45
2.7 Cut-offs and Electrostatics 48
2.7.1 The Distance Cut-off 48

2.7.2 Long-range Dispersion Correction and The Smooth Particle Mesh Ewald (PME) 49
2.8 Simulation Resolution 49
Chapter 3 – Structure and Membrane Interactions of the Antibiotic Daptomycin 51
3.1 Introduction 51
3.2 Aims 56
3.3 Daptomycin Micelle Formation 56
3.3.1 Methods and Simulation Setup 56
3.3.2 Results of Daptomycin Micelle Formation in Solvent 59
3.3.3 Results of Daptomycin Models Micelle Formation with the *S. aureus* Membrane 66
3.3.4 Conclusions 76
3.4 Daptomycin Behaviour PC Model Membrane versus Realistic *S. aureus* Membrane 78
3.4.1 Methods and Simulation Setup 78
3.4.2 Results 78
3.4.3 Conclusions 88
3.5 Increased Daptomycin Concentration with *S. aureus* Membrane Study 88
3.5.1 Methods and Simulation Set up 89
3.5.2 Results 89
3.5.3 Conclusions 100
Chapter 4 - Chlorhexidine Mode of Action on the *S. aureus* Membrane 101
4.1 Introduction 101
4.2 Chlorhexidine in Solvent with Varying Ions 103
4.2.1 Methods and Simulation Set-up 104
4.2.2 Results 105
Conclusions 117
4.3 Chlorhexidine Simulated with *S. aureus* Membrane and Varying Counter Ions & Components 118
4.3.1 Methods and Simulation Set-up 118
4.3.2 Results 118
4.3.3 Conclusions 138
Chapter 5 - Force Field Effect on Structure and Membrane Interactions of Chlorhexidine 140
5.1 Introduction 140
5.2 Chlorhexidine Equilibrium Simulations 143
5.2.1 Methods and Simulation Set-up 143
5.2.2 Results 145
5.2.3 Conclusions 160
5.3 Chlorhexidine Electroporation Simulations 162

5.3.1 Electroporation Background and Aims 162
5.3.2 Methods and Simulation Set-up 162
5.3.3 Results 163
5.3.4 Conclusions 176
Chapter 6 - TCP Co-aggregation in Presence of Bacterial Products 177
6.1 Introduction 177
6.2 Initial TCP Co-aggregation Simulations 179
6.2.1 Methods and Simulation Set-up 179
6.2.2 Results 180
6.2.3 Initial Conclusions 191
6.3 Increasing LTA and PGN Ratio to TCP 192
6.3.1 Methods and Simulation Set-up 192
6.3.2 Results 193
6.3.3 Conclusions 205
Appendix 206
Bibliography 211

List of Figures

Figure 1.1: Simplified examples of bacterial morphology[1]. 24
Figure 1.2: Schematic showing some of the key features of the Gram-negative cell envelope. 25
Figure 1.3: Schematic showing some of the key features of the Gram-positive cell envelope. 26
Figure 1.4: *S. aureus* lipids A) PG B) Lysl-PG and C) DPG. 29
Figure 1.5: Chemical structures of examples of antibiotics from the classes discussed. 31
Figure 1.6: Chemical structures of polymyxin class antibiotic (colistin) and daptomycin. 32
Figure 1.7: Chemical structures of the antiseptics discussed. 34
Figure 2.1: Diagram showing the basic method of MD simulations. 40
Figure 2.3: Harmonic potential used to model bond stretching, bond angles and improper dihedrals, K_r and K_θ, are the equilibrium values for different bonds and angles. 46
Figure 2.4: The Lennard-Jones potential to model the Van der Waals interactions. The ε_{ij} term describes the shape of the curve, the depth of the well. R_{min} is the distance between two adjacent atoms at LJ potential minimum. 47
Figure 2.5: The electrostatic potential to model the point charges. 47
Figure 2.6: Chemical structure of PC with schematic comparing UA PC and CG PC below. 50
Figure 3.1: Daptomycin structure, A) chemical structure and B) amino acid sequence[81]. 52
Figure 3.2: A) Tsushimycin amino acid sequence and B) Stereoview of the superposition of all 12 tsushimycin cyclic regions with suggested Ca^{2+} position in centre[86]. 54

Figure 3.3: Snapshots of starting conformations of both daptomycin models shown in cyan, red, blue and white. The Ca^{2+} fixed in the centre of the Ca^{2+} bound model is shown in green. 58
Figure 3.4: Snapshot of 15 daptomycin models, original non-Ca^{2+} and Ca2+ conjugated structure at end of 500 ns simulations. Solvent has been omitted for clarity. The polar region is shown in blue and the hydrophobic region in red. The Ca^{2+} fixed in the centre of the Ca^{2+} bound model is shown in green. 59
Figure 3.5: Average distance (nm) between daptomycin molecules over last 20 ns of each simulation. The blacked out regions omit self-contact of molecules. 60
Figure 3.6: Hydrogen bonds between 15 daptomycin molecules over time (ns). The donor acceptance distance was set to 3.0 Å and the angle cut off 20 degrees. 61
Figure 3.7: SASA for polar and hydrophobic regions (nm^2) of over time (ns). 62
Figure 3.8: Average R(g) (nm) of both daptomycin models measured over time (ns). 63
Figure 3.9: RMSD (nm) of both daptomycin models over time (ns). 64
Figure 3.10: Analysis of Ca^{2+} ions with both daptomycin models - A) number of contacts <0.6 nm between daptomycin and Ca^{2+} ions over time (ns) and B) average minimum distance between daptomycin and Ca^{2+} ions over time (ns). The Ca^{2+} ions conjugated to the centre of the loop in the Ca^{2+} model have been omitted from this analysis. 65
Figure 3.11: The 5 most common conformations of daptomycin models within each system based on conformational cluster analysis. The percentage each cluster represents is shown in the bottom right corner of each cluster. The molecules are shown in cyan with the exception of the aspartates shown in green. 66
Figure 3.12: Snapshot of 15 daptomycin models, non-Ca^{2+} and Ca^{2+} conjugated structure (cyan, red, blue and white) at end of 2.5 μs

simulations with *S. aureus* membrane (green). Solvent has been omitted for clarity. 67
Figure 3.13: Densities of daptomycin models *S. aureus* membrane lipid heads, tails and solvents. Measured over last 100 ns of simulations. 68
Figure 3.14: Membrane thickness of S*. aureus* membrane with different daptomycin models. Measured over last 100 ns of simulations..... 69
Figure 3.15: Phosphate densities kg/m^3) in Y direction of *S. aureus* membrane with different daptomycin models. Measured over last 100 ns of simulations. 70
Figure 3.16: APL of the lipids in *S. aureus* membrane with different daptomycin models measured over time. 71
Figure 3.17: Deuterium order parameters (Scd per atom) of each lipid tail chain calculated over each simulation. 72
Figure 3.18: SASA for polar and hydrophobic regions of over time. 74
Figure 3.19: Number of contacts <0.6 nm between *S. aureus* lipids and daptomycin models measured over time (ns). Data has been normalised to account for difference in lipid numbers. 75
Figure 3.20: Analysis of Ca^{2+} ions with both daptomycin models - A) number of contacts <0.6 nm between daptomycin and Ca^{2+} ions over time and B) average minimum distance between daptomycin and Ca^{2+} ions over time. The Ca^{2+} ions conjugated to the centre of the loop in the Ca^{2+} model have been omitted from this analysis. 76
Figure 3.21: Snapshots of end point simulations (1 us) of non-Ca^{2+} daptomycin molecule and Ca^{2+} conjugated daptomycin (both in cyan, red, blue and white) molecule in PC (lilac) and *S. aureus* (green) membranes. Solvent and counter ions have been omitted for clarity. . 79
Figure 3.22: Densities of both daptomycin models with PC and *S. aureus* membrane lipid heads, tails and solvents. Measured over last 100 ns of simulations. 81
Figure 3.23: Membrane thickness of PC and *S. aureus* membranes with different daptomycin models. Measured over last 100 ns of simulations. 82

Figure 3.24: Phosphate densities in Y-direction of PC and *S. aureus* membranes with different daptomycin models. Measured over last 100 ns of simulations. 83
Figure 3.25: APL of the lipids in PC and *S. aureus* membranes with different daptomycin structures measured over time. 84
Figure 3.26: Z coordinates of different daptomycin loops and tails relation to the top and bottom leaflet of membranes over time. 86
Figure 3.27: Deuterium order parameters of each lipid tail chain calculated over each simulation. 87
Figure 3.28: Snapshots of end point (1 μs) of 5 daptomycin molecules (cyan, red, blue and white) with *S. aureus* membrane (green). Solvent and ions have been omitted for clarity. 90
Figure 3.29: Densities of both daptomycin models *S. aureus* membrane lipid heads, tails and solvents. Measured over last 100 ns of simulations. 91
The membrane thickness, Figure 3.30, showed that the membrane containing the Ca^{2+} daptomycin molecules was slightly thinner than the one with the non-Ca^{2+} model. This suggests that this realistic membrane model was more disrupted by the Ca^{2+} bound daptomycin. 91
Figure 3.30: Membrane thickness of *S. aureus* membrane with different daptomycin models. Measured over last 100 ns of simulations..... 92
Figure 3.31: Phosphate densities in Y-direction of *S. aureus* membrane with different daptomycin models. Measured over last 100 ns of simulations. 92
Figure 3.32: APL of the lipids in *S. aureus* membrane with different daptomycin models measured over time. 93
Figure 3.33: Deuterium order parameters (Scd per atom) of each lipid tail chain calculated over each simulation. 94
Figure 3.34: Number of contacts <0.6 nm between *S. aureus* lipids and daptomycin models measured over time (ns). Data has been normalised to account for difference in lipid numbers 95

Figure 3.35: Z-coordinates of different daptomycin loops and tails relation to top and bottom leaflet of membranes over time. 97
Figure 3.36: Analysis of Ca^{2+} ions with both daptomycin models - A) number of contacts <0.6 nm between daptomycin and Ca^{2+} ions over time and B) average minimum distance between daptomycin and Ca^{2+} ions over time. The Ca^{2+} ions conjugated to the centre of the loop in the Ca^{2+} model have been omitted from this analysis. 99
Figure 4.1: Structure of chlorhexidine highlighting biguanides, hexamethylene bridge and 4-chlorophenyls. 101
Figure 4.2: Structure of guanidine unit. 102
Figure 4.3: Structure of gluconate. 103
Figure 4.4: Snapshots of chlorhexidine only simulations at time = 200 ns, shown in cyan, blue and white with cations in red and anions in green. The solvents are listed above each snapshot. Water has been omitted for clarity. 105
Figure 4.5: Superposition of the first five clusters onto RMSD of all frames to show the frequency of those conformations of chlorhexidine. 108
Figure 4.6: Cluster sizes showing all the conformations that fall into a cluster as well as the outliers that did not in red, with solvent shown above. 109
Figure 4.7: The conformations of chlorhexidine (cyan, blue and white) in the 5 most common clusters in each simulation. The percentage each cluster represents is shown in the bottom right corner of each cluster. 110
Figure 4.8: Average R(g) of each chlorhexidine in each simulation with the added solvent shown. 111
Figure 4.9: Average distance between chlorine atoms (cyan) on either end of each chlorhexidine (blue) in each simulation with the added solvent shown. This aimed to show whether the hexamethylene bridge was bending and if this was dependent on the available ions. 112

Figure 4.10: Average SASA of all chlorhexidine with added solvent shown..... 113
Figure 4.11: Average number of contacts between chlorhexidine and A) anions and B) cations, with the solvent shown. This data was normalised to each chlorhexidine with an average ion due to the different availability of ions in each simulation. 115
Figure 4.12: The RDF was calculated to show the probable distances between chlorhexidine molecules in each simulation, with the added solvents shown. 116
Figure 4.13: The RMSF of each atom was calculated to show the mean fluctuations each atom in chorhexidine with respect to the starting structure over time, with the added solvents shown. This too aimed to show the effect of ion availability on the conformation of chlorhexidine. 117
Figure 4.14: Snapshots of chlorhexidine (cyan, blue and white) with *S. aureus* membrane (green) simulations time = 200 ns. The solvents are listed above each snapshot and gluconate shown in orange. Water and ions have been omitted for clarity. 119
Figure 4.15: Densities of chlorhexidine, lipid head-groups and tails, solvent and gluconate where relevant. Calculated for the last 20 ns of the simulation. 122
Figure 4.16: Superposition of the first five clusters onto RMSD of all frames to show the frequency of those conformations of chlorhexidine with the membrane, with the solvent shown above. 124
Figure 4.17: Cluster sizes showing all the conformations that fall into a cluster as well as the outliers that did not in red, with solvent shown above. 125
Figure 4.18: The conformations of chlorhexidine (cyan, blue and white) in the 5 most common clusters in each simulation. The percentage each cluster represents is shown in the top left corner of each cluster. 126
Figure 4.19: Membrane thickness of each simulation. 127

Figure 4.20: Deuterium order parameters of each lipid tail chain calculated over the simulation..... 129
Figure 4.21: APL over each simulation. 130
Figure 4.22: Average SASA of each chlorhexidine throughout the simulation. 131
Figure 4.23: Average distances between chlorine atoms (cyan) on either end of each chlorhexidine (blue) in each simulation with the added solvent shown. This aimed to show whether the hexamethylene bridge was bending and if this was dependent on the available ions. 132
Figure 4.24: The average number of contacts less than 0.6 nm between chlorhexidine and lipid heads and tails. 133
Figure 4.25: Average number contacts between chlorhexidine and different lipid head-groups. This has been normalised to per lipid due to the differing numbers of each lipid type in the membrane. 135
Figure 4.26: Z-coordinates of 4 random chlorhexidine in each simulation in relation to top and bottom leaflet of membrane over time. Note that jumps across the membrane at the beginning of the simulation are a remnant of PBCs and chlorhexidine does not cross the membrane..... 137
Figure 5.1: Snapshots of chlorhexidine (cyan, blue and white) with *S. aureus* membrane simulations at 500 ns, with the membranes shown in green and pink for CHARMM and GROMOS force field simulations respectively. The solvents and force field are listed above each snapshot. Water and ions have been omitted for clarity. 145
Figure 5.2: Densities of chlorhexidine, lipid head-groups and tails and solvent. This was calculated for the last 20 ns of the simulation. The force fields are shown above. 146
Figure 5.3: Membrane thickness of each simulation. The force fields are shown above. 147
Figure 5.4: Phosphate density of lipid head-groups phosphates in Y-direction. The force fields are shown above. 148
Figure 5.5: Average number contacts between chlorhexidine and different lipid head-groups, less than 0.6 nm, over time. This has been

normalised to per lipid due to the differing numbers of each lipid type in the membrane. The force fields are shown above. 149
Figure 5.7: APL over each simulation over time. The force fields are shown above. 152
Figure 5.8: Hydrogen bonds between chlorhexidine and each A) PG B) Lysl-PG and B) DPG lipid on average over time. The donor acceptance distance was set to 3.0 A and the angle cut off 20 degrees..... 154
Figure 5.9: The average number of contacts less than 0.6 nm between chlorhexidine and lipid heads and tails over time. This was normalised due to the greater number of tails than heads. The force fields are shown above. 155
Figure 5.10: Average number of contacts between chlorhexidine and cations over time. This data was normalised to each chlorhexidine with an average ion due to the different availability of ions in each simulation. The force fields are shown above. 156
Figure 5.11: Average distance between chlorine atoms (cyan) on either end of each chlorhexidine (blue) in each simulation over time. The force fields are shown above. 157
Figure 5.12: Z coordinates of 4 random chlorhexidine molecules in each force field system in relation to top and bottom leaflet or membrane over time. Note that the jumps across the membrane at the beginning of the simulation are a remnant of PBCs and chlorhexidine does not cross the membrane. 159
Figure 5.13: Snapshots of pore formation in electroporation simulations. The phosphate heads are shown in lime green and pink for CHARMM and GROMOS systems respectively, whilst chlorhexidine is in cyan, blue and white and water in lilac. Lipid tails have been omitted for clarity. The force fields are shown above. 164
Figure 5.15: Densities of chlorhexidine, lipid head-groups and tails and solvent. This was calculated for the last 20 ns of the simulation. The force fields are shown above. 165

Figure 5.16: Membrane thickness of each electroporation simulation. The force fields are shown above. 166
Figure 5.17: Phosphate density of lipid head groups' phosphates in y-direction in electroporation simulations. The force fields are shown above. 167
Figure 5.18: Average number contacts between chlorhexidine and different lipid head-groups over time. This has been normalised to per lipid due to the differing numbers of each lipid type in the membrane. The force fields are shown above. 168
Figure 5.19: Number of hydrogen bonds between chlorhexidine and each A) PG B) Lysl-PG and C) DPG lipid on average over time. The data has been normalised to represent the different number of lipids available in each system. The donor acceptance distance was set to 3.0 A and the angle cut off 20 degrees. 171
Figure 5.20: APL over each electroporation simulation over time. The force fields are shown above. 172
Figure 5.21: SASA of chlorhexidine over time in each electroporation simulation. The force fields are shown above. 173
Figure 5.22: The average number of contacts less than 0.6 nm between chlorhexidine and lipid heads and tails over time. This was normalised due to the greater number of tails than heads. The force fields are shown above. 174
Figure 5.25: Z-coordinates (nm) of 4 random chlorhexidine molecules in each force field system in relation to top and bottom leaflet or membrane over time in electroporation simulations. Note that the jumps across the membrane at the beginning of the simulation are a remnant of PBCs and chlorhexidine does not cross the membrane..... 175
Figure 6.1: Schematic showing TLR relay for bacterial LPS recognition. 178
Figure 6.2: Snapshots showing progress of simulations showing point of aggregation at 0.25 μs and the end point of 1 μs. LTA, PGN and LPS are shown in purple with the TCP shown in various other colours..... 181

Figure 6.3: Mean intermolecular distance between TCP96 fragments following co-aggregation simulations in the presence/absence of the microbial products. The black boxes in the centre of each matrix were to omit self-contact. 182
Figure 6.4: The RDF measuring the probability of TCP96 distances with other TCP96 molecules. 184
Figure 6.5: The probable average distance between TCP96 molecules in each system. This was measured for each 200 ns section of the simulation with the average shown. The P-value in reference to the TCP only probable distance shows they are all significantly different from the control. The error bars are the standard deviation taken from the averages. 185
Figure 6.6: Superposition of the first five clusters onto RMSD of all frames to show the frequency of those conformations of TCP96 in the presence and absence of microbial products. 187
Figure 6.7: Cluster sizes of TCP96 conformations in the presence and absence of microbial products that fall into a cluster as well as the outliers from any cluster in red. 189
Figure 6.8: Number of contacts <0.6 nm between TCP96 and antimicrobial products over time. 190
Figure 6.9: Minimum distance between TCP96 and microbial products over time. 190
Figure 6.10: R(g) of TCP96 molecules over time in the presence and absence of microbial products. 191
Figure 6.11: Snapshots showing progress of simulations showing point of aggregation at 0.25 μs and the end point of 1 μs. LTA and PGN are shown in purple with the TCP shown in various other colours. 193
Figure 6.12: Mean intermolecular distance between TCP96 fragments following co-aggregation simulations in the presence/absence of the microbial products. The black boxes in the centre of each matrix were to omit self-contact. 194

Figure 6.13: The RDF measuring the probability of TCP96 distances with other TCP96 molecules with differing ratios of TCP:LTA/PGN. 196
Figure 6.14: The probable average distance between TCP96 molecules in each system. This was measured for each 200 ns section of the simulation with the average shown. The P-value in reference to the probable distance in the 1:1 ratio simulation shows they are all significantly different from the control. The error bars are the standard deviation taken from the averages. 197
Figure 6.15: Superposition of the first five clusters onto RMSD of all frames to show the frequency of those conformations of TCP96 in the presence and absence of microbial products. 199
Figure 6.16: Cluster sizes of TCP96 conformations in the presence and absence of microbial products that fall into a cluster as well as the outliers from any cluster in red. 201
Figure 6.17: SASA of TCP96 molecules in the presence and absence of LTA and PGN at differing ratios. 202
Figure 6.18: Minimum distance between TCP96 and different ratios of LTA and PGN over time. 203
Figure 6.19: R(g) (nm) of TCP96 molecules over time (ns) in the presence LTA and PGN at differing ratios. 203
Figure 6.20: R(g) of LTA and PGN in the presence of TCP96 at differing ratios over time. 204
A.1: The 5 most common conformations of daptomycin models within each system based on conformational cluster analysis in systems with 15 daptomycin molecules and *S. aureus* membrane. The molecules are shown in cyan, red blue & white, with the exception of the aspartates shown in green. The percentage each cluster represents is shown in the bottom right corner of each cluster. 206
Figure A.2: Deuterium order parameters (Scd per atom) of each lipid tail chain calculated over the simulations at equilibrium. The force fields are shown above. 207

Figure A.3: Deuterium order parameters (Scd per atom) of each lipid tail chain calculated over the electroporation simulations. The force fields are shown above. 208
Figure A.4: The conformations of TCP96 in the 5 most common clusters in each simulation in the presence of different bacterial products. 209
Figure A.5: The conformations of TCP96 in the 5 most common clusters in each simulation with 1:2 ratio of TCP:/LTA. 210

List of Tables

Table 3.2: The lipid diffusion rates of lipids in *S. aureus* with both daptomycin models. Measured between 1.5-2 μs..... 73
Table 3.3: Simulations in the second section of the daptomycin work researching daptomycin PG dependence. 78
Table 3.4: The lipid diffusion rates of lipids in *S. aureus* with both daptomycin models. Measured between 400-800 ns. 88
Table 3.5: Simulations in the third section of the daptomycin work researching daptomycin interaction with the *S. aureus* membrane. 89
Table 3.6: The lipid diffusion rates of lipids in *S. aureus* with both daptomycin models. Measured between 400-800 ns. 96
Table 4.1: Table of simulations of chlorhexidine with differing salts but without *S. aureus* membrane. 104
Table 4.2: Table of simulations of chlorhexidine with differing salts with *S. aureus* membrane. 118
Table 4.3: The lipid diffusion rates of lipids throughout each simulation.....130
Table 5.1: List of simulations with differing force fields and ion availability.....143
Table 5.2: The lipid diffusion rates of lipids throughout each simulation.....150
Table 5.3: List of simulations with differing force fields, electric fields and ion availability.....163
Figure 5.14: Snapshots of end point of low electric field simulations, 500 ns. Lipids are shown in lime green and pink for CHARMM and GROMOS systems respectively, whilst chlorhexidine is in cyan, blue and white. Water and ions have been omitted for clarity. The force fields are shown above. 164
Table 6.1: Contents, solvent and length of simulations conducted. 180

Table 6.2: Contents, solvent and length of simulations conducted, varying the ratio of LTA/PGN to TCP. 192

List of Accompanying Materials

DOI for data set underpinning thesis: https://doi.org/10.5258/SOTON/D1791

Data set name: Eilish McBurnie PhD Thesis MetaData

Research Thesis: Declaration of Authorship

Print name: Eilish Walker McBurnie

Title of Thesis: Molecular Dynamics Simulations of Complex Bacterial Membranes.

I declare that this thesis and the work presented in it are my own and have been generated by me as the result of my own original research.

I confirm that:

1.This work was done wholly or mainly while in candidature for a research degree at this University;

2.Where any part of this thesis has previously been submitted for a degree or any other qualification at this University or any other institution, this has been clearly stated;

3.Where I have consulted the published work of others, this is always clearly attributed;

4.Where I have quoted from the work of others, the source is always given. With the exception of such quotations, this thesis is entirely my own work;

5.I have acknowledged all main sources of help;

6.Where the thesis is based on work done by myself jointly with others, I have made clear exactly what others and what I have contributed myself did;

7.Parts of this work have been published as: J. Petrlova, G. Petruk, R.G. Huber, E.W. McBurnie, M.J.A. van der Plas, Peter J. Bond, M. Puthia, A. Schmidtchen, *Journal of Biological Chemistry,* 2020, 295(11):3417-3430.

Signature: Date:

Acknowledgements

I owe a huge thank you to both of my supervisors, Professor Syma Khalid and Dr. Peter Bond, for providing ceaseless support, advice and insight throughout my PhD. I am grateful to them for not only ensuring my projects were running smoothly but also giving me the incredible opportunity to work in two amazing groups.

I would also like to thank both the Khalid and Bond groups, both past and present, for their hands on help, insightful discussions and their friendship making the transitions to Southampton and Singapore enjoyable. I would like to particularly thank my friend and flatmate in Southampton and Singapore, Lauren Reid.

The support of my family and friends has been invaluable throughout this process. Thank you to my husband, Adam Patmore for his unwavering confidence and love that have brought us through every storm and for never allowing me to doubt my ability to reach this goal. I would like to thank my whole family for their support, especially my parents, Neil & Jennifer McBurnie. I could never have reached this stage without their encouragement and sacrifices. Thank you for their unconditional love and support that made this achievement possible. Finally, I'd like to thank my friends, particularly Sarah Kinnaird, Ciara Diamond & Ryan McNair, for seeing me through the highs and lows of the last four years with a glass of wine in hand.

I would like to dedicate this work in memory of my grandfathers, Eric McBurnie and George Dickson, who are both very missed and vital to me reaching this goal through their encouragement, support and belief.

Definitions and Abbreviations

AA All atom

APL Area per lipid

ATB Automated topology builder

CG Coarse-grained

DPG Diphosphatidylglycerol

IM Inner Membrane

LBP LPS binding protein

LJ Lennard Jones

LPS Lipopolysaccharides

LTA Lipoteichoic acids

Lysl-PG Lysl-phosphatidylglycerol

MD Molecular dynamics

MD-2 Myeloid differentiation factor 2

OM Outer Membrane

PAMP – Pathogen-associated molecule pattern

PBP Penicillin binding protein

PBC Period boundary condition

PC Phosphatidylcholine

PG Phosphatidylglycerol

PGN Peptidoglycan

PGN Peptidoglycan

PME Particle Mesh Ewald

R(g) Radius of gyration

RDF Radial distribution function

RMSD Root mean squared deviation

RMSF Root mean square fluctuation

SASA Solvent accessible surface area

TCP Thrombin-derived C-terminal peptide

TCP96 96 Amino acid TCP

TLRs Toll-like receptors

UA united atom

VDW Van der Waals

WF Antifreeze

Chapter 1 - Introduction

This chapter provides an introduction to the background biology that constitutes the foundations and motivations of the original research presented later in the thesis.

1.1 Bacterial Cells

Prokaryotes are unicellular organisms that do not traditionally have any membrane bound organelles. An organelle is any subunit within the cell that performs a specialised function, such as the nucleus or ribosomes in eukaryotic cells. Prokaryotes are divided into two groups, bacteria, the focus of this work, and Archaea. Bacterial cells come in a range of shapes, or morphologies, as shown schematically in Figure 1.1.

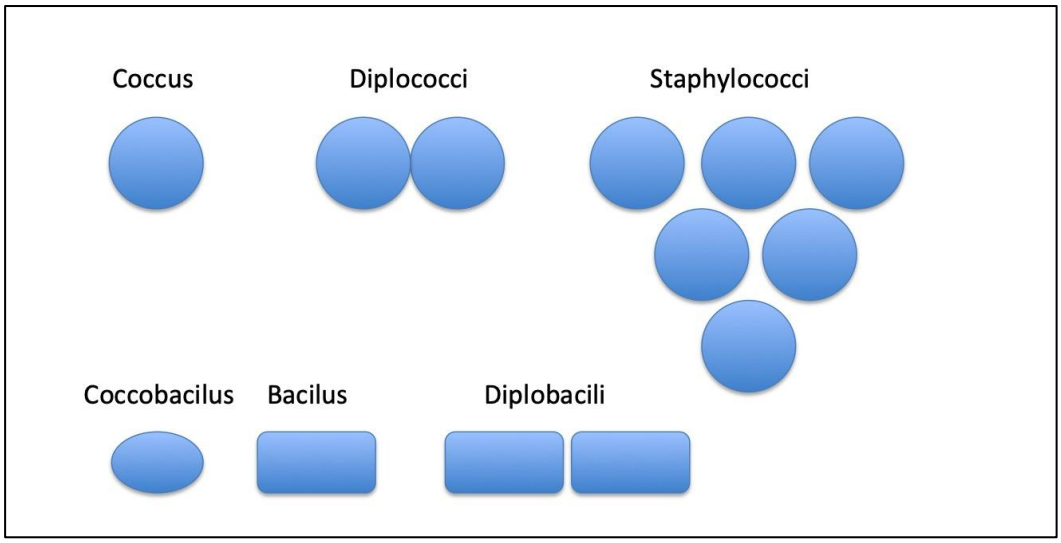

Figure 1.1: Simplified examples of bacterial morphology[1].

Bacteria are broadly divided into two categories, Gram-negative and Gram-positive. This terminology comes from the differences in the way they respond to a stain known as Gram's stain. Gram-positive bacteria become stained violet when treated with the stain, whereas Gram-negative bacteria do not[2]. These differences arise due to the architecture of their respective cell envelopes.

1.2 Bacterial Cell Envelopes

1.2.1 Gram-negative Bacterial Cell Envelopes

The Gram-negative envelope is comprised of an inner membrane (IM), an outer membrane (OM) and an aqueous region known as the periplasm, which contains a cell wall of composed peptidoglycan[2] (Figure 1.2). The precise number of layers of the cell wall differs between species of Gram-negative bacteria.

Beginning from the outside of the cell inwards, the first layer met is the OM. The OM is a lipid bilayer but notably not a pure phospholipid bilayer; rather only the inner leaflet of the OM contains phospholipids. The OM outer leaflet is made of glycolipids, specifically lipopolysaccharides (LPS) that protrude far from the core of the OM, from 40-100 nm with this length dependent on species[3]. LPS provides much of the protective aspects of the OM as it is a formidable barrier, which antibiotics and antiseptics must either disrupt or negotiate to gain access to the interior of the cell[4]. A large number of transmembrane proteins inhabit the OM. They can be broadly categorised into lipoproteins and beta barrel proteins such as the porins[5].

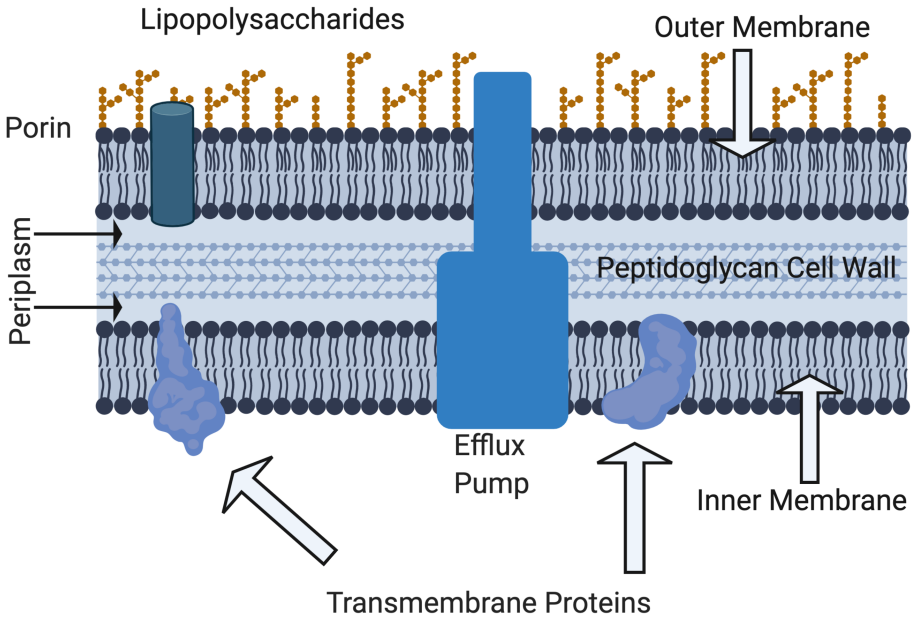

Figure 1.2: Schematic showing some of the key features of the Gram-negative cell envelope.

The peptidoglycan cell wall of Gram-negative bacteria acts as an exoskeleton providing protection and structure to the cell. Peptidoglycan is composed of repeating disaccharide N-acetyl glucosamine-N-actyl muramic acid units, which are cross-linked by pentapeptide side chains[6]. The OM is attached to the underlying peptidoglycan by a lipoprotein known as Braun's lipoprotein (Lpp or BLP)[7]. Comparatively, the IM is relatively simple in composition. It contains phospholipids in both membranes although it has recently been shown that the two leaflets are not identical in composition[8]. The proteins embedded in the IM are based on a helical architecture (either a single helix or multiple helices connected by loops or short turns). The lipids within the IM vary between species of Gram-negative bacteria[9].

1.2.2 Gram-positive Bacterial Cell Envelopes

The Gram-positive cell envelope is distinct in several ways from the Gram-negative envelope, Figure 1.3. Importantly, Gram-positive bacteria lack an OM.

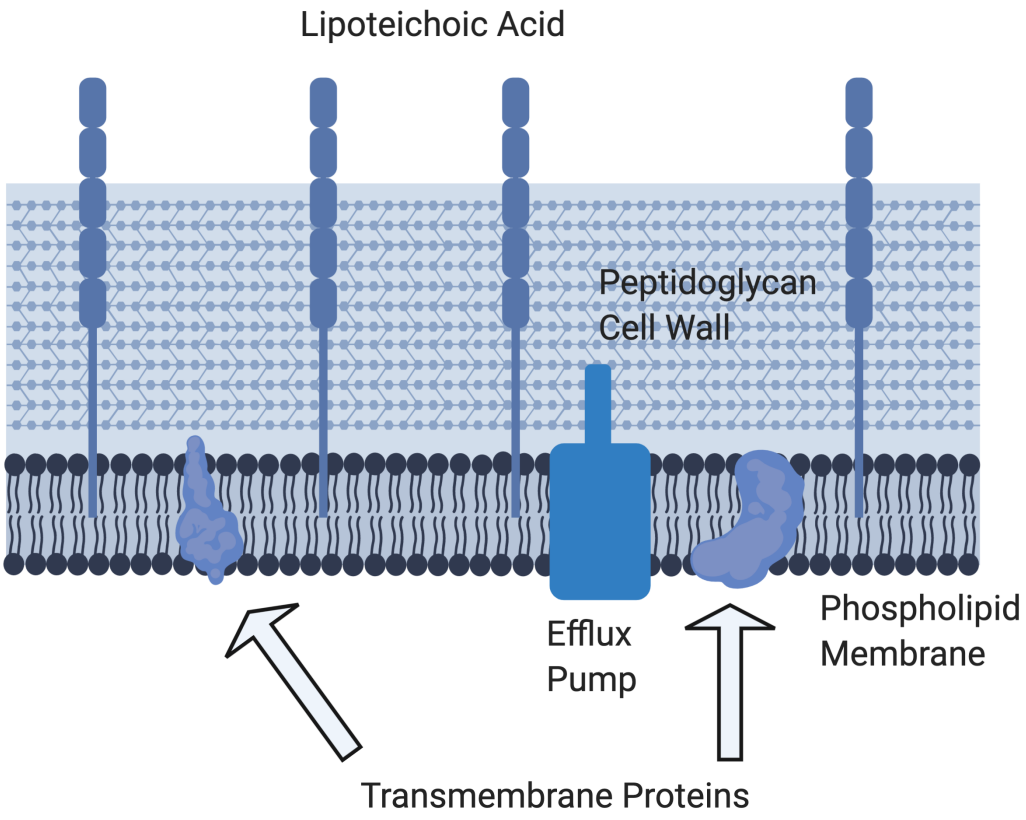

Figure 1.3: Schematic showing some of the key features of the Gram-positive cell envelope.

In order to account for the loss in protection and structure from not having an OM, Gram-positive bacteria have a thicker peptidoglycan cell wall. Whilst the compositions of cell walls between bacterial types are similar, Gram-negative bacteria tend to only have a few layers of peptidoglycan whilst the Gram-positive cell wall can be 30-100 nm thick with many layers[6]. Threading through these layers of peptidoglycan are long anionic polymers called teichoic acids that are largely made of glycerol phosphate, glucosyl phosphate or ribotol phosphate units. Lipoteichoic acid (LTA) is an important teichoic acid, particularly in regards to the immune system recognising Gram-positive infections, and is attached to the phosphates heads of the lipid within the bilayer[10]. The lipid composition of the Gram-positive membrane is similar to the Gram-negative IM. It is a symmetrical membrane composed of phospholipids that again vary between species of Gram-positive bacteria[11].

There are many examples of Gram-positive bacteria; one of the most studied and the focus of a great deal of this work is *Staphylococcus aureus.*

1.3 *Staphylococcus aureus*

S. aureus is a very common and well understood Gram-positive bacterium and so was used for this work. Whilst *S. aureus* is a commensal bacterium, with an estimated 30% of the population hosting reservoirs, most of which will not experience an infection, in certain circumstances it can cause serious illness[12]. Whilst its presence is most common in the nares, it is also commonly found in broken skin, pharynx, vagina as well as catheters[12]. Due to this diversity of possible locations in a host and the variety of pathogenic mechanisms, *S. aureus* can cause illnesses ranging from relatively mild ailments such as impetigo and cellulitis to extremely virulent conditions including toxic shock syndrome, endocarditis and bacteraemia, particularly catheter related infections[13,14]. Whilst the more mild conditions are usually easily treated by less specialised antibiotics, bacteraemia and endocarditis are increasingly being treated with daptomycin due to the rise of MRSA and the growing knowledge of the

limitations and tendency for staphylococcal resistance of late stage antibiotics such as vancomycin[13–15].

Due to the range and concern of infections caused by *S. aureus,* its membrane must be well understood and has been extensively studied. *S. aureus* is a Gram-positive, non-motile cocci bacterium. As with all other Gram-positive bacteria, the cell envelope structure consists of a single lipid membrane with an outer thick peptidoglycan (cell wall) tethered to the membrane by diacylglycerol[16]. Beyond the single membrane, a 20-80 nm thick peptidoglycan wall surrounds it. For comparison, the Gram-negative wall is usually a monolayer ranging between 5-10 nm. The cell wall contains covalently bonded cell wall polymers such as teichoic acid. Teichoic acid is understood to be important to cell shape, division and needed for beta-lactam resistant MRSA[16,17]. In regards to the cell membrane, other components include protein A, which is integral to *S. aureus* cell signalling and again cell attachment, as well as alpha-hemolysin channels[18]. These channels are embedded within the cell membrane and form spontaneous ion channels, within freestanding bilayer lipid membranes, which allow cells to have a resting membrane potential[19].

This work in this thesis focused on how the antimicrobials interacted with the cell membrane and did not include the cell wall. Focusing on *S. aureus,* the membrane is made up of phosphatidylglycerol (PG), diphosphatidlyglycerol/cardiolipin (DPG) and lysl-phosphatidylglycerol (Lysl-PG)[20]. Notably, LPG is unique to *S. aureus* and is positively charged unlike the negatively charged PG and DPG or neutral lipids found in other Gram-positive bacterial membranes such as phosphatidylcholine, (PC). This is thought to aid *S. aureus* to be resistant to membrane disrupting properties of cationic antimicrobials[14,21]. The structures of PG, Lys-PG and DPG are shown in Figure 1.4.

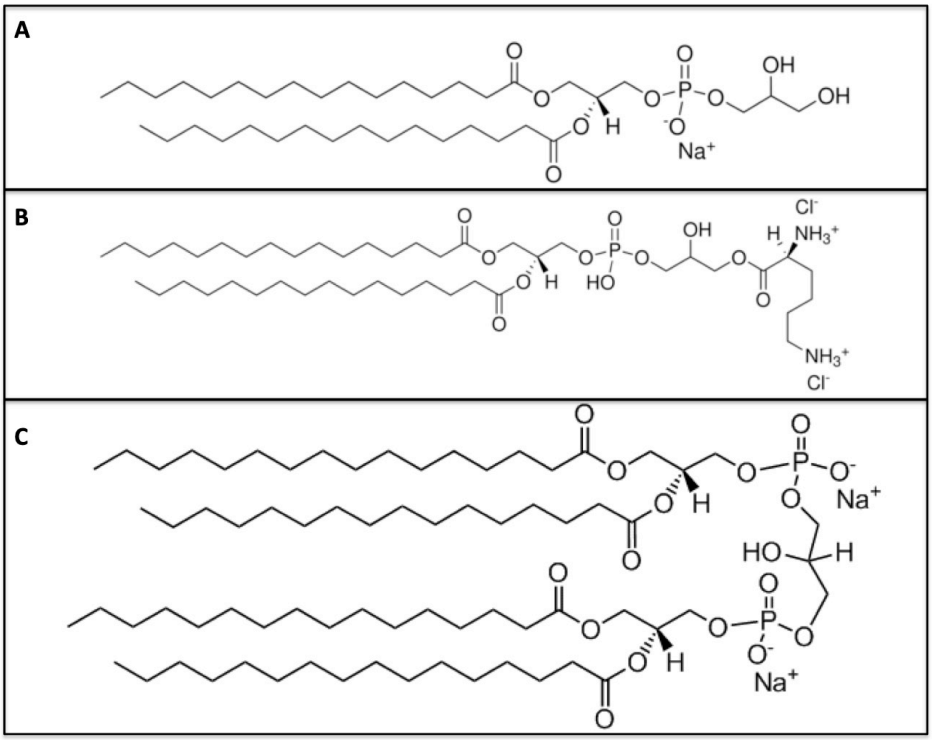

Figure 1.4: *S. aureus* lipids A) PG B) Lysl-PG and C) DPG.

1.4 Antibiotics

Due to the broad spectrum of infections caused not only by *S. aureus* but also other Gram-positive and Gram-negative bacteria, antibiotics are a corner stone of modern medicine. Antibiotics are generally classified based upon their mechanism of action with antibiotics aimed at a plethora of bacterial cell targets. The main classes of antibiotics and some examples of each will be discussed below[22].

1.4.1 Inhibitors of Protein Biosynthesis

Firstly, some antibiotics target protein biosynthesis. Protein biosynthesis in bacteria are controlled by the 70s ribosome which is comprised of two ribonucleoprotein subunits, 30S and 50S. Antimicrobials inhibit protein biosynthesis by targeting the 30S subunit, such as tetracycline, or the 50S subunit, such as macrolides, of the bacterial ribosome[23]. This activity stops the bacterial cell from being able to produce proteins essential to its function and replication[24].

1.4.2 Inhibitors of DNA/RNA Replication

Antibiotics can also directly inhibit DNA. Quinolones inhibit bacterial DNA gyrase, which is an enzyme important for the formation of properly replicated protein and therefore stops bacteria from replicating[25]. Similarly, drugs such as rifampin, which inhibits RNA polymerase, can target RNA synthesis therefore stopping the protein biosynthesis in a different manner[26]. An additional class of antibiotics include folic acid metabolism inhibitors with drugs such as the sulphonamides (e.g. trimethoprim). Sulphonamides inhibit an early part of folic acid metabolism dihydropteroate synthase whilst trimethoprim inhibits dihydrofolate reductase, a later component of folic acid metabolism[27]. Folic acid is necessary for bacteria to synthesize the nucleic acids needed for their DNA[28].

1.4.3 Antibiotics Targeting Cell Walls

A major class of antibiotics are those that target the bacterial envelope. As discussed, peptidoglycan is a vital structural component of both Gram-negative and Gram-positive bacterial cell walls. Beta-lactam and glycopeptides both inhibit cell wall synthesis. The glycan strands of peptidoglycan are cross-linked by transglycosidases, and the peptide chains extend from the sugars in the polymers and form cross-links, one peptide to another. The D-alanyl-alanine portion of peptide chain is cross linked by glycine residues in the presence of penicillin binding proteins (PBPs)[29]. It has been suggested that the beta-lactam ring mimics the D-alanyl D-alanine portion of peptide chain that is normally bound by PBPs. The PBP interacting with the beta-lactam ring means it cannot synthesise new peptidoglycan causing the lysis of the bacterial cell[30]. Similarly, glycopeptides bind to the D-alanyl D-alanine section of the peptide side chain of the precursor peptidoglycan subunit whilst vancomycin averts binding of this D-alanyl subunit with PBPs and therefore also inhibits cell wall synthesis[31]. The chemical structures of the antibiotics from the classes discussed this far are shown in Figure 1.5.

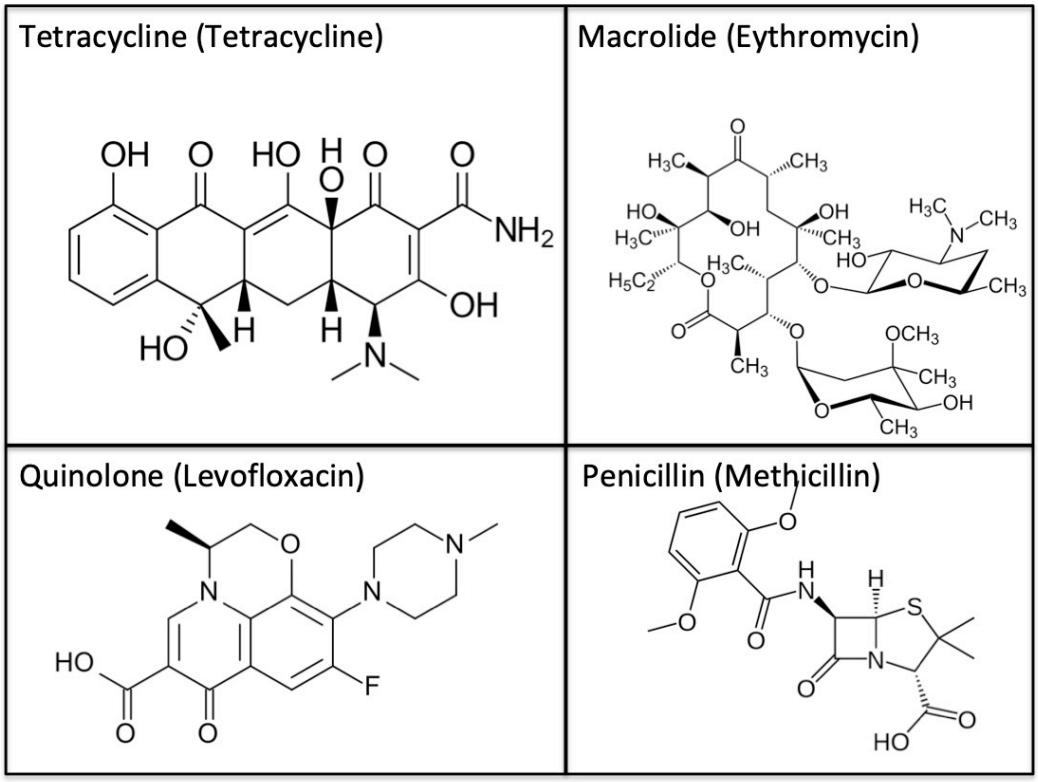

Figure 1.5: Chemical structures of examples of antibiotics from the classes discussed.

1.4.4 Antibiotics Targeting Phospholipid Membranes

The final class of antibiotics are those that target the cell membrane including polymyxin. Polymyxin binds to LPS in Gram-negative bacteria and disrupts both inner and outer membranes causing damage to the cell and eventual cell death[32]. Whilst polymyxin is effective against Gram-negative bacteria, daptomycin is a last resort antibiotic that targets the Gram-positive membrane[33]. Much of the mode of action and behaviours of daptomycin are debated and not well understood, and therefore the first chapter of this work studies this antibiotic. The chemical structures of a polymyxin antibiotic (colistin) and daptomycin are shown in Figure 1.6.

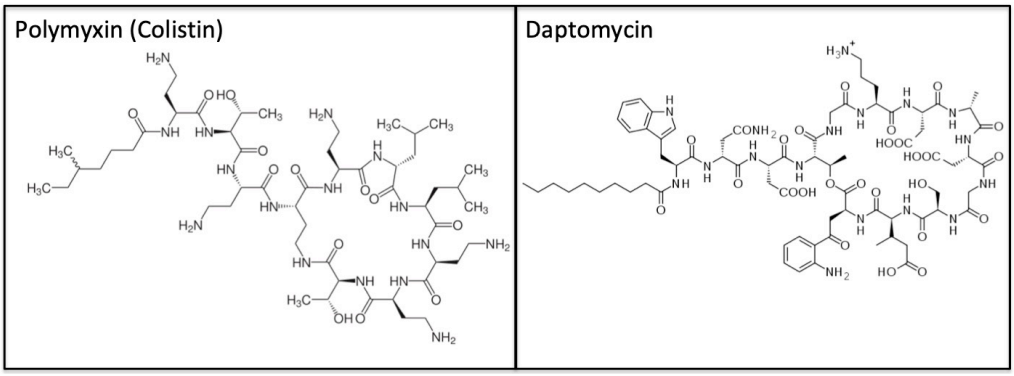

Figure 1.6: Chemical structures of polymyxin class antibiotic (colistin) and daptomycin.

Furthermore, host immune system components have been found to target phospholipid membranes. Thrombin is an enzyme produced upon injury to the skin which helps coagulation of red blood cells to help seal the wound[34]. However beyond this role, thrombin is also proteolysed by human neutrophil elastase into thrombin-derived C-terminal peptides (TCPs) of differing sizes[35]. TCPs are found in wound fluids and have been shown to have antiendotoxic and antimicrobial functions, including smaller TCPs having the capacity to permeablise liposomes[36]. Whilst some TCPs display antimicrobial behaviour, their immunomodulatory functions are studied in the final chapter of this thesis.

1.5 Antiseptics

Antibiotics are often the focus of research aimed at combatting bacterial infections, with particular emphasis on developing and understanding new and existing drug options. This is driven by the development of bacterial resistance to existing antibiotics. However, the integral role of antiseptics as a preventative, first line of defence against bacteria should not be overlooked[37]. While antibiotics work to end active bacterial infections, antiseptics are used to prevent an infection occurring in the first place, and as the adage goes 'prevention is better than cure' (although of course not always possible). Antiseptics stop or slow the growth of microorganisms. They are customarily used in hospital settings to prevent an infection by being applied on skin prior to surgery, wounds, surgical instruments and hands. Furthermore, antiseptics

can be used topically on skin infections, disinfect mucous membranes and treat throat and mouth infections[38].

There is a wide range of broad-spectrum antiseptics available, each with a distinct mechanism of action and targets. They often work by disrupting the cellular membrane, once again highlighting the importance of improving molecular-level understanding of the bacterial cell envelope[39]. The following antiseptics are amongst the most commonly used and will be discussed to give a grounding of the background of antiseptics focusing on those that act upon the cell membrane. Firstly, hydrogen peroxide is a common 'at home' prevention against infection due to its broad spectrum, affordability and rapid onset. Hydrogen peroxide forms extremely reactive free radicals that target and oxidise cellular machineries including membrane lipids[40]. However, it is not as effective against Gram-negative bacteria as it is against Gram-positive bacteria - requiring higher concentrations and longer exposure to kill the former as well as bacterial spores, fungi and viruses[40]. Furthermore, benzalkonium chloride is a cationic surfactant that acts by irrevocably binding to membrane phospholipids and proteins[41]. Although bactericidal against both Gram-positive and Gram-negative bacteria, it has limited affectivity against fungi, viruses and mycobacteria.

In addition, povidone-iodine works by oxidizing membrane lipids. It is effective against a broad spectrum of antimicrobials including bacterial spores, viruses, protozoa and fungi[42]. Moreover, isopropyl alcohol is a hydrophilic alcohol that denatures proteins and destroys the bacterial membrane[43]. Whilst having minimal residual activity and least broad spectrum, it works extremely quickly and is often used in conjunction with other antiseptics such as povidone-iodine and chlorhexidine[44]. The chemical structures of the antiseptics discussed are shown in Figure 1.7.

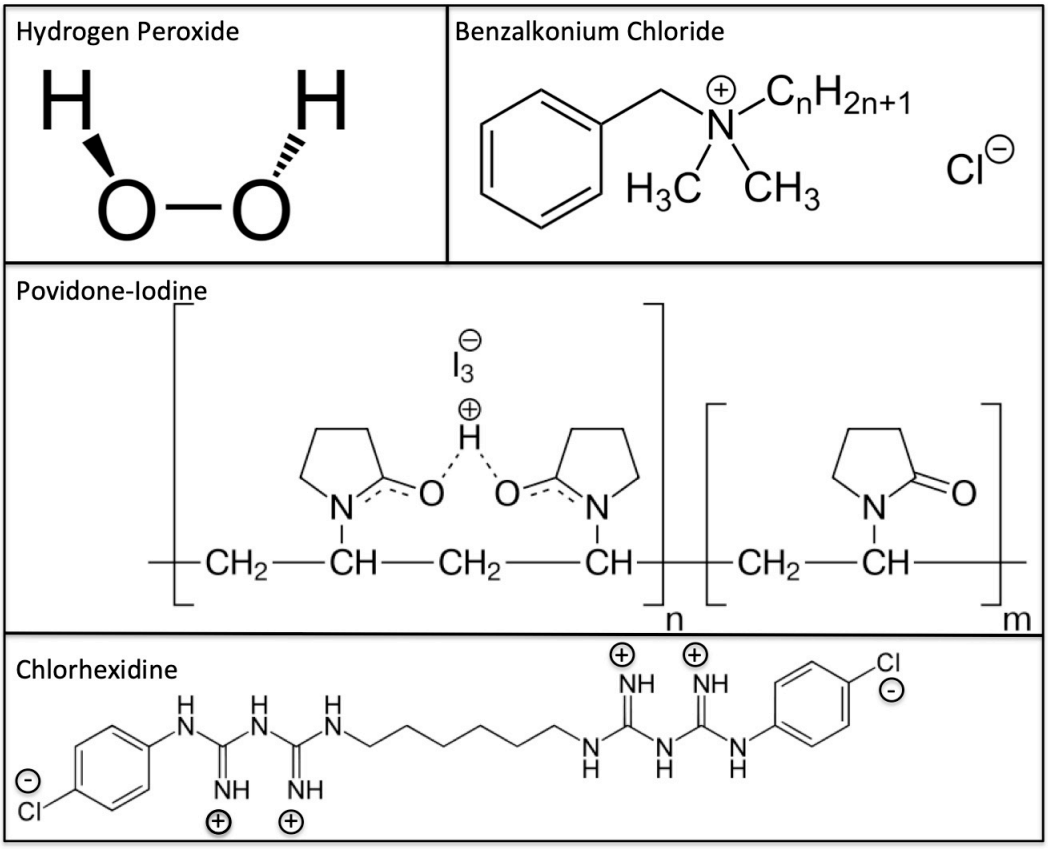

Figure 1.7: Chemical structures of the antiseptics discussed.

Chlorhexidine is one of the most popular antiseptics used and therefore the focus of this work. Notably, chlorhexidine is extensively used in surgery and dentistry, particularly in mouthwash to treat gingivitis and prevent mouth infections[45]. It is particularly popular as it has a broad spectrum, targeting Gram-negative and Gram-positive bacteria in addition to some fungi and amoeba[46]. It is effective quickly, and, unlike the other antiseptics listed, has continued action after being wiped away from skin by remaining bound to the outer layer of the epidermis[47]. This makes it preferable to the narrower target spectrum of benzalkonium chloride and the short-lived activity of povidone-iodine[48]. Based on the benefits of chlorhexidine over other antiseptics this was the antiseptic used for focus of this work.

In medical use since the 1950s, chlorhexidine is one of the safest and most effectual medicines as determined by the World Health Organization's List of

Essential medicines[41]. Chlorhexidine is used in several different manners. Firstly, chlorhexidine is used in the same manner as previously described for antiseptics, with evidence that it is more effective than similar antiseptics such as povidone-iodine. Chlorhexidine has low incidences of adverse reactions and is an inexpensive medicine, making it popular for several other uses[43]. Chlorhexidine is frequently used to treat the umbilical cord of infants[44]. Chlorhexidine has been found to reduce occurrences of umbilical cord inflammation by 50% and neonatal mortality by 12%[45]. Finally, chlorhexidine eye drops can be used in the treatment of *Acanthamoeba keratitis*[49]. As well, as with isopropyl alcohol, chlorhexidine is often used with surfactants and particularly with gluconate to improve the efficacy of the medicine[50]. The frequency of use and importance of chlorhexidine made it the focus of a great deal of this work.

1.6 Mechanisms of Bacterial Resistance to Antibiotics

Antibiotics are an extremely important aspect of modern medicine and as a society we are reliant upon them. However, bacteria are becoming increasingly resistant to a wide range of antibiotics with the World Health Organisation estimating 700,000 people die each year due to drug-resistant bacterial infections with the potential for this number to raise to 10 million by 2050[51]. Bacteria have developed different ways to become resistant to antibiotics with some of the major mechanisms discussed below.

1.6.1 Efflux Pumps

Bacteria have proteins within the membrane capable of exporting antibiotics from the cell. These proteins are called efflux pumps[52]. These pumps within the cytoplasmic membrane allow for bacteria to drive antibiotics out of the cell as quickly as they enter[53]. Efflux pumps tend to be able to transport various antibiotics, including macrolides and tetracyclines, and therefore are a large contributor of multidrug resistant organisms[52].

1.6.2 Modification of Target Molecules

Bacteria have natural variations in the target sites of antibiotics and as antibiotics are usually very specific this has become a pathway for antibiotic

resistance to develop. This can include alteration to the 30S or 50S subunit meaning drugs targeting the ribosome are ineffective[54]. Furthermore, alteration to PBP occurs often in Gram-positive bacteria and is a technique used by *S. aureus*[55].

1.6.3 Antibiotic Inactivation

Bacteria are able to inactivate antibiotics by producing enzymes that modify them, with one major example being beta-lactamases[56]. These are able to hydrolyse most beta-lactams that have ester and amide bonds such as penicillin[22]. Beta-lactamases are a defence produced by Gram-negative bacteria such as *Escherichia coli* and *Klebsiella pneumoniae*[57].

1.7 Aims

The above described biology and biochemistry demonstrates the importance of the bacterial cell envelope components in protecting bacteria from harmful substances such as antibiotics and antiseptics. Conversely from the human, animal and healthcare perspective, it is important that we understand how to make antibiotics and antiseptics that do more damage to pathogenic bacteria. In order to do this, we must first understand how existing therapeutics work against their target bacteria. It is also important to understand how hosts react to bacterial infections and how this is managed in a robust manner without causing a detrimental immune overreaction. Better understanding of the immune response to a bacterial infection could improve the outcome for those with severe bacterial infections. In respect to the duality of how antibiotics and antiseptics interact with bacteria and how host immune mechanisms interact with bacterial infections the aims of my work were as follows:

- Chapter 2 aimed to give an outline of the theory of molecular dynamics and simulation techniques.
- Chapter 3 aimed to ascertain the mode of action of daptomycin on membranes and its relationship with calcium ions.
- Chapter 4 intended to understand the behaviour of chlorhexidine in solvent with different salts and with the *S. aureus* membrane.

- Chapter 5 aimed to compare the effect of using different force fields when simulating chlorhexidine with the *S. aureus* membrane.
- Chapter 6 was designed to try and understand how bacterial envelope components are recognised by host defences.

Chapter 2 - Computational Methods

2.1 Molecular Dynamics

Currently, studying the conformational dynamics of biological molecules, such as biological membranes and their associated proteins, with atomistic or near-atomistic detail using experimental techniques is not a viable method. Due to the need for this level of accuracy to further understanding of biological questions, computational methods are becoming increasingly used. Molecular dynamics (MD) simulations are a common way of studying biological molecules over time on an atomistic level and with computational power growing MD is being employed frequently.

Classical simulations use statistical mechanics to understand the macroscopic behaviours and characteristics of a biological system or molecule by focusing on the thousands of atoms in a simulation. A computational simulation must use realistic conditions for the given system to be realistic and accurate in accordance with experimental conditions, in regards to considerations such as temperature and pressure. In addition to MD simulations, Monte Carlo is another computational method, which is not time-dependent like MD. MD is the only method used in this work.

MD utilises Newton's second law of motion to calculate the motion and position of all atoms in the system over time. MD simulations require a force field to be applied that holds all the details of the atom-atom interactions that are then used to calculate the negative gradient ($-\nabla i$) of the potential energy of the system (E_{system}). Calculating this for all of the atoms within the system gives the force exerted on the system (F_i), Equation 2.1.

$$F_i = -\nabla E_{system}$$

Equation 2.1

When the force is calculated and mass of each particle in the system (m_i) is known, Newton's second law of motion can be used to calculate the acceleration of the particles (a_i), Equation 2.2, and this concept is used to determine the dynamic behaviour of every atom in the system.

$$F_i = m_i\, a_i$$

Equation 2.2

Combining these two equations gives the updated coordinate (r_i) of the atoms. This can then be used to calculate the potential energy of the system over the simulation time (t), Equation 2.3.

$$-\frac{\delta E_{system}}{\delta r_i} = m_i \frac{\delta^2 r_i}{\delta t^2}$$

Equation 2.3

The following flowchart, Figure 2.1, displays the basic MD simulation protocol to calculate a finishing point from using the previous equations to determine potential energy and the motion of the atoms.

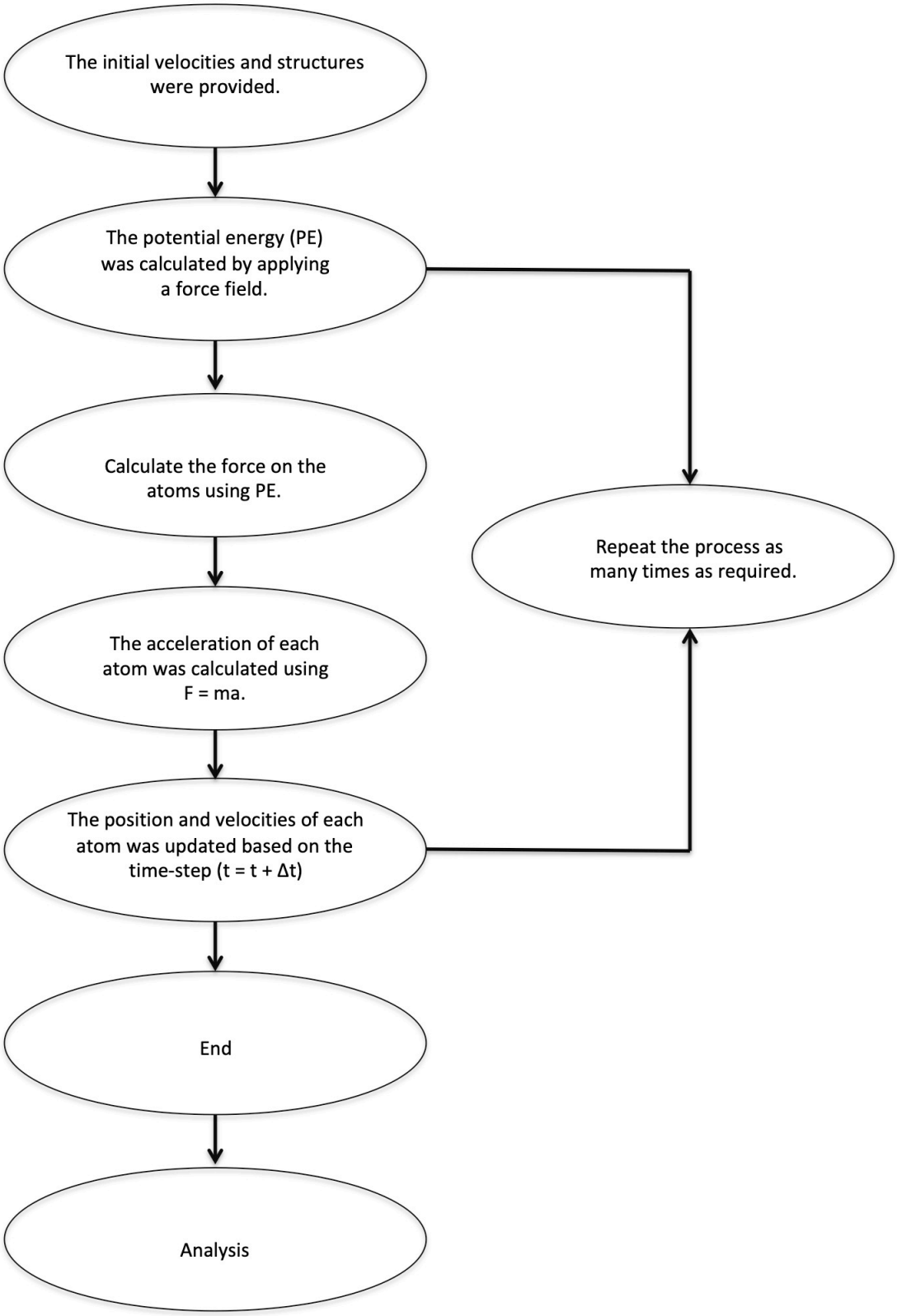

Figure 2.1: Diagram showing the basic method of MD simulations.

2.2 The Integrator

Usually, the force acting on each particle is dependent upon its position relative to other particles. This in conjunction with the nature of the motion of the particle gives rise to a complex problem meaning the equations of motion cannot be solved analytically. This means integrators are used to integrate the equations of motion numerically. Integration algorithms employ Taylor series expansions to estimate new atomic positions, velocities and accelerations as each time step passes. Integrators work by using the acceleration from the previous time-step from the force of an atom, the initial position and velocity at time *t* to determine these parameters at the next time step, $t + \delta t$. Whilst the position and velocity is updated with each time step, the force remains the same. The main algorithms used in MD are the leap-frog and Verlet algorithm[58,59]. The leap-frog algorithm was used in this work.

2.2.1 Leap-frog Algorithm

The leap-frog algorithm works by initially calculating the velocities *v* at time step ($t+1/2\delta t$) from the first velocity at half time step ($t-1/2\delta t$) and acceleration *a* at time step *t,* shown in Equation 2.4. The positions, *r*, are determined at ($t+\delta t$) using the velocity calculated in Equation 2.5. The positions are updated by leaping over the velocity to give their new values at time step ($t+\delta t$). Finally the velocity can be again determined at time step ($t+3/2\delta t$) repeating until the simulation has completed.

$$v(t+\tfrac{1}{2}\delta t) = v(t-\tfrac{1}{2}\delta t) + \delta t[a(t)]$$

Equation 2.4

$$r(t+\delta t)=r(t)+\delta t[v(t+\tfrac{1}{2}\delta t)]$$

Equation 2.5

2.2.3 The Time-step

The regularity of which the potential energy of the systems is recalculated to acquire the new velocity and acceleration to update the atom positions is determined by the time-step. The atomistic simulations in this work used a time step of 2 fs meaning that the positions are updated this often as per the MD protocol previously described. In order to do this, hydrogen-containing bonds are constrained using the LINCS option within GROMACS[60]. Choosing the appropriate time-step is vital, if it is too small the simulation will be very computationally expensive then the trajectory will only cover a very small proportion of the run; if it is too large the atoms can move too far before the next time-step meaning there is a high energy overlap between atoms. This latter scenario could cause the system to explode due to the instability of these high energies. Therefore, selecting a time-step must be computationally efficient and allow for the phase space to be covered properly so any collisions can happen well. A larger time-step of 20 fs was used for the coarse-grained (CG) simulations.

2.3 Energy Minimisation

Energy minimisation is a standard and important protocol to ensure the system is at the lowest local potential energy possible prior to the simulation beginning. There are several methods however this work uses the steepest descent method to find a local minimum by gradually altering the atom coordinates to remove overlapping atoms from the system setup. This process removes large forces and allows for the system to be a in a more stable energetic state. The steepest descent method uses the force of the initial structure position of the system to take a step down the negative gradient, down the energy pathway of the system. This is repeated until a local minimum is found and stops. This change from one step to the next and is continued until the maximum potential energy of the system is less than the tolerance value or the iteration number is reached.

2.4 Thermodynamic Ensembles

MD simulations use several different types of ensembles, some of which are:

- Microcanonical-fixed (NVE)
- Canonical-fixed (NVT)
- Isothermal-isobaric-fixed (NPT)

Where *N* is fixed atom number, *V* is fixed volume, *E* is fixed energy, *P* is fixed pressure and *T* is fixed temperature. Whilst NVT is commonly used, NPT is the most commonly used in MD as it is most accurate to *in vivo* conditions. This work was thus run in an NPT ensemble.

2.4.1 Temperature & Pressure Coupling

Within the NPT ensemble, the temperature and pressure must remain constant. Depending on the stage and goals of the simulation, there are various thermostats and barostats that can be used.

2.4.2 Thermostats

The Berendsen thermostat is efficient to ease the system to a goal temperature by using a weak-coupling scheme. It is commonly used for equilibration as temperature fluctuation during this stage is larger meaning the weak-coupling scheme allows this greater fluctuation of the system[61]. Often, for the MD run the Nosé-Hoover thermostat is used as it gives a better range of dispersal of the temperatures and provides the right ensemble[62].

2.4.3 Barostats

The Berendsen barostat works similarly to the Berendsen thermostat in that it works with a weak-coupling scheme[63]. However, this work uses the Parrinello-Rahman barostat which works similarly to the Nosé-Hoover thermostat in that it gives the correct ensemble for the simulation by using a strong pressure coupling scheme[62,64].

2.5 Periodic Boundary Conditions

Unless the simulation has clusters of atoms or molecules with a well-defined number of constituents, the numbers of particles used to stimulate bulk properties of macroscopic system is essential. Therefore for very large systems, like membranes, periodic boundary conditions (PBC) are used, unless one is

interested in surface effects. This is due to molecules on the surface facing different forces to molecules in the centre of the simulation. Using PBC implies that particles are enclosed within a box that is replicated to infinity by rigid translation in all three Cartesian directions thereby completely filling the space. By surrounding the box with replicas, surface atoms are no longer an issue. Therefore as a particle moves out of the simulation box, an image particle moves into its place. The number of particles in the central box remains constant. Figure 2.2 depicts the method of PBC. PBC only works if the box shape can tile perfectly into a 3D crystal so whilst spheres, droplets and irregular shapes cannot be used; cubes/cuboids are commonly used, as they are the simplest to build and have been used in these simulations. However other shapes such as truncated octahedrons or rhombic dodecahedrons can be used to reduce the computational expense of excess water.

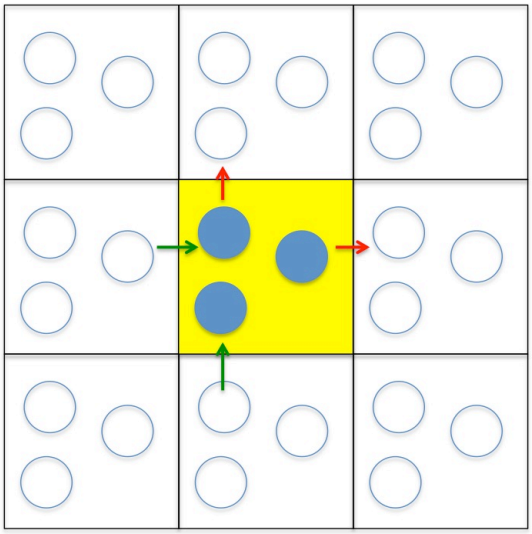

Figure 2.2: Schematic of a simulation system to which PBCs have been applied. The yellow box is the initial simulation system whilst all the other boxes are the periodic images of the system. Particles leaving the top and right-hand side of the box will reappear on the bottom and left-hand side of the box respectively.

2.6 Force fields

Force fields define the parameters used to calculate the potential energy of a system. These parameters include the calculations for bonded interactions, non-bonded interactions and electrostatics. These parameters must come from

experimental data or quantum mechanics calculations or a combination of these.

2.6.1 Bonded Interactions

Potential energy of a system is the sum of bonded and non-bonded interactions, Equation 2.6.

$$V = \Sigma \text{ bonded} + \Sigma \text{ non-bonded}$$

Equation 2.6

Bonded interactions apply to the stretching of bonds, bond angle distortion, improper dihedrals, Figure 2.3, and bond torsional rotation, Equation 2.7, and are the sum of all the bonded pairs of atoms. These are modeled using harmonic potentials and the shape of the harmonic well is defined by K_r, K_ϑ, and K_Φ. r_O, ϑ_O and Φ_o. are three equilibrium values for bonds, angles and improper dihedrals. These values come from the force field parameters. Whilst the proper dihedrals are the rotation of a bond between two neighbouring bonds therefore are described by the cosine potential, as rotations of the dihedral angles are periodic. Within equation 5, K_x signifies the heights of the energetic barrier, whilst n is the multiplicity per 360^0 and σ is the value of dihedral at zero.

$$E_{bonded} = \sum_{bonds} K_r (r_{AB} - r_O)^2 + \sum_{angles} K_\vartheta (\vartheta_{AB} - \vartheta_O)^2 + \sum_{improper} K_\Phi (\Phi - \Phi_o)^2 + \sum_{proper} K_x [1 + \cos)n\chi - \sigma)]$$

Equation 2.7

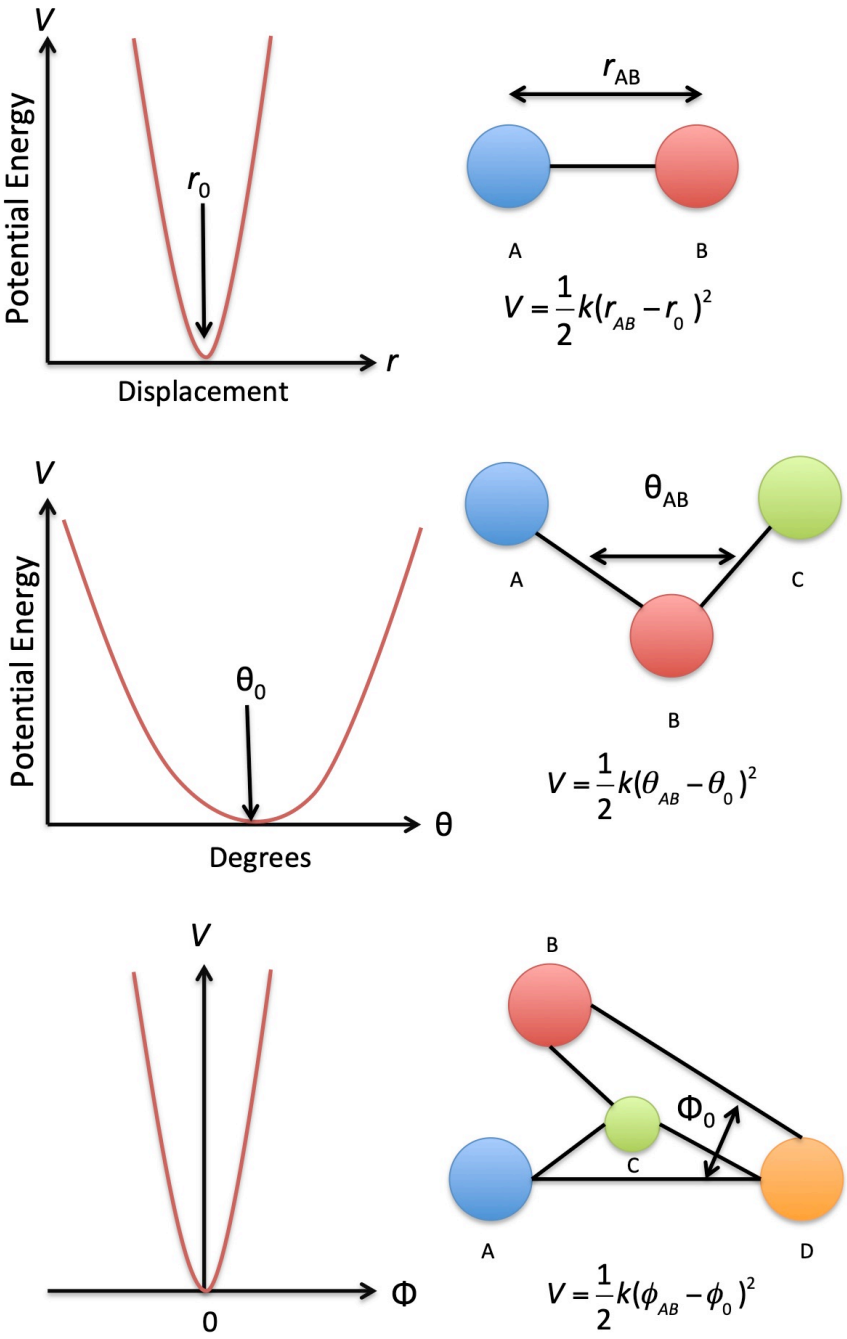

Figure 2.3: Harmonic potential used to model bond stretching, bond angles and improper dihedrals, K_r and K_θ, are the equilibrium values for different bonds and angles.

Non-bonded interactions are made up of Lennard Jones (LJ) repulsion and dispersion (Van der Waals), Figure 2.4, and Coulomb's electrostatics, Figure 2.5.

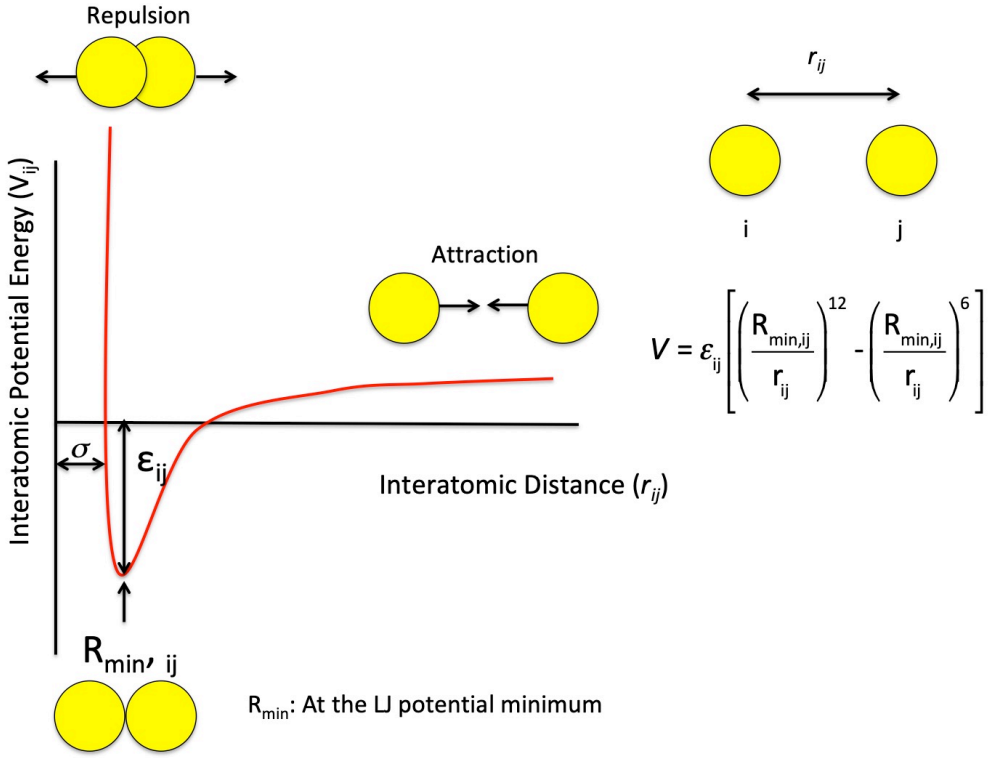

Figure 2.4: The Lennard-Jones potential to model the Van der Waals interactions. The ε_{ij} term describes the shape of the curve, the depth of the well. R_{min} is the distance between two adjacent atoms at LJ potential minimum.

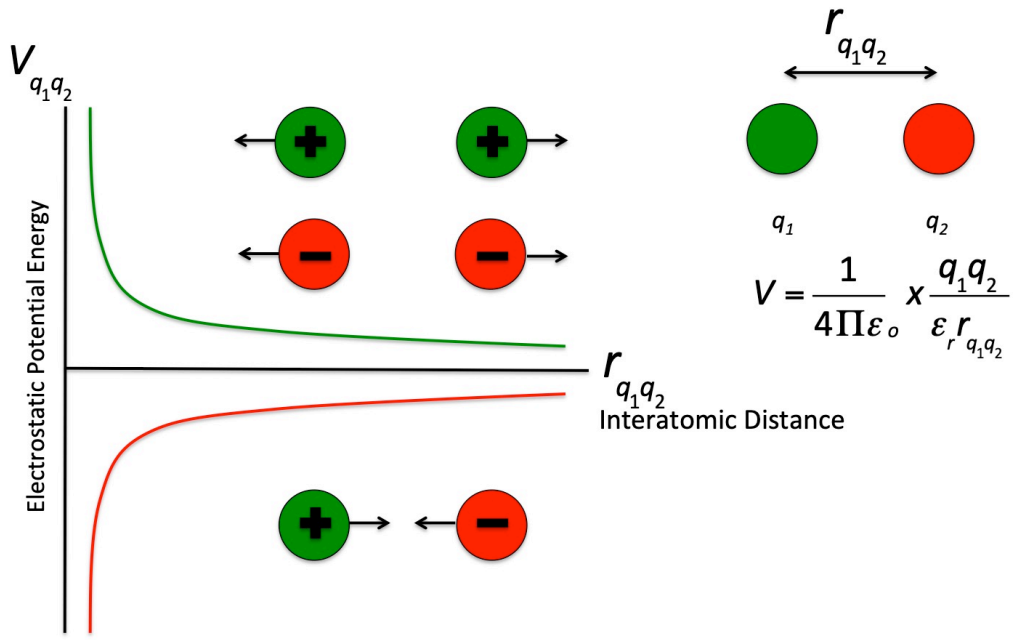

Figure 2.5: The electrostatic potential to model the point charges.

As for the non-bonded interactions, the two terms, van der Waals and electrostatics are defined using LJ potentials and Coulomb's Law, Equation 2.8, with each part of the equation representing each respectively. The 6th order of the LJ potential defines the attractive forces between two adjacent atoms and come from the instantaneous-induced dipoles interaction. Whilst the 12th order term is the repulsive forces between two atoms when they move too close and the overlap of the electron density of these atoms become unfavourable energetically. The shape and depth of the well are described by ε_{ij} whilst R_{min} is the distance between two adjacent atoms at LJ potential minimum. In regards to Coulomb's law, r_{ij} is the distance between two atoms *i* and *j*, $q_i q_j$ is the charge of these atoms and finally ε_r is the relative permittivity of the medium.

$$E_{non\text{-}bonded} = \sum_{Pairs(ij)} \left\{ \varepsilon_{ij} \left[\left(\frac{R_{min,ij}}{r_{ij}} \right) \right]^{12} - \left(\frac{R_{min,ij}}{r_{ij}} \right)^{6} \right] + \left(\frac{q_i q_j}{r_{ij} \varepsilon_r} \right) \right\}$$

Equation 2.8

2.7 Cut-offs and Electrostatics

2.7.1 The Distance Cut-off

To minimise the computational expense of a simulation, a distance cut-off is used for calculating the non-bonded interactions. This means that only interactions between atoms/beads that fall within this range are calculated rather than all of them. It has been observed that movement between adjacent atoms/beads within the cut-off do not change much over approximately 10 time-steps meaning it is still accurate to use this cut-off system. In addition, the distance cut-off avoid the atoms/beads interacting with itself across the periodic boundary thus the cut-off cannot be more than half the length of the cell. Cut-offs are used for electrostatics such as Van der Waals interactions and long-range dispersion. Cut-offs vary between AA and CG models and between force fields.

2.7.2 Long-range Dispersion Correction and The Smooth Particle Mesh Ewald (PME)

Firstly, the long-range dispersion correction is used to treat Van der Waals interactions outside its cut-off. Electrostatic interactions beyond the electrostatic cut-off use the PME method, which is based on the Ewald summation. The Ewald summation was commonly used in MD however this became a computationally expensive approach due to the increasing number of atoms involved in simulations. The PME method is one of the most popular fast Ewald methods due to its ease of application. PME combines the Ewald summation with a fast computation method called fast Fourier transforms. The standard Ewald method calculation of the reciprocal energy is the most intensive aspect in the evaluation of the long-range electrostatic correction. This calculation scales roughly to N^2, where N is the number of particles. The calculation is significantly quicker using the PME method and approximately scales to NlogN[65,66].

2.8 Simulation Resolution

There are various levels of resolution at which simulations can be conducted. CHARMM is an all atom (AA) force field meaning every atom is explicitly represented by a point. GROMOS is a united atom (UA) force field meaning aliphatic hydrogens are not represented. This allows for a computational speed up of the simulations. This work uses the several different force fields including a comparative study between the GROMOS and CHARMM force fields[67,68]. A further speed up can be achieved by reducing the resolution of the models further. These are called coarse-grained (CG) models. CG models group together single atoms into one larger bead. The mapping of AA models to CG models and grouping of atoms varies between CG force fields; with some, beads may only represent a few atoms, and in others, a bead can represent e.g. a tertiary domain of a protein.

Coarse-grained MD simulations can see a speed up of orders of magnitude due to the fewer particles to calculate the positions of and a simpler energy landscape allowing for a large step (20 fs) to be taken compared to 1-2 fs for AA

and UA simulations. The CG portion of this work used the Martini force field where four heavy atoms are typically mapped to one CG particle[69,70]. Whilst Martini simulations have increased computational efficiency, limitations of the force field include; poor performance for solid or gas phase simulations and Martini has no diregctional hydrogen bonding meaning preotein secondary structure cannot be maintained[71,72]. A comparison of PC in UA versus CG is shown in Figure 2.6.

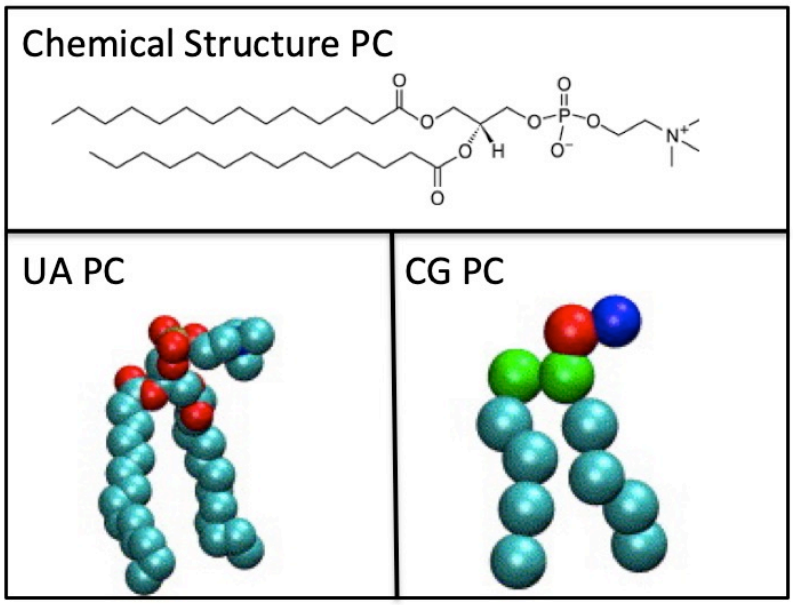

Figure 2.6: Chemical structure of PC with schematic comparing UA PC and CG PC below.

Chapter 3 – Structure and Membrane Interactions of the Antibiotic Daptomycin

3.1 Introduction

Daptomycin is a calcium-dependent cyclic lipopeptide, which is only active against Gram-positive bacteria. It was isolated in the 1980s from *Streptomyces roseosporus,* a Gram-positive soil actinomycete[73,74]. Daptomycin was not approved for use as an antibiotic until 2003 due to side effects of the drug, but was eventually approved due to the need for novel antibiotics in the wake of increases in antibiotic resistance to other drugs[75]. Due to this daptomycin has been designated as a last resort antibiotic, amongst others such as vancomycin, for infections that cannot otherwise be treated successfully with standard antibiotics[76]. Specifically, daptomycin is used to treat Gram-positive infections caused by *S. aureus*, particularly methicillin-resistant strains (MRSA)[77]. Although other cyclic lipopeptide antibiotics have been the discovered and developed, daptomycin is still the only one approved for clinical use. Despite the clear importance of daptomycin, the mode of action of the drug is not clearly understood and is much debated clinically. Improving the understanding of daptomycin would help pave the way for development of new novel antibiotics of the same class as daptomycin.

Daptomycin is comprised of 13 amino acids, of which 10 are arranged in a cyclic structure, and a decanoyl fatty acid tail, Figure 3.1[78]. The cyclic area of daptomycin has numerous noncanonical and D-amino acids, two of which have been shown to be crucial to the mode of action of daptomycin – kynurenine and 3-methlyglutamic acid. Modifications of these amino acids cause a 5 times increase to the minimum inhibitory concentration of daptomycin[79]. Unusually compared to other lipopeptides, daptomycin has a -3 *e* charge at pH 7[80]. The mode of action of daptomycin is therefore thought to largely dependent on Ca^{2+} ions[81]. Daptomycin-calcium complexes tend to form at a ratio of 2 daptomycin molecules to three Ca^{2+} ions[82]. This complex formation is believed to allow

daptomycin to better interact with negatively charged bacterial membrane lipids, in particular PG, due to the functional change in charge of daptomycin. Some studies have found that binding with PG causes a second conformational change to daptomycin allowing membrane insertion and causing it to form its final active conformation[81]. However, other research has conflicted with these findings and suggests that daptomycin may not undergo a conformational change upon binding with Ca^{2+} with only two conformational states being free and membrane-bound[82]. Therefore further research is required to understand if daptomycin is required to be bound to Ca^{2+} for its mode of action to work.

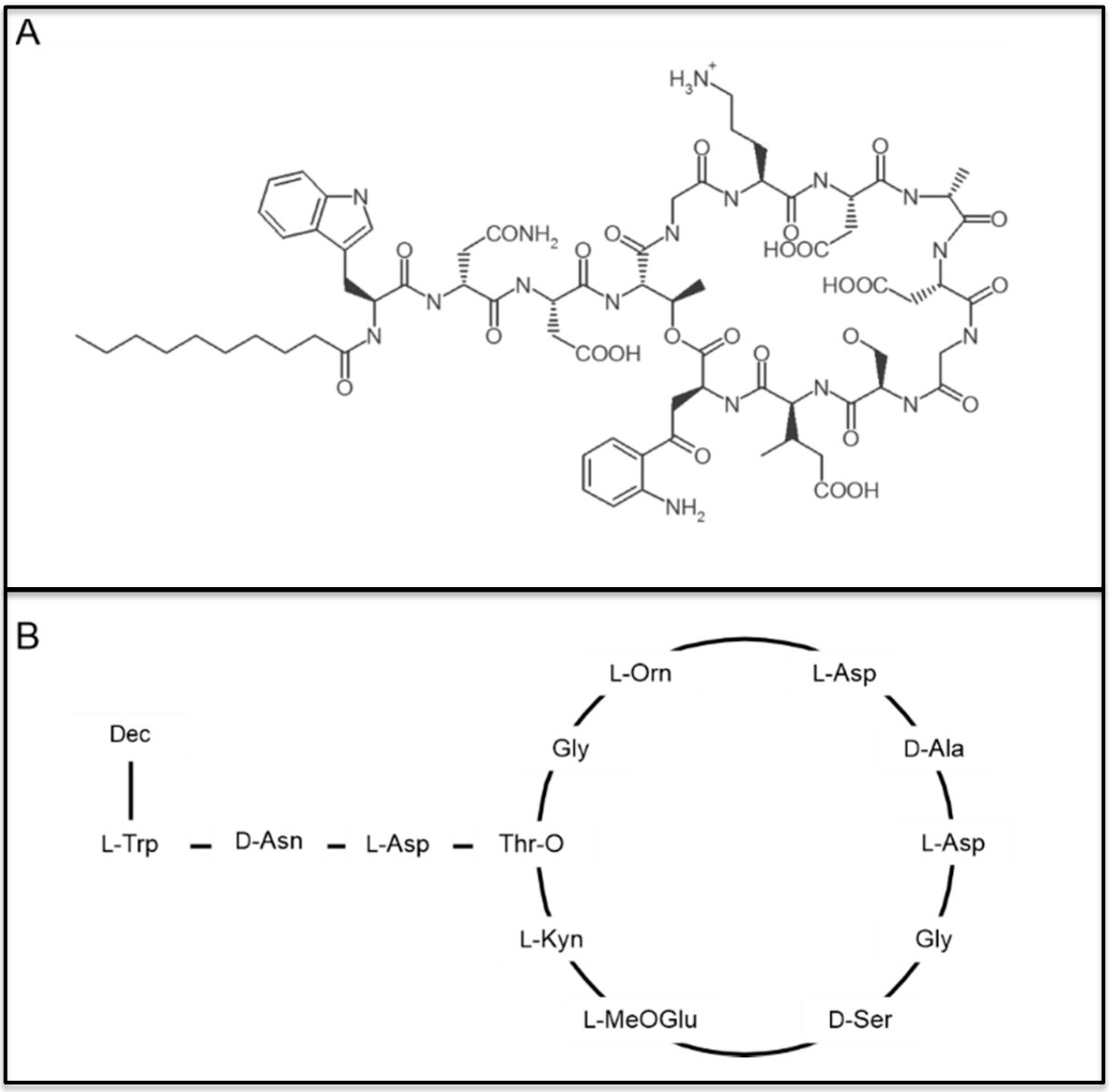

Figure 3.1: Daptomycin structure, A) chemical structure and B) amino acid sequence[83].

Daptomycin has been found to form micelles triggered by the presence of Ca^{2+} ions, which are suggested by some studies to be important to the mode of action of daptomycin[84]. The exact number of daptomycin molecules that form a micelle is heavily debated with some studies suggesting a micelle forms with 6-7 monomers but others suggesting around 12-15 monomers constitute a daptomycin micelle[81,84,85].

In addition to discrepancies with exact micelle size, there is also debate around the exact conformation of a daptomycin molecule bound to Ca^{2+} ions and indeed whether a conformational change occurs. Current NMR structures of daptomycin do not show the precise location of any calcium ions. However, a similar cyclic lipopetide antibiotic to daptomycin and derivative of amphomycin, namely tsushimycin, has also been shown to have a dependence on calcium ions as is the case with many lipopeptide antibiotics[86]. Whilst this antibiotic has a similar acyl tail and ten amino acid ring structure, the amino acids within the cyclic region are distinct from daptomycin as shown in Figure 3.2[87]. In a study aiming to find the relationship between tsushimycin and calcium ions, the drug was crystallised and its structure determined to 1 Å resolution[88]. The structure of the cyclic loop of tsushimycin was stabilised by a Ca^{2+} ion and suggests the reason for the Ca^{2+} dependence of the antibiotic class. The calcium ion was coordinated by negatively charged aspartic acid (Asp5 and Asp7) therefore changing the conformation of the peptide core of tsushimycin.

Calcium ions were also found to 'cross-link' tsushimycin monomers, forming dimers, which could suggest that calcium ions could be important for aggregation of antibiotics of this class. However, this could be an artefact of the crystallographic environment. Whilst tsushimycin is distinct from daptomycin, the similarities between it, daptomycin and other antibiotics of their class may suggest daptomycin interacts with calcium ions in a similar way. The interaction between tsushimycin and calcium ions acted as guide in this work for how daptomycin may coordinate calcium ions.

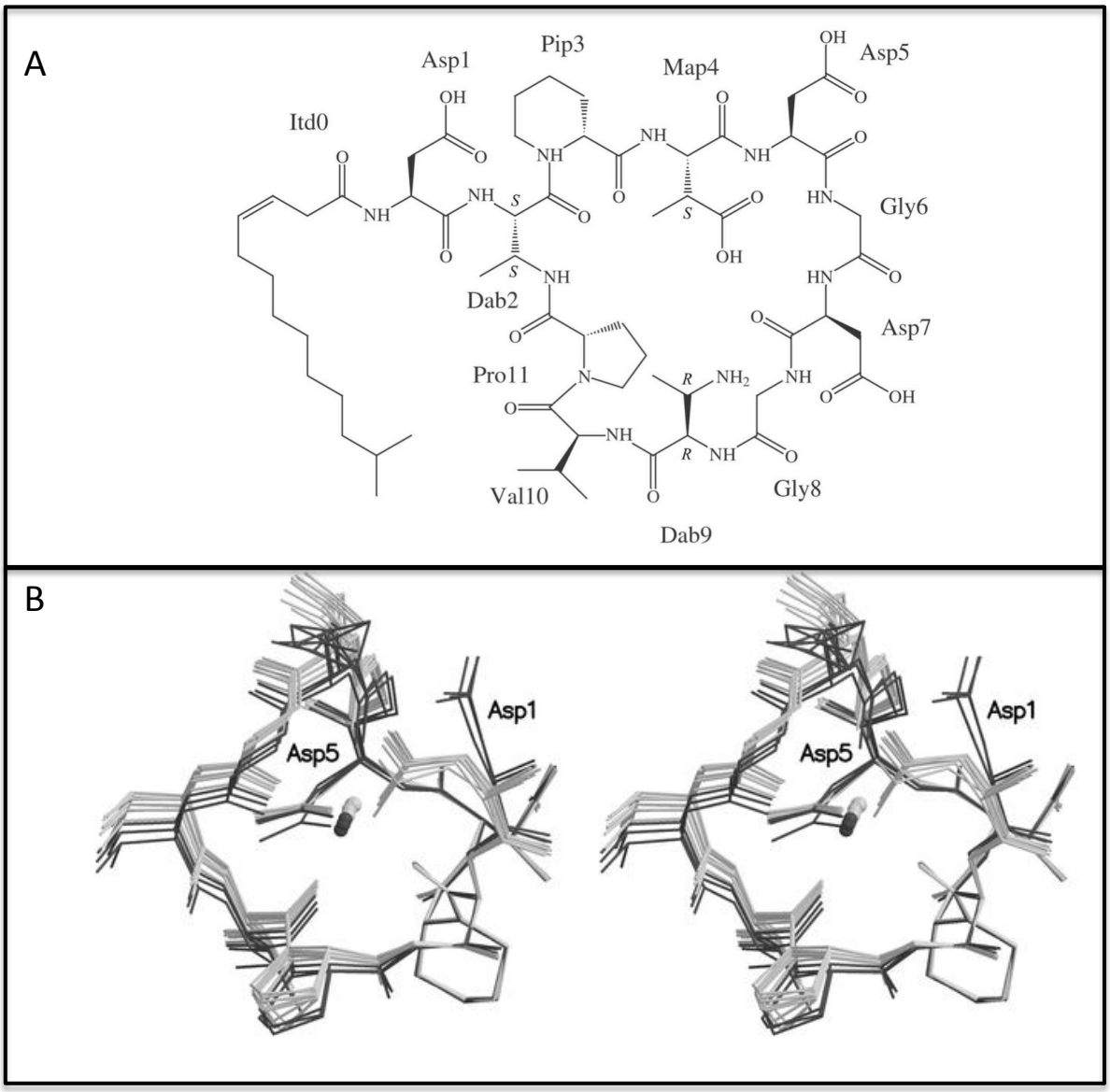

Figure 3.2: A) Tsushimycin amino acid sequence and B) Stereoview of the superposition of all 12 tsushimycin cyclic regions with suggested Ca^{2+} position in centre[88].

As previously mentioned, daptomycin has been shown to be dependent on the presence of PG in order to enter the membrane. PG-dependent oligomerisations of daptomycin has been demonstrated in studies using model membrane systems, isolated bacterial membranes and bacterial cells[89]. Furthermore, daptomycin was shown to form distinct daptomycin-PG domains *in vitro* with PG the 'docking molecule' for daptomycin[90]. PG is particularly

prevalent in bacterial membranes and thought to be important for the specificity of daptomycin on bacteria rather than targeting mammalian cells[91]. Furthermore, PG is particularly abundant in Gram-positive bacteria, more so than Gram-negative, suggesting why daptomycin is not as effective in Gram-negative bacteria[92,93]. PG is also the most abundant lipid in the *S. aureus* membrane[77].

As described above, much of our understanding of daptomycin is heavily debated and this is no exception with the mode of action. There have been several theories and proposals as to the exact molecular mechanism of daptomycin within the membrane, partially due to it behaving differently in different model systems. There is inconsistency due to different behaviour between lipids with different tail lengths, membrane composition and membrane fluidity[83]. The current, main theory is that daptomycin inserts via its tail, interacting with PG, and then aggregates forming a aggregate or micelle. This aggregate is then thought to alter the curvature of the membrane, creating leaks that cause the cell to depolarize, inhibiting protein and DNA synthesis, resulting in cell death[33,85]. More recent work has given more clarity to how these leaks are caused. It has been proposed that daptomycin causes the membrane to become rigid. This in turn causes the membrane proteins to delocalise, causing deformations to the cell envelope and blocking cell growth. This process causes cellular depolarisation[94,95].

From a literature review of daptomycin, there is a huge scope for improving our understanding of this important, last resort, antibiotic. Furthermore, a better knowledge of the modes of action of daptomycin could also translate to similar antibiotics and perhaps other lipopeptides. This would help bring novel antibiotics to market, which would relieve the reliance upon daptomycin and other last-resort antibiotics and in turn reduce concern about the consequences of antibiotic resistance.

3.2 Aims

This work falls into three sections aiming to understand several aspects rose above regarding our gaps in the knowledge of daptomycin activity. All aspects of the work compared two possible structural models: (i) one based on an NMR structure of daptomycin taken from the PDB (non-Ca^{2+} model); and (ii) daptomycin with a Ca^{2+} modelled (Ca^{2+} model) as bound to the centre of the cyclic loop, in a similar conformation to a crystal structure of tsushimycin. This second model saw the calcium ion bound with the aspartates orienting into the ring to coordinate it. This aimed to understand the conformational changes that daptomycin might undergo.

The first section involved understanding daptomycin micelle formation and how such a micelle may interact with the *S. aureus* membrane. Based on experimentally measured daptomycin micelle size, both daptomycin models were simulated in solution and in the presence of the *S. aureus* membrane.

The second section involved better understanding exactly how the two alternative daptomycin models would interact with a membrane with and without PG present, based on the experimentally suggested dependence of PG for daptomycin. This work compared how a daptomycin monomer would interact with a pure PC membrane versus the *S. aureus* membrane.

The third and final section of this work focused on better understanding how daptomycin may interact with the *S. aureus* membrane at higher concentrations.

3.3 Daptomycin Micelle Formation

The aim of this section was to study whether daptomycin formed micelles, in solvent and with the *S. aureus* membrane, and understand the interactions driving such behaviours.

3.3.1 Methods and Simulation Setup

The simulations were performed used the GROMACS 2018 code, the CHARMM36 force field and the TIP3P water model[68,96,97]. Each simulation was run in triplicate for the times stated in Table 3.1. The temperature was maintained at 313 K using the Nosé-Hoover thermostat at a time constant of 1 ps[62]. The pressure was maintained semiisotropically for the systems with a

membrane and isotropically for the ones without, at 1 atm using the Parrinello-Rahman barostat with a time constant of 1 ps[98]. LINCS constraints were applied to hydrogen containing covalent bonds[60]. A time step of 2 fs was used and long-range electrostatic interactions were calculated using the PME method[65]. For both the electrostatic and Van der Waals interactions a cut-off value of 1.2 nm was used[66]. Systems were neutralised in a 0.1 M $CaCl_2$ solution to ensure there was sufficient availability of calcium ions.

The *S. aureus* membrane comprised of 54% PG, 36% Lysl-PG and 10% DPG in line with experimental estimations[99,100] The models for the membrane were generated using CHARMM-GUI[101,102]. The original daptomycin structure without Ca^{2+} bound came from the PDB and was based on an NMR defined conformation in the presence of calcium ions but did not show the exact bound position of any Ca^{2+} ions[86]. A calcium ion was then manually placed in the cyclic region of the daptomycin and restrained. The restraints were slowly released to allow the ring to adopt an equilibrium conformation, which stably coordinated the calcium ion in the centre. These simulation trajectories required for this took 300 ns. In line with the experimental results of tsushimycin and other daptomycin work, the calcium ion was coordinated by the aspartates in the daptomycin ring. Snapshots of the starting conformations of both daptomycin models are shown in Figure 3.3. For this micelle study, 15 daptomycin molecules were in each system in line with the maximum estimation of micelle size. Note that the simulations with a membrane were run for longer in an attempt to see the daptomycin micelle diffuse into the bilayer as suggested by experimental data.

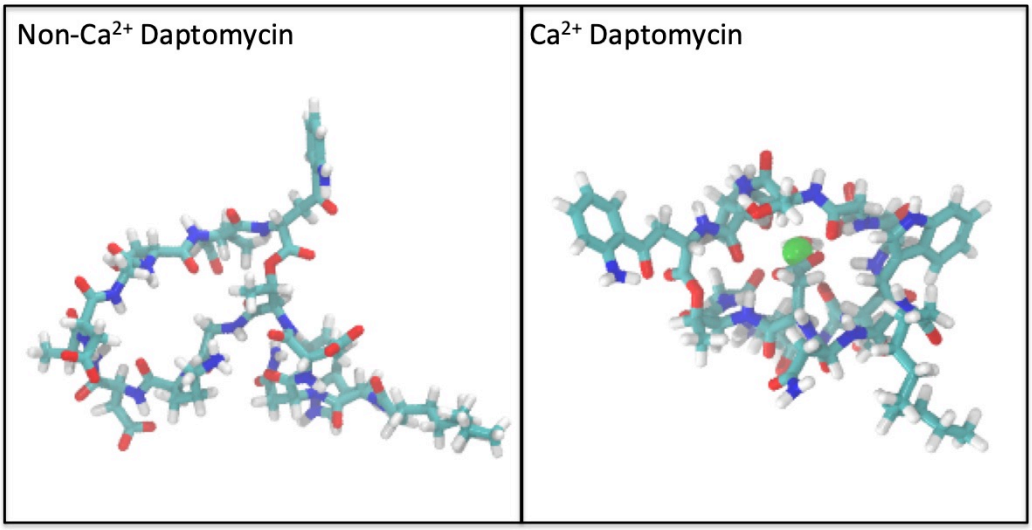

Figure 3.3: Snapshots of starting conformations of both daptomycin models shown in cyan, red, blue and white. The Ca^{2+} fixed in the centre of the Ca^{2+} bound model is shown in green.

Most analysis used GROMACS tools however the area per lipid was measured using FATSLiM and membrane thickness used Monticelli's GROMACS4 *g_thickness* script[103]. VMD was used for visualisation whilst analysis primarily used GROMACS tools[96,104–107]. BitClust was used for conformational cluster analysis; with a cut-off of 0.1 nm used to define a cluster[104].

Daptomycin Model	**Membrane**	**Solvent**	**Simulation Length**
15 x Original NMR (non-Ca^{2+} bound)	None	35055 H_2O, 91 Ca^{2+}, 137 Cl^-	500 ns x 3
15 x Ca^{2+} bound	None	35761 H_2O, 91 Ca^{2+}, 137 Cl^-	500 ns x 3
15 x Original NMR (non-Ca^{2+} bound)	*S. aureus*	25740 H_2O, 130 Ca^{2+}, 139 Cl^-	2.5 µs x 3
15 x Ca^{2+} bound	*S. aureus*	25790 H_2O, 130 Ca^{2+}, 139 Cl^-	2.5 µs x 3

Table 3.1: Simulations in the first section of the daptomycin work researching daptomycin micelle formation.

3.3.2 Results of Daptomycin Micelle Formation in Solvent

The snapshots of the end point, 500 ns, of the simulations aiming to show daptomycin micelle formation are shown in Figure 3.4. In this time frame neither the non-Ca^{2+} daptomycin model nor the Ca^{2+} conjugated daptomycin model formed one distinctive micelle. However, there was clearly a greater tendency for daptomycin with a conjugated Ca^{2+} ion to aggregate into a micelle structure. The larger aggregate of this model showed the tails of daptomycin pointing inwards with the cyclic loop of the daptomycin outside. This is presumed to be due to the hydrophobicity of the daptomycin tails as shown from the snapshots. It should be noted the Ca^{2+} ion fixed in the ring remained in place throughout the simulation. Meanwhile, the non-Ca^{2+} model without any conjugated Ca^{2+} ions were not so liable to aggregation. The calcium ions did not enter the centre of the ring of this model spontaneously. This may suggest that calcium ions are important for micelle formation and also that this calcium conjugated model was more accurate at representing the hypothesised interactions between daptomycin molecules.

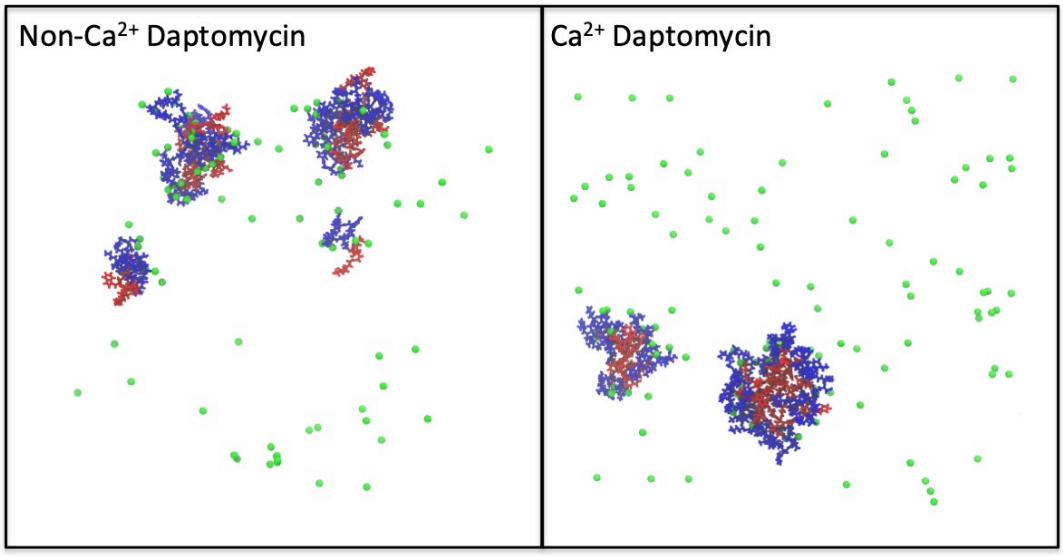

Figure 3.4: Snapshot of 15 daptomycin models, original non-Ca^{2+} and Ca2+ conjugated structure at end of 500 ns simulations. Water has been omitted. The polar and hydrophobic regions are in blue and red respectively. The Ca^{2+} are in green.

The mean distance between daptomycin molecules was measured over the last 20 ns of the simulation and plotted in a matrix shown in Figure 3.5. This data supported the suggestions made from the snapshots of the end point of the simulations. There were clearly more areas showing close contact with the Ca^{2+} model than the non-Ca^{2+} model as shown by the larger number of orange/yellow areas in the former.

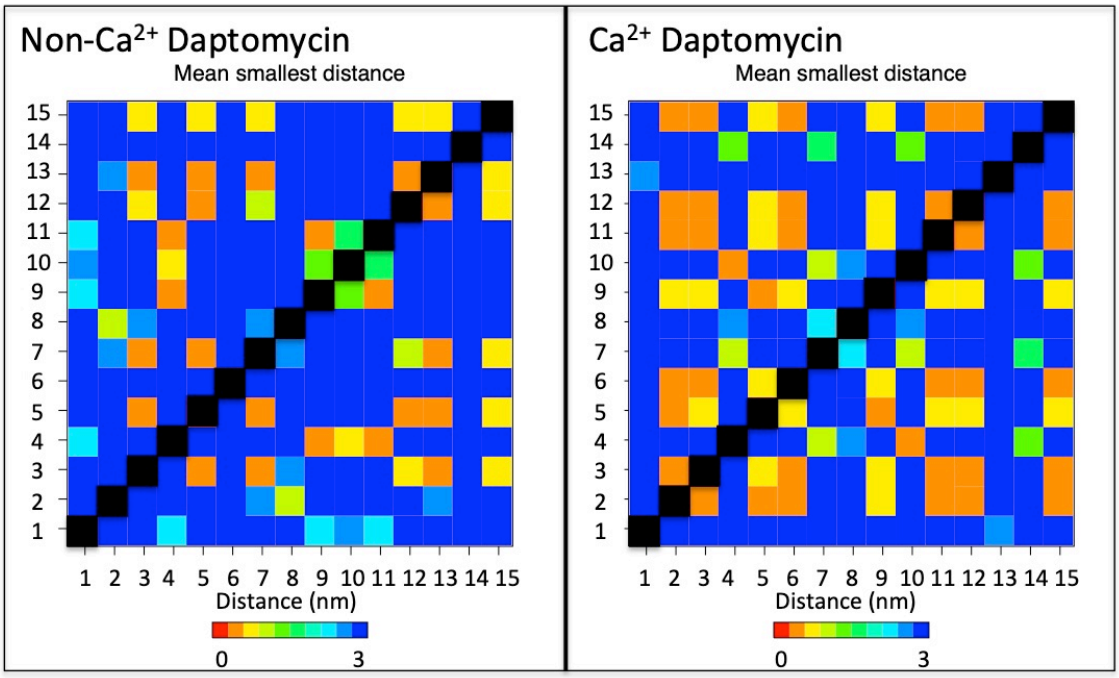

Figure 3.5: Average distance (nm) between daptomycin molecules over last 20 ns of each simulation. The blacked out regions omit self-contact of molecules.

Despite there clearly being closer contacts between Ca^{2+} bound daptomycin than the non-Ca^{2+} bound daptomycin, the latter saw a slightly larger number of hydrogen bonds between molecules than the former, Figure 3.6. hydrogen bonds, drove the aggregation between the Ca2+ bound daptomycin. Furthermore, the slightly larger number of hydrogen bonds between the non-Ca^{2+} bound daptomycin suggested they were coming into contact a similar amount but these interactions were not long lived, meaning the mean distance was larger as shown in Figure 3.4. This may be due to this model having a higher negative charge therefore making long-lasting bonds between molecules less favourable.

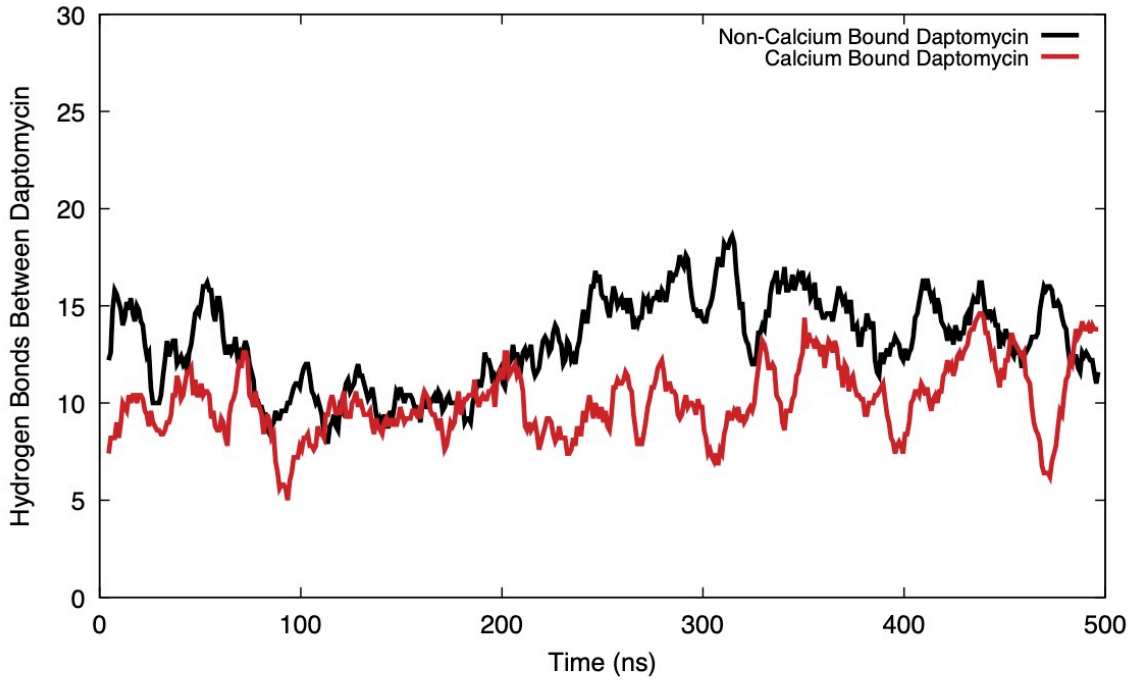

Figure 3.6: Hydrogen bonds between 15 daptomycin molecules over time (ns). The donor acceptance distance was set to 3.0 Å and the angle cut off 20 degrees.

The solvent accessible surface area (SASA) was measured collectively for all molecules (nm^2) over time (ns) of both daptomycin models, Figure 3.7. The SASA was measured for the polar and hydrophobic regions of the molecules and averaged to per atom to normalise the data. The SASA of the Ca^{2+} conjugated lower over the duration of the simulation supporting the larger micelle formation seen in this model. Based on dividing the acyl tail and cyclic units of the daptomycin, this aggregation appeared to be driven by both the acyl hydrophobicity and polar interactions. The SASA of non-Ca^{2+} daptomycin acyl tail was higher than the other components. This may suggest that the molecules that did aggregate in this system were not driven by hydrophobic interactions but rather by polar, charge-driven interactions. The Ca^{2+} ions in solution were seen to aggregate around the polar, cyclic region of the daptomycin molecules that appeared to bridge between the ring regions. The presence of Ca^{2+} ions may have made the charges favourable between the cyclic loops for aggregation to occur, hence them having a smaller SASA. The bridging of daptomycin molecules, via the cyclic loop, is in line with the tsushimycin study that informed this work[88]. This may inform how daptomycin micelles formation.

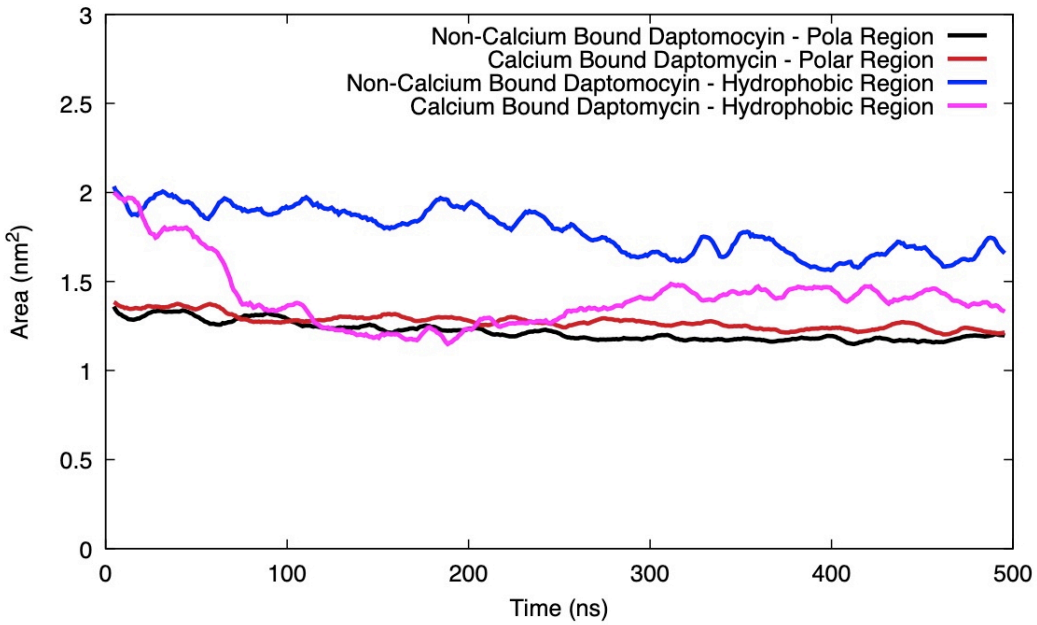

Figure 3.7: SASA for polar and hydrophobic regions (nm^2) of over time (ns).

The radius of gyration (R(g)) (nm) was measured for both models over time (ns), Figure 3.8. The R(g) was measured for each daptomycin molecule and the average taken. The R(g) was consistently slightly larger over the duration of the simulation for the non-Ca^{2+} bound model than the Ca^{2+} bound model. A larger r(g) suggests more aggregation which is counter to the previous analyses however this may be due to the non-Ca^{2+} bound model forming more small aggregates rather than the one large Ca^{2+} aggregate.

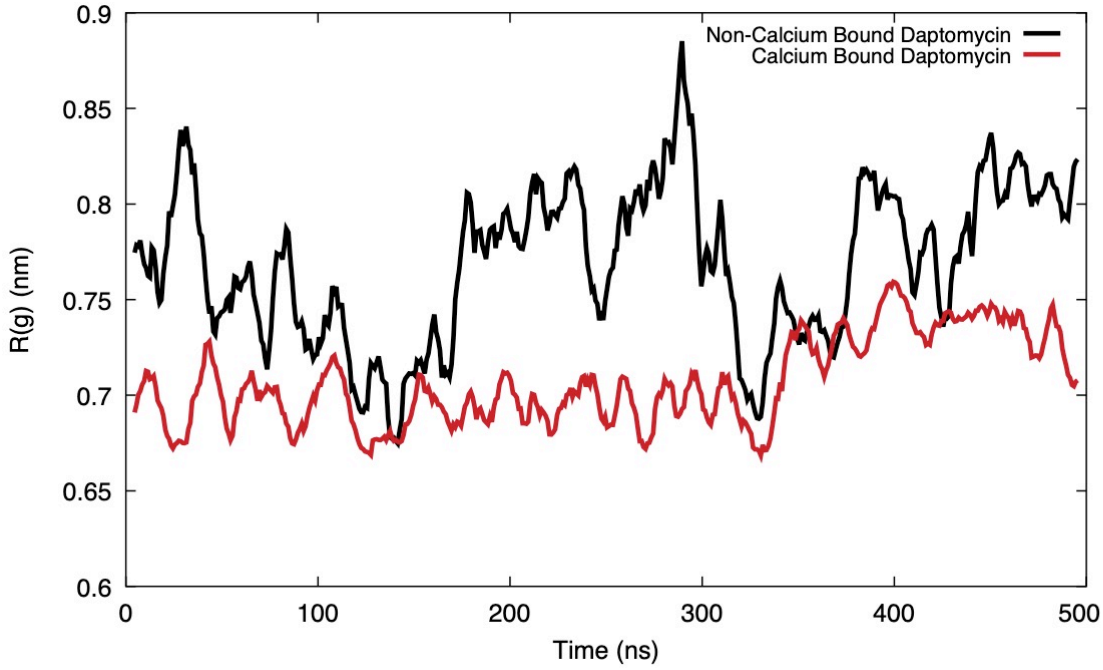

Figure 3.8: Average R(g) (nm) of both daptomycin models measured over time (ns).

The root mean squared deviation (RMSD) (nm) of the models was measured over time (ns), Figure 3.9. This was measured for each daptomycin molecule and averaged. The RMSD measures the average distance between the atoms, after a least-squares fit to the original structure. This was another way to measure the stability and changes in structure over time. As with the R(g), the non-Ca^{2+} bound daptomycin saw a larger RMSD over time than the Ca^{2+} bound daptomycin, this could be again due to aggregation and restriction of the loop region in Ca^{2+} model reducing the RMSD. Interestingly in the Ca^{2+} model there is an increase in the RMSD over time until the point previously shown to be where

the aggregates of daptomycin molecules stabilise. This may suggest there is a difference in the necessary conformation of daptomycin for it to aggregate in comparison to the initial structure.

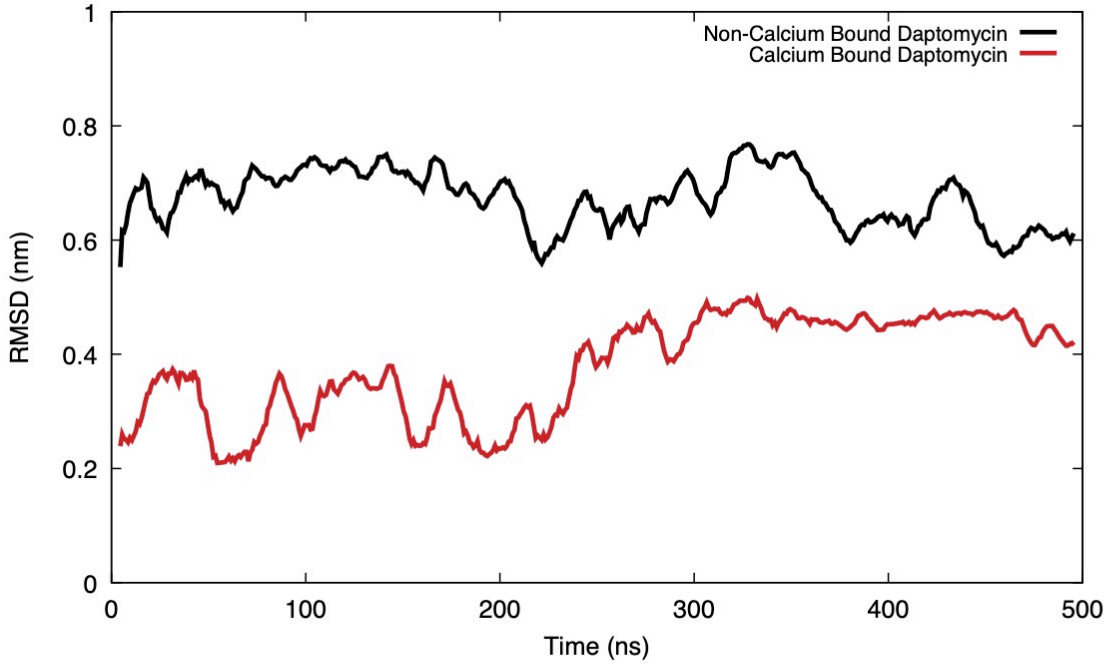

Figure 3.9: RMSD (nm) of both daptomycin models over time (ns).

The interactions between daptomycin molecules and Ca^{2+} ions in solution were measured over time, Figure 3.10. These analyses omitted the Ca^{2+} ion conjugated to the centre of the daptomycin molecule in the Ca^{2+} bound model to allow more accurate comparison between the two models. Figure 3.10 shows A) the number of contacts less than 0.6 nm between daptomycin and Ca^{2+} ions in solution and B) the minimum distance (nm) between daptomycin molecules and Ca^{2+} ions both measured over time (ns). Whilst there are a greater number of Ca^{2+} contacts between the non-Ca^{2+} bound molecule than the pre-Ca^{2+} bound model, the minimum distance is relatively similar between both models. This suggests that preferential distance between both models and Ca^{2+} models are similar but there are a greater number of contacts between Ca^{2+} ions and the non-Ca^{2+} bound model due to there being more aggregates in this simulation and therefore greater chances for these interactions to happen. It is expected that Ca^{2+} ions would similarly come into contact with both models as both models have a net negative charge.

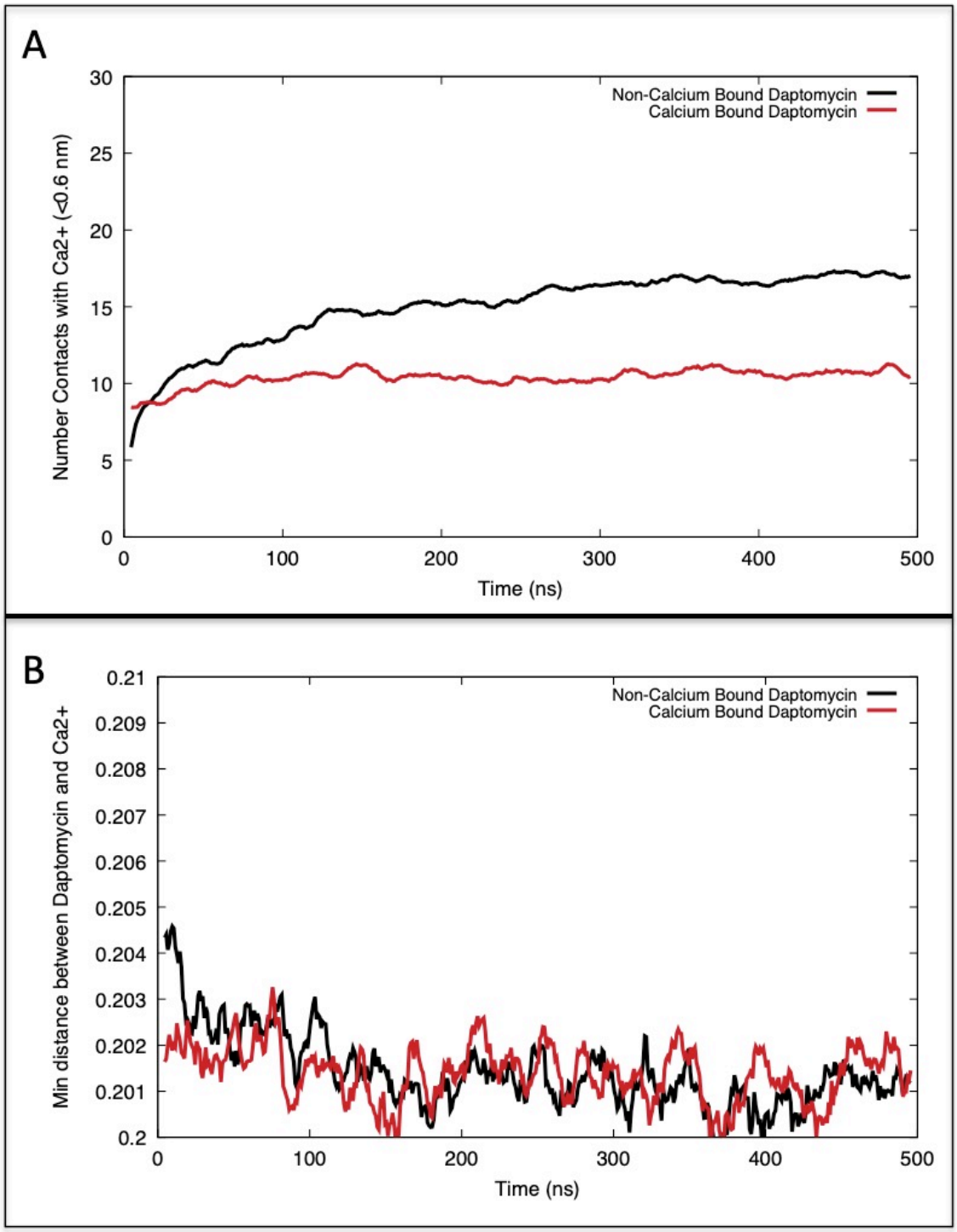

Figure 3.10: Analysis of Ca^{2+} ions with both daptomycin models - A) number of contacts <0.6 nm between daptomycin and Ca^{2+} ions over time (ns) and B) average minimum distance between daptomycin and Ca^{2+} ions over time (ns). The Ca^{2+} ions conjugated to the centre of the loop in the Ca^{2+} model have been omitted from this analysis.

The 5 most common conformations of daptomycin in each system were determined using conformational cluster analysis, Figure 3.11. The aspartates in each molecule are shown in green. The aspartates of the non-Ca^{2+} model were uncoordinated towards the centre of the ring, in comparison with that seen with the Ca^{2+} model. In the latter model the aspartates remained fixed by the central calcium ion whilst with the former they were able to "flip out" to interact with calcium ions outside the molecule. This supports the previous analyses between daptomycin and the Ca^{2+} within the systems.

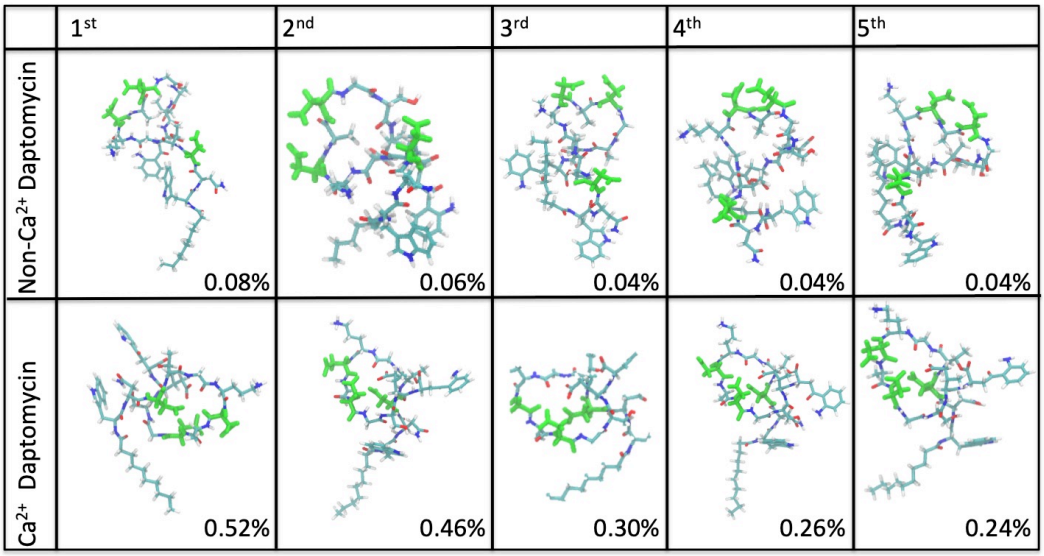

Figure 3.11: The 5 most common conformations of daptomycin models within each system based on conformational cluster analysis. The percentage each cluster represents is shown in the bottom right corner of each cluster. The molecules are shown in cyan with the exception of the aspartates shown in green.

3.3.3 Results of Daptomycin Models Micelle Formation with the *S. aureus* Membrane

Moving on to the simulations of 15 daptomycin molecules with the *S. aureus* membrane, snapshots of the end point, 2.5 μs, of these simulations are shown in Figure 3.12. The molecules starting position was ~5 nm above the membrane and at least 2 nm from other daptomycin molecules in all directions. Firstly, the non-Ca^{2+} conformation did not form a single micelle or aggregate and only one molecule entered the membrane with the others remaining in solvent. This model formed aggregates of between 3 – 4 monomers. Whereas, 14 of the Ca^{2+}

bound daptomycin molecules formed a larger aggregate but did not diffuse into the membrane, which may be a constraint of the timescales achievable by this work. The aggregate formed by this model was extremely stable throughout the simulation and remained on top of the membrane. In both simulations, one daptomycin molecule entered the membrane via the tail region of the model with the cyclic region remaining outside the membrane. The aggregates formed with the membrane were similar to those formed previously in the absence of a membrane.

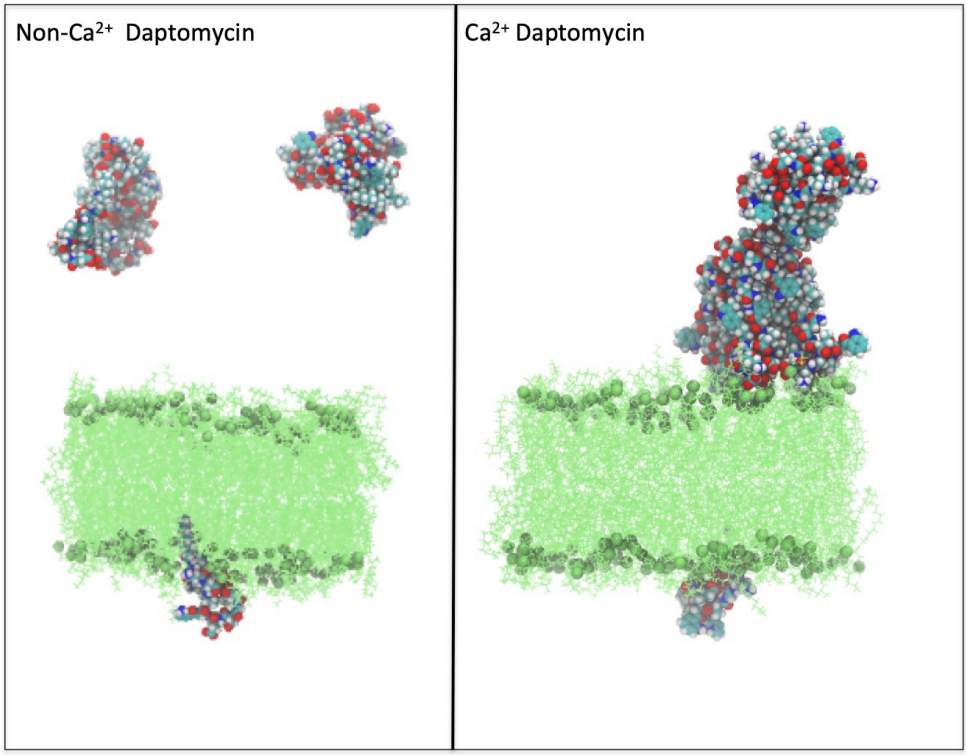

Figure 3.12: Snapshot of 15 daptomycin models, non-Ca^{2+} and Ca^{2+} conjugated structure (cyan, red, blue and white) at end of 2.5 μs simulations with *S. aureus* membrane (green). Solvent has been omitted for clarity.

The densities of the membrane lipids and tails, solvent and daptomycin tails and cyclic region were measured for the last 100 ns of the simulations, Figure 3.13. This showed the majority of the non-Ca^{2+} bound daptomycin remaining far from the membrane with the exception of the one molecule known to have entered the membrane. In contrast, the Ca^{2+} bound aggregate clearly sits closer to the membrane with some regions entering the head-group region of the bilayer.

This analysis is in line with the conclusions drawn from the visualisations. Furthermore, the molecules that entered the membrane singularly both saw the tail of daptomycin enter further into the bilayer with the cyclic region remaining largely outside. Finally, the Ca^{2+} bound molecule that entered did so further into the bilayer than the non-Ca^{2+} model molecule.

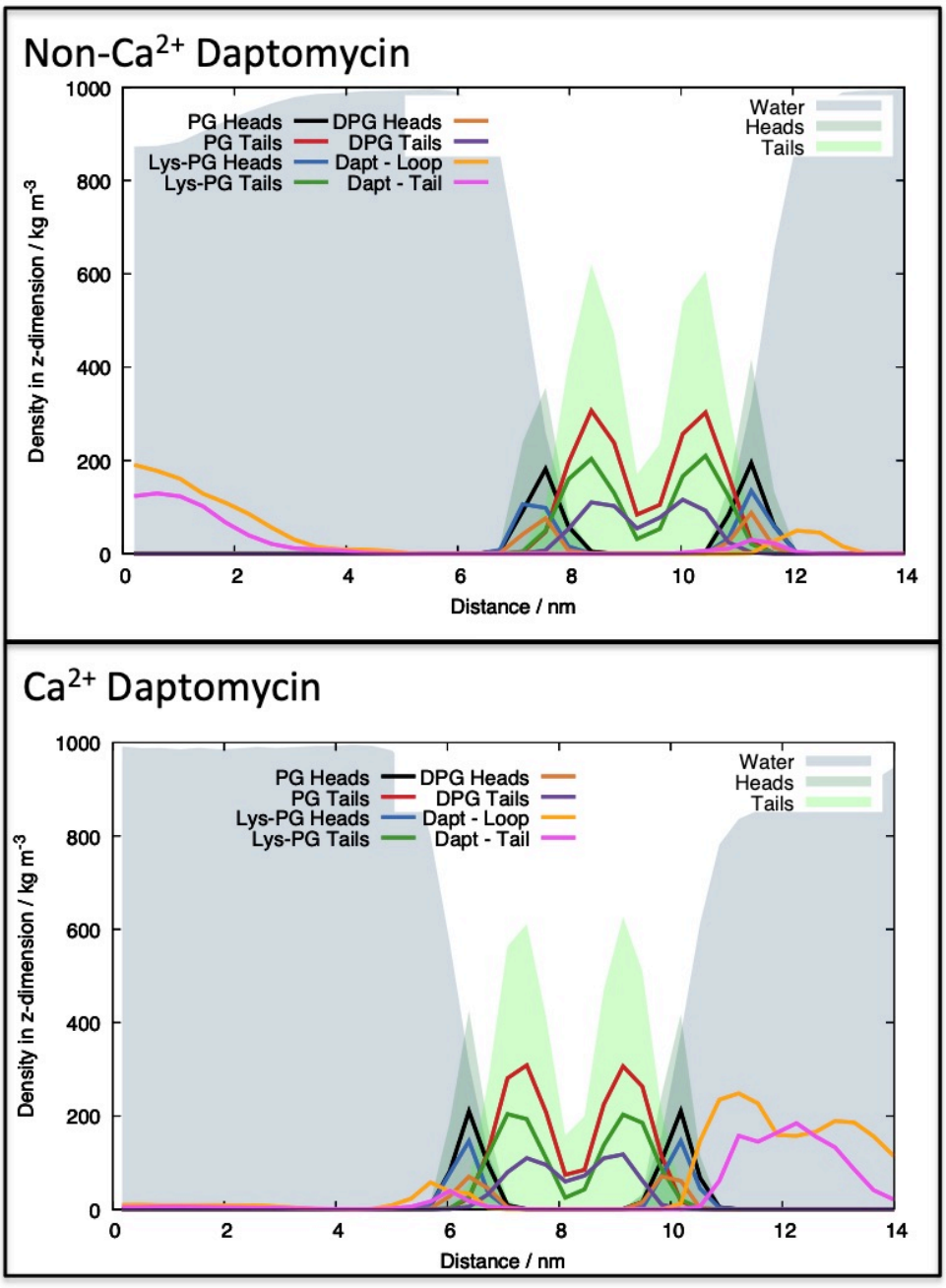

Figure 3.13: Densities of daptomycin models *S. aureus* membrane lipid heads, tails and solvents. Measured over last 100 ns of simulations.

The membrane thicknesses were measured over the last 100 ns, Figure 3.14. There was little difference between the thicknesses of the membranes between simulations; however the membrane exposed to Ca^{2+} bound daptomycin perhaps was slightly thinner. This may be due to the large micelle sitting on the membrane. The little difference in the thicknesses was probably due to daptomycin not fully entering the membrane.

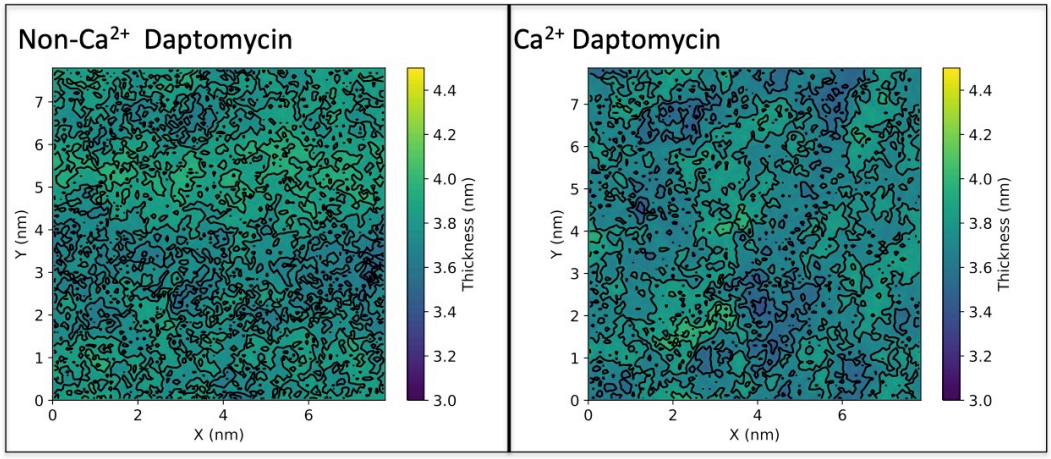

Figure 3.14: Membrane thickness of S*. aureus* membrane with different daptomycin models. Measured over last 100 ns of simulations.

The phosphate densities were measured in the Y-direction over the last 100 ns, Figure 3.15. There was little difference in the curvature and thickness of the phosphate regions between the bilayers.

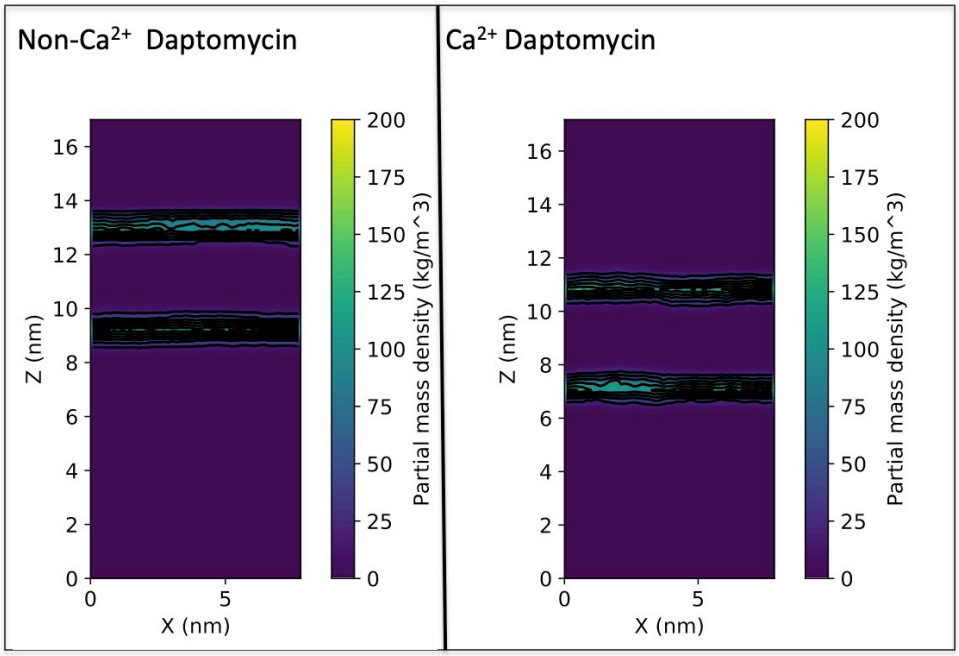

Figure 3.15: Phosphate densities kg/m^3) in Y direction of *S. aureus* membrane with different daptomycin models. Measured over last 100 ns of simulations.

The area per lipid (APL) was measured for both systems over the duration of the simulations, Figure 3.16. There was very little difference in the APL of the bilayers in both systems, which supported the findings of the membrane thickness analysis. This gradual decrease in APL may be due to membrane thickening slightly as most daptomycin molecules are unable to enter in these systems. This suggests that in this setup neither daptomycin model could fully enter and disrupt the membrane.

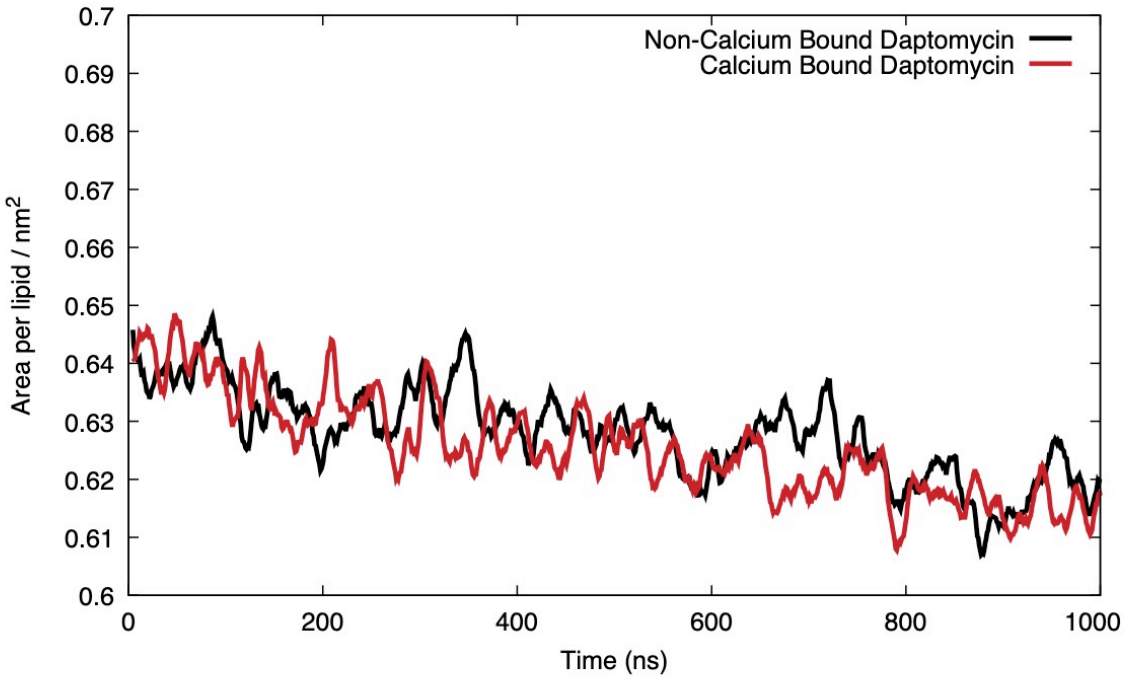

Figure 3.16: APL of the lipids in *S. aureus* membrane with different daptomycin models measured over time.

The deuterium order parameters (Scd) were measured for the carbon tails of the lipids in the bilayers of both systems, Figure 3.17. As with the previous analysis there is not a significant difference for this measure of the membrane disorder. This would suggest that there was not a significant difference in the order of the membranes between bilayers.

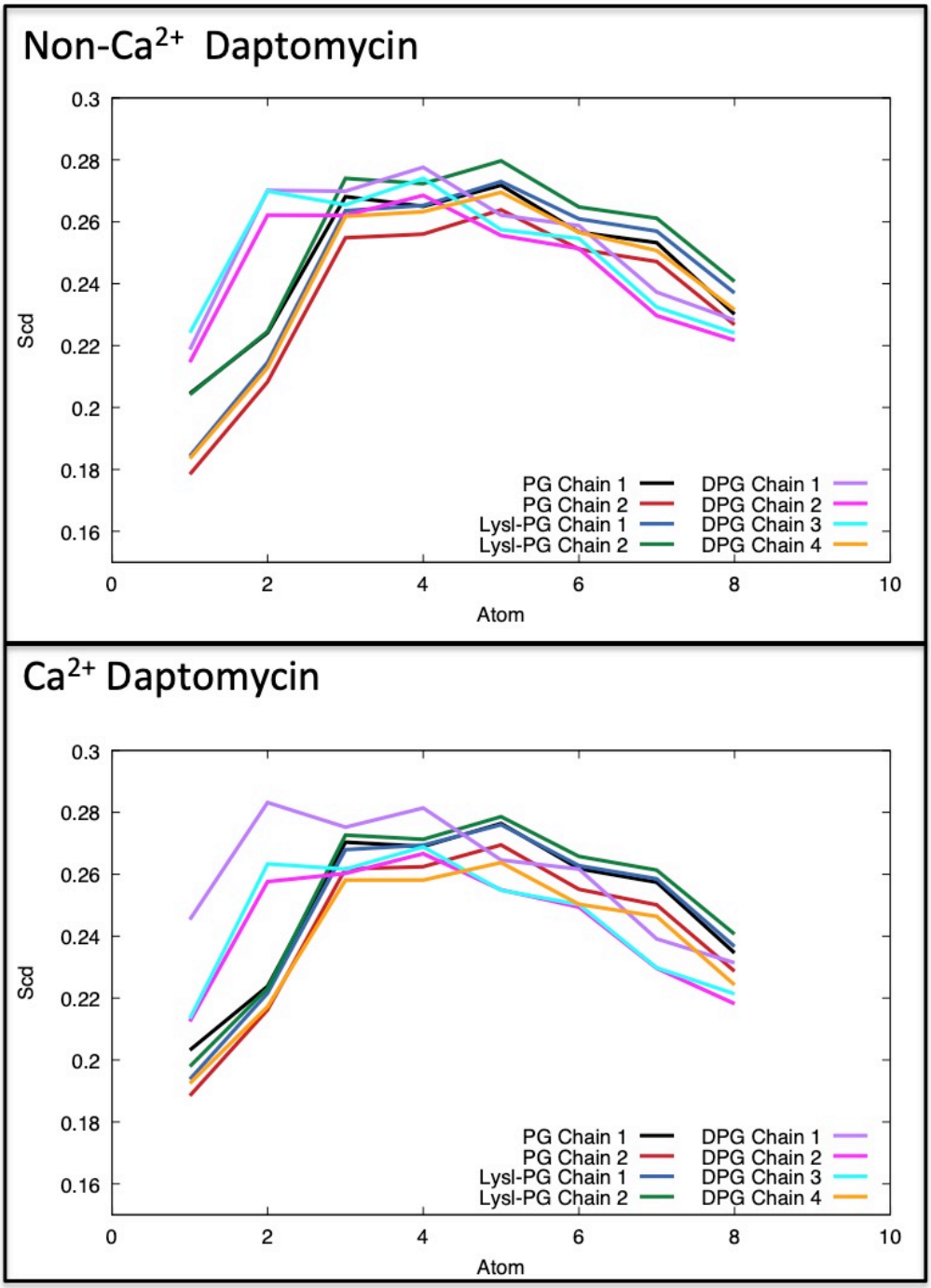

Figure 3.17: Deuterium order parameters (Scd per atom) of each lipid tail chain calculated over each simulation.

The lipids diffusion rates were measured for all lipids in both systems from 1.5-2 μs, Table 3.2. The lipids in the system with Ca^{2+} bound diffused slower than those with the original non-Ca^{2+} bound present. This difference is most likely due to the large Ca^{2+} bound daptomycin aggregate sitting on the membrane slowing down diffusion rates. Furthermore, the Ca^{2+} bound monomer that did insert into the membrane did so further than the non-Ca^{2+} bound that did. This and the large aggregate in the Ca^{2+} bound system could be crowding this membrane thereby slowing down lipid diffusion. There was little difference of the diffusion rate between lipid types.

Structure	PG Diffusion Rate (1e-5 cm^2/s)	Lysl-PG Diffusion Rate (1e-5 cm^2/s)	DPG Diffusion Rate (1e-5 cm^2/s)
Non-Ca^{2+} Daptomycin	0.0925 (±0.0428)	0.0925 (± 0.0428)	0.0919 (± 0.0454)
Ca^{2+} Daptomycin	0.0582 (± 0.0353)	0.0586 (± 0.0360)	0.0594 (± 0.0372)

Table 3.2: The lipid diffusion rates of lipids in *S. aureus* with both daptomycin models. Measured between 1.5-2 μs.

The total SASA of the polar and hydrophobic regions of daptomycin molecules was measured as a total over time, Figure 3.18. This data was again normalised to account for the cyclic loop being larger than the acyl tail. Broadly speaking the SASA was similar for both models. The similarity between SASA was possibly due to both models aggregating to an extent and both models having one monomer enter the bilayer via the daptomycin tail. The smaller SASA of the atoms within the polar region of daptomycin compared to the acyl chain suggests aggregation was driven by polar interactions.

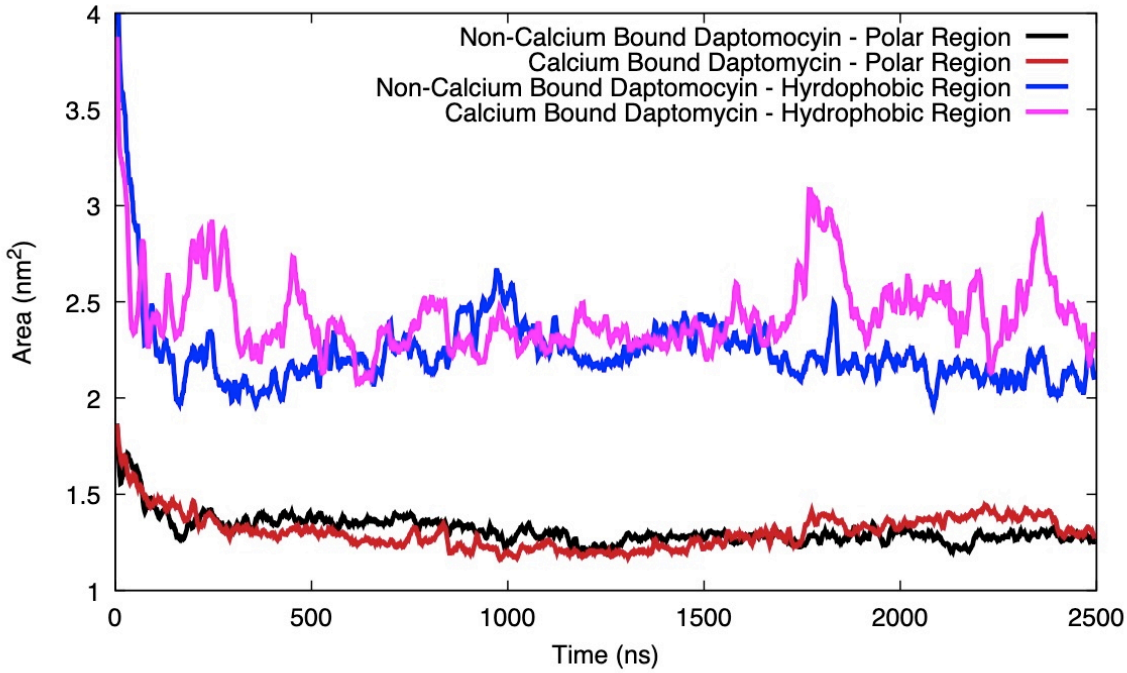

Figure 3.18: SASA for polar and hydrophobic regions of over time.

The number of contacts between daptomycin and the lipid head group was measured over time, Figure 3.19. Overall, the Ca^{2+} bound daptomycin made more contacts with the lipid heads than the non-Ca^{2+} bound, particularly when comparing contacts with PG. This could suggest that this Ca^{2+} bound model better shows the relationship between daptomycin and PG than the non-Ca^{2+} bound model. Furthermore, the greater collective contacts between the Ca^{2+} bound model and head groups was indicative of the aggregate of this model sitting on the membrane. This model was also shown to interact with the membrane more quickly than the original, non-Ca^{2+} model. Notably, both models showed a preference for DPG, despite the daptomycin and this lipid being negatively charged. This suggested that perhaps the calcium ions in solution were interacting with and binding to them thereby changing the charge of both daptomycin models. Both models not contacting the positively charged Lysl-PG significantly over the simulations support this suggestion.

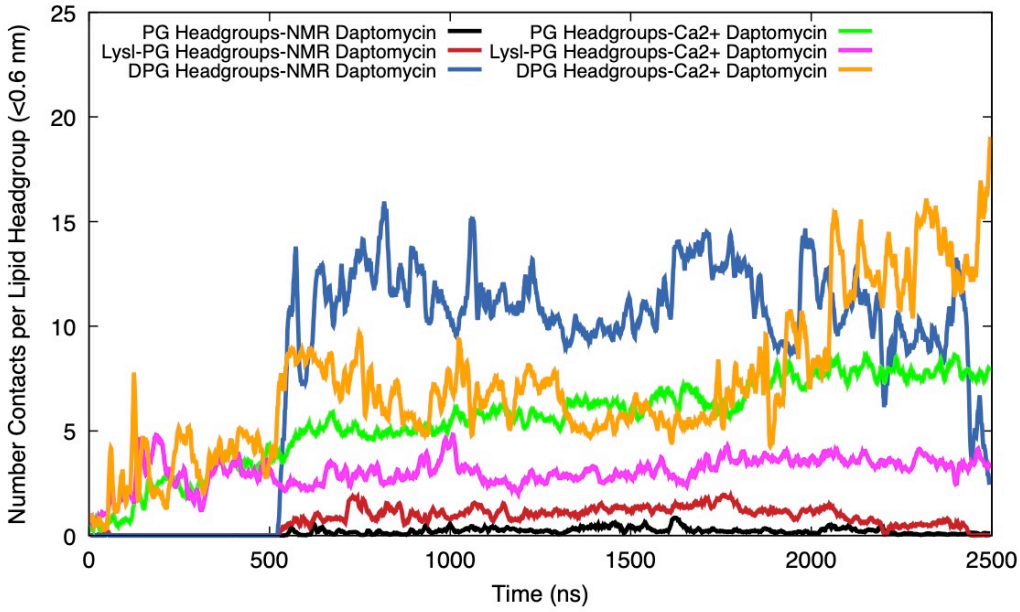

Figure 3.19: Number of contacts <0.6 nm between *S. aureus* lipids and daptomycin models measured over time (ns). Data has been normalised to account for difference in lipid numbers.

In order to support the proposal that both daptomycin models bound to calcium ions in solution, the contacts between them were measured, Figure 3.20. The number of contacts (A) and the average distance (B) were measured with calcium ions. The Ca^{2+} bound to the centre of the altered conformation were omitted to make the analysis comparable between both models. There were again more contacts between non-Ca^{2+} bound daptomycin and calcium ions; however the number of contacts for both systems was stable throughout both simulations. This could suggest that the interactions were long-lived. Furthermore, the greater number of calcium contacts between the non-Ca^{2+} bound and calcium ions versus the Ca^{2+} bound models could be due to the former being more freely dynamic in solvent therefore being more available to make such contacts. In addition, the distance between both daptomycin models and calcium ions were similar suggesting the contacts were long-lived and altered the charge of the daptomycin models allowing them to interact with the negatively charged lipids. Based on this the conformational cluster analysis was again determined and is shown in the Appendix, A.1. The 5 most common conformations for both models were very similar to the conformations

previously shown, Figure 3.11. This suggests that the daptomycin models interacted similarly with calcium ions in the presence and absence of a membrane.

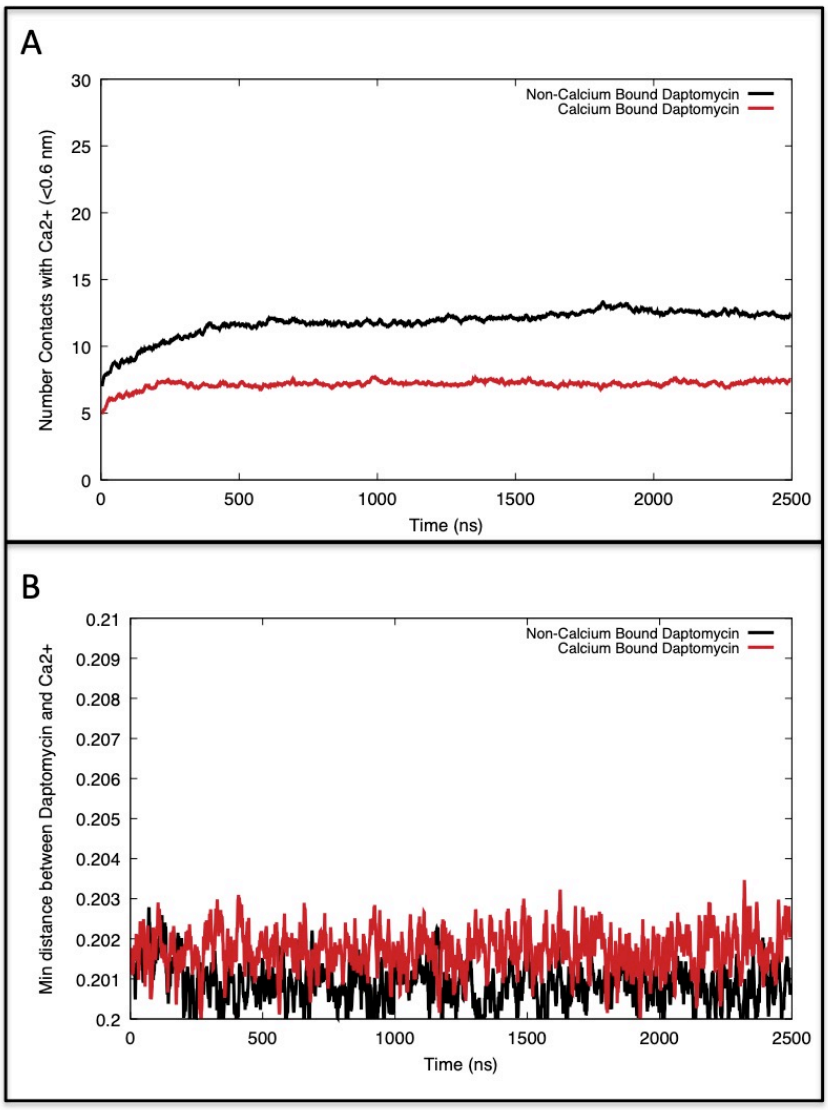

Figure 3.20: Analysis of Ca^{2+} ions with both daptomycin models - A) number of contacts <0.6 nm between daptomycin and Ca^{2+} ions over time and B) average minimum distance between daptomycin and Ca^{2+} ions over time. The Ca^{2+} ions conjugated to the centre of the loop in the Ca^{2+} model have been omitted from this analysis.

3.3.4 Conclusions

Firstly, focusing on the results from the simulations without a membrane, there were significant differences between the two models. The Ca^{2+} bound

molecules came into closer contact than the non-Ca^{2+} bound model, as shown throughout several forms of analyses, particularly the structural analysis. This could suggest this model better shows the micelle formation suggested by experimental work. It also could suggest the conformation formed by the cyclic ring of daptomycin when a calcium ion is important to the formation of micelles. As the ion-bound state is stable with the Ca^{2+} ion remaining in place, this could be the dominant species in solution. Furthermore, both models were shown to interact closely and fairly steadily with other calcium ions, further indicating that this interaction is favourable. This work suggested this interaction may be important to micelle formation by bridging cyclic regions. Also, the Ca^{2+} bound aggregate formed was on the larger side of suggested size with around 14 monomers within the aggregate. This may indicate the actual size of the micelle formed *in vivo* and support work that suggests micelles of this size.

In regards to the work with daptomycin and the *S. aureus* membrane, most molecules did not enter the membrane. However, the Ca^{2+} bound model behaved in line with experimental suggestions that it aggregates and sits on the membrane. Whilst the large aggregate on the membrane did not cause significant disruption to the bilayer, this could be due to constraints with the time scale of simulation work. The non-Ca^{2+} bound model did not form into a singular large aggregate and did not particularly interact with the membrane, further supporting that the modified daptomycin model better represents the *in vivo* conformation. Whilst daptomycin has been heavily dependent on PG, this work suggested a relationship between it and DPG. However, from the contact analysis it appeared the bound Ca^{2+} bound model first contact PG before coming into contact with DPG. This suggests a mechanism of daptomycin first docking with PG prior to interacting with other lipids as suggested in the literature. Finally, the non-Ca^{2+} bound daptomycin model interacted very little with PG, in contrast to the expectations. This further supports that the original, NMR structure does not best show the conformation that is required to interact with the bilayer and that the calcium ion being bound to the centre of the

peptide core is important for its mode of action, and my represent the dominant species in solution, prior to membrane targeting.

3.4 Daptomycin Behaviour PC Model Membrane versus Realistic *S. aureus* Membrane

The aim of this section was to understand the differences of daptomycin behaviour with a realistic (*S. aureus*) membrane and a model (PC) membrane, and particularly measure the dependence of daptomycin upon PG.

3.4.1 Methods and Simulation Setup

The daptomycin models and the *S. aureus* membrane parameters and structures were the same as previously described. Whilst the PC membrane was pure phosphatidylcholine and was made using membrane builder within CHARMM-GUI[96,108]. The protocols and force field were the same as previously described for simulations containing a membrane and were run above gel transition temperature for both membranes. All systems were again neutralised with 0.1 M $CaCl_2$ and set up as shown in Table 3.3.

Daptomycin Model	Membrane	Solvent	Simulation Length
1 x Original NMR (non-Ca^{2+} bound)	PC model	11743 H_2O, 42 Ca^{2+}, 81 Cl^-	1 μs x 3
1 x Ca^{2+} bound	PC model	11753 H_2O, 42 Ca^{2+}, 81 Cl^-	1 μs x 3
1 x Original NMR (non-Ca^{2+} bound)	*S. aureus*	15069 H_2O, 85 Ca^{2+}, 93 Cl^-	1 μs x 3
1 x Ca^{2+} bound	*S. aureus*	15057 H_2O, 85 Ca^{2+}, 93 Cl^-	1 μs x 3

Table 3.3: Simulations in the second section of the daptomycin work researching daptomycin PG dependence.

3.4.2 Results

Snapshots of the end point, 1 μs, of the simulations comparing the non-Ca^{2+} bound daptomycin and the Ca^{2+} bound daptomycin with a pure PC and *S. aureus* membranes, Figure 3.21. The molecules began ~5 nm above the membrane. In all simulations both daptomycin modes inserted into the bilayers via the tail region with the cyclic area largely remaining outside of the membrane. Visually

it appeared that both daptomycin models were able to penetrate slightly further enter into the PC membrane than the *S. aureus* membrane, yet the *S. aureus* membrane looked less organised and thinner than the PC bilayer. It appeared that daptomycin entering the PC membrane caused order and gel phase within the membrane. Further analysis was required to investigate this further.

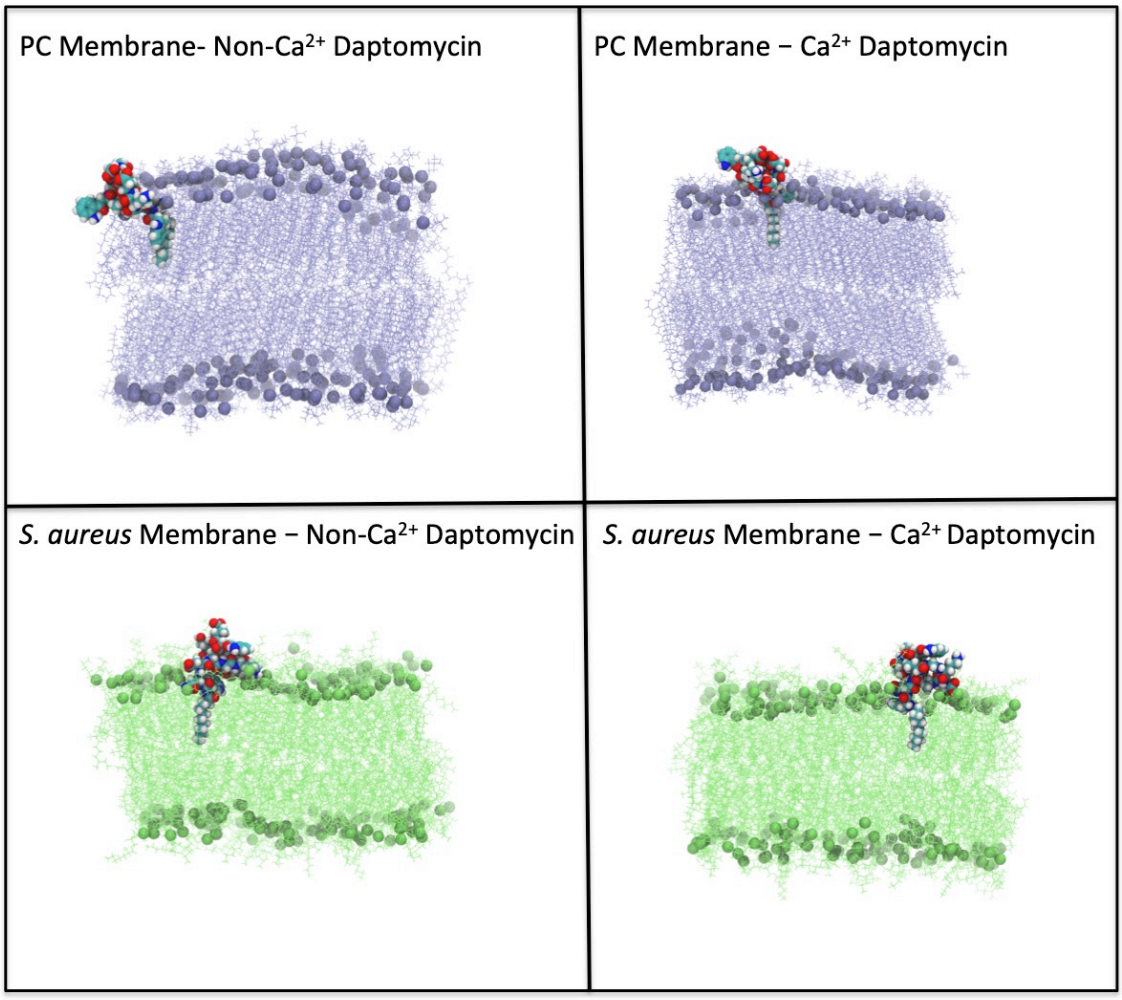

Figure 3.21: Snapshots of end point simulations (1 us) of non-Ca^{2+} daptomycin molecule and Ca^{2+} conjugated daptomycin (both in cyan, red, blue and white) molecule in PC (lilac) and *S. aureus* (green) membranes. Solvent and counter ions have been omitted for clarity.

The densities were measured for the lipid heads and tails, solvent, and daptomycin loop and tail regions for all systems over the last 100 ns, Figure 3.22. From this it can be seen that in all systems, the daptomycin tail enters

further into the membranes than the cyclic loop. In addition, the PC membrane appears to be more organised than the *S. aureus* bilayer, given the taller narrower peaks of the lipid heads and tails in the PC membrane plots. This supports the evidence from the visualisation. However, the solvent appears to be further into the head group region of the PC membrane.

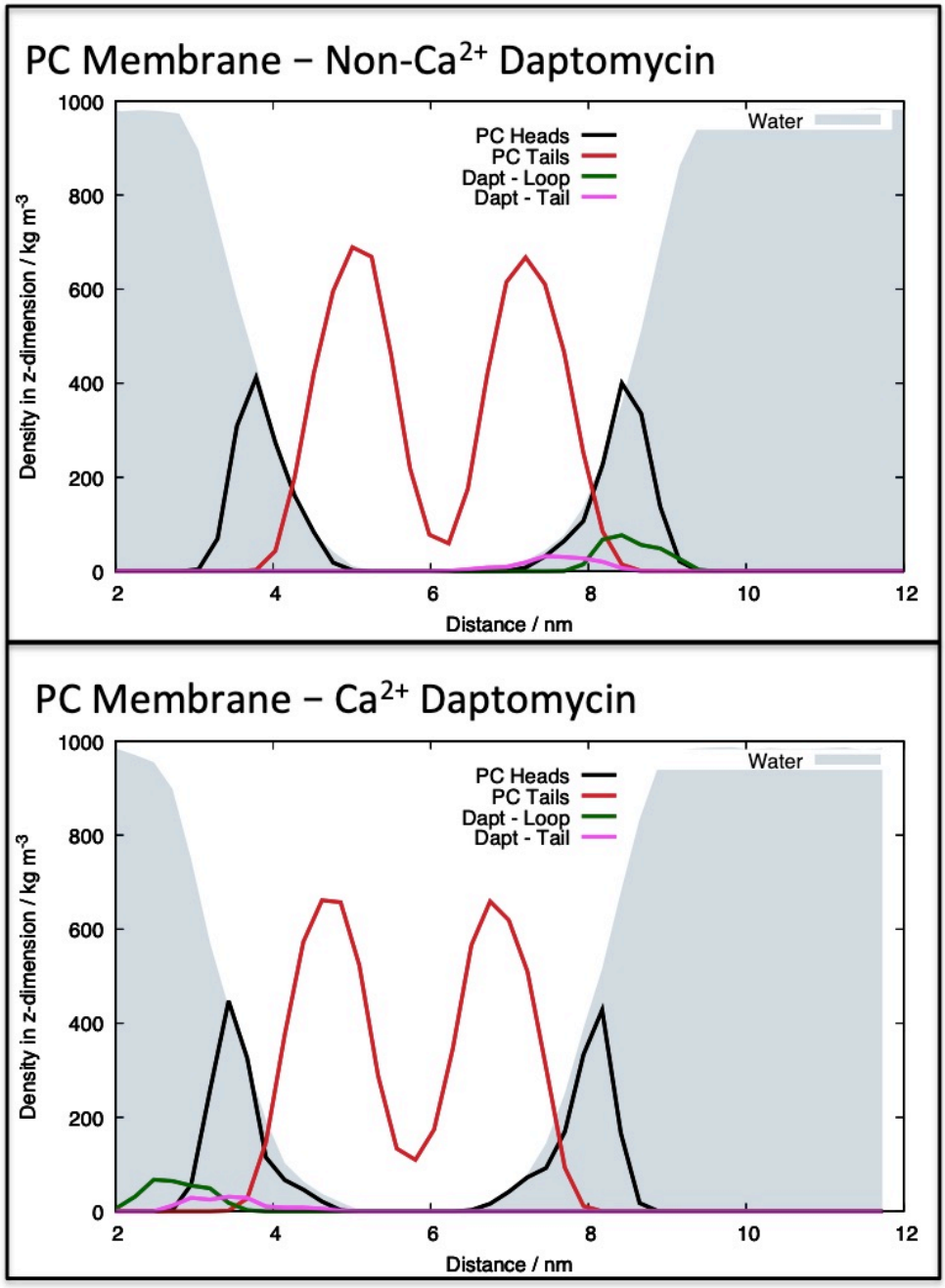

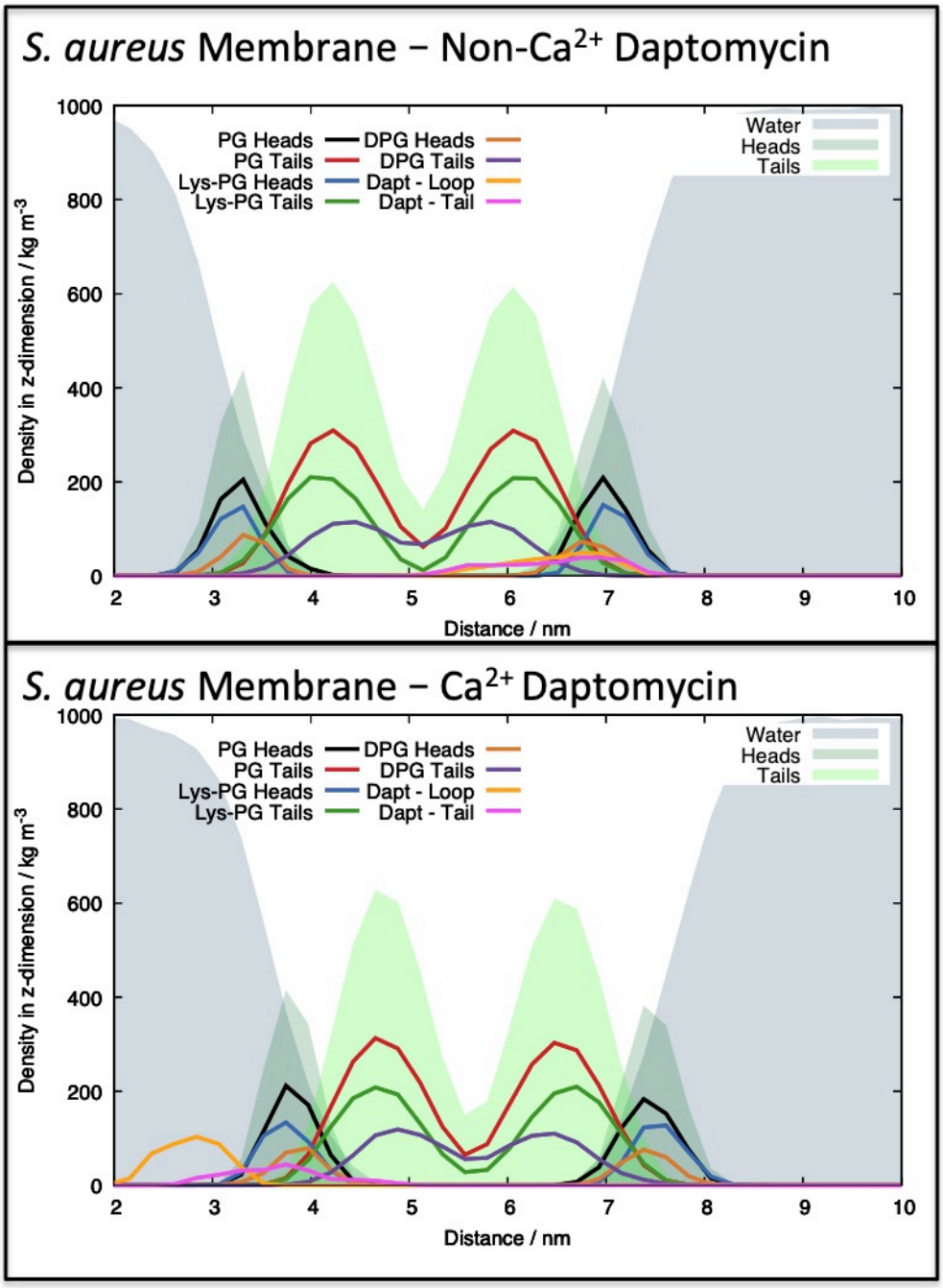

Figure 3.22: Densities of both daptomycin models with PC and *S. aureus* membrane lipid heads, tails and solvents. Measured over last 100 ns of simulations.

The membrane thicknesses were measured for all systems for the last 100 ns of the simulations, Figure 3.23. Clearly the *S. aureus* membrane is thinner in the presence of either daptomycin model compared to the PC membrane, as shown by the darker blue regions. In the PC membrane there are clearly thinner areas where the daptomycin tail has inserted, whereas, the *S. aureus* membrane is overall thinner across the whole bilayer. The thicker PC membrane may due to daptomycin appearing to cause membrane order in this model. Furthermore, the Ca^{2+} bound daptomycin appears to have caused increased membrane thinning of both bilayers suggesting that this model was better able to disrupt membranes, particularly the *S. aureus* membrane. This may suggests that the Ca^{2+} bound model is a better representation of active daptomycin *in vivo* and supports experimental evidence that daptomycin behaves in the presence of PC membranes versus realistic membranes.

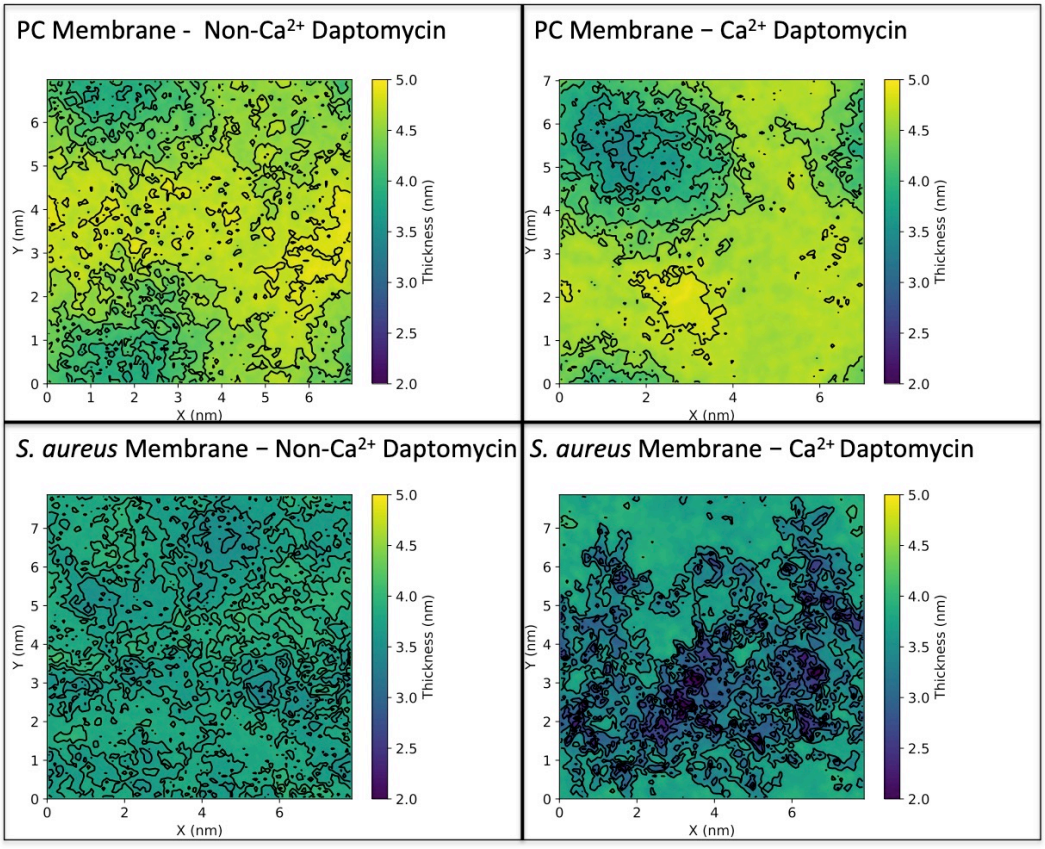

Figure 3.23: Membrane thickness of PC and *S. aureus* membranes with different daptomycin models. Measured over last 100 ns of simulations.

The densities of the phosphates in both bilayers were also measured, Figure 3.24. This clearly showed greater disruption of the head groups in the PC membrane where the daptomycin tail had inserted, particularly with the Ca^{2+} bound model, as shown by the deformations in the plot. This suggests that the initial suggestion made from the snapshots that daptomycin further into the PC membrane was accurate. This insertion may be causing the order and gel phase seen in the PC membrane or these plots are curved due to this effect. However, there was also slight curvature in the phosphate densities plotted for the *S. aureus* membrane. Comparing between models rather than membranes, deformation of the membrane appeared similar with both models.

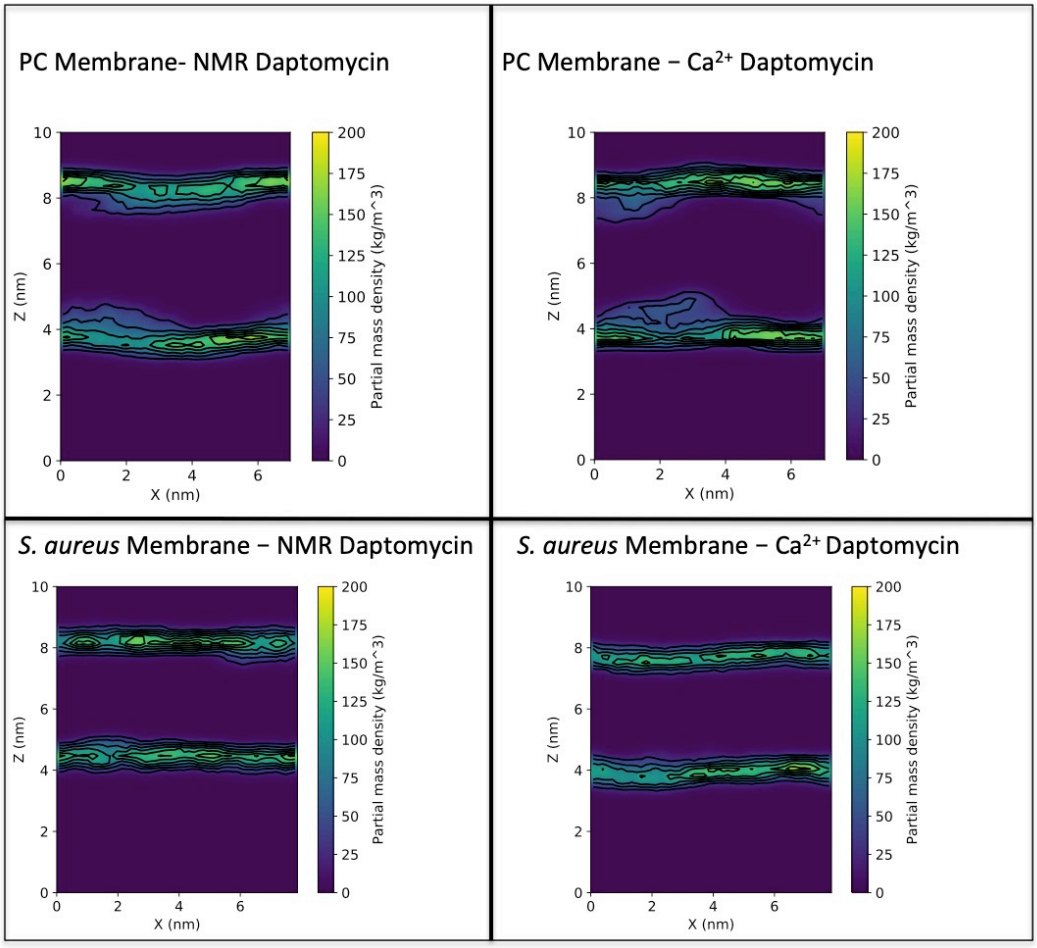

Figure 3.24: Phosphate densities in Y-direction of PC and *S. aureus* membranes with different daptomycin models. Measured over last 100 ns of simulations.

The APL was measured over time and these results were in line with the previous results, Figure 3.25. The APL was higher for the *S. aureus* membrane simulations, which is known to inversely correlate to membrane thickness meaning the thinner *S. aureus* systems had a larger APL as anticipated. Between daptomycin models however there was very little difference in the APL. The gradual drop of the APL in the PC membrane, particularly in the first 200 ns, was due to the membrane entering a gel phase. Based on visualizing the trajectories in this time frame the daptomycin entered the membrane then appeared to induce the formation of a gel phase. The APL analysis supports this and it would appear thus appear that daptomycin caused membrane order in this model.

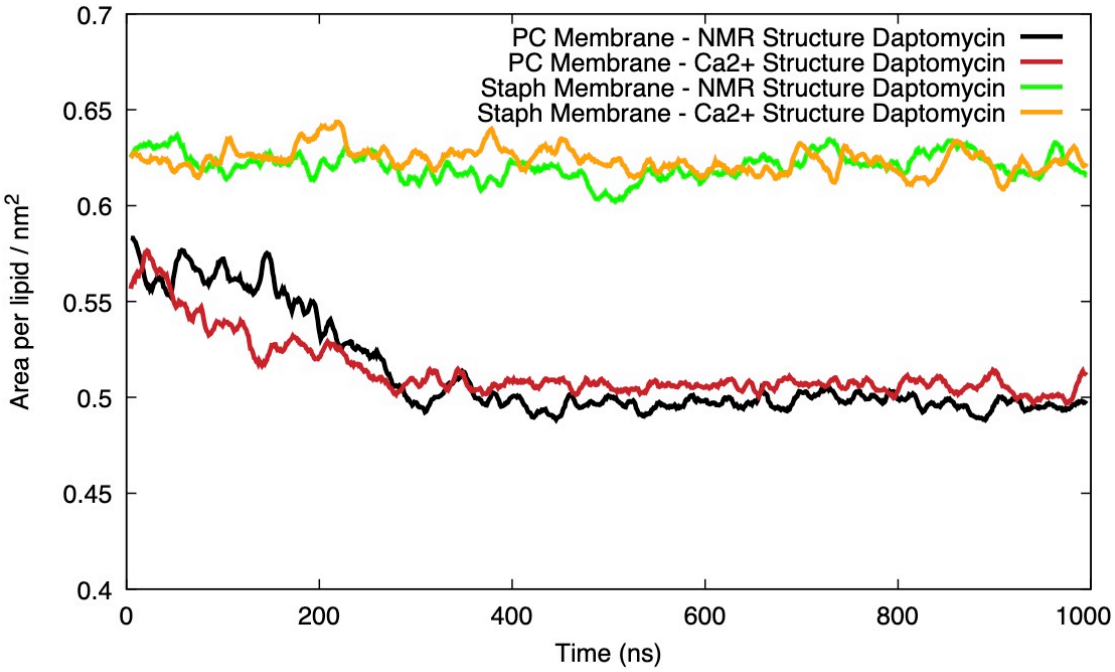

Figure 3.25: APL of the lipids in PC and *S. aureus* membranes with different daptomycin structures measured over time.

The Z co-ordinates were measured of the daptomycin cyclic loops and tails in reference to the lipid head groups over time, Figure 3.26. This showed both daptomycin models entering further into the PC membrane than the *S. aureus* membrane, particularly the daptomycin tails. However for the *S. aureus* bilayer, the Ca^{2+} bound daptomycin appears to enter the membrane further than the non-Ca^{2+} bound model, particularly the daptomycin tail. This may support

suggestions that the Ca^{2+} ion being in the centre of the cyclic loop is important to the mode of action of the drug. It also highlights the difference between the behaviour of daptomycin in a model membrane in comparison to a realistic one.

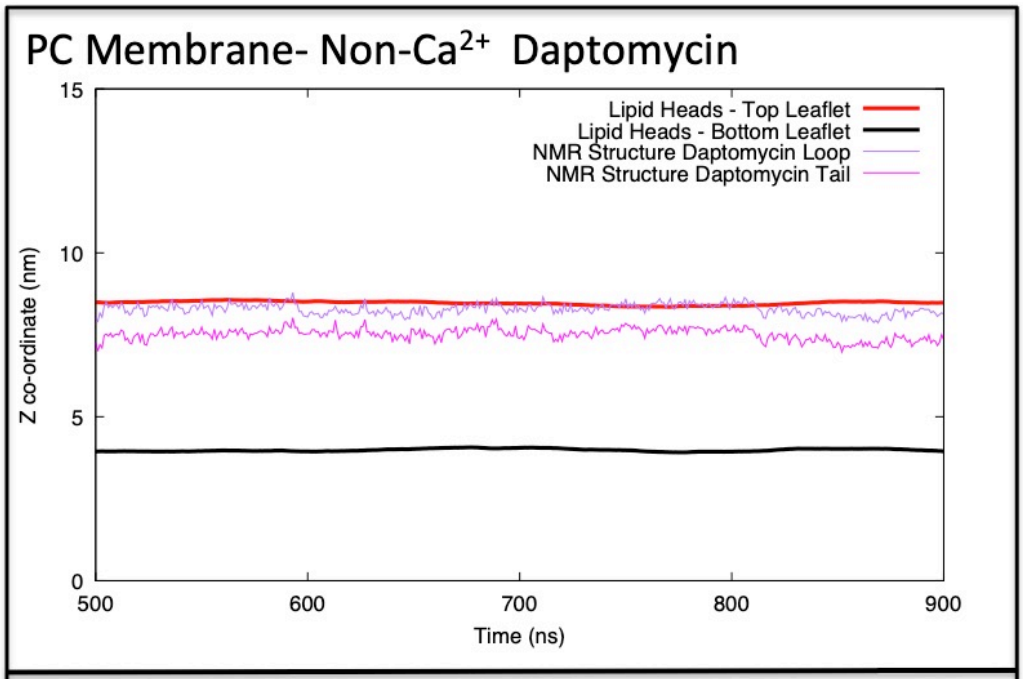

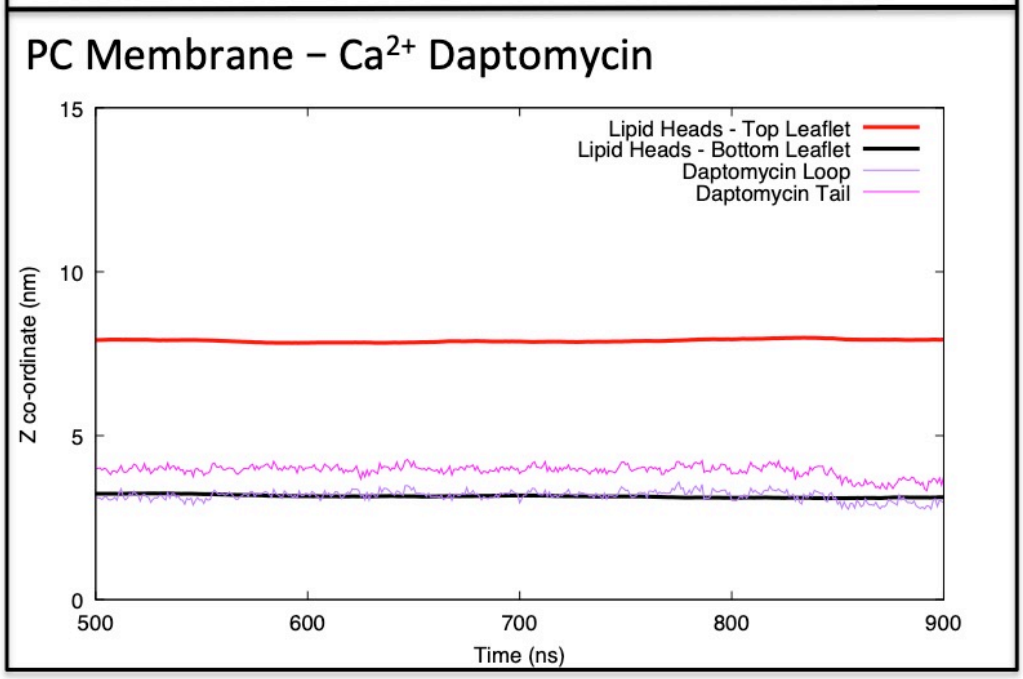

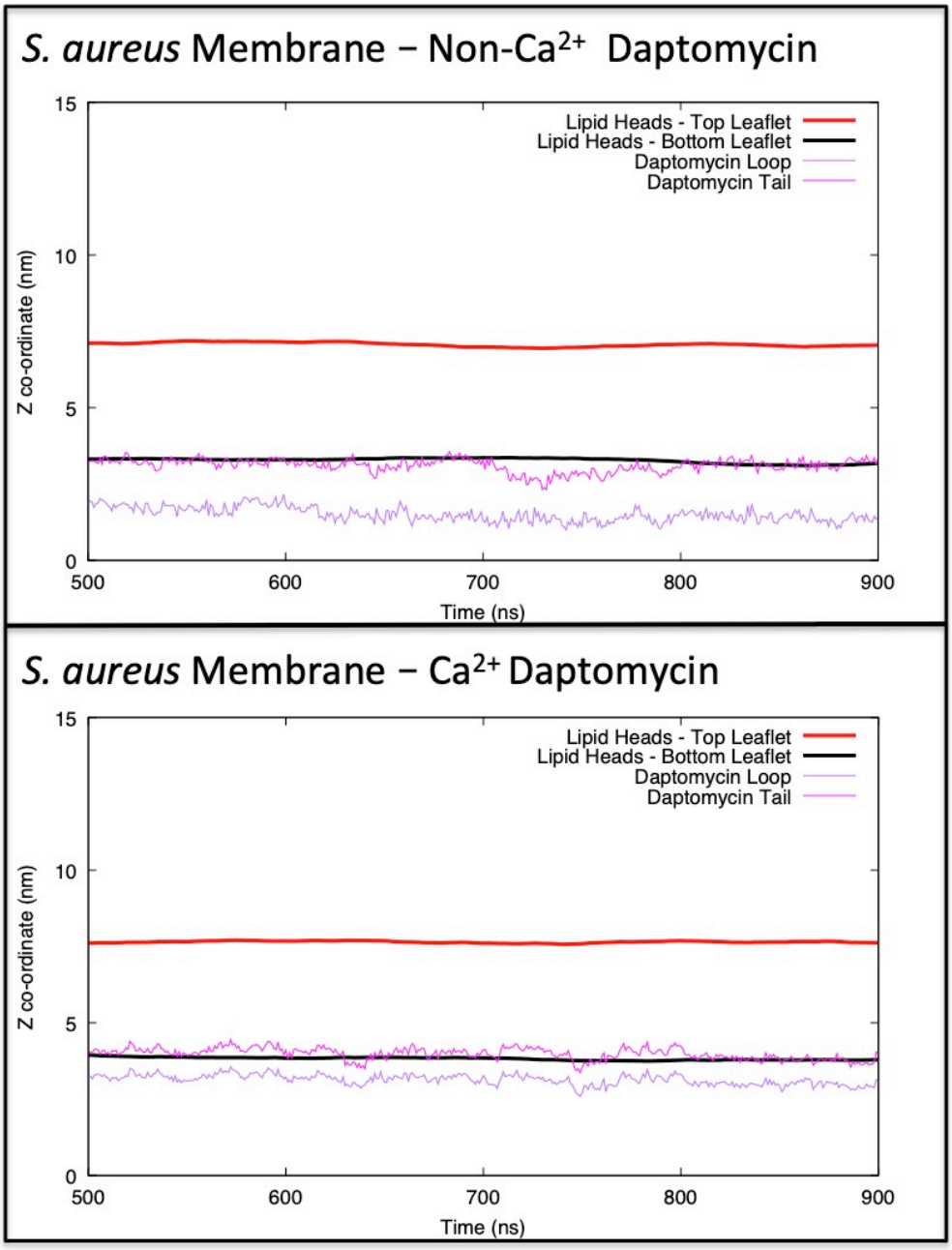

Figure 3.26: Z coordinates of different daptomycin loops and tails relation to the top and bottom leaflet of membranes over time.

In addition, the deuterium order parameters (Scd) for the lipid tails were measured, Figure 3.27. This showed that the lipid tails of the PC membrane were more organised and therefore supporting that it was in a gel phase, which is in agreement with the previous analyses.

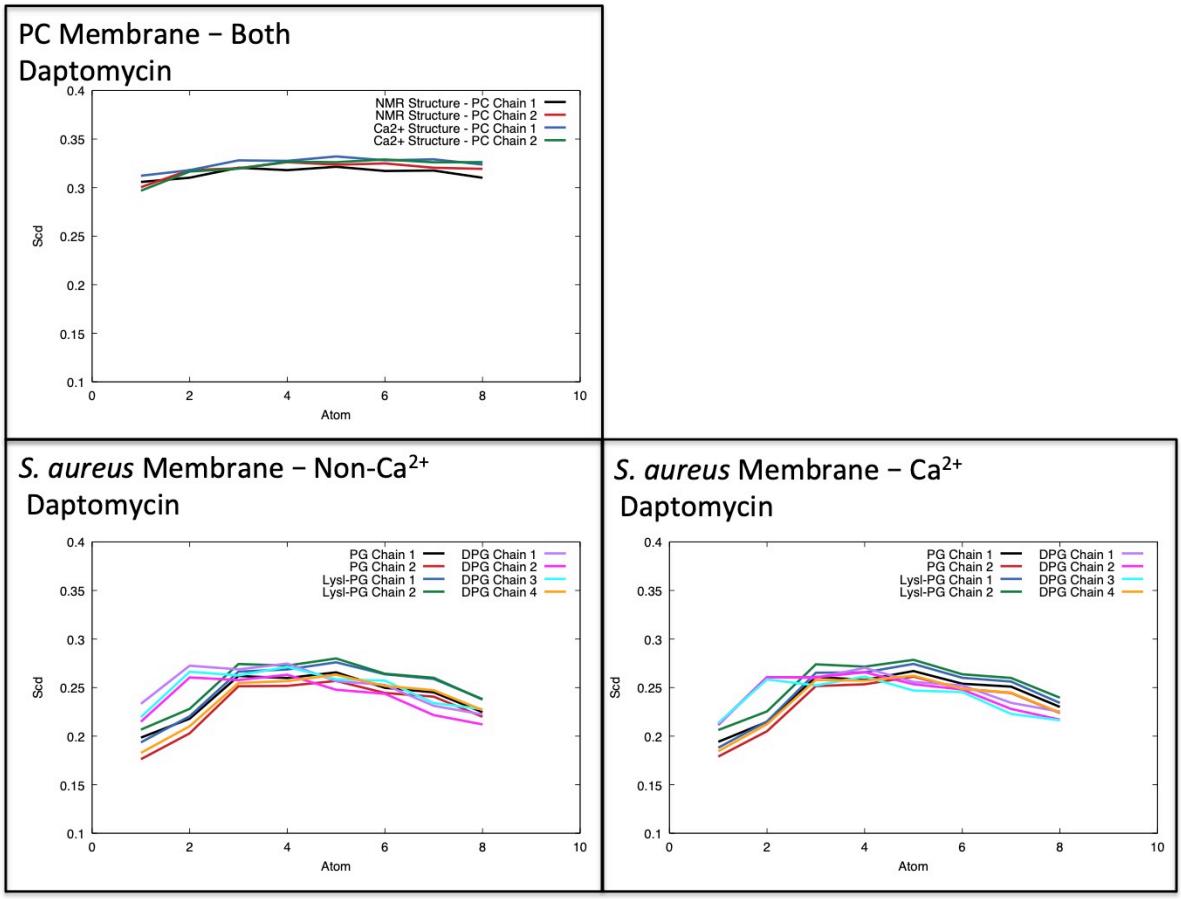

Figure 3.27: Deuterium order parameters of each lipid tail chain calculated over each simulation.

Finally, the lipid diffusion rates were also measured for the middle section of the simulations, 400-800 ns, Table 3.4. The *S. aureus* lipids that contained the Ca^{2+} bound daptomycin molecule had inserted diffused the most slowly, suggesting the greatest effect resulted from the combination of this daptomycin model and the realistic membrane model. Membrane lipids often diffuse more slowly when the membrane is crowded. In both membranes with the Ca^{2+} bound daptomycin the lipids moved more slowly.

Structure	PC Diffusion Rate (1e-5 cm^2/s)	PG Diffusion Rate (1e-5 cm^2/s)	Lysl-PG Diffusion Rate (1e-5 cm^2/s)	DPG Diffusion Rate (1e-5 cm^2/s)
Non-Ca^{2+} Daptomycin	0.0456 (±0.0139)	0.0829 (±0.0286)	0.0814 (±0.0287)	0.0805 (±0.0264)
Ca^{2+} Daptomycin	0.0591 (±0.0383)	0.0348 (±0.0160)	0.0348 (±0.0153)	0.0331 (±0.0143)

Table 3.4: The lipid diffusion rates of lipids in *S. aureus* with both daptomycin models. Measured between 400-800 ns.

3.4.3 Conclusions

Firstly, comparing the level of disruption between the two membranes, the *S. aureus* membrane was clearly more disordered by the daptomycin model than the PC membrane as evidenced by the *S. aureus* membrane being less ordered. Usually, it would be expected that a membrane inserting peptide would better disrupt a simpler membrane but this was not the case in this example. Indeed, it appeared that daptomycin caused order and gel phase in the PC membrane which was counter to what would be anticipated. This may be due to daptomycin being dependent on PG for its mode of action. Whilst both daptomycin models did insert into the PC membrane, both models caused greater disordering to the *S. aureus* as displayed by membrane thinning.

In regards to the two different models, both inserted into both membranes via the tail, in line with experimental work, driven by hydrophobic interactions. The Ca^{2+} bound model disrupted both membranes more than the original daptomycin model. The densities showed this model further inserting into the membrane whilst the lower lipid diffusion rates of membranes with this model further inserted thereby crowding the bilayer.

3.5 Increased Daptomycin Concentration with *S. aureus* Membrane Study

The aim of this section was to study a larger number of daptomycin molecules with the *S. aureus* membrane to allow the investigation of membrane action of daptomycin.

3.5.1 Methods and Simulation Set up

The final section of this work is focused on investigating how a larger concentration of daptomycin molecules would interact with the *S. aureus* membrane without them forming large aggregates. The aim of this was to see how a larger number of daptomycin inserting would affect the bilayer. The parameters and structures for the daptomycin models and *S. aureus* membrane were the same as previously described at the beginning of this chapter. The simulations were run using the same force field and method as previously described. The systems were again neutralised in 0.1 M $CaCl_2$ and the contents of the simulations are described in Table 3.5.

Daptomycin Model	**Membrane**	**Solvent**	**Simulation Length**
5 x Original NMR (non-Ca^{2+} bound)	*S. aureus*	14380 H_2O, 87 Ca^{2+}, 93 Cl^-	1 μs x 3
5 x Ca^{2+} bound	*S. aureus*	14482 H_2O, 87 Ca^{2+}, 93 Cl^-	1 μs x 3

Table 3.5: Simulations in the third section of the daptomycin work researching daptomycin interaction with the *S. aureus* membrane.

3.5.2 Results

The snapshots of the end point (1 μs) of the simulations containing each containing 5 daptomycin molecules, with the *S.* aureus membrane are shown in Figure 3.28. The molecules began ~5 nm above the membrane and at least 2 nm from other daptomycin molecules in all directions. From this it can be seen the Ca^{2+} model has further inserted into the membrane than the non-Ca^{2+} model. The non-Ca^{2+} bound molecule formed a large aggregate and did not fully insert, whereas the Ca^{2+} bound models interacted less with one another and inserted via the tail again as with the previous analysis.

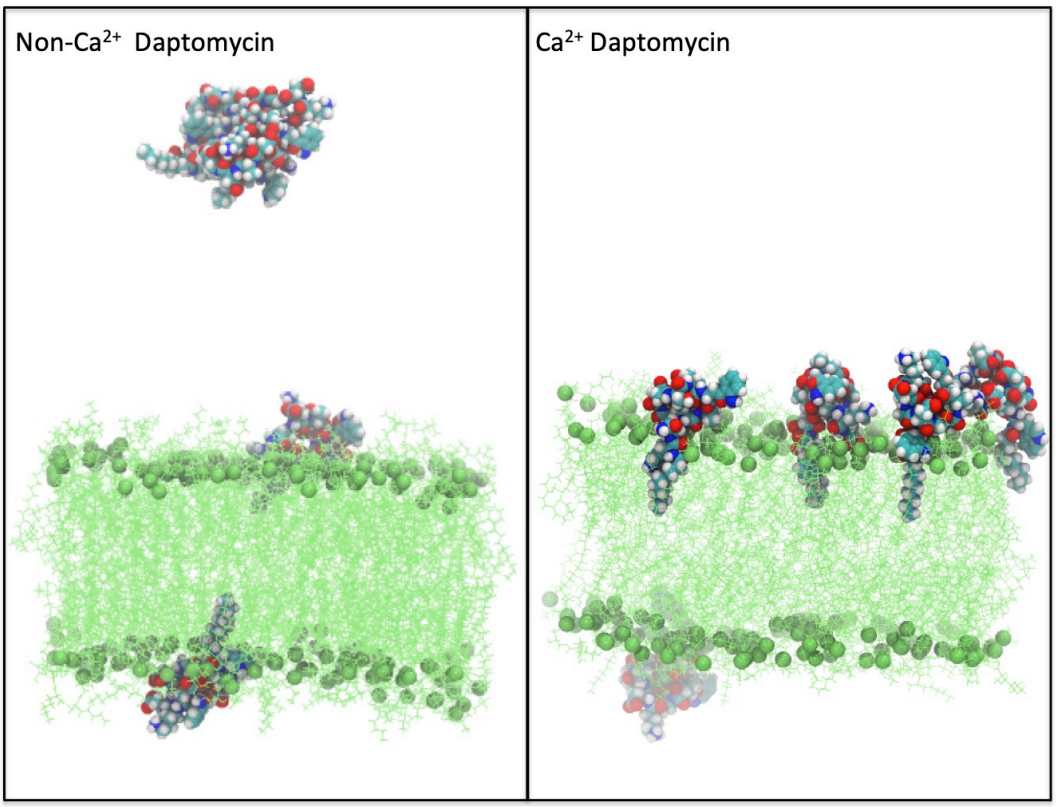

Figure 3.28: Snapshots of end point (1 μs) of 5 daptomycin molecules (cyan, red, blue and white) with *S. aureus* membrane (green). Solvent and ions have been omitted for clarity.

The densities were again measured for the membrane heads and tails, solvent and the daptomycin loops and tails, Figure 3.20. This clearly showed the Ca^{2+} bound daptomycin further entering the membrane than the non-Ca^{2+} daptomycin, with the tail inserting more so into the bilayer. The Ca^{2+} bound daptomycin has also entered into both sides of the membrane. However the non-Ca^{2+} bound daptomycin had not inserted into the membrane as far. This suggests that the Ca^{2+} bound model is better at replicating the *in vivo* mechanism of daptomycin particularly at this higher concentration in reference to the previous section of work. However, this could be stochastic and not indicative that the non- Ca^{2+} cannot enter the membrane at this concentration.

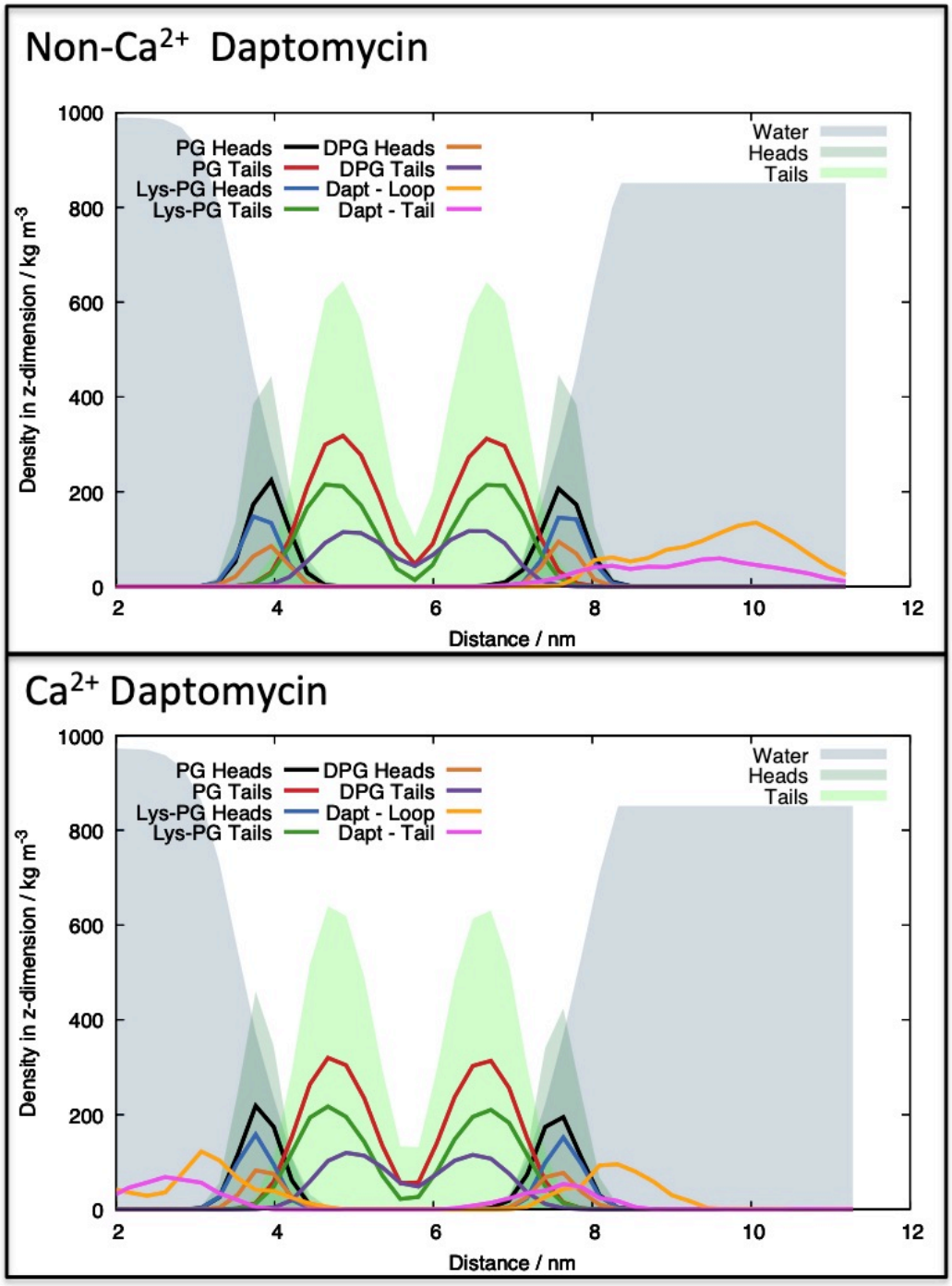

Figure 3.29: Densities of both daptomycin models *S. aureus* membrane lipid heads, tails and solvents. Measured over last 100 ns of simulations.

The membrane thickness, Figure 3.30, showed that the membrane containing the Ca^{2+} daptomycin molecules was slightly thinner than the one with the non-Ca^{2+} model. This suggests that this realistic membrane model was more disrupted by the Ca^{2+} bound daptomycin.

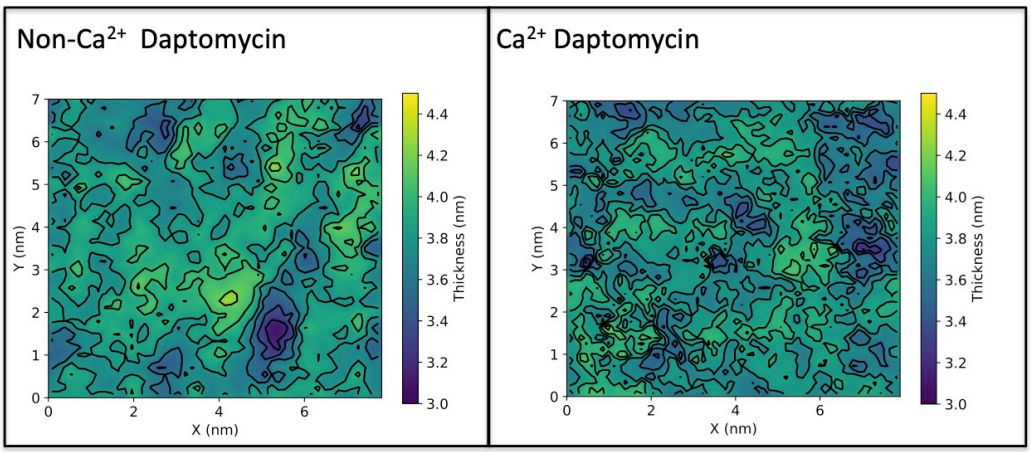

Figure 3.30: Membrane thickness of *S. aureus* membrane with different daptomycin models. Measured over last 100 ns of simulations.

The phosphate densities were measured for the head groups in both systems, Figure 3.31. The system with the Ca^{2+} daptomycin models showed a slightly larger overall curve in the head groups suggesting this daptomycin model had disrupted the membrane to cause a curvature of the bilayer. In the non-Ca^{2+} model system, there was a slight curvature of the densities most probably due to the points where daptomycin had inserted.

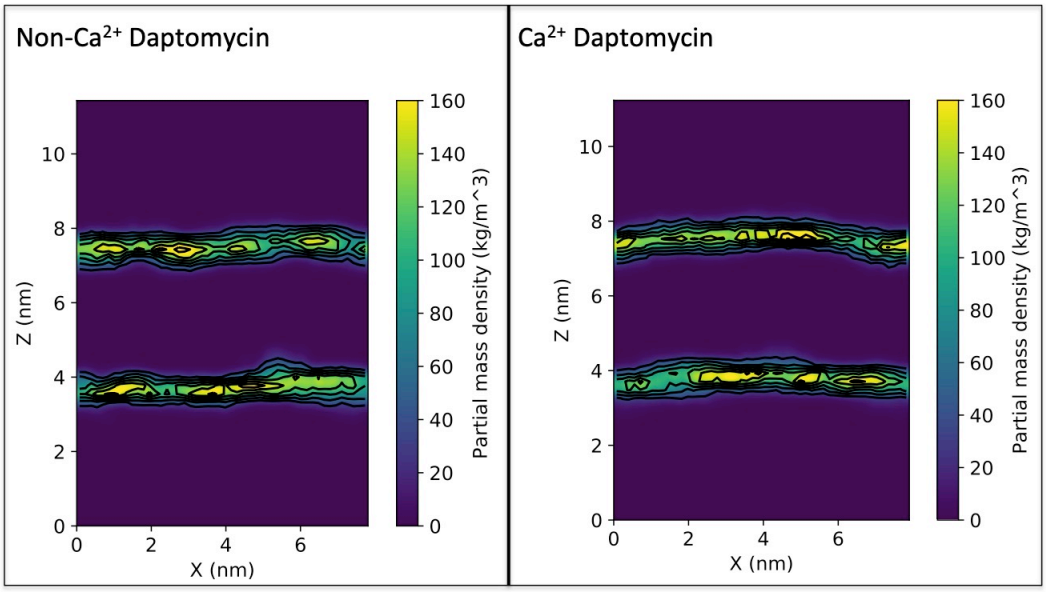

Figure 3.31: Phosphate densities in Y-direction of *S. aureus* membrane with different daptomycin models. Measured over last 100 ns of simulations.

The APL was similar across both systems, Figure 3.32, however it was slightly larger in the system with Ca^{2+} bound daptomycin throughout most of the simulation. This is in line with the indications of the membrane being slightly thinner in the presence its presence.

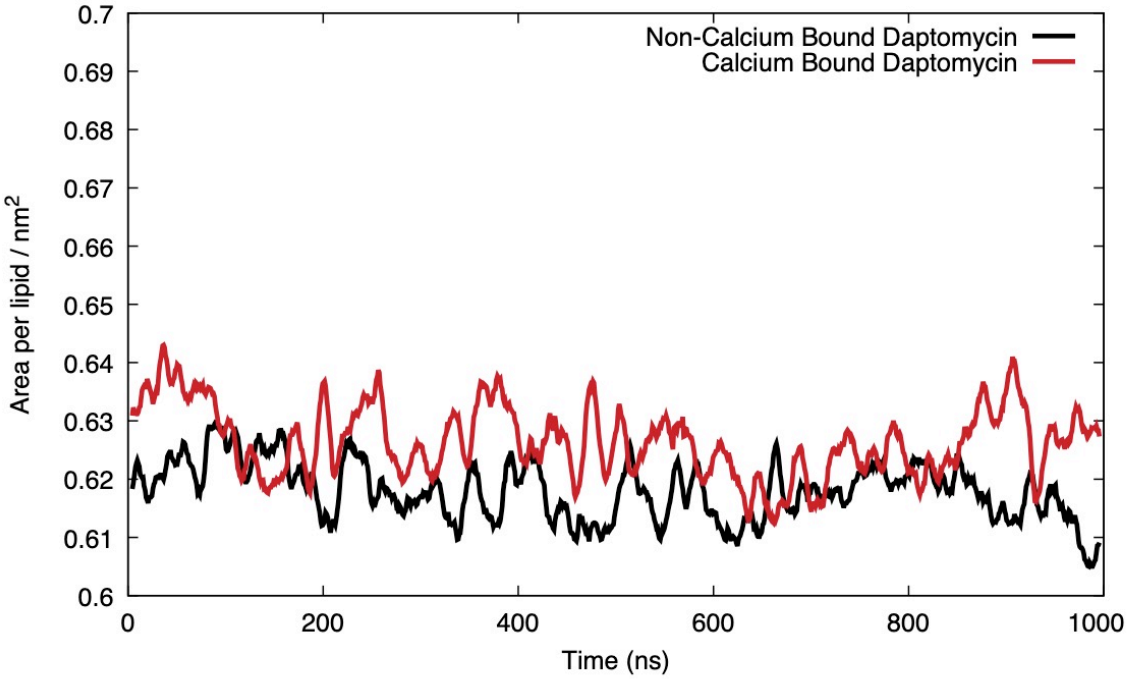

Figure 3.32: APL of the lipids in *S. aureus* membrane with different daptomycin models measured over time.

The order parameters (Scd) for the lipid tails of both systems are shown in Figure 3.33. There was not a large difference between systems with this analysis however the top of the lipid tails appear less organised when in contact with the Ca^{2+} bound model suggesting the area of the bilayer in this system was more disrupted. This was most probably due to the daptomycin tail inserting and in line with the previous results.

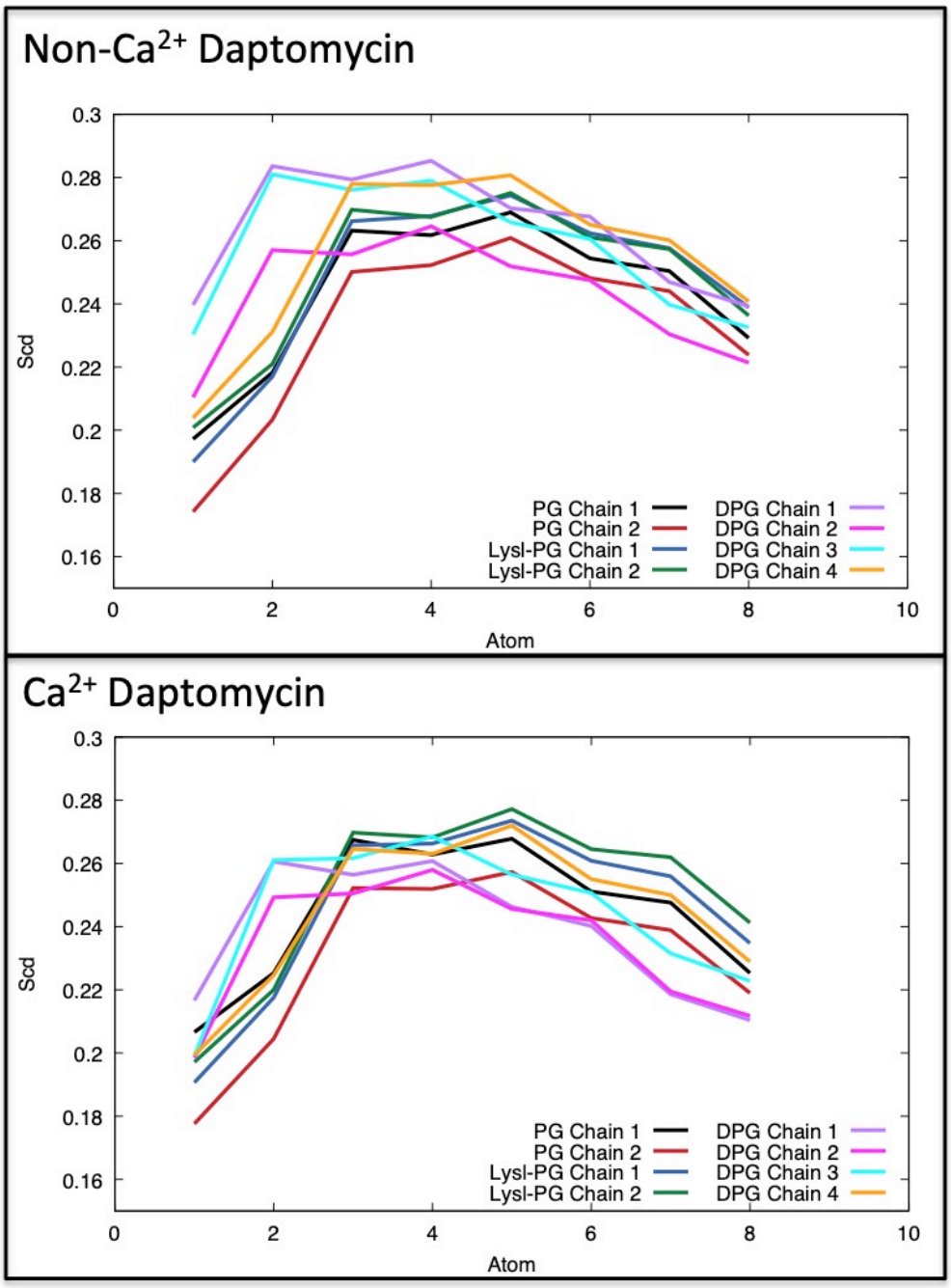

Figure 3.33: Deuterium order parameters (Scd per atom) of each lipid tail chain calculated over each simulation.

The number of contacts, <0.6nm, between the head groups of each lipid in the bilayer and the daptomycin models were measured over time (ns), Figure 3.34. This data was normalised to account for the differing availability of each lipid type within in the membrane. A significant difference between the models was observed regarding the preference for the Ca^{2+} bound daptomycin to interact

with DPG. This was most likely due to the change in charge involved with the Ca^{2+} bound to the centre of the loop making an interaction between this daptomycin model and the more negatively charged lipid. Furthermore, overall there were more contacts between the Ca^{2+} bound daptomycin and lipid heads, which supports the suggestion from previous data that this model interacted more with the bilayer.

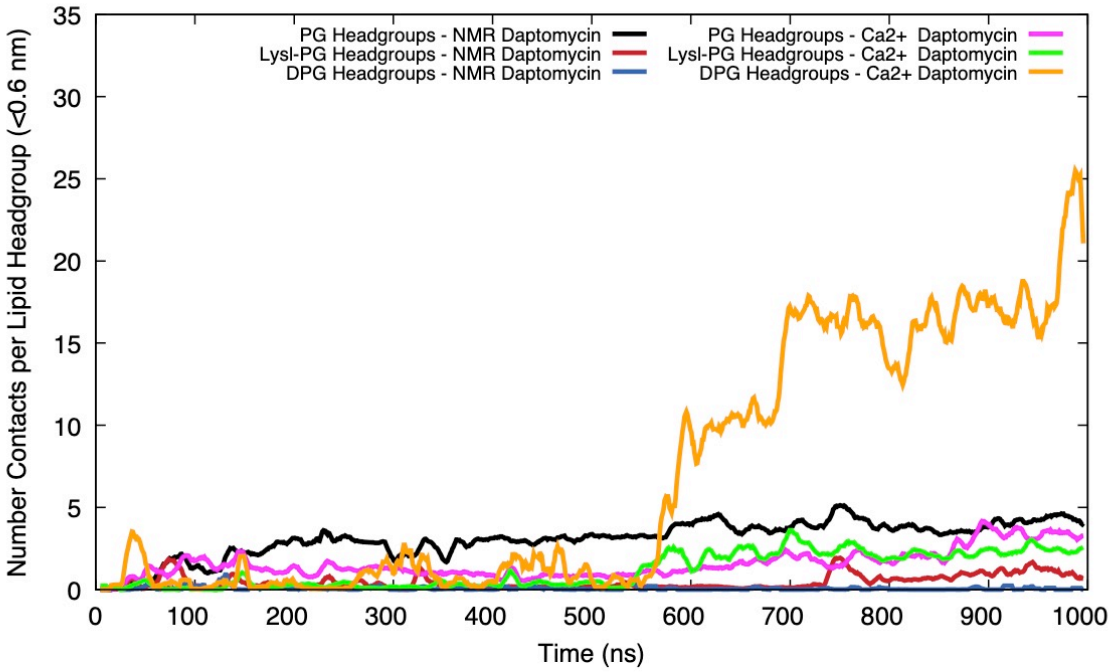

Figure 3.34: Number of contacts <0.6 nm between *S. aureus* lipids and daptomycin models measured over time (ns). Data has been normalised to account for difference in lipid numbers

The lipid diffusion rates of all lipid types in both systems were measured over the durations of the simulations, Table 3.6. The lipids in contact with the Ca^{2+} bound daptomycin molecules moved significantly slower, two orders of magnitude slower, than the lipids that came into contact with the non-Ca^{2+} model. This suggested that this system was more crowded therefore slowing down the diffusion of the lipids and supported the previous analyses that showed the Ca^{2+} bound model further entered and disrupted the *S. aureus* bilayer.

Structure	PG Diffusion Rate (1e-5 cm^2/s)	Lysl-PG Diffusion Rate (1e-5 cm^2/s)	DPG Diffusion Rate (1e-5 cm^2/s)
Non-Ca^{2+} Daptomycin	0.0690 (±0.0466)	0.0688 (±0.0473)	0.0684 (± 0.0469)
Ca^{2+} Daptomycin	0.0006 (±0.0002)	0.0006 (± 0.0001)	0.0007 (±0.0001)

Table 3.6: The lipid diffusion rates of lipids in *S. aureus* with both daptomycin models. Measured between 400-800 ns.

The Z-coordinates of a randomly chosen daptomycin cyclic loop and tail were measured again in reference to the Z-coordinates of the phosphates of the lipid head groups, Figure 3.35. Note that the jump seen in the non-Ca^{2+} plot is due to PBC and not daptomycin crossing the membrane. This showed the daptomycin tail of the Ca^{2+} bound model entered into the membrane whereas the tail of the non-Ca^{2+} model did not enter the bilayer. Notably again, the cyclic loop of both models did not enter the membrane supporting the evidence that the cyclic region of daptomycin does not enter the membrane.

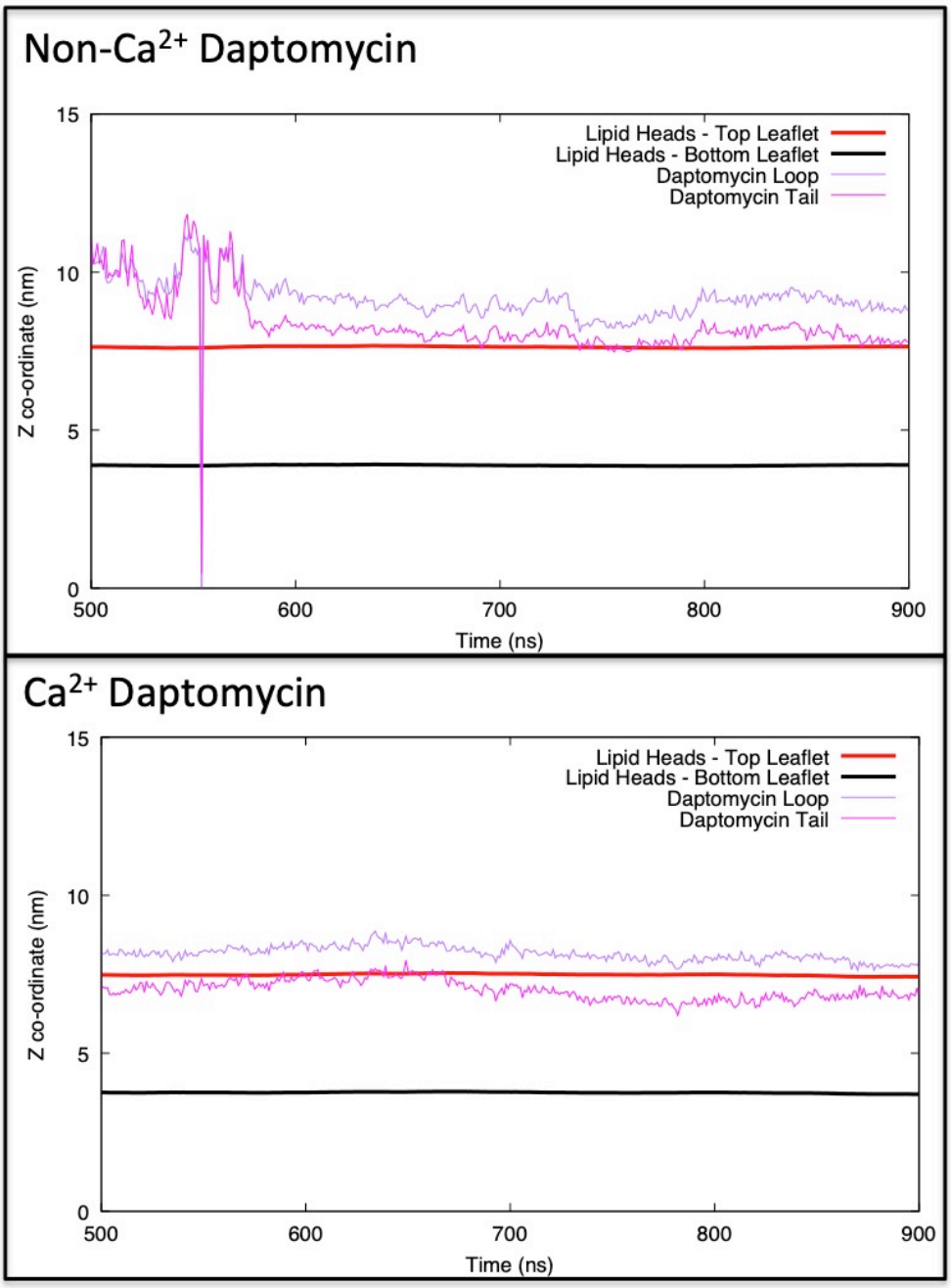

Figure 3.35: Z-coordinates of different daptomycin loops and tails relation to top and bottom leaflet of membranes over time.

Finally, the interactions between Ca^{2+} ions and both daptomycin models were measured, Figure 3.36 with A) showing the number of contacts between daptomycin and Ca^{2+} ions <0.6 nm and B) the minimum distance between daptomycin and Ca^{2+} ions. The Ca^{2+} ions bound to the centre of the cyclic loop of the altered structure were omitted for parity. Interestingly, there were more contacts between non-Ca^{2+} bound daptomycin and Ca^{2+} ions than with the Ca^{2+} ions whilst the inverse was true for the minimum distance between Ca^{2+} ions and daptomycin models. This may suggest that the interactions between Ca^{2+} ions and the Ca^{2+} bound model were longer lived and perhaps assisted the model in entering the membrane and further altering the charge to allow the interaction with DPG to be more favourable. Meanwhile, the non-Ca^{2+} model had more contacts with but had a further over all distance from Ca^{2+} ions suggesting that these interactions are less long lived, due to this model being more in solvent exposed.

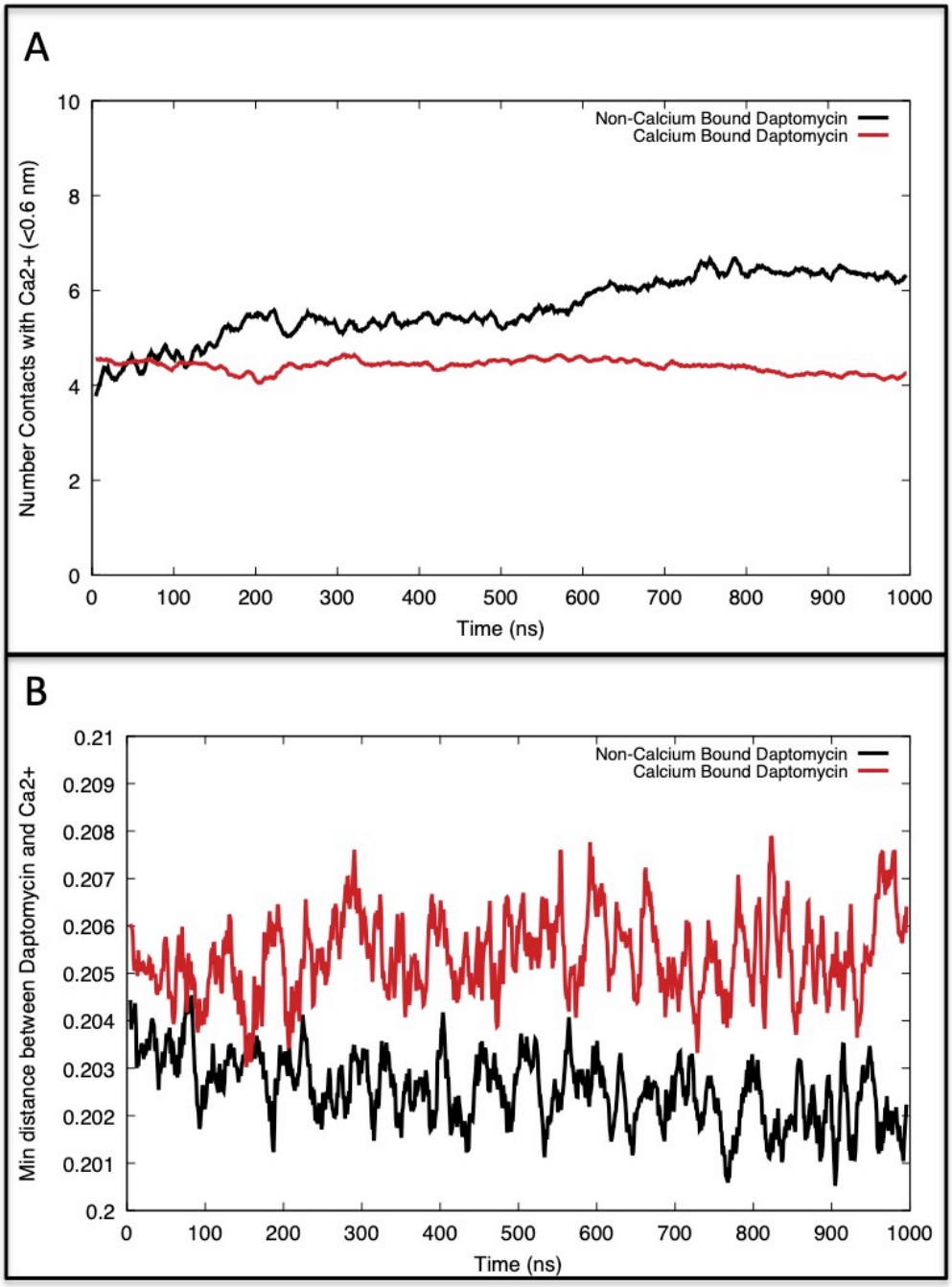

Figure 3.36: Analysis of Ca^{2+} ions with both daptomycin models - A) number of contacts <0.6 nm between daptomycin and Ca^{2+} ions over time and B) average minimum distance between daptomycin and Ca^{2+} ions over time. The Ca^{2+} ions conjugated to the centre of the loop in the Ca^{2+} model have been omitted from this analysis.

3.5.3 Conclusions

This work achieved the aim of showing how a larger number of daptomycin molecules would interact with the realistic *S. aureus* membrane model. Unlike the initial work with 15 daptomycin molecules, this lower concentration better showed insertion and membrane disruption, though it did not show aggregation to the same extent. Whilst this concentration is not as reflective of the realistic concentrations used clinically, therefore not showing micelles or aggregation, this concentration gave better opportunity to observe spontaneous daptomycin-membrane interaction. This number of daptomycin molecules allowed for a different aspect of its mechanism to be studied given the sampling constraints of simulation work and the more complicated interactions involved in large aggregates.

This work further cemented the conclusions from previous analysis suggesting that Ca^{2+} bound daptomycin caused greater disruption to the *S. aureus* membrane than the non-Ca^{2+} model. This highlights the potential importance of a calcium ion being bound to the peptide core of daptomycin and the conformation this induces. This model also came into closer contact with other calcium ions, not including the one bound, suggesting calcium ions are extremely important to the mechanism of daptomycin. Interestingly, this model came into close contact frequently with DPG. This could suggest the calcium ions interacting with this daptomycin model neutralised the negative charge therefore making it more favourable for the daptomycin-calcium ion complex interact with the most negatively charged lipid, DPG.

Finally, this work overall supports that daptomycin inserts into the membrane via the tail region. This is consistent across all of the work in this chapter and was clearly driven by hydrophobic interactions.

In conclusion, this work suggests a conformation for daptomycin bound to a calcium ion that could be the active conformation of the drug and should be considered moving forward with daptomycin research. This work was also was in agreement with much of the experimental work including micelle formation and daptomycin-PG dependence.

Chapter 4 - Chlorhexidine Mode of Action on the *S. aureus* Membrane

4.1 Introduction

Given the broad efficacy, affordability and safety of chlorhexidine, it is vital that this medicine is well understood to ensure it is being used in all appropriate capacities[39]. The mode of action is based on its dicationic nature with cations being released that act upon the bacterial membrane. Chlorhexidine is member of chemically related group of antimicrobials called bisbiguanides, which are group of chemically related compounds with bactericidal capabilities. The structure of chlorhexidine contains two (4-chlorophenyl) guanide units connected by a hexamethylene bridge, Figure 4.1[46,109].

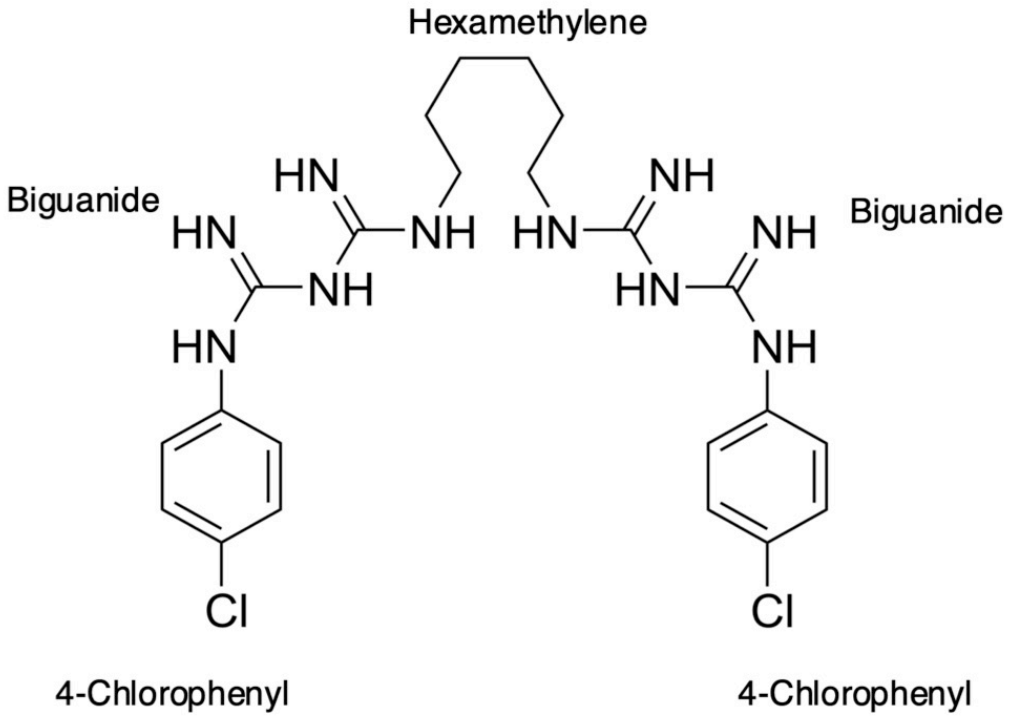

Figure 4.1: Structure of chlorhexidine highlighting biguanides, hexamethylene bridge and 4-chlorophenyls.

The biguanide units within chlorhexidine are responsible for the positive charge and the cations released. Biguanides are a type of guanidine molecule, Figure 4.2 [110]. Guanidine is a strong base, pK_a 13.6, with most guanidine by-products comprising the conjugate acid called the guanidinium cation, ($C(NH_2)^+_3$), this cation is highly stable. Due to the dications of the biguanides region of chlorhexidine, it has a charge of +2 *e* [46,111].

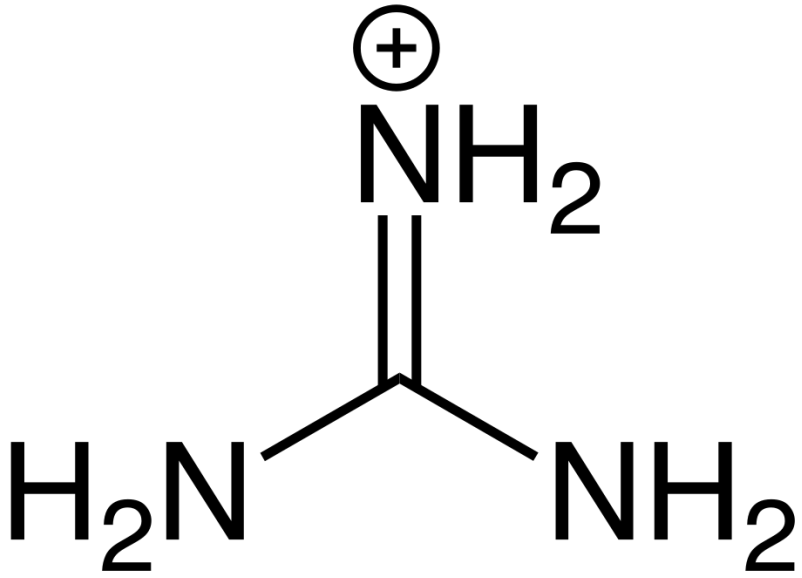

Figure 4.2: Structure of guanidine unit.

These cations of chlorhexidine are why it is so effective against bacterial membranes[112]. Chlorhexidine is extremely attractive for anions. Due to positive charge on either side of the hexamethylene bridge, cations are released when chlorhexidine dissociates at physiological pH[113,114]. Bacterial envelopes are negatively charged, including *S. aureus* despite positively charged Lysl-PG, allowing these cations to attach to the cell membrane[11]. Dependent on the concentration of chlorhexidine, this can either cause bacteriostatic, that is halting bacterial replication and growth, at low concentrations or bactericidal at higher concentrations[115]. Furthermore, chlorhexidine has been shown to cause dented areas on the cellular envelope of both Gram-positive and Gram-negative bacteria by the use of an environmental scanning electron microscope[116]. These dents are believed to cause cell leaking thus stopping cellular proliferation at

low concentrations and so many dented areas at high concentrations that the cells rupture[45,117].

As previously discussed in Chapter 1, chlorhexidine is often used with alcohols and surfactants, however it is frequently administered with gluconate added to the solution, known as chlorhexidine digluconate, with two gluconate molecules to every one chlorhexidine molecule, figure 4.3[118].

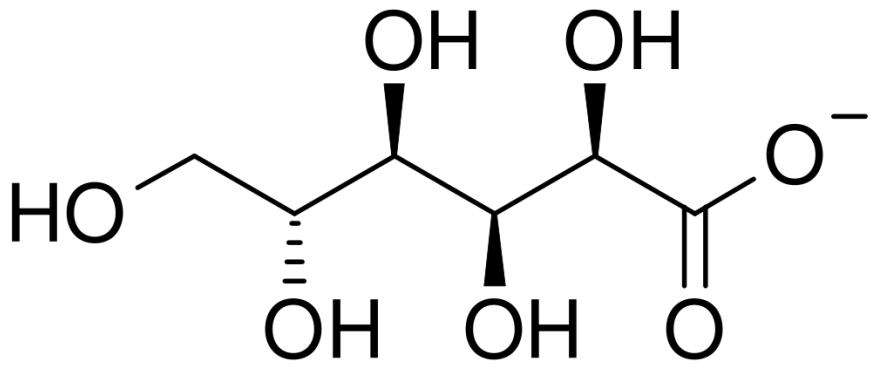

Figure 4.3: Structure of gluconate.

From previous experimental studies, chlorhexidine is known to rely upon membrane disruption to enable cell death[119,120]. This work aimed to use molecular dynamics techniques to zoom in on this membrane disrupting mechanism of chlorhexidine. The aim of this is to enable a better understanding of how these work on a molecular level within the Gram-positive membrane, particularly the ubiquitous yet concerning *S. aureus*[121]. It also aimed to understand the effect of differing salts on the efficacy as well as to determine the importance of gluconate to the mode of action of chlorhexidine.

4.2 Chlorhexidine in Solvent with Varying Ions

This section aimed to understand how chlorhexidine interacts with other chlorhexidine molecules in solvent, in addition to the influence of ions on the behaviours and conformations of chlorhexidine.

4.2.1 Methods and Simulation Set-up

Initially, simulations of chlorhexidine molecules without the *S. aureus* membrane were run with differing solvents in order to understand the behaviour of chlorhexidine alone and the effect of different salts on aggregation, conformation and other effects that could have an influence on its efficacy when introduced to the membrane. The table showing the initial simulations are shown below in Table 4.1.

Contents of Simulation	**Salt & Concentration**	**Simulation Length**
10 chlorhexidine, 3783 H_2O, 20 Cl^-	Cl^- counter ions	3 x 200 ns
10 chlorhexidine, 3742 H_2O, 11 Ca^{2+}, 42 Cl^-	0.15 M $CaCl_2$	3 x 200 ns
10 chlorhexidine, 3758 H_2O, 11 K^+, 31 Cl^-	0.15 M KCl	3 x 200 ns
10 chlorhexidine, 3556 H_2O, 75 Ca^{2+}, 170 Cl^-	1 M $CaCl_2$	3 x 200 ns
10 chlorhexidine, 3628 H_2O, 75 K^+, 95 Cl^-	1 M KCl	3 x 200 ns

Table 4.1: Table of simulations of chlorhexidine with differing salts but without *S. aureus* membrane.

The simulations were performed using the GROMACS 2018 code, the CHARMM36 force field with the TIP3P water model[68,96,97]. Each simulation was run in triplicate for 200 ns. The temperature of 313 K was maintained using the Nosé-Hoover thermostat at a time constant of 1 ps[62]. The pressure was maintained isotropically at 1 atm using the Parrinello-Rahman barostat with a time constant of 1 ps[98]. LINCS constraints were applied to hydrogen containing covalent bonds[60]. A time step of 2 fs was used and long-range electrostatic interactions were calculated using the PME method[65]. For both the electrostatic and van der Waals interactions a cut-off value of 1.2 nm was used[66]. Systems were neutralised as described in table 1. VMD was used for visualising the simulations whilst analysis primarily used GROMACS tools[96,108]. BitClust was used for conformational cluster analysis; with a cut-off of 0.1 nm used to define a cluster[104].

4.2.2 Results

Visual inspection was the first analysis performed. The initial snapshots of the simulations at time = 200 ns are shown in Figure 4.4 with solvent labelled. Based on visual analysis alone, it appears that the greater the number of ions in a solution, the bigger the resulting chlorhexidine aggregates. This is particularly noticeable in the 1 M $CaCl_2$ simulation. Whilst the visualisation is important and can give an initial insight into the outcomes of a simulation, more insightful analysis is required.

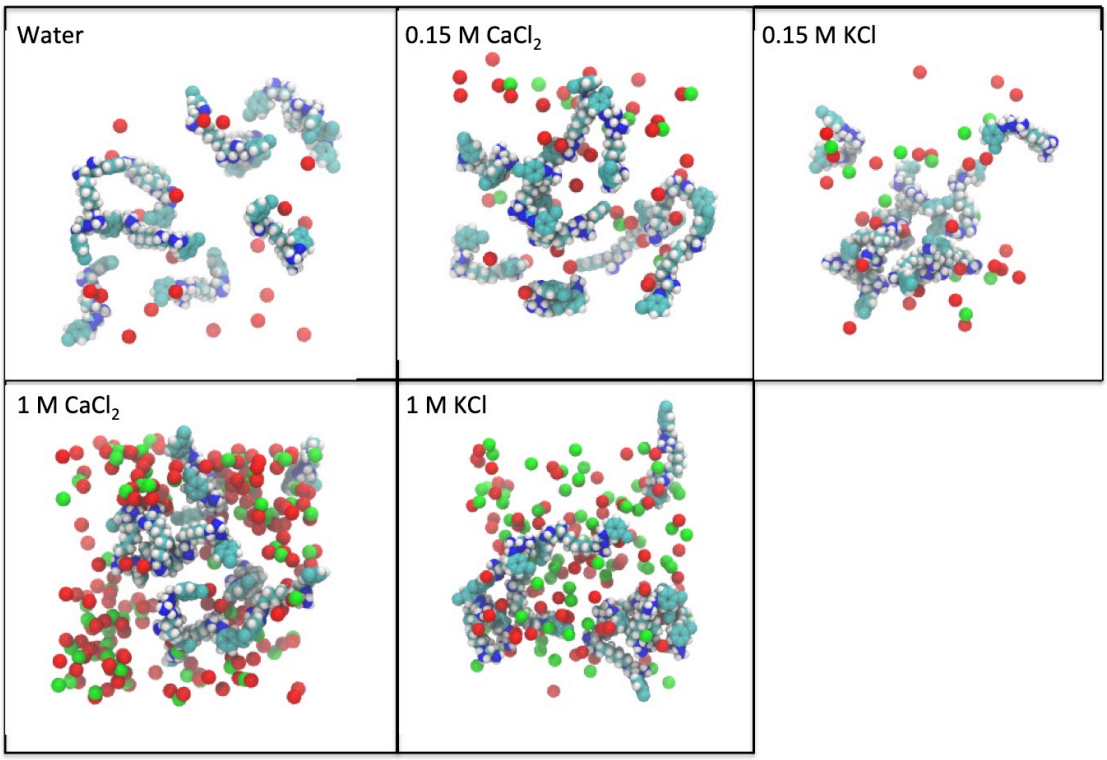

Figure 4.4: Snapshots of chlorhexidine only simulations at time = 200 ns, shown in cyan, blue and white with cations in red and anions in green. The solvents are listed above each snapshot. Water has been omitted for clarity.

Structural clustering is a pervasive method of analysis for MD trajectories that allows for interesting details to be obtained by creating clusters. It has been successfully used to study the active conformation of membrane active antimicrobial peptides[122–124]. This works by grouping frames that are similar into sets that are known as clusters. Frames within the same cluster are more similar to one another than to frames from different clusters. There are several

different methods to measure this but the most common uses calculating the RMSD. This method has been implemented in many different tool packages however for this work BitClust was used to determine structural clusters.

In Figure 4.5, the RMSD of all chlorhexidines in all frames are shown with the five most common (cluster 1 being the most frequent, 2 the next most frequent and so on). In the water simulation, there appears to be fewer occurrences of the most common clusters. This may suggest that in water only, without any cations, chlorhexidine is forming more conformations meaning there is more variety or that the conformations of chlorhexidine are more stable meaning less clusters. Overall, there is a smaller range of clusters when chlorhexidine is in water and 1 M KCl.

Whilst there is not a significant difference between the number of clusters formed when additional salt is present in the solution, or the frequency of the five most common clusters, there is one exception. With regards to the chlorhexidine with 1 M $CaCl_2$ simulation, there appears to be more incidences of the five most common clusters, in particular with the most frequent, cluster 1. Interestingly, cluster 1 in this example does not occur until the second half of the simulation, with the conformations being clustered into more distinct time periods of the simulation in comparison to the others. This is in contrast to the chlorhexidine and 1 M KCl simulation where the most common clusters do not happen with much regularity at the end.

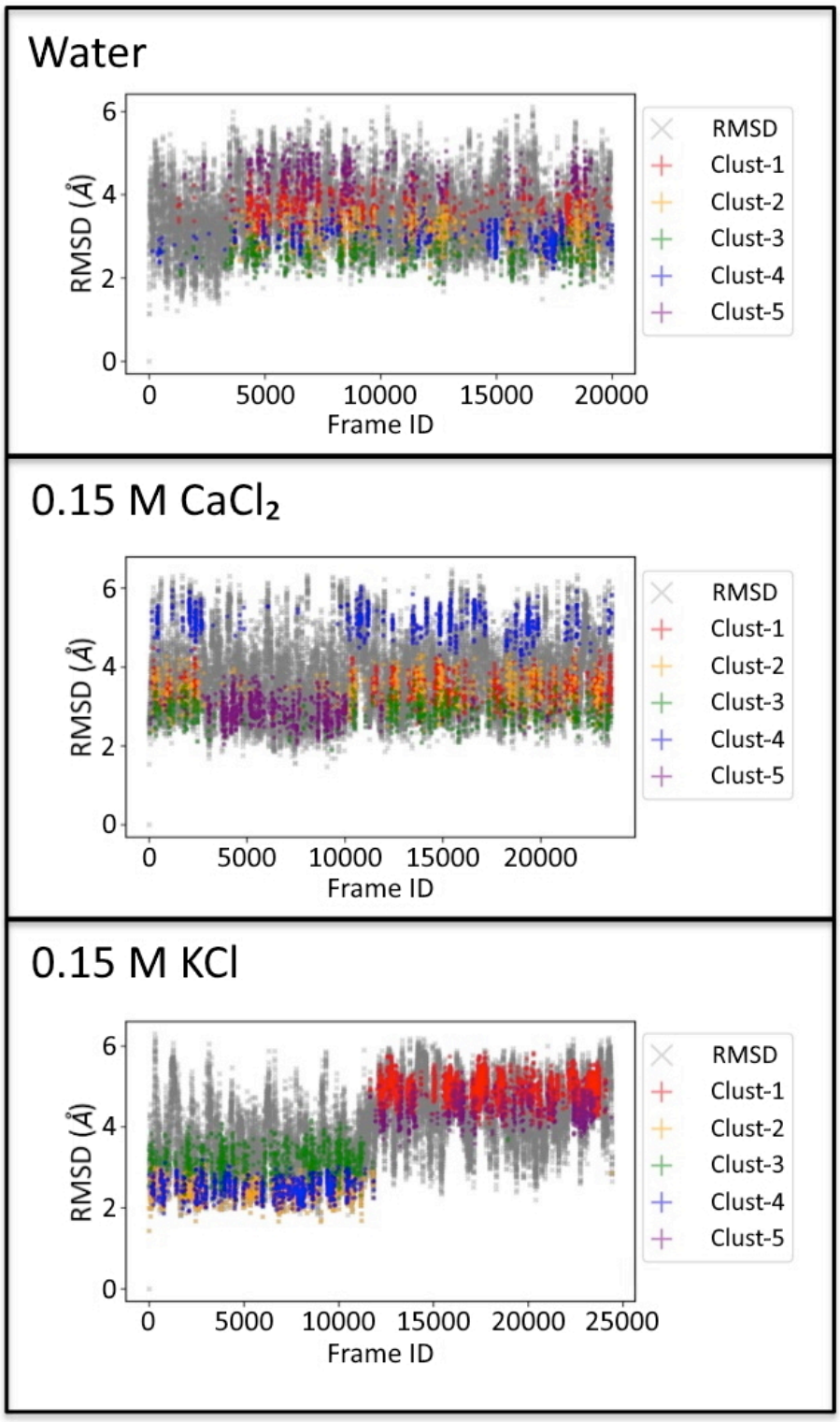
Water
RMSD (Å)
Frame ID
RMSD
Clust-1
Clust-2
Clust-3
Clust-4
Clust-5
0.15 M CaCl₂
RMSD (Å)
Frame ID
RMSD
Clust-1
Clust-2
Clust-3
Clust-4
Clust-5
0.15 M KCl
RMSD (Å)
Frame ID
RMSD
Clust-1
Clust-2
Clust-3
Clust-4
Clust-5

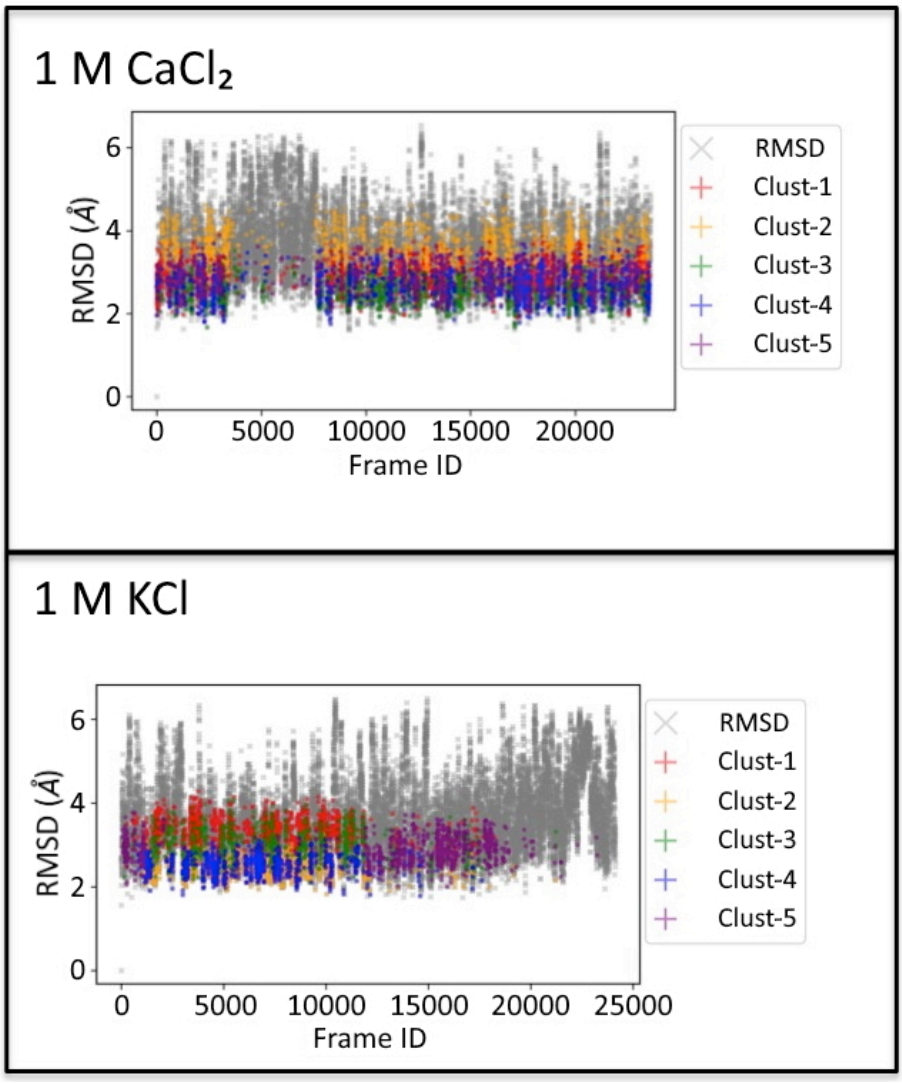

Figure 4.5: Superposition of the first five clusters onto RMSD of all frames to show the frequency of those conformations of chlorhexidine.

Also using the BitClust software, Figure 4.6 shows the cluster size of all the conformations that were clustered, with outliers shown in red i.e. conformations that have not been clustered. Focusing on the size of the most frequent cluster, i.e. how often that conformation occurs, in the chlorhexidine with water and 0.15 M $CaCl_2$ the largest cluster makes up for a little under 4% of the clusters whilst chlorhexidine 0.15 & 1 M KCl it is higher at around 6% & 8% respectively. However, the 1M $CaCl_2$ is much higher than the 0.15M $CaCl_2$ at 12.5%. This aligns to the most frequent cluster, in red in Figure 4.5. Notably, in all simulations there are very few conformations that do not fall into a cluster.

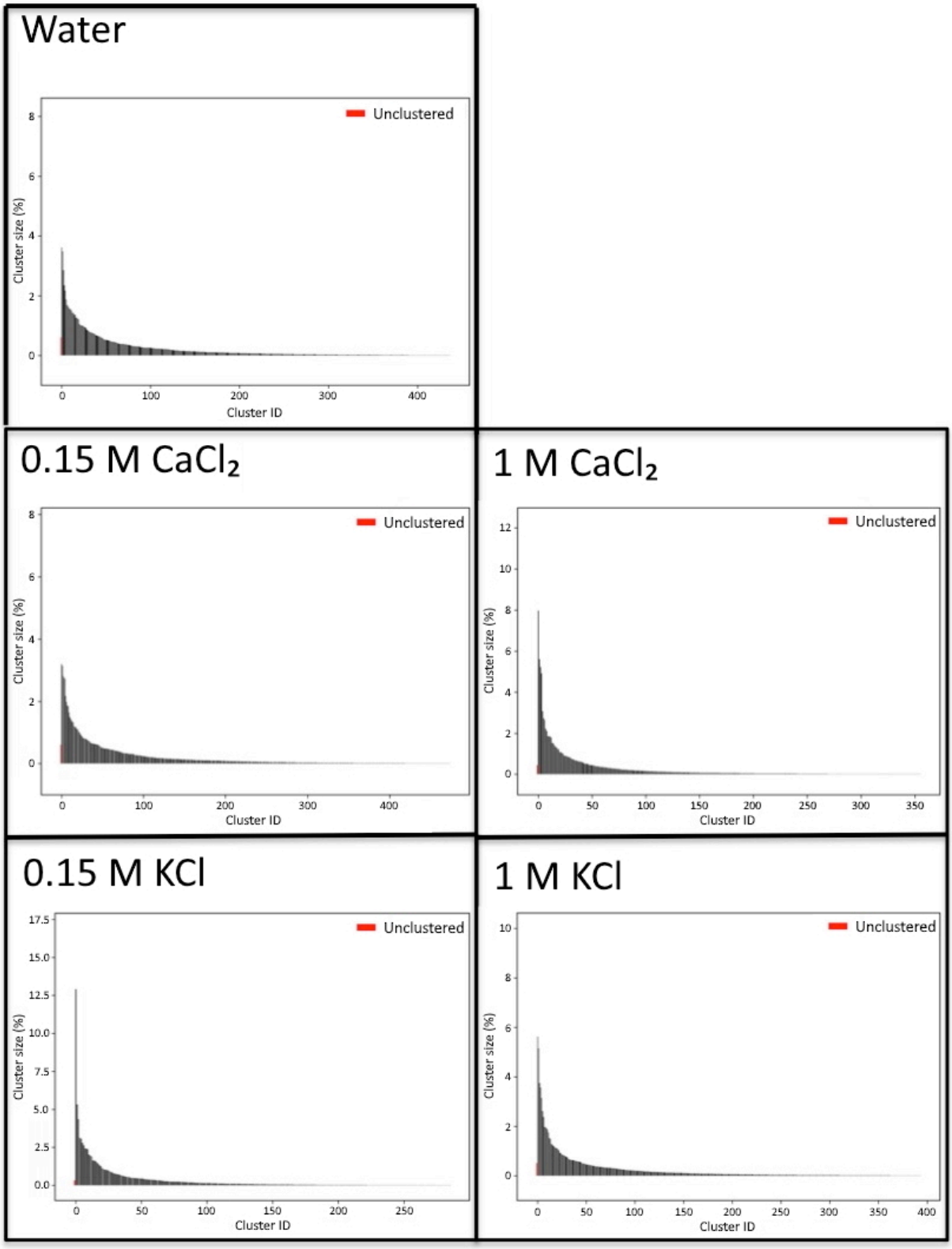

Figure 4.6: Cluster sizes showing all the conformations that fall into a cluster as well as the outliers that did not in red, with solvent shown above.

The 5 most common clusters of chlorhexidine within each simulation are shown in Figure 4.7. Generally, the chlorhexidine was relatively straight in most clusters. The most frequent conformation of each simulation varies, with chlorhexidine in 1 M $CaCl_2$ being the most different to the other most common clusters, not only occurring more than twice as frequently as the other most frequent clusters, but also showing a very bent hexamethylene bridge, with close contact of the chlorophenlys. It appeared that chlorhexidine molecules were more curved/bent in the presence of salts. This may have contributed to the aggregation seen in these systems.

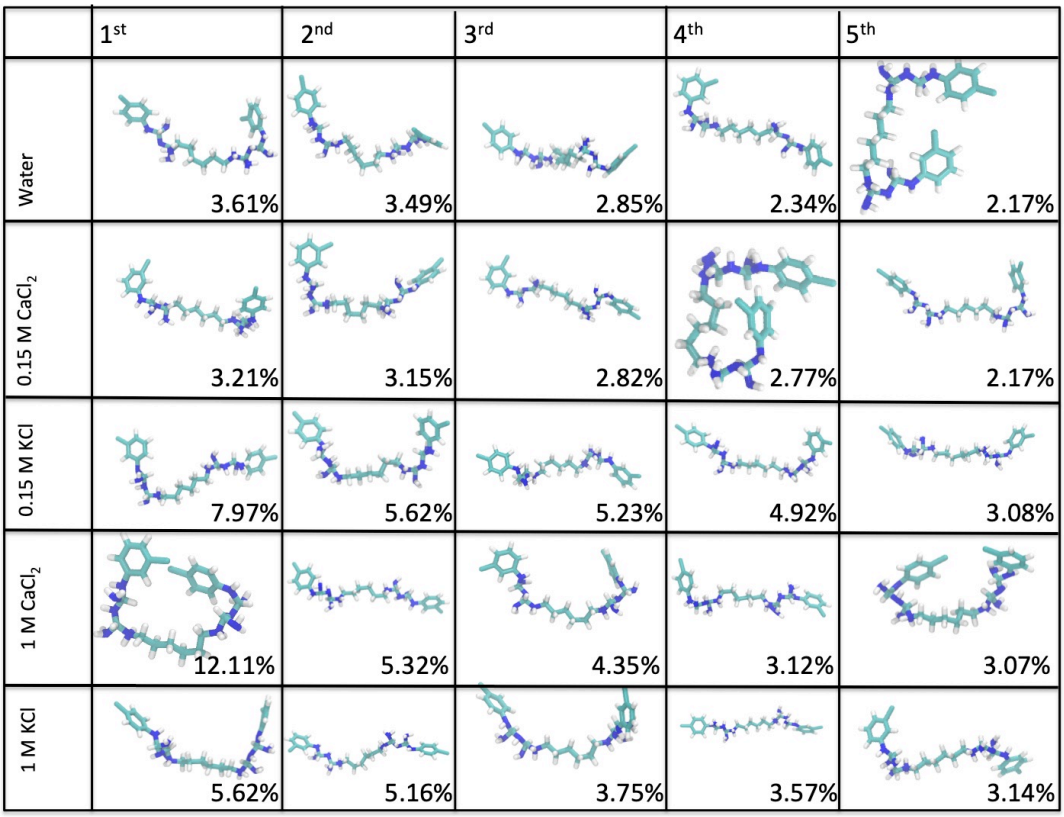

Figure 4.7: The conformations of chlorhexidine (cyan, blue and white) in the 5 most common clusters in each simulation. The percentage each cluster represents is shown in the bottom right corner of each cluster.

Further analysis was conducted to better understand the behaviour of chlorhexidine in different salts. The average R(g) of each chlorhexidine molecule in each simulation was measured, Figure 4.8. There is not a significant difference however both systems with the higher 1 M salts, show an overall smaller R(g) consistently unlike the systems which fluctuate more towards the end of the simulation. The R(g) is overall larger in the chlorhexidine and water simulation, this may support initial visualisation suggestions that could suggest chlorhexidine did aggregate in this system at points, particularly in the early stage of the simulation.

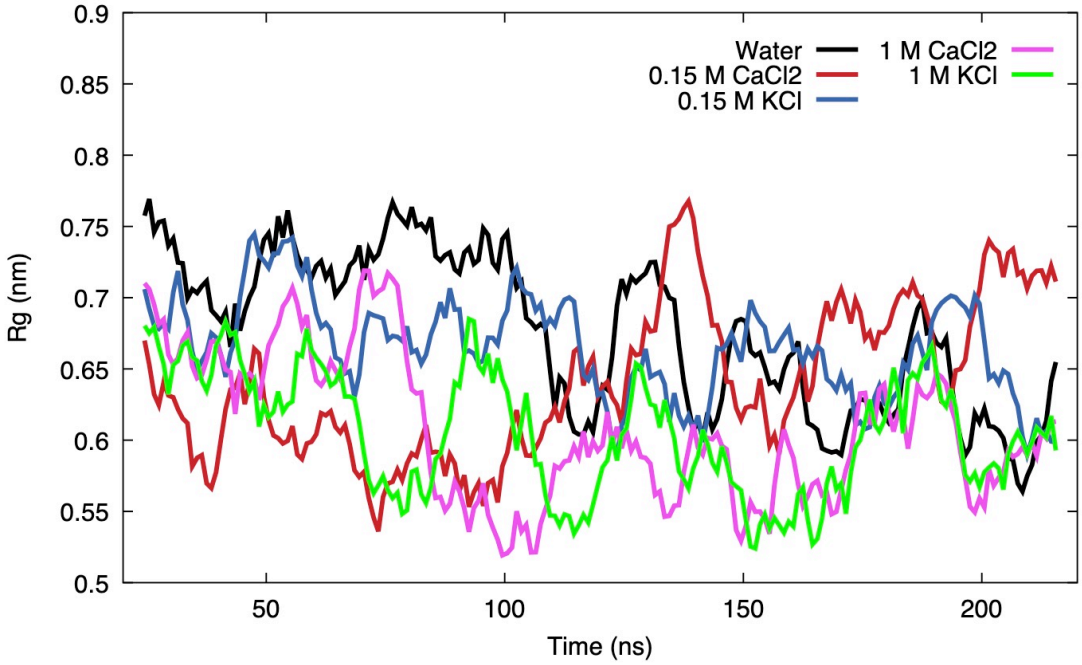

Figure 4.8: Average R(g) of each chlorhexidine in each simulation with the added solvent shown.

Next, the average distance between the ends of each chlorhexidine to the other end of the same chlorhexidine was measured i.e. the distance between the chlorines on each chlorophenyl, Figure 4.9. Throught the simulations, the chlorhexidine and 1 M salt show the ends of chlorhexidine to be coming into closer contact, this supports the conformationfor the most frequent conformation in both simulations, which is more bent thant the other simulations, with 1 M $CaCl_2$ being particularly curved. Notably, all simulations end with Cl-Cl distances similar with the exception of 0.15 M $CaCl_2$.

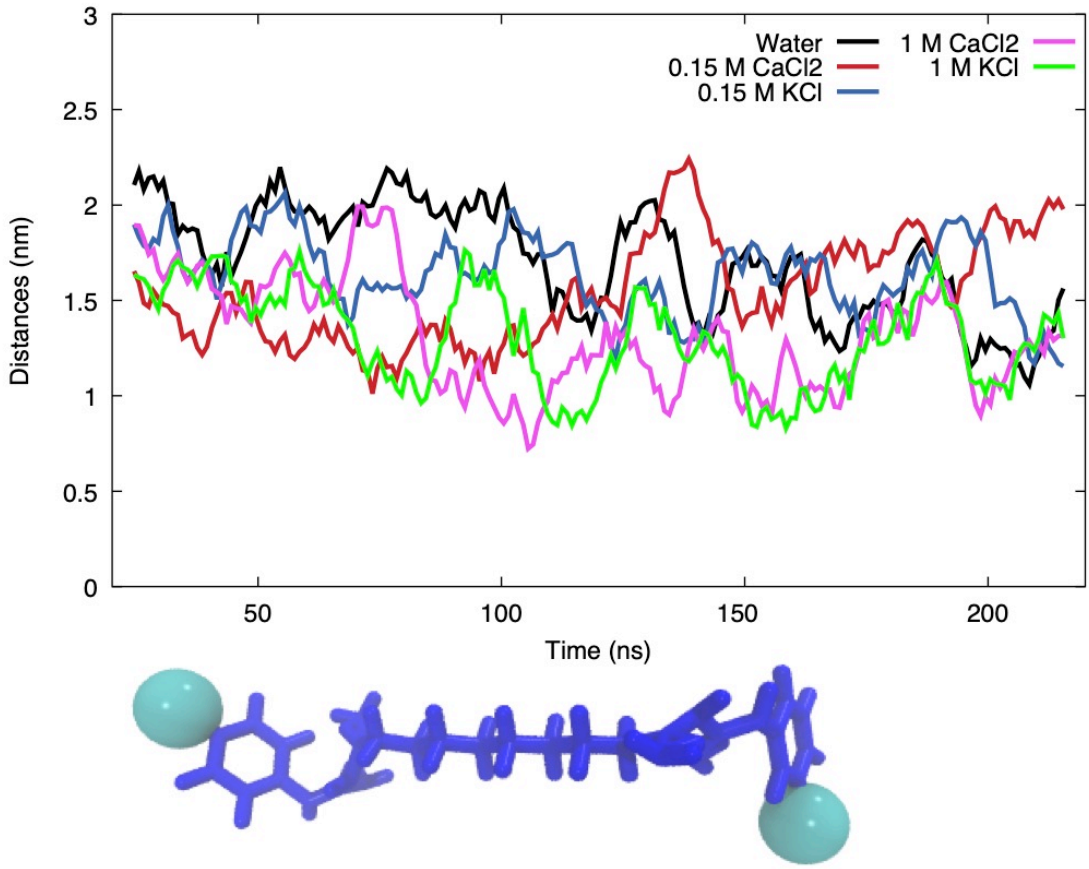

Figure 4.9: Average distance between chlorine atoms (cyan) on either end of each chlorhexidine (blue) in each simulation with the added solvent shown. This aimed to show whether the hexamethylene bridge was bending and if this was dependent on the available ions.

Furthermore, the total SASA for all the chlorhexidine molecules in each simulation was measured, Figure 4.10. Overall the simulations with 1M salts had a smaller surface accessible area, this is most likely due to firstly aggregation of the chlorhexidine molecules in these systems but also interactions between chlorhexidine and the more abundant Cl^- ions in these setups; which would reduce the SASA of chlorhexidine in these systems. Otherwise there is little difference between the chlorhexidine with water and 0.15 M salt simulations, suggesting these do not aggregate as much as the 1 M salt simulations. This again may be due to the 1 M salt cations causing chlorhexidine to aggregate, which is supported by the lowest SASA being shown by 1 M $CaCl_2$.

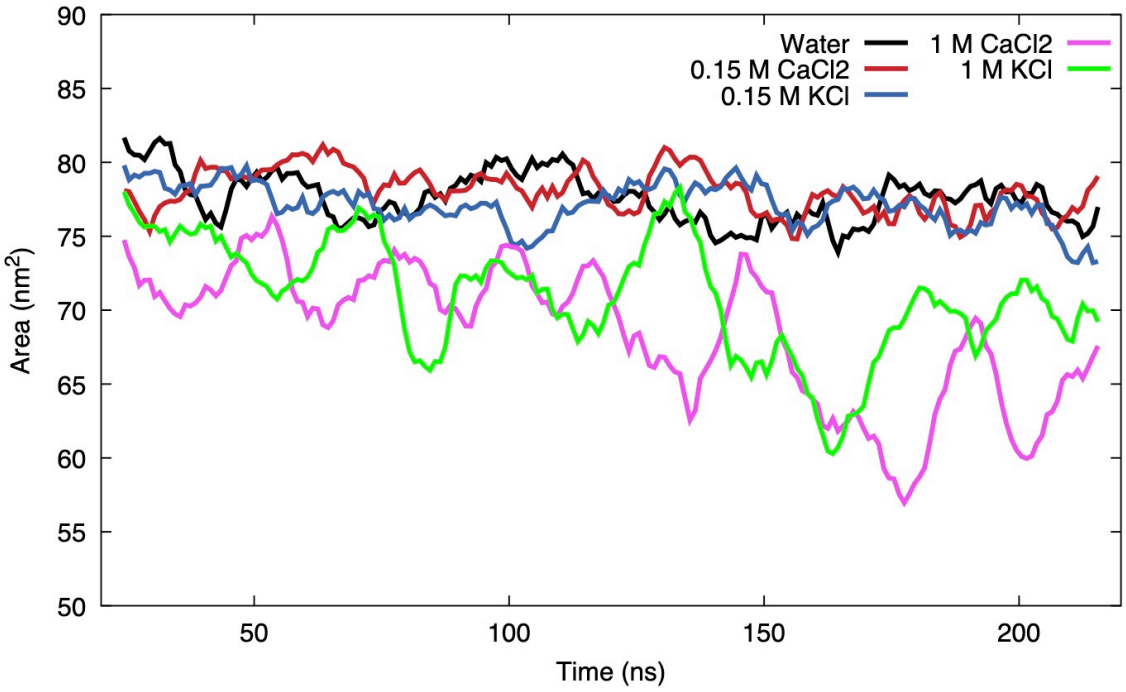

Figure 4.10: Average SASA of all chlorhexidine with added solvent shown.

To gain a better understanding of the interactions of chlorhexidine and the ions in each simulation, the number of contacts between each chlorhexidine and A) anions and B) cations were calculated, Figure 4,11. Note, that due to the different number of ions in each simulation this was normalised to per ion. Firstly looking at the number of contacts between chlorhexidine and Cl^- ions, chlorhexidine interacts more so with the anions in the chlorhexidine and 0.15 M salt simulations particularly in comparison to the chlorhexidine and 1 M salt simulations. This may support that in the higher concentration salt simulations there is greater aggregation, thereby reducing the number of contacts with other ions. Comparatively, looking at B, there are far less interactions between chlorhexidine and cations than with anions. This is to be expected due to the positive charge of chlorhexidine. However, there are still more contacts with cations in the 0.15 M salt simulations than the 1 M salt simulations, further supporting that there is greater aggregation when there is a higher salt concentration present in the system.

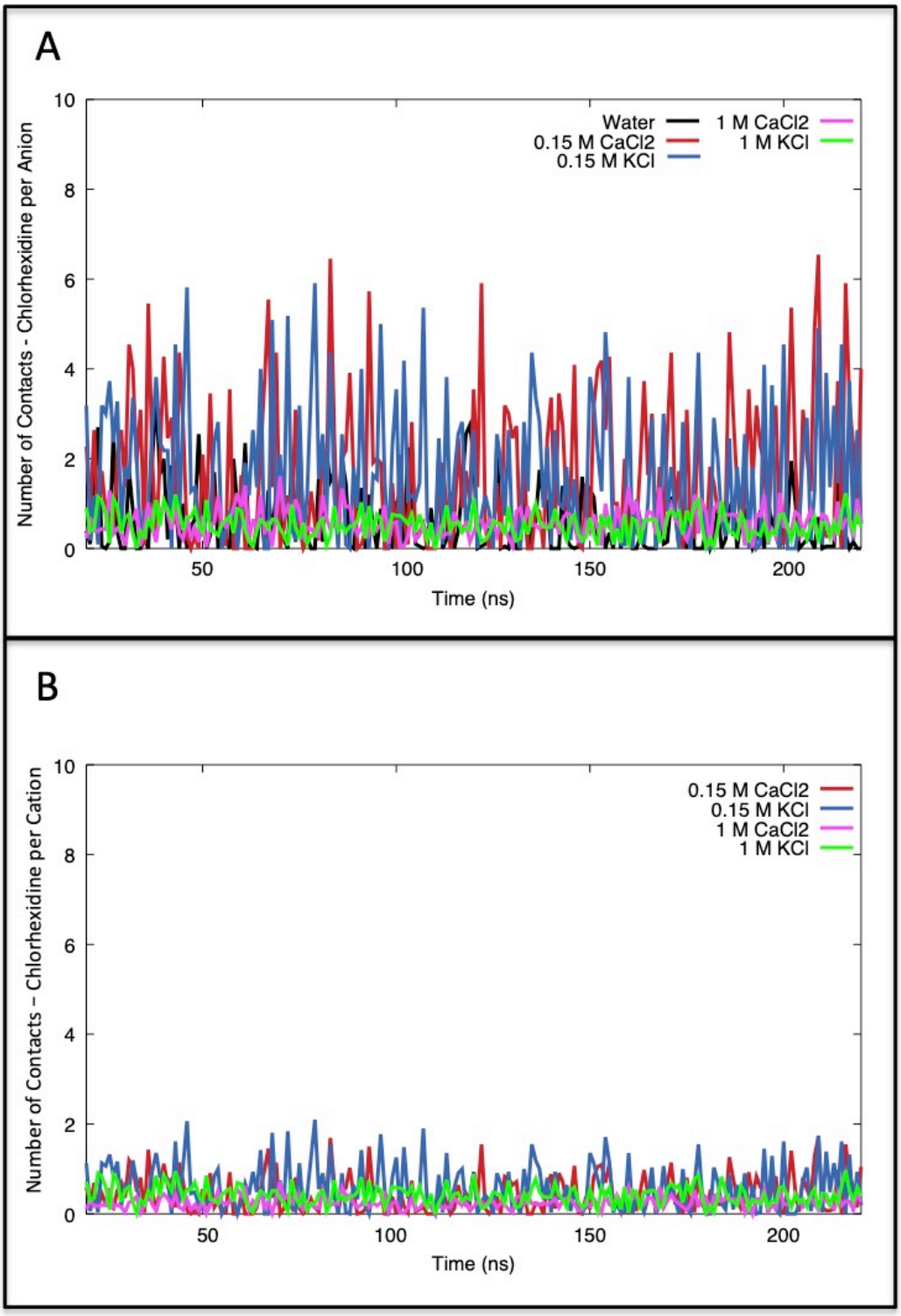

Figure 4.11: Average number of contacts between chlorhexidine and A) anions and B) cations, with the solvent shown. This data was normalised to each chlorhexidine with an average ion due to the different availability of ions in each simulation.

To better understand if chlorhexidine is aggregating in certain conditions, a radial distribution function (RDF) was used to calculate the probable distance between chlorhexidine molecules in each setup, Figure 4.12. This was calculated for each 50 ns block and the average determined. As was anticipated, in the chlorhexidine 1 M $CaCl_2$ and KCl simulations, the chlorhexidine molecules were more likely to come into contact, with the probable distance likely to be less than 0.5 nm in each high concentration simulation. Whereas the other simulations, which are all very similar have and approximate peak, although not as clear as with the other simulations at over 1 nm. This supports all the previous evidence that the higher salts are causing chlorhexidine to aggregate.

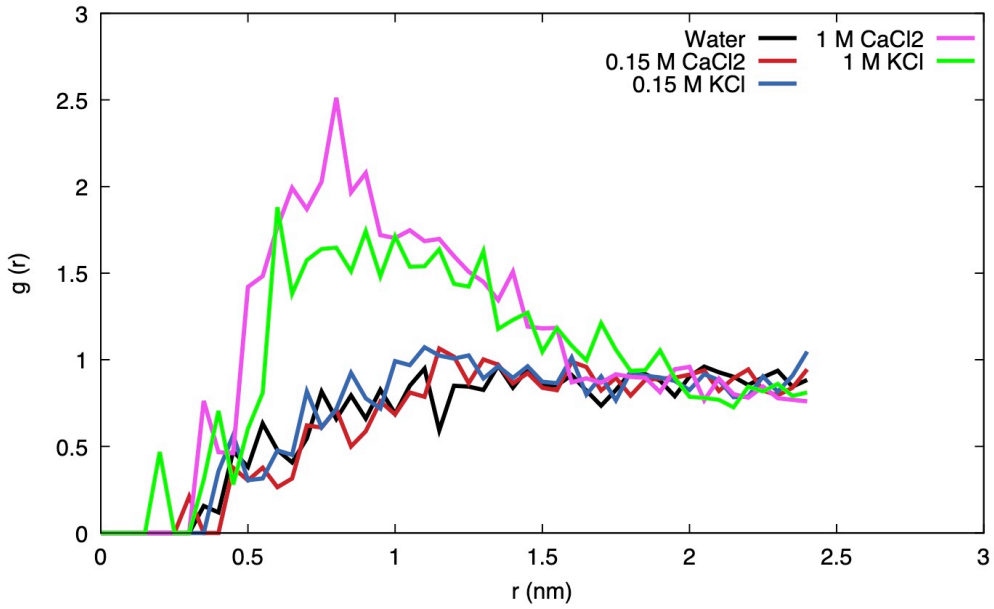

Figure 4.12: The RDF was calculated to show the probable distances between chlorhexidine molecules in each simulation, with the added solvents shown.

Finally, the root mean square fluctuation (RMSF) was calculated for each atom to determine the deviation of each chlorhexidine atom in regard to a reference position over time, Figure 4.13. This was measured for each chlorhexidine molecule and averaged. Overall, there was very little difference for the RMSF between setups meaning despite the difference in how the chlorhexidine molecules are interacting with other chlorhexidine molecules, the behaviour of each atom is relatively similar. The consistent RMSF of chlorhexidine in the different systems may suggest the conformational forms taken by chlorhexidine

is independent of the solvent present and this form may be important to its ability to aggregate. However, over the whole molecule, the RMSF for each atom is generally higher in the chlorhexidine and water simulation. This is in line with the suggestion that chlorhexidine aggregates less in water from the initial visuals and SASA.

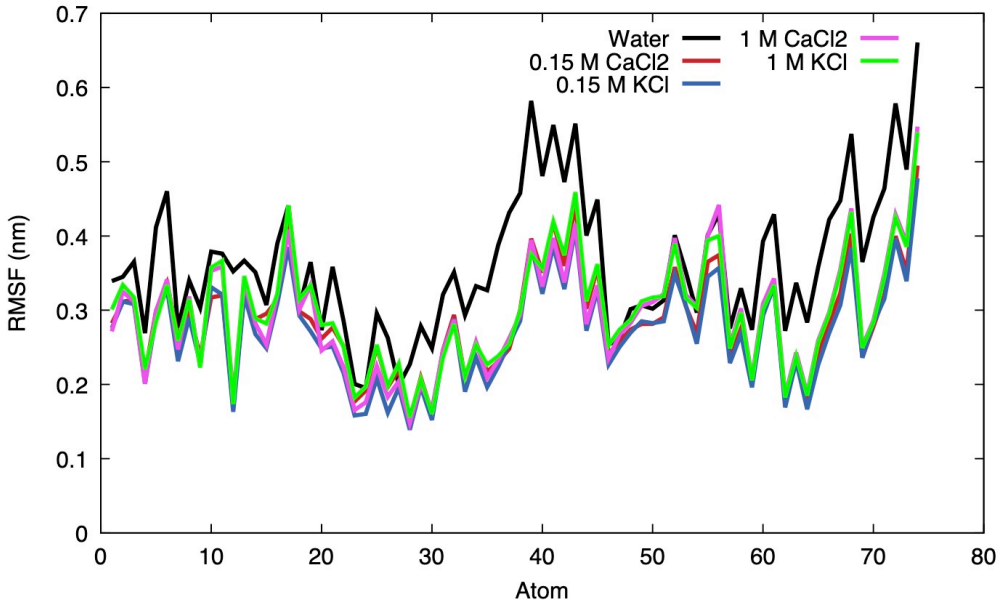

Figure 4.13: The RMSF of each atom was calculated to show the mean fluctuations each atom in chorhexidine with respect to the starting structure over time, with the added solvents shown. This too aimed to show the effect of ion availability on the conformation of chlorhexidine.

Conclusions

Overall, this section of the study suggested that chlorhexidine was more prone to aggregation in the presence of higher salt concentrations. It may be thought that this is due to interactions with the greater availability of counter ions in the system. From the cluster analysis and the average distances between the ends of the chlorhexidine, it appeared that chlorhexidine molecules in higher salt concentrations were more bent. This conformation is known to be the most favourable conformation of chlorhexidine with membranes therefore simulating chlorhexidine with a higher concentration of salts allows for it to adopt a more favourable conformation to interact with the membrane which could be of relevance to *in vivo* conditions[125].

4.3 Chlorhexidine Simulated with *S. aureus* Membrane and Varying Counter Ions & Components

This section aimed to understand the interaction between chlorhexidine with the *S. aureus* membrane in the presence of varying salts and gluconate.

4.3.1 Methods and Simulation Set-up

Upon completion of simulations with chlorhexidine without any membrane, simulations were then run with the *S. aureus* membrane. The membrane comprised of 54% PG, 36% Lysl-PG and 10% DPG in line with experimental estimations[99,100]. In addition to the membrane, in one simulation gluconate was added with two gluconate to every one chlorhexidine molecule. This was to mimic how chlorhexidine is often used in a chlorhexidine digluconate form. The protocol for the simulations was largely the same with the notable exception of the pressure being maintained semiisotropically. The simulations are listed in Table 4.2. Most analysis used GROMACS tools. The area per lipid was measured using FATSLiM whilst the membrane thickness used Monticelli's GROMACS4 *g_thickness* script[96,104–107]. BitClust was used for conformational cluster analysis; a cut-off of 0.1 nm was used to define a cluster[104].

Contents of Simulation	**Salt & Concentration**	**Simulation Length**
10 chlorhexidine, *S. aureus,* 18915 H_2O, 28 Ca^{2+}	Ca^{2+} counter ions	3 x 200 ns
10 chlorhexidine, *S. aureus,* 18672 H_2O, 109 Ca^{2+}, 162 Cl^-	0.15 M $CaCl_2$	3 x 200 ns
10 chlorhexidine, *S. aureus,* 18725 H_2O, 137 K^+, 81 Cl^-	0.15 M KCl	3 x 200 ns
10 chlorhexidine, *S. aureus,* 10 gluconate, 18855 H_2O, 38 Ca^{2+}	Cl^- counter ions	3 x 200 ns

Table 4.2: Table of simulations of chlorhexidine with differing salts with *S. aureus* membrane.

4.3.2 Results

The snapshots from the end point, 200 ns, of the simulations with both chlorhexidine and the *S. aureus* membrane shown below, Figure 4.14. Whilst

acknowledging the limitations of visualisation, in that it is not quantitative analysis, it is noteworthy that all chlorhexidine molecules inserted into at least the head region of the membrane with the exception of the simulation with 0.15 M $CaCl_2$. In this simulation, there are 3 chlorhexidine molecules that have not come into contact with the membrane. Furthermore, in the simulation with water and gluconate, the latter has not entered the membrane any more than the chlorhexidine however some have penetrated to the same level as the chlorhexidine molecules. From a visual perspective, it would appear that the membrane is less organised in the water and gluconate simulation. Finally, it appears that chlorhexidine molecules have more fully entered the membrane, in a flatter conformation, in the presence of 0.15 M KCl.

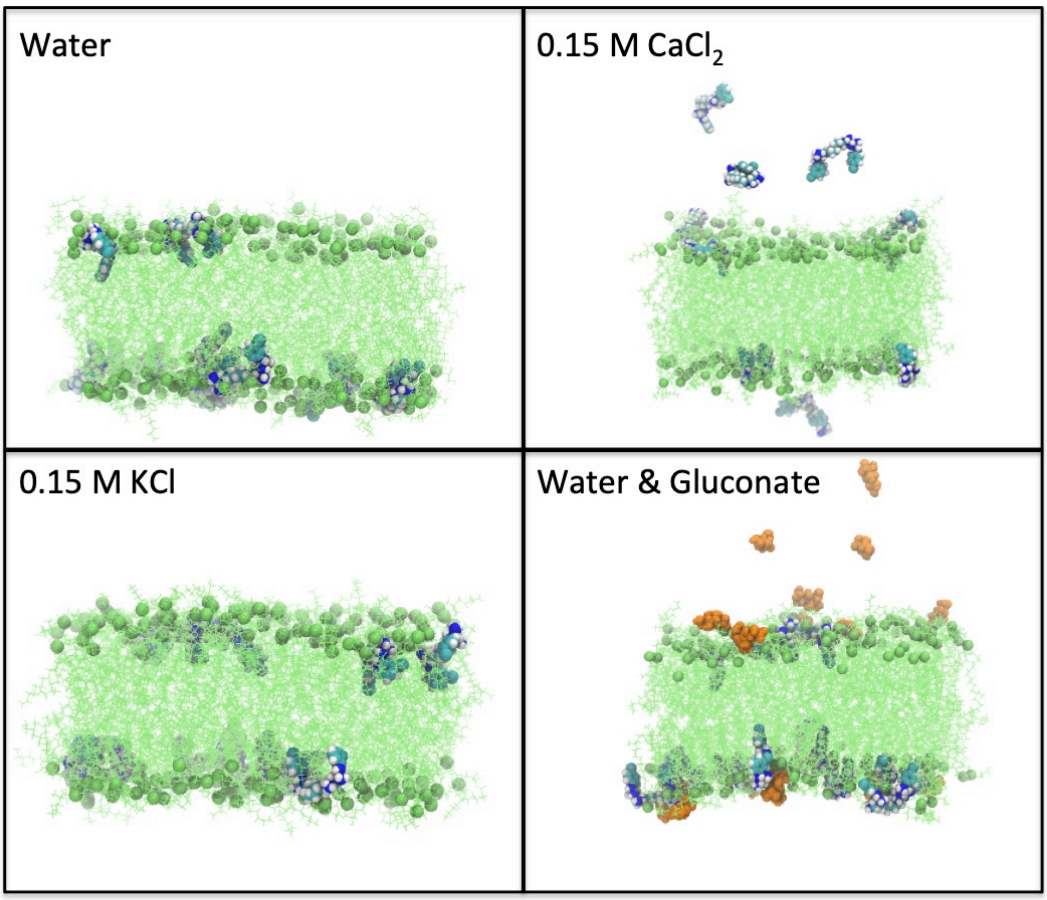

Figure 4.14: Snapshots of chlorhexidine (cyan, blue and white) with *S. aureus* membrane (green) simulations time = 200 ns. The solvents are listed above each snapshot and gluconate shown in orange. Water and ions have been omitted for clarity.

The density plots for these simulations are shown below in Figure 4.15. The densities were measured over the last 20 ns of each simulation. From these it would appear that in all simulations chlorhexidine has entered the head region of the membrane. However, in line with the conclusions drawn from the initial visualisations, chlorhexidine has entered further into the membrane in the 0.15 M KCl, sitting in towards the tail regions. In this example, water appears to be further into the head group region than in any of the simulations. This may mean the chlorhexidine entering is allowing some water into this area of the membrane. Furthermore, it should be noted that gluconate does not sit so far in the membrane as the chlorhexidine in that simulation. However, chlorhexidine in all cases is not able to fully enter the membrane, which may have been expected. Despite the chlorhexidine entering to a greater or lesser extent in all simulations, water has not come in to the core of the membrane and the lipid density is approximately the same. This would suggest that despite chlorhexidine entering the membrane to a degree, it causes minimal disruption to the membrane.

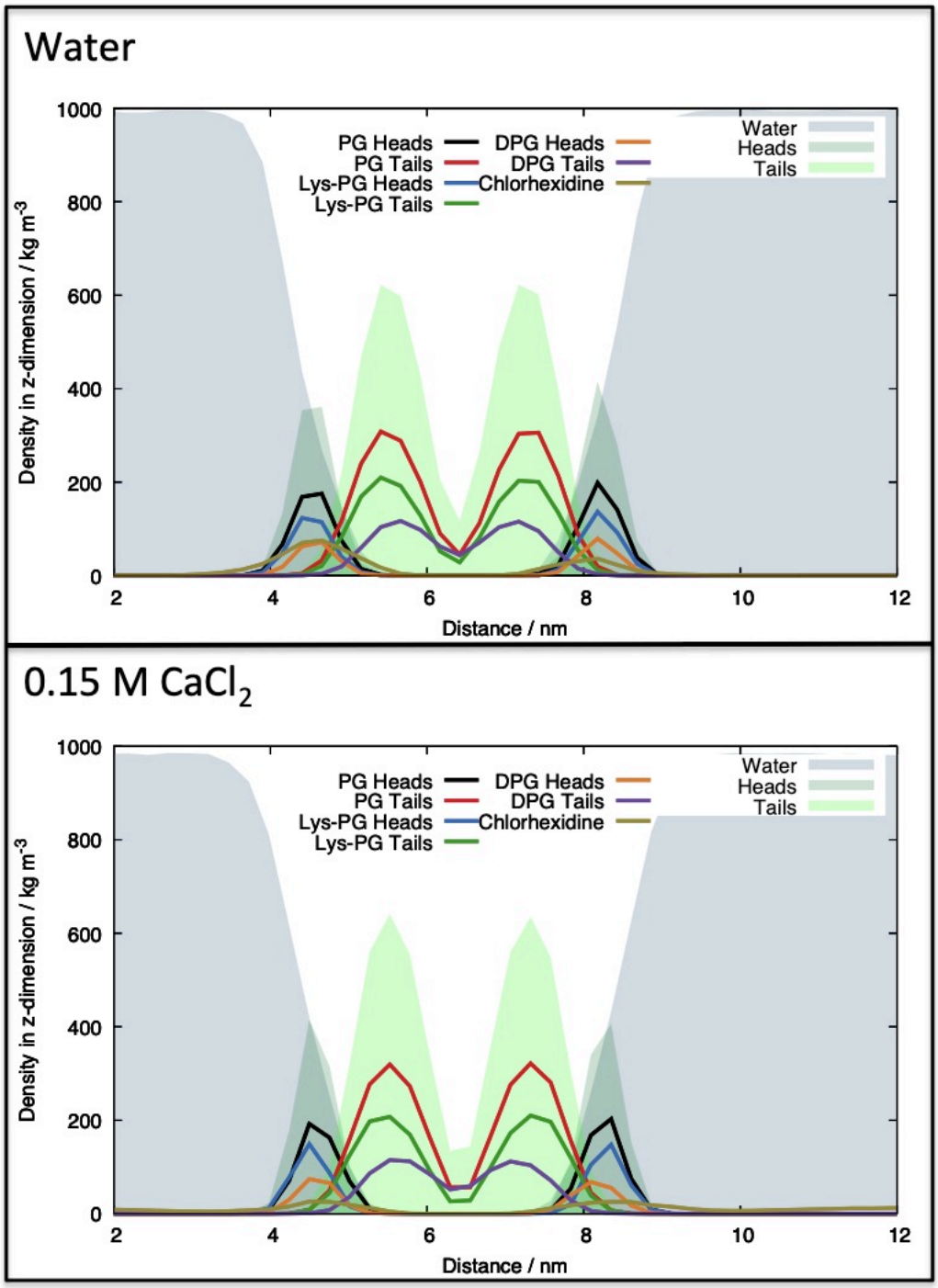
Water
PG Heads
PG Tails
Lys-PG Heads
Lys-PG Tails
DPG Heads
DPG Tails
Chlorhexidine
Water
Heads
Tails
Density in z-dimension / kg m-3
Distance / nm
0.15 M CaCl2
PG Heads
PG Tails
Lys-PG Heads
Lys-PG Tails
DPG Heads
DPG Tails
Chlorhexidine
Water
Heads
Tails
Density in z-dimension / kg m-3
Distance / nm

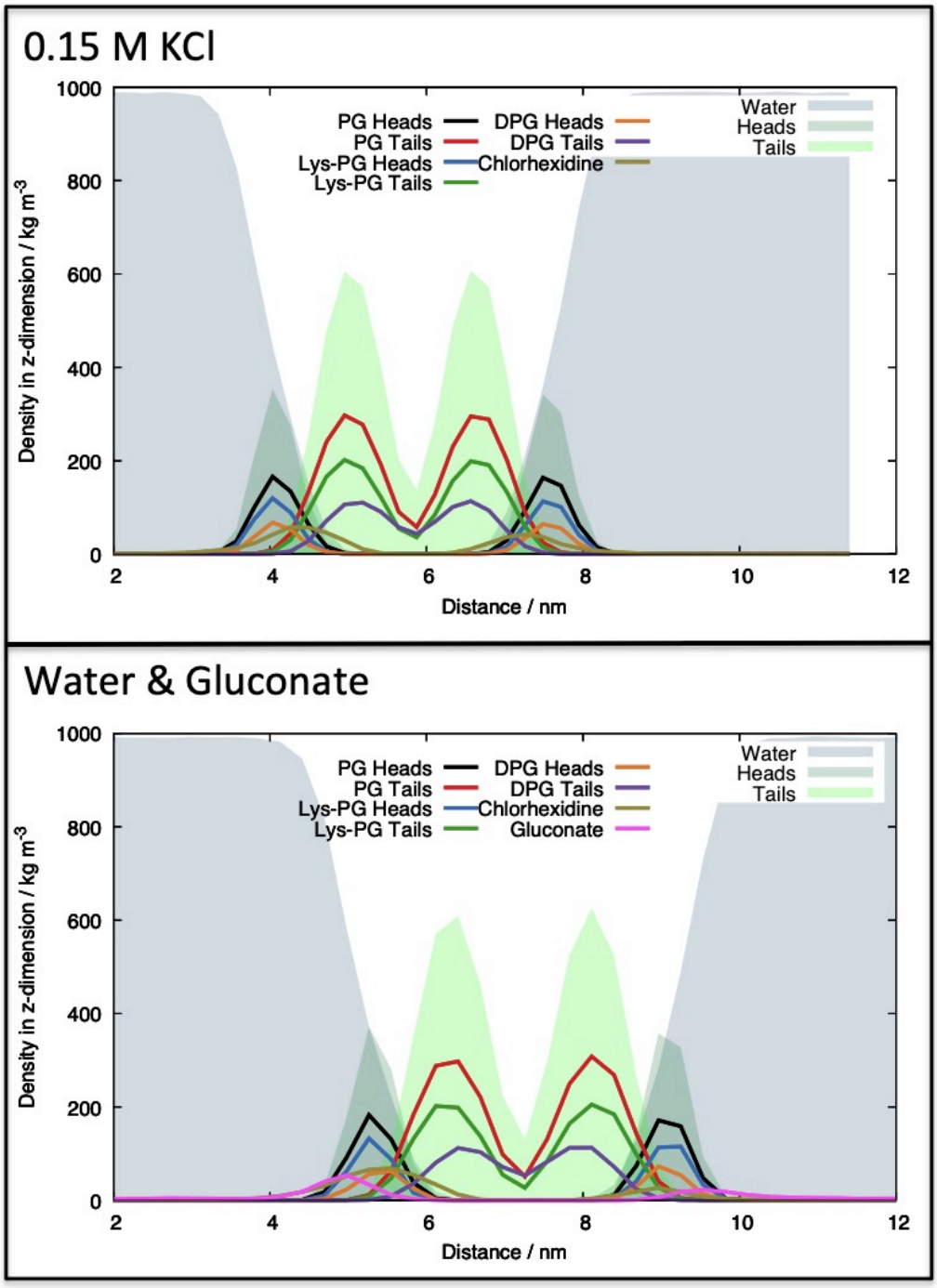

Figure 4.15: Densities of chlorhexidine, lipid head-groups and tails, solvent and gluconate where relevant. Calculated for the last 20 ns of the simulation.

As with the simulations without a membrane, cluster analysis was carried out on the membrane simulations also, Figure 4.16. There is a notable difference compared to the chlorhexidine only simulations in that the most common conformations happen far less frequently, this is most probably due to the

limitations of the ability for chlorhexidine to move so freely due to it being in contact with the membrane. However, even within these simulations, the chlorhexidine and 0.15 M $CaCl_2$ simulations had very few clusters compared to the other simulations in this case. This is surprising as not all of the chlorhexidine molecules in this system entered the membrane. Whilst the simulations where chlorhexidine had more interaction with the membrane. 0.15 M KCl and with gluconate, the clusters were larger and more frequent.

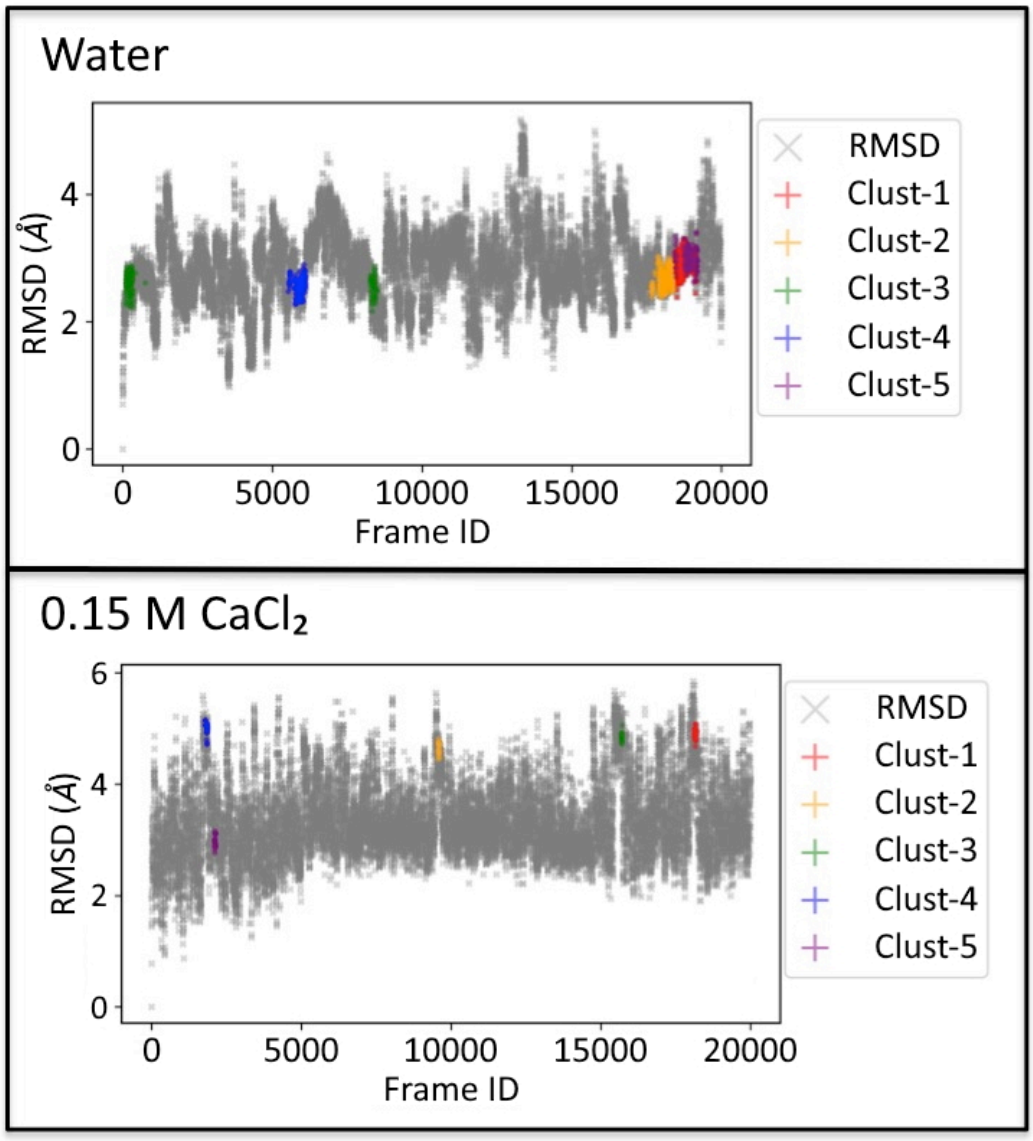

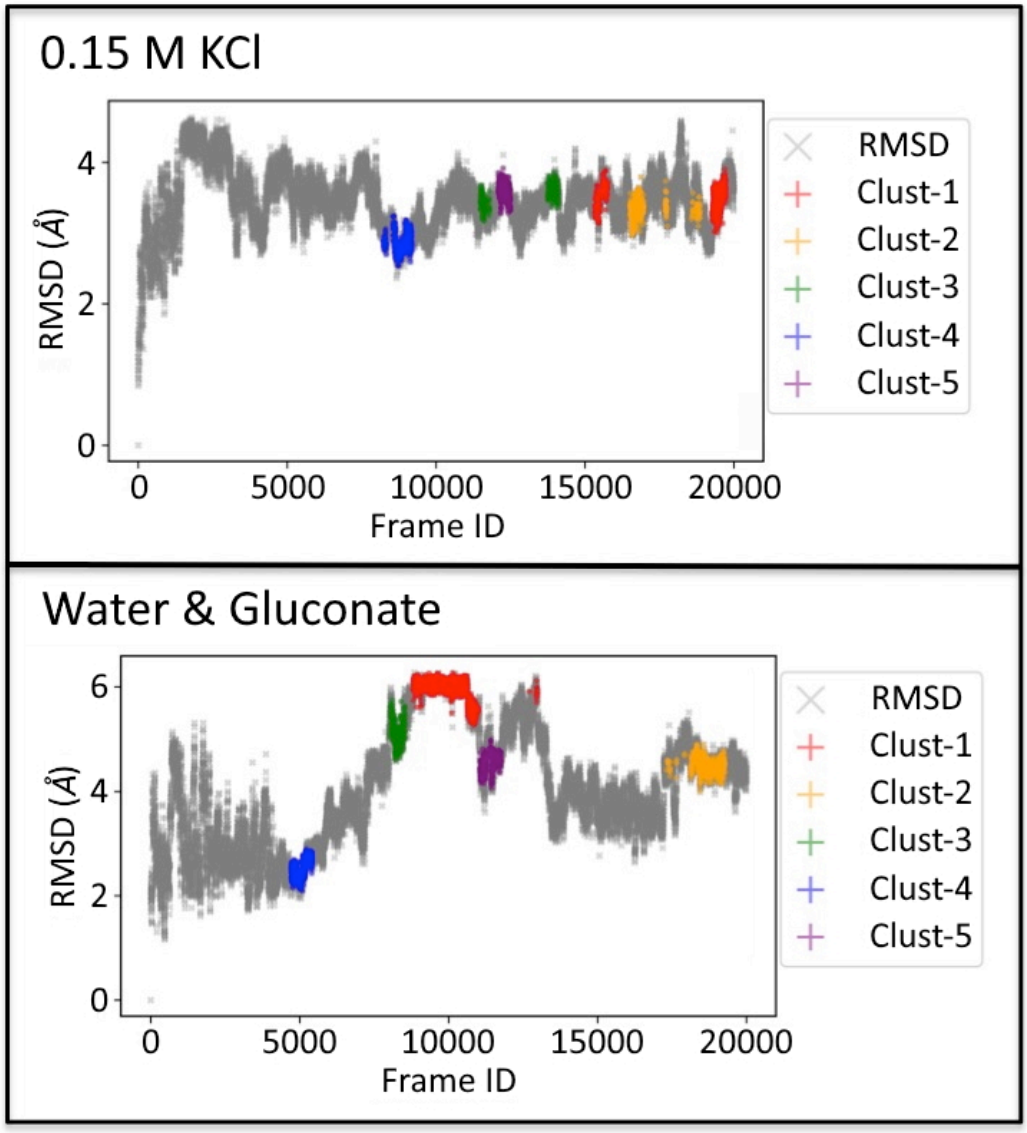

Figure 4.16: Superposition of the first five clusters onto RMSD of all frames to show the frequency of those conformations of chlorhexidine with the membrane, with the solvent shown above.

Again, looking at the cluster sizes, Figure 4.17, as suggested by the previous data there are far less clustered conformations in these simulations. This may mean that chlorhexidine is forming more conformations in this scenario meaning they cannot be clustered into similar groups. The most unclustered frames occur in the 0.15 M $CaCl_2$ simulation whilst the least is in the 0.15 M KCl has the least.

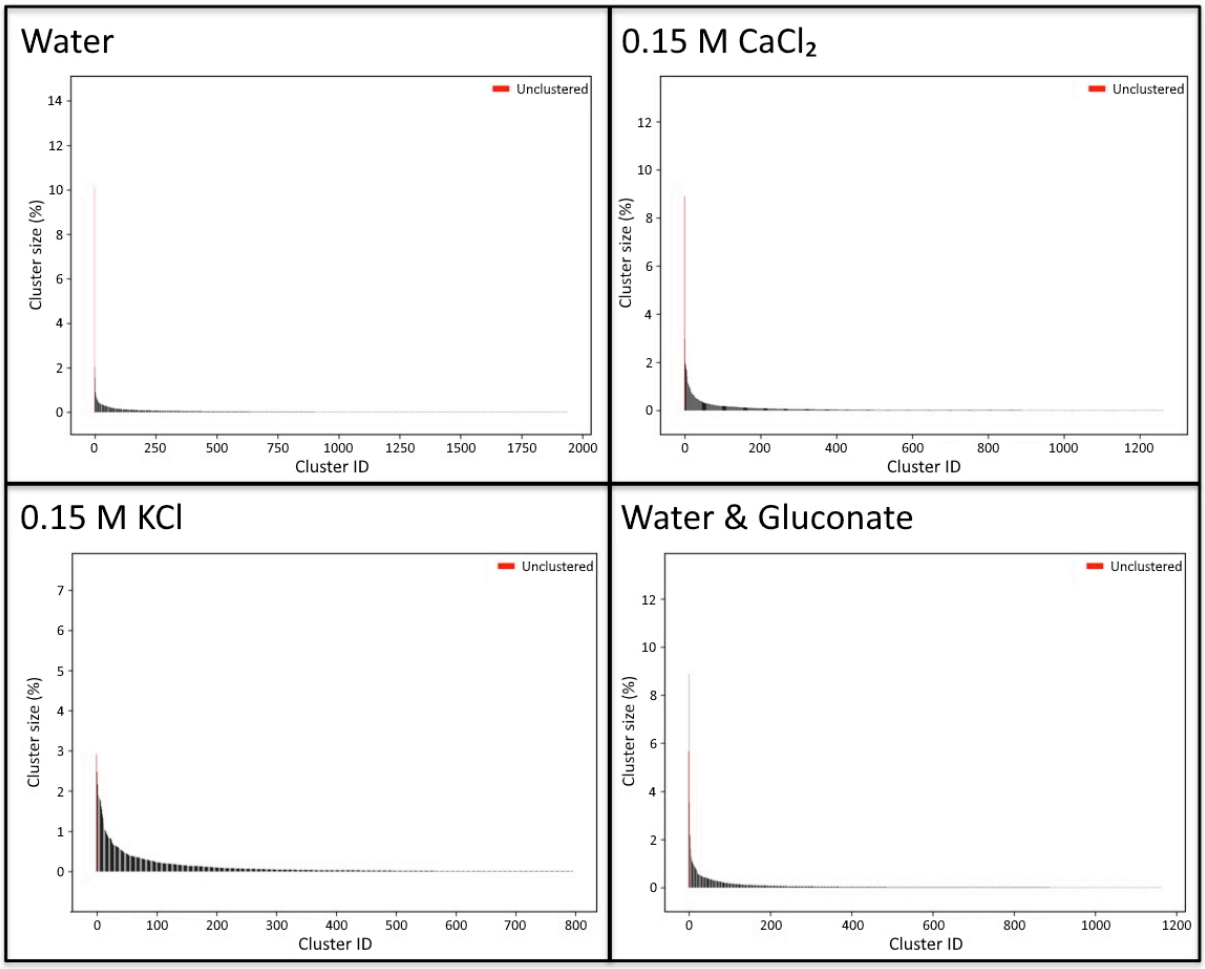

Figure 4.17: Cluster sizes showing all the conformations that fall into a cluster as well as the outliers that did not in red, with solvent shown above.

The five most common conformations of each cluster are shown in Figure 4.18. In all of the systems, the most common cluster showed chlorhexidine bent at the bridge region of the molecule. This suggests that this is either optimal for chlorhexidine entering the membrane or the appropriate conformation for chlorhexidine within the membrane. The latter is likely true due to other studies suggesting this is the conformation of chlorhexidine within the membrane driven by hydrophobic interactions[125].

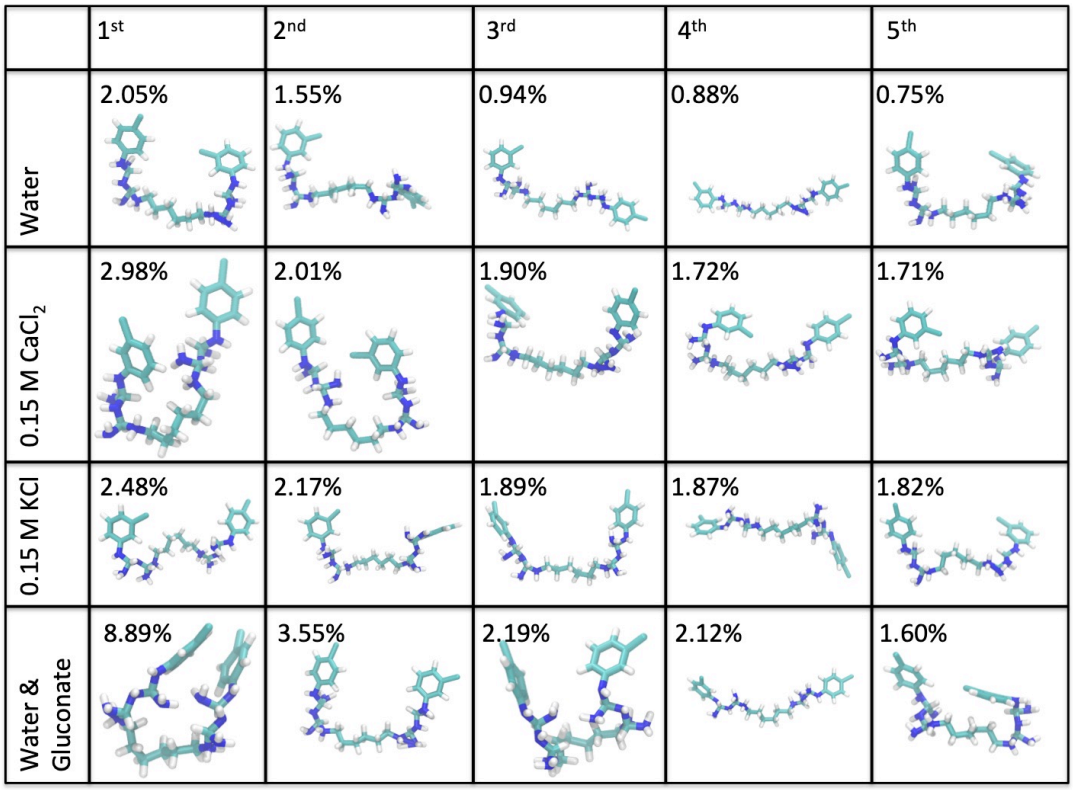

Figure 4.18: The conformations of chlorhexidine (cyan, blue and white) in the 5 most common clusters in each simulation. The percentage each cluster represents is shown in the top left corner of each cluster.

In addition to the density profiles of the systems, measuring the membrane thickness in each simulation is a useful tool. The membrane thicknesses of the systems are shown in Figure 4.19. Whilst there is not much discernable difference in membrane thickness between the chlorhexidine with water, 0.15 M $CaCl_2$, and with gluconate the system with 0.15 M KCl is bluer, therefore thinner, than the other simulations. This supports other analysis which suggests in this setup chlorhexidine is more able to enter the membrane.

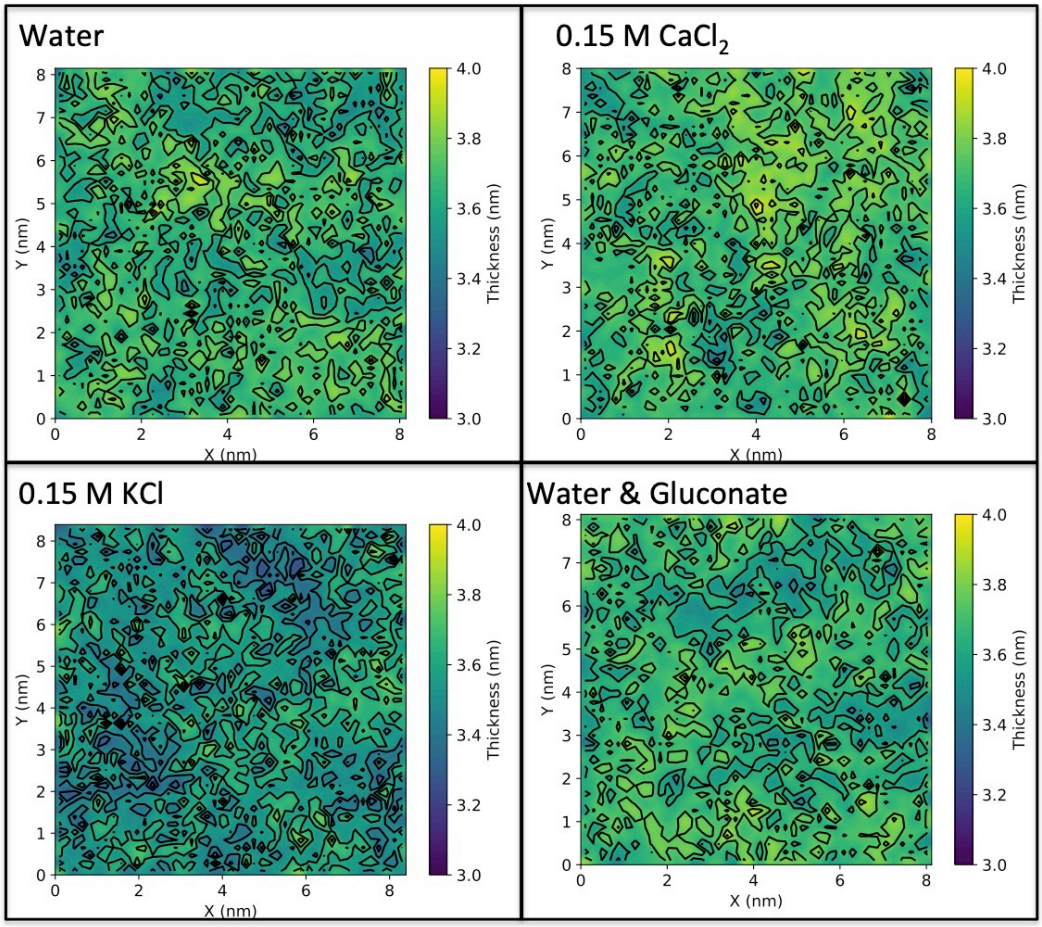

Figure 4.19: Membrane thickness of each simulation.

The deuterium order parameters of the acyl chains of the lipid tails were measured for each lipid in each simulation, Figure 4.20. Within each setup, each acyl chain trends similarly. The system with chlorhexidine and 0.15 M KCl has the overall lowest Scd, i.e. the lowest chain order. This is anticipated based on this simulation having the thinnest membrane. In contrast, the chain order is increased in the chlorhexidine and 0.15 M $CaCl_2$ system. This would suggest this is the thickest membrane with the tightest lipid packing, suggesting that chlorhexidine is not disrupting the membrane so much.

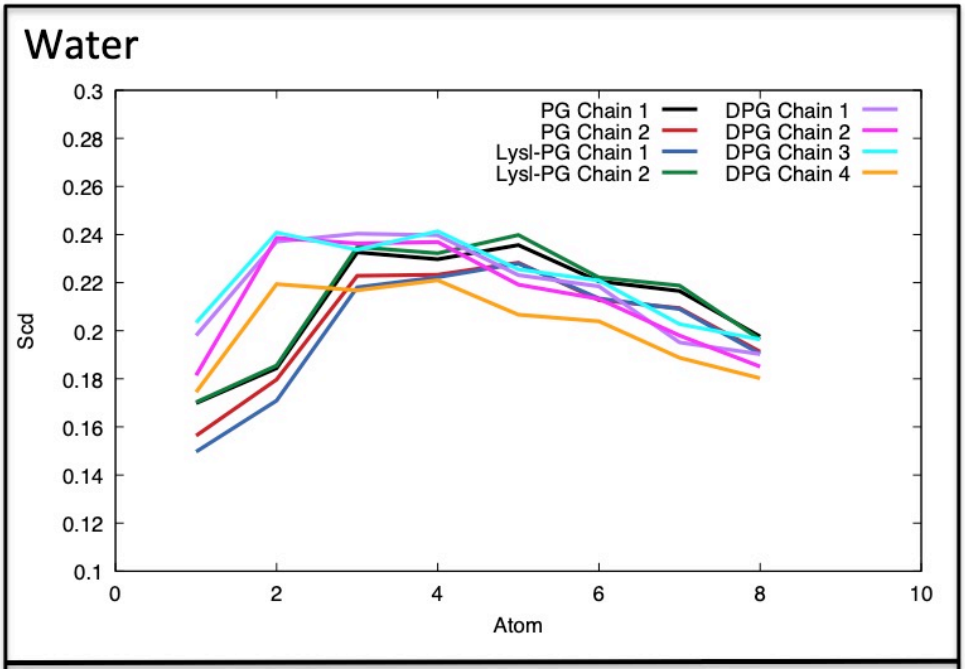
Water
PG Chain 1
PG Chain 2
Lysl-PG Chain 1
Lysl-PG Chain 2
DPG Chain 1
DPG Chain 2
DPG Chain 3
DPG Chain 4
Scd
Atom
0.3
0.28
0.26
0.24
0.22
0.2
0.18
0.16
0.14
0.12
0.1
0
2
4
6
8
10

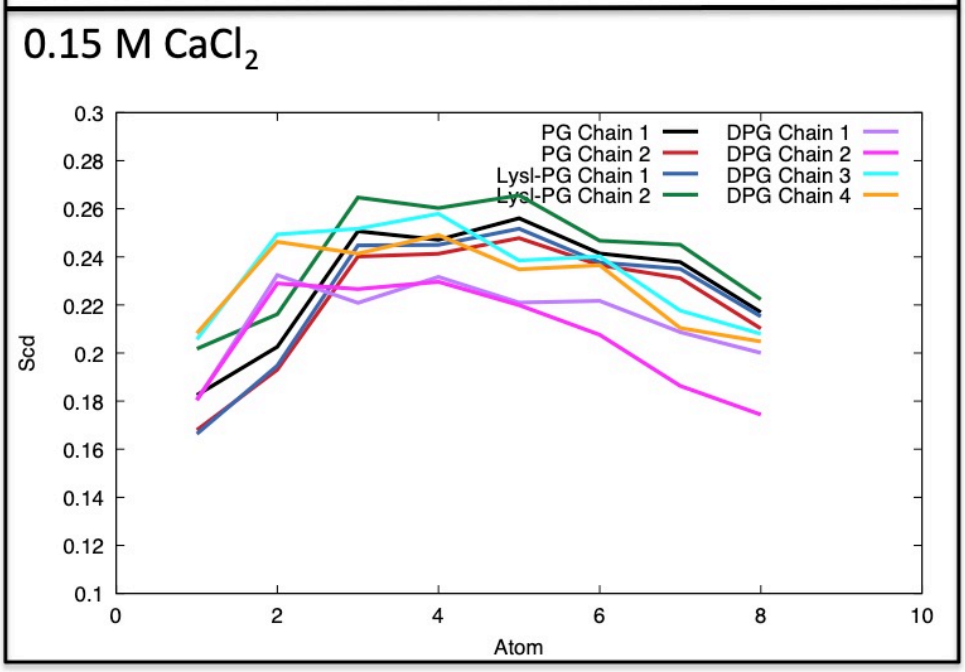
0.15 M CaCl2
PG Chain 1
PG Chain 2
Lysl-PG Chain 1
Lysl-PG Chain 2
DPG Chain 1
DPG Chain 2
DPG Chain 3
DPG Chain 4
Scd
Atom
0.3
0.28
0.26
0.24
0.22
0.2
0.18
0.16
0.14
0.12
0.1
0
2
4
6
8
10

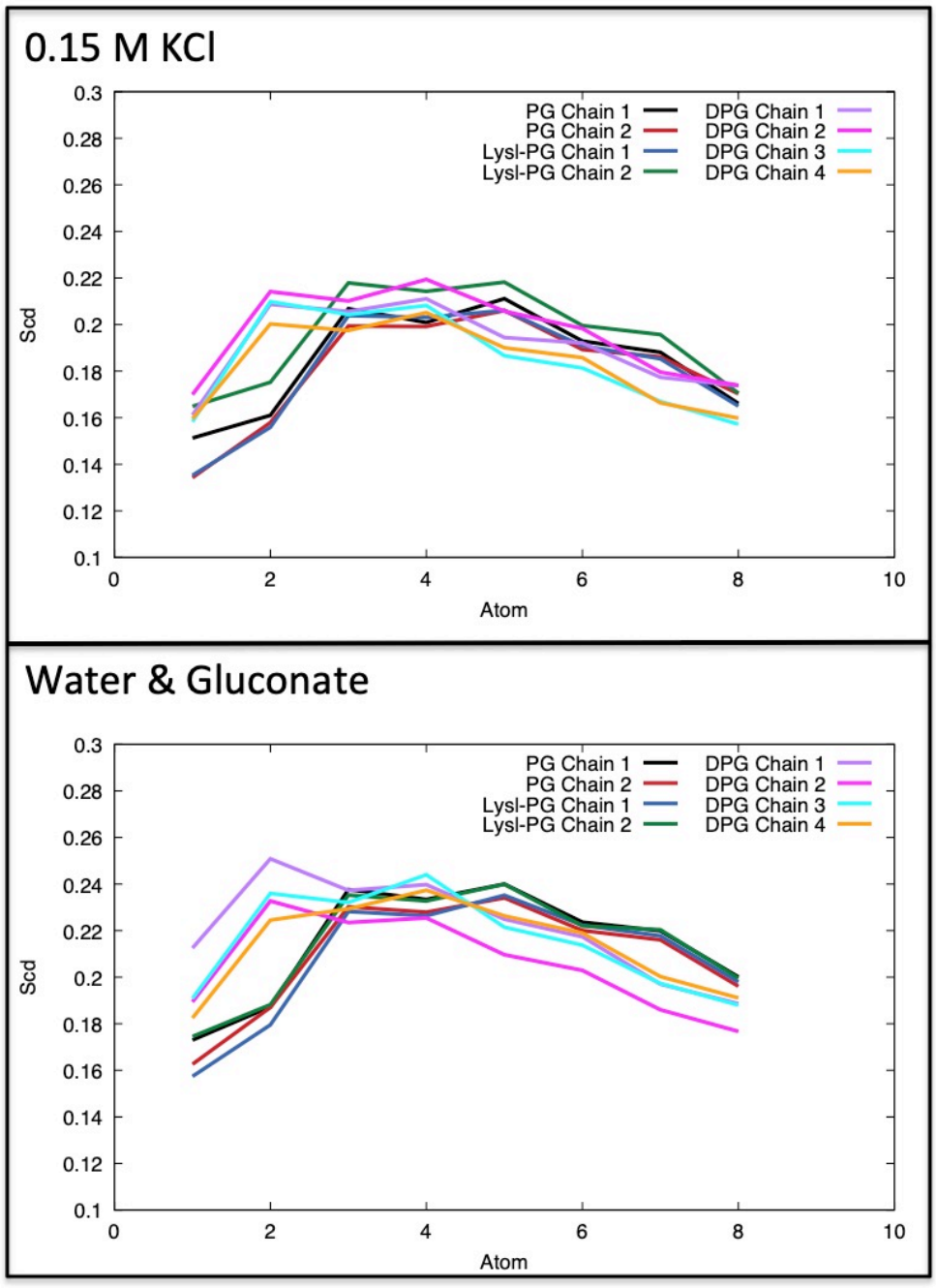

Figure 4.20: Deuterium order parameters of each lipid tail chain calculated over the simulation.

The lipid diffusion rates were also measure for each simulation, Table 4.3. For the simulations with chlorhexidine and water and 0.15 M $CaCl_2$ there is some difference in the later diffusion rates, with lipids in the presence of 0.15 M $CaCl_2$ moving more quickly. However, the diffusion rates are around 10x slower for the chlorhexidine and 0.15 M KCl simulations. Furthermore, the simulations

with the gluconate in the setup saw the highest lipid diffusion rates. Overall, there was little difference in the diffusion rate between lipid types in all simulations.

Simulation	PG Diffusion Rate (1 e-5 cm^2/s)	Lysl-PG Diffusion Rate (1 e-5 cm^2/s)	DPG Diffusion Rate (1 e-5 cm^2/s)
Water	0.0110 (± 0.0069)	0.0104 (± 0.0068)	0.0108 (± 0.0076)
0.15 M CaCl2	0.0182 (±0.0059)	0.0182 (± 0.0056)	0.0165 (± 0.0048)
0.15 M KCl	0.00307 (± 0.0212)	0.00283 (± 0.0210)	0.00269 (± 0.0209)
Gluconate	0.0838 (± 0.0370)	0.0822 (± 0.0383)	0.0831 (± 0.0314)

Table 4.3: The lipid diffusion rates of lipids throughout each simulation.

In addition to the analysis also described, the APL was measured for each simulation, Figure 4.21. These are in line with the membrane thickness simulations as the system with 0.15 M KCl has the highest APL. Membrane thickness is inversely proportional to APL so the thinner the membrane the larger the APL. The lowest APL is the system with 0.15 M $CaCl_2$, suggesting this membrane is the thickest and therefore has had less disruption from chlorhexidine.

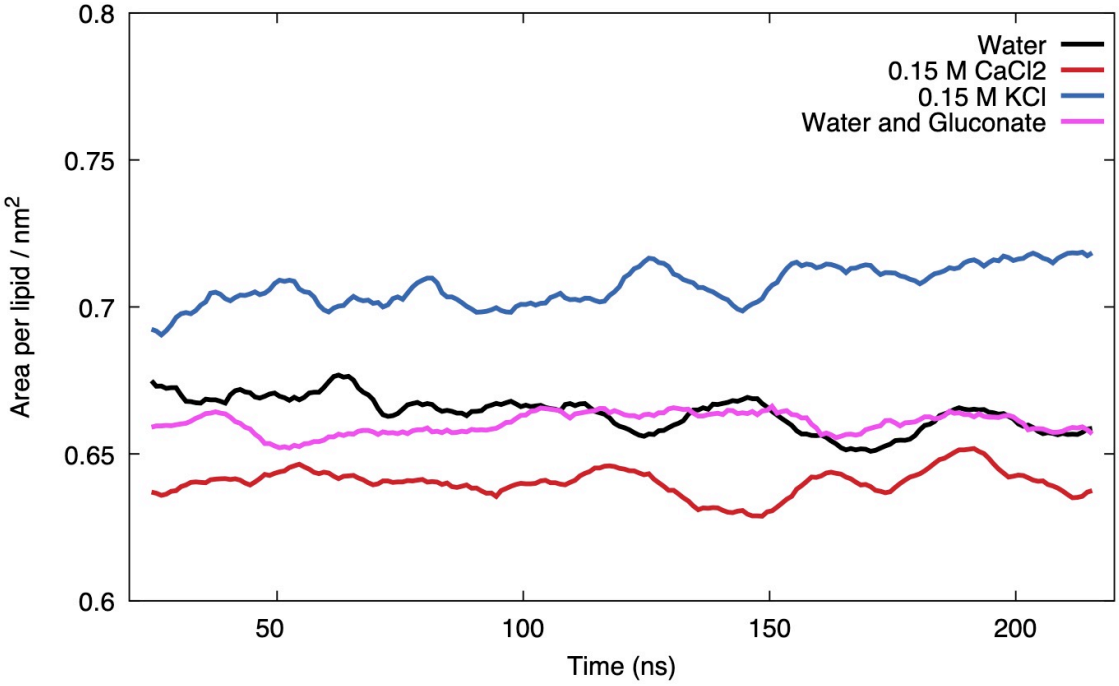

Figure 4.21: APL over each simulation.

Further analysis included the SASA of chlorhexidine when in the presence of the membrane, Figure 4.22. As expected the chlorhexidine in the presence of 0.15 M $CaCl_2$ had the largest SASA over the simulation, which was expected as not all chlorhexidine molecules entered the membrane in this circumstance. Despite not being the example where chlorhexidine most fully entered the membrane, the system with gluconate had the smallest SASA, which may be indicative of interactions between chlorhexidine and gluconate thereby reducing the SASA. Overall the simulations with water and gluconate both see a greater reduction in SASA than the other two setups. However focusing on the 0.15 M KCl simulation, there is a drop in the SASA around 150 ns which then increases. As previously discussed, in this setup some water entered the head group region from looking at the density plots. This drop and increase of chlorhexidine SASA may suggest that the decrease is from the chlorhexidine entering then the following increase is due to water entering the head groups and being thereby being able to contact the chlorhexidine.

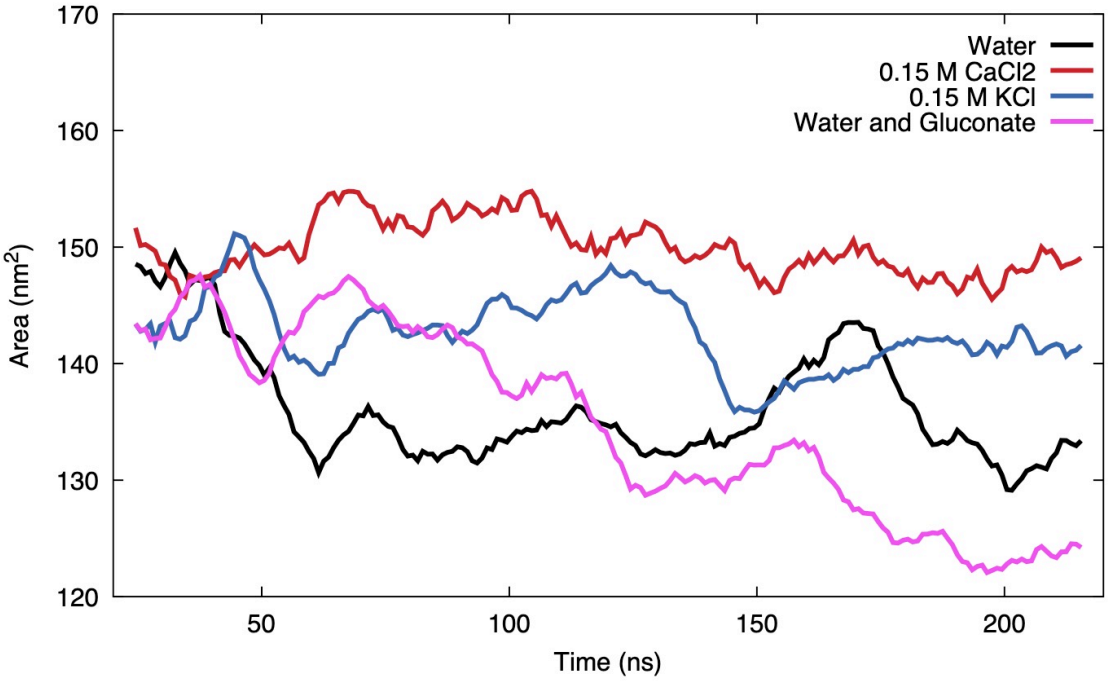

Figure 4.22: Average SASA of each chlorhexidine throughout the simulation.

As with the previous simulations, the distance between the chlorine atoms on each chlorhexidine molecule was measured throughout the simulation in an attempt to give an insight into the conformation of the chlorhexidine molecules in the presence of a membrane, Figure 4.23. Overall, the simulations with a salt present see a smaller distance between chlorine atoms on each chlorhexidine than the simulations with only water as a solvent. The system with gluconate present has the largest Cl-Cl distance suggesting that gluconate is interacting with chlorhexidine and effecting the conformations of the chlorhexidine molecules.

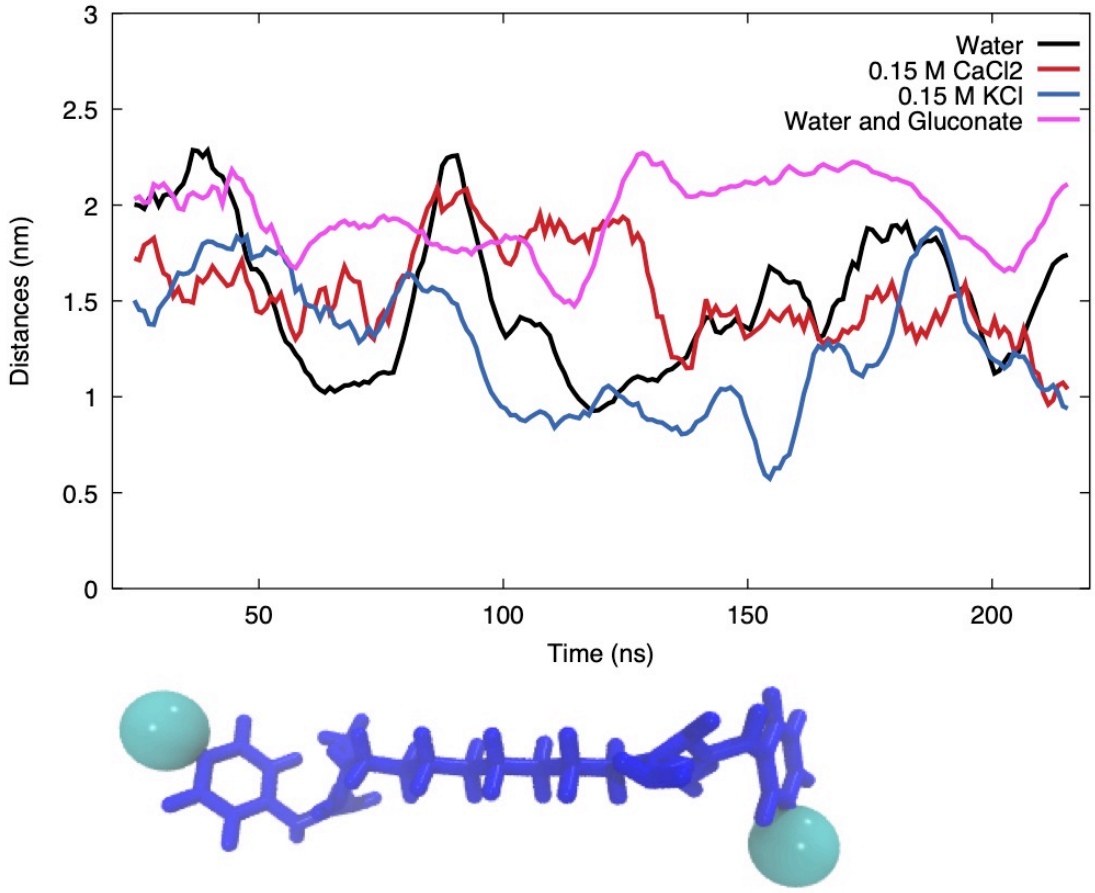

Figure 4.23: Average distances between chlorine atoms (cyan) on either end of each chlorhexidine (blue) in each simulation with the added solvent shown. This aimed to show whether the hexamethylene bridge was bending and if this was dependent on the available ions.

As well as measuring the Cl-Cl distances, the number of contacts between chlorhexidine and lipid heads and tails in each simulation were calculated, Figure 4.24. The least number of contacts with either lipid component was with the 0.15 M $CaCl_2$; the lack of contact with either heads or tails supports the evidence that in this simulation chlorhexidine is interacting with the membrane less. Contrastingly, the most contacts occurred between chlorhexidine and lipids in the presence of 0.15 M KCl. This is in support with all the previous data.

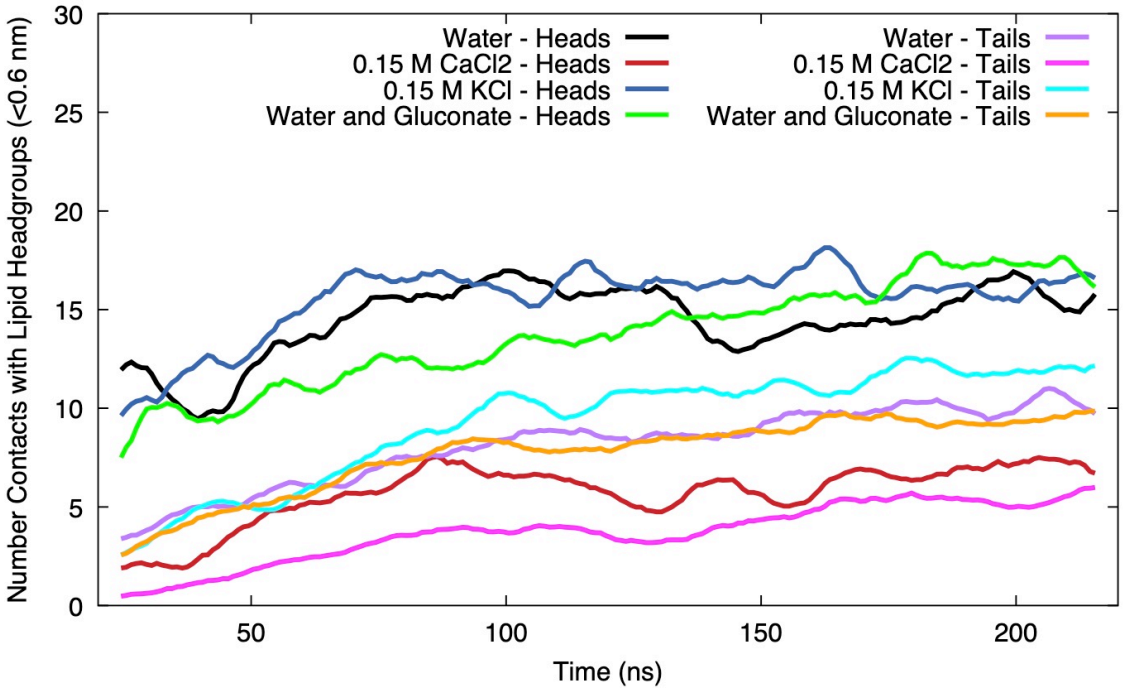

Figure 4.24: The average number of contacts less than 0.6 nm between chlorhexidine and lipid heads and tails.

In order to ascertain if chlorhexidine shows a preference to one particular lipid type, the average number of contacts between each chlorhexidine and each lipid type, Figure 4.25. Due to the difference in abundance of each lipid type, this data has been normalised to account for this. In all systems, chlorhexidine showed a preference for DPG, with the most contacts consistently occurring between it and chlorhexidine compared to the other lipids. Generally, the least contacts occurred between chlorhexidine and Lysl-PG. This would be anticipated as both are positively charged.

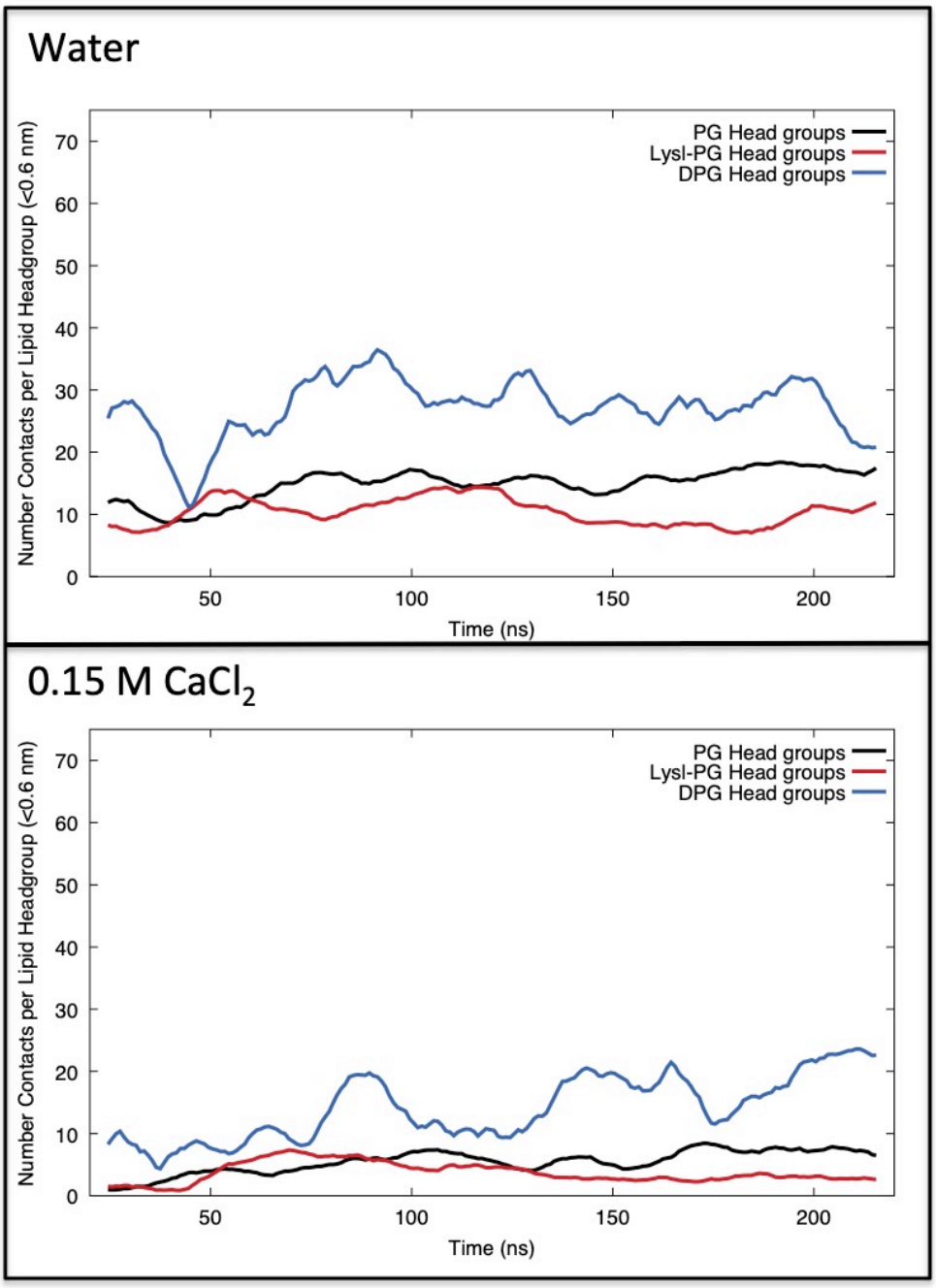

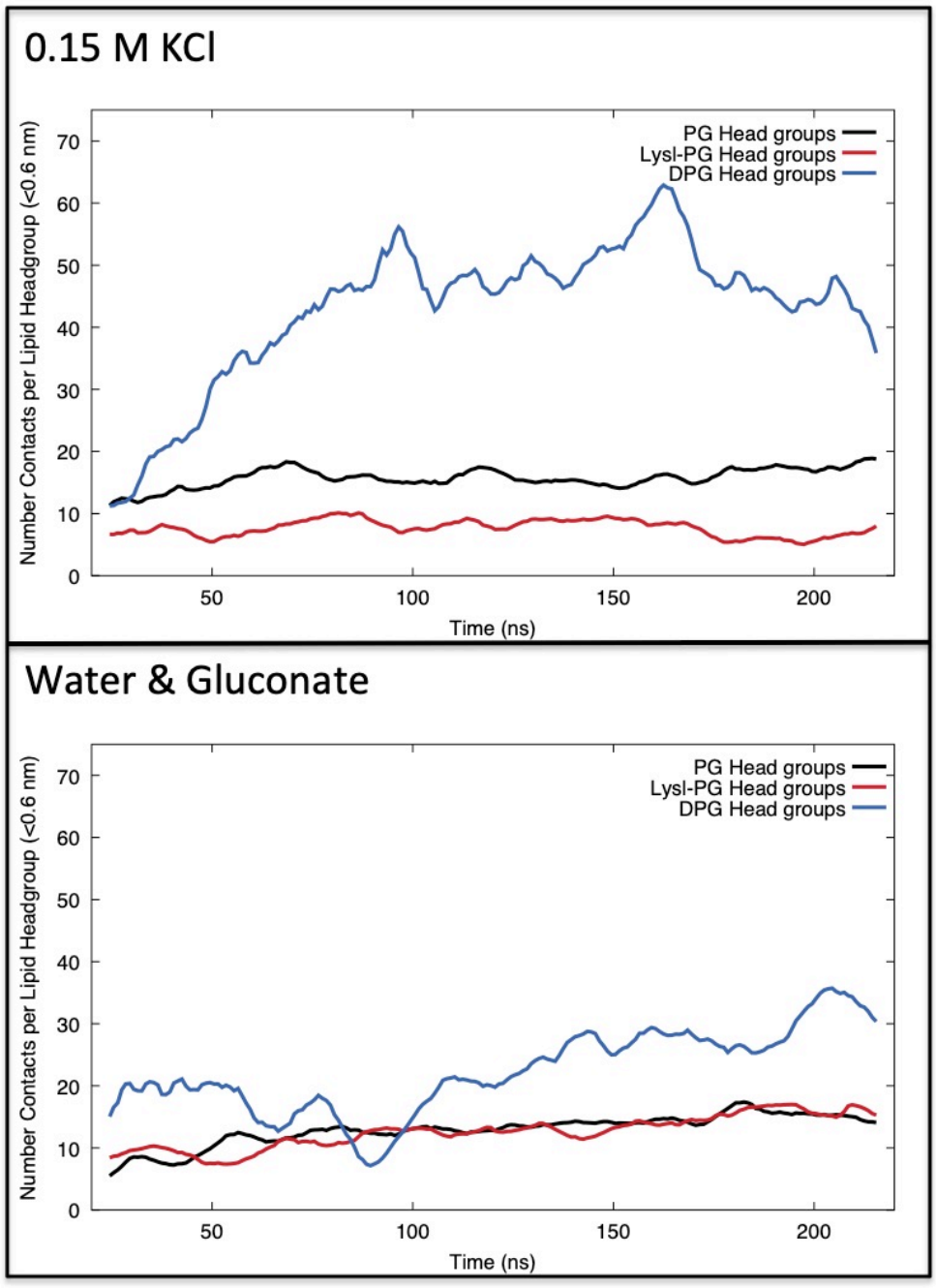

Figure 4.25: Average number contacts between chlorhexidine and different lipid head-groups. This has been normalised to per lipid due to the differing numbers of each lipid type in the membrane.

Finally, in order to confirm in which set up chlorhexidine furthest entered the membrane, the Z-coordinates of 4 random chlorhexidine molecules were tracked in comparison to the Z-coordinates of the phosphates in the lipid bilayer of time, Figure 4.26. This figure clearly shows chlorhexidine entering the

membrane most in the bottom two plots, particularly the 0.15 M KCl simulation. The position of chlorhexidine is at a similar depth in the water and 0.15 M $CaCl_2$ simulations. This supports the previous data that suggests 0.15 M KCl allows chlorhexidine to further enter the membrane. Furthermore, this may suggest gluconate has a role in allowing chlorhexidine to enter the membrane more fully.

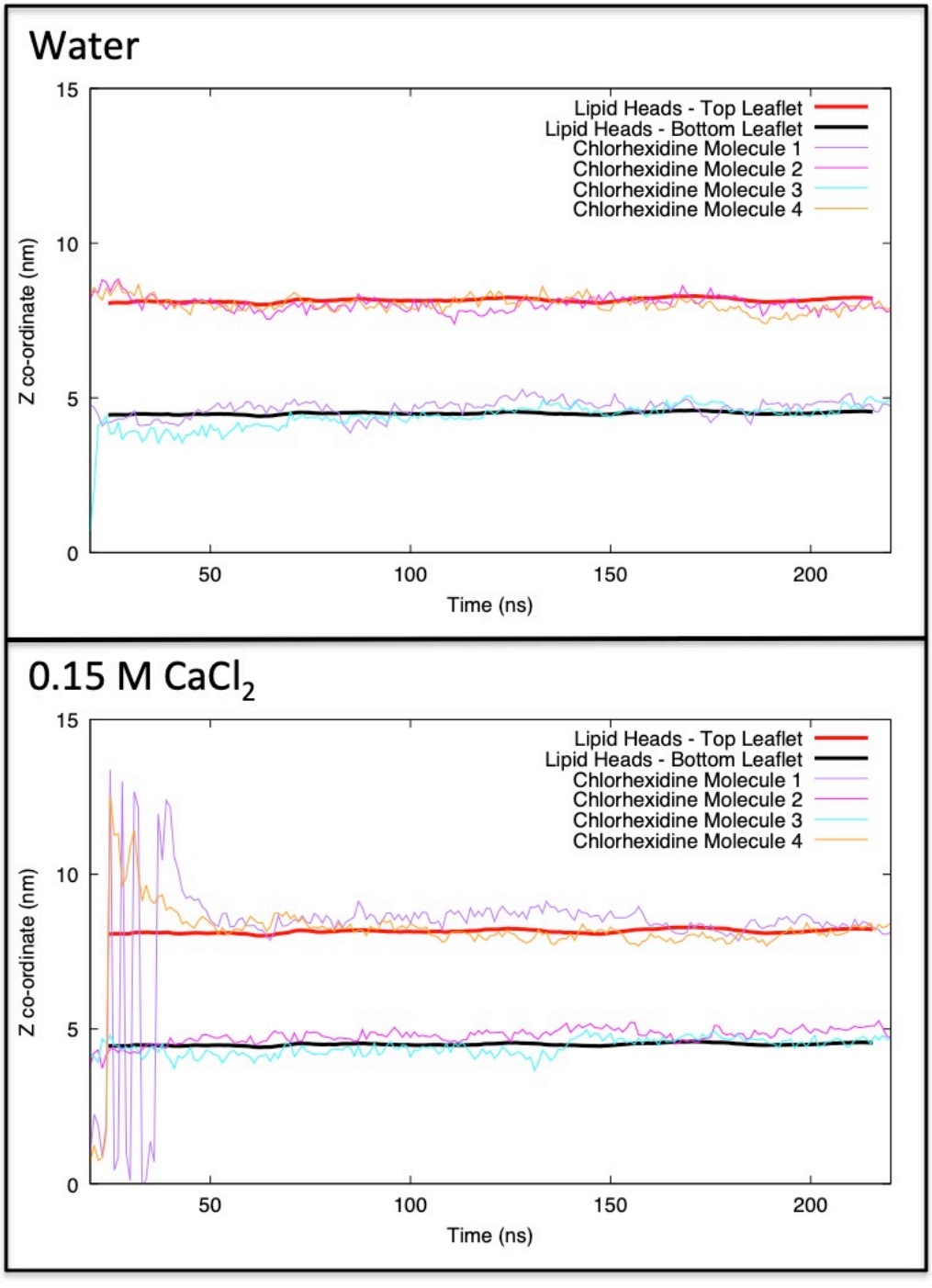

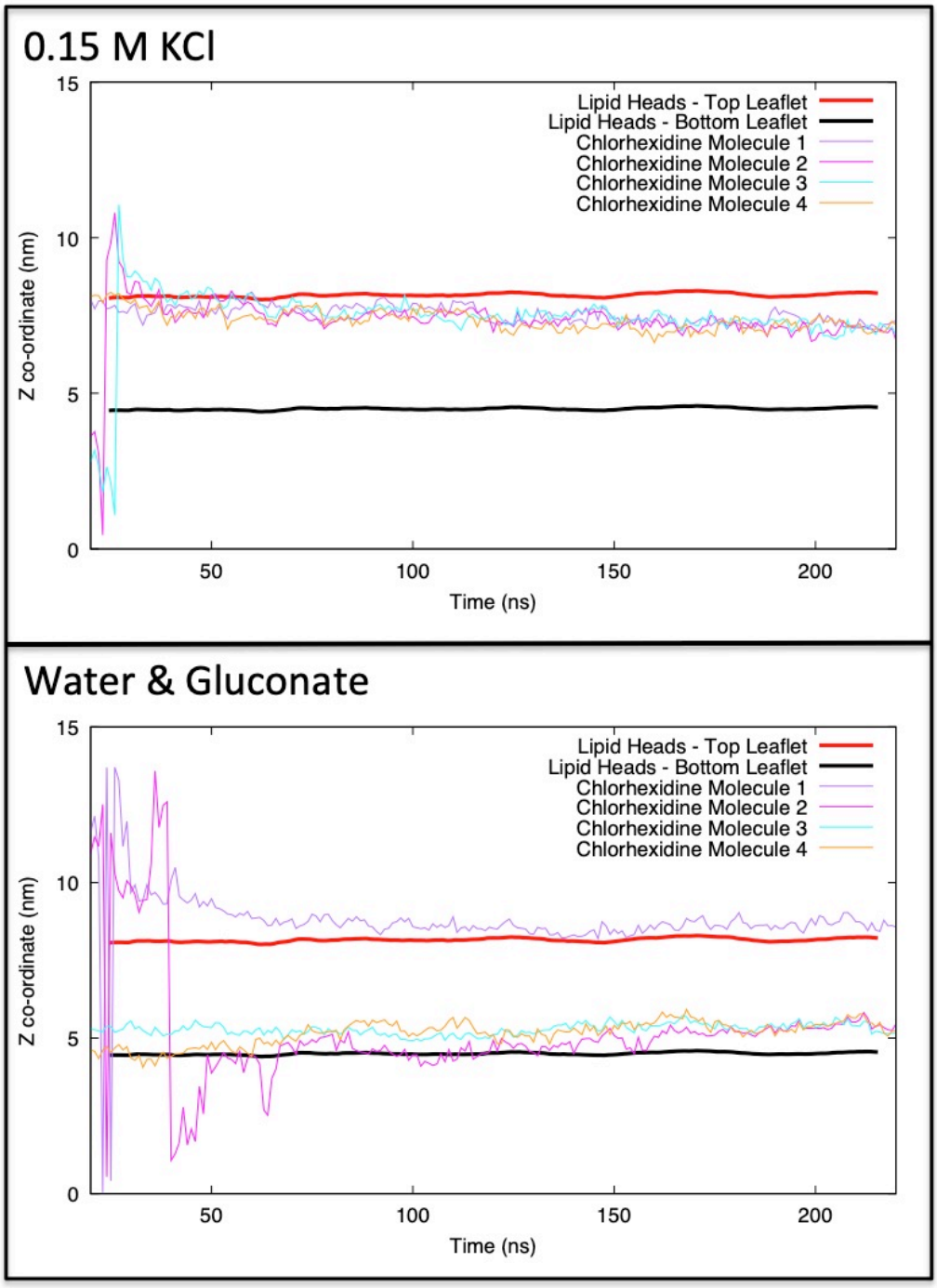

Figure 4.26: Z-coordinates of 4 random chlorhexidine in each simulation in relation to top and bottom leaflet of membrane over time. Note that jumps across the membrane at the beginning of the simulation are a remnant of PBCs and chlorhexidine does not cross the membrane.

4.3.3 Conclusions

From these simulations, it can be seen that chlorhexidine is not able to fully enter the membrane given the current setups used in this work. This may highlight the importance of using chlorhexidine with a surfactant or with alcohol. However, the favoured position of chlorhexidine has previously been shown to be within the head region of the membrane. This may suggest that the dents and deformations caused by chlorhexidine only require the molecule to sit within the head groups. This may also explain why chlorhexidine works extremely quickly and is therefore an effective topical antiseptic, as it is not required to enter the membrane in order to have bacteriostatic and bactericidal effects[126]. However, we are limited by the timescales of MD and the particular force fields used.

One interesting consistency between the simulations is the preference of chlorhexidine to come into contact with DPG over other lipids in the bilayer. It would be expected this interaction occurs due to the stronger negative charge of DPG due to the two phosphate groups within the head group. There are no experimental studies of this specific interaction, which would be suggested in the future. If having highly negatively charged lipids within the membrane is important for the efficacy of chlorhexidine then this could be used to more effectively administer the antiseptic for more appropriate infections. It has been shown that bacteria resistant to certain antibiotics see reduced susceptibility to chlorhexidine, with susceptibility reducing with repeat exposure, highlighting the importance of appropriate use[127]. It may also explain why it has been previously experimentally evidenced that Gram-positive bacteria are more susceptible than Gram-negative bacteria to chlorhexidine as the latter is believed to typically contain slightly less DPG within the bilayer[9,99,117].

Despite chlorhexidine being ubiquitously administered with gluconate, in this work the gluconate does have a slight influence on the apparent efficacy of chlorhexidine. However, it appears that chlorhexidine is used with gluconate most frequently due to its ability to dissolve in water. This may suggest that any

benefit of gluconate in the efficacy of chlorhexidine is a useful consequence of the manufacturing process. However it is interesting to note that the gluconate is not itself interacting with the membrane particularly yet chlorhexidine does seem to enter the membrane more fully in this case, yet did not disrupt the bilayer as much as the 0.15 M KCl simulation.

The other takeaway from this work is that available counter ions seem to have an important effect on the efficacy of chlorhexidine. The chlorhexidine had the largest effect on the bilayer causing membrane thinning and increasing the APL. There is no experimental support of this therefore experiments of this would be helpful to confirm this. It could be that KCl interferes with the bacterial membrane therefore allowing chlorhexidine to further enter the membrane. However, Ca^{2+} ions are known to disrupt bacterial membranes therefore why this is only seen in the KCl simulation remains unclear[91].

As previously stated, whilst the simulation work shows interesting results and suggestions for the behaviours of chlorhexidine, experimental data would be useful to confirm these findings.

Chapter 5 - Force Field Effect on Structure and Membrane Interactions of Chlorhexidine

5.1 Introduction

As previously described in the methods, force fields underpin all the calculations computed during a MD simulation. In MD simulations, a molecule is described as series of balls (atoms) linked by springs (atoms). In order to understand the progress of bond lengths, bond angles, torsions, van der Waals and electrostatic interactions, a force field is used. The force field is an assembly of equations and related constants intended to replicate molecule geometry and chosen properties of established structures.[128] Increasingly, MD simulations are an important and powerful tool to help in our understanding of biological systems, particularly membranes, lipids and their associated interactions. This work and research as given rise to a number of different force fields to simulate such systems, which are freely and readily available. Each force field has different parameter sets for biological molecules and therefore has different strengths, weaknesses and different force fields are appropriate depending on the system setup and the desired outcomes. Therefore, this work looks at the difference between two popular and commonly used force fields to test if one is better at demonstrating the mode of action of chlorhexidine with the *S. aureus* membrane. The work compared the CHARMM36 and GROMOS54a7 force fields[67,129]. The aim of this work was to firstly try to determine how chlorhexidine disrupts bacterial membranes but also the differences these force fields have on lipids and their interactions with chlorhexidine.

Since the 1970s, force fields have undergone constant study and improvement[130,131]. These early force fields primarily aimed to accurately produce the parameters for small molecules and focused on protein structural data[132,133]. As the field developed, and computational power improved, bigger and more complex molecules and systems could be simulated and therefore the

force fields developed to represent these larger systems[134]. Due to lipids and membranes being present in all orders of biological life, parameterising and simulating these molecules are of particular interest as well as understanding the molecules, peptides and proteins that interact with these membranes.

Both CHARMM and GROMOS have been extensively used to simulate such systems. Whilst both are atomistic force fields, CHARMM36 is an all atom force field meaning that every atom in a given molecule is explicitly represented. Whereas, GROMOS54a7 is a united atom force field meaning that hydrogen atoms on non-polar groups are not considered. In order to still represent hydrogen bonding however, polar hydrogen atoms are explicitly represented. Whilst there are other slight differences between the force fields, this distinction is key. In order to calibrate these force fields in relation to experimental results, area per lipid, lipid diffusion rates, acyl-chain deuterium and order parameters are methods of analysis used to compare the MD results to experimental results[135,136]. These methods of analysis are also frequently used to analyse how molecules such as membrane disrupting antimicrobials affect bacterial lipids.

Several other studies have been done to ascertain how well different membranes are calibrated in relation to parameters found experimentally. A study within the Khalid group has previously compared force fields with respect to PC membranes. These results demonstrated a significant difference in the physical properties of membranes between different force fields. Whilst all of the force fields, including CHARMM and GROMOS, were determined to have advantages and disadvantages to reproduce experimental results, the key differences were in the deuterium order parameters and lipid diffusion rates[137]. A similar study from this time found that the GROMOS54A7 force field was best for matching to experimental results of PC membranes however this was only in comparison to the GROMOS53A6 force field[138].

In regards to studying lipid interactions with other molecules, a 2017 study compared force fields in relation to protein-lipid interactions at the membrane interface again focusing on a PC membrane. This work found significant difference between force fields in regards to the tilt of trans-membrane peptides and membrane insertion depths[139]. This could suggest that different force fields may be better for simulating membrane interactions with other molecules, which could be of particular importance when studying antimicrobial interactions with the bacterial membrane. Furthermore, a study comparing force fields focusing on membrane active antimicrobial peptides found that the secondary structure of such peptides within the bilayer is strongly force field dependent[140].

From all of these studies showing that simulation results are highly force field dependent, it is difficult to say which is the most appropriate force field to use in every circumstance. These differences also highlight the importance of validating simulations with experimental work.

Therefore, this work aimed to assess the difference between CHARMM and GROMOS force fields when simulating chlorhexidine with the *S. aureus* membrane. This is of particular interest as most data comparing force fields currently focuses on simpler membranes, such as PC membranes. Whereas this work not only aimed to show the difference in the effect of chlorhexidine between force fields but also if differences between results are equally as force field dependent when using a more complex membrane. Furthermore, the effect of chlorhexidine on the *S. aureus* membrane under an electric field was also compared across the two different force fields.

5.2 Chlorhexidine Equilibrium Simulations

The initial simulations in this section aimed to compare how chlorhexidine interacted with the *S. aureus* membrane at equilibrium in the different force fields, in order to try to predict which force field best modelled this interaction.

5.2.1 Methods and Simulation Set-up

The simulations carried out for the initial stage of this work are listed in Table 5.1.

Contents of Simulation	**Force field**	**Simulation Length**
10 chlorhexidine, *S. aureus* membrane, 22143 H_2O, 28 Ca^{2+}	CHARMM36	3 x 500 ns
10 chlorhexidine, *S. aureus* membrane, 22577 H2O, 28 Ca^{2+}	GROMOS54a7	3 x 500 ns

Table 5.1: List of simulations with differing force fields and ion availability.

The membrane used the same lipid composition of PG, Lysl-PG and DPG as the previous chapter described and the same chlorhexidine model. The CHARMM models were adapted from GROMOS model using CGenFF[101,102]. The membrane for GROMOS came from previous in house work[20]. The chlorhexidine model was converted to a GROMOS model using the automated topology builder (ATB)[141].

For the CHARMM simulations, the simulations were performed used the GROMACS2018 code, the CHARMM36 force field with the TIP3P water mode[96,97,129]l. The temperature of 313 K was maintained using the Nosé-Hoover thermostat at a time constant of 1 ps[62]. The pressure was maintained semi-isotropically at 1 atm using the Parrinello-Rahman barostat with a time constant of 1 ps[64]. LINCS constraints were applied to hydrogen containing covalent bonds[60]. A time step of 2 fs was used and long-range electrostatic interactions were calculated using the PME method[66]. For both the electrostatic and Van der

Waals interactions a cut-off value of 1.2 nm was used[65,66]. Both systems were neutralised with Ca^{2+} counter ions.

For the GROMOS simulations, the GROMOS54A7 force field was used with the SPC water model, again using the GROMACS2018 code[67,96,97]. The membrane was again equilibrated before production. The temperature of 313 K was maintained using the Nosé-Hoover thermostat at a time constant of 1 ps[62]. The pressure was maintained semi-isotropically at 1atm using the Parrinello-Rahman barostat with a time constant of 1 ps[64]. LINCS constraints were applied to all bonds[60]. A time step of 2 fs was used and long-range electrostatic interactions were calculated using the PME method[66]. For both the electrostatic and van der Waals interactions a cut-off value of 1.4 nm was used[65]. Systems were neutralised as described in table 1.

For both force fields, each simulation was run in triplicate for 500 ns. VMD was used for visualising the simulations whilst analysis primarily used GROMACS tools[108]. The membrane thickness and phosphate density used Monticelli's GROMACS4 *g_thickness* and *g_mydensity* scripts respectively[106,107]. The area per lipid was measured using FATSLiM[105].

5.2.2 Results

The snapshots of the systems at the end point of the simulations (500 ns) are shown in Figure 5.1, in both force fields, all chlorhexidine molecules have inserted into the membrane with none remaining within the solvent.

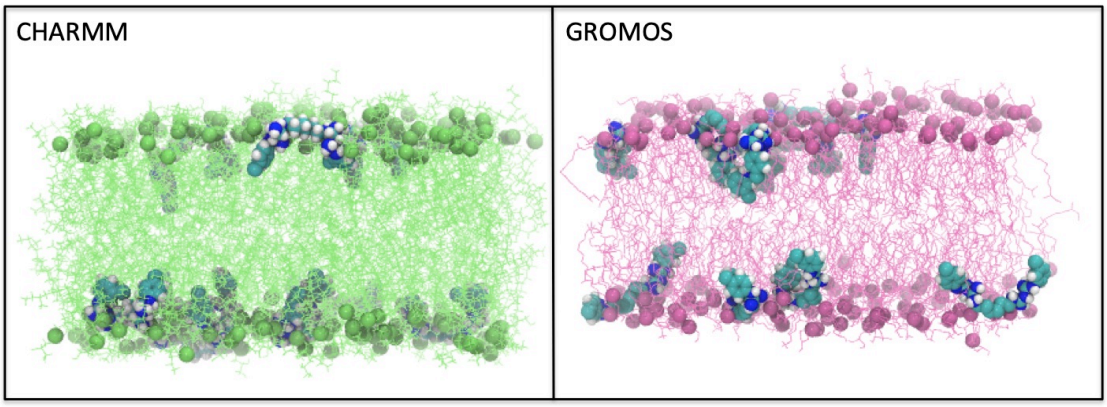

Figure 5.1: Snapshots of chlorhexidine (cyan, blue and white) with *S. aureus* membrane simulations at 500 ns, with the membranes shown in green and pink for CHARMM and GROMOS force field simulations respectively. The solvents and force field are listed above each snapshot. Water and ions have been omitted for clarity.

The densities of lipids, solvent and chlorhexidine are shown in Figure 5.2. From these it appears that chlorhexidine entered further into the membrane in the GROMOS simulation compared to the CHARMM simulation. In the GROMOS simulation, the density of chlorhexidine was within the tail region of the bilayer whilst in the CHARMM simulation chlorhexidine sat within the head-groups. Notably, chlorhexidine did not sit within the centre of the membrane in either force field. However, in the CHARMM simulation, the solvent appeared to enter slightly further into the head-group region.

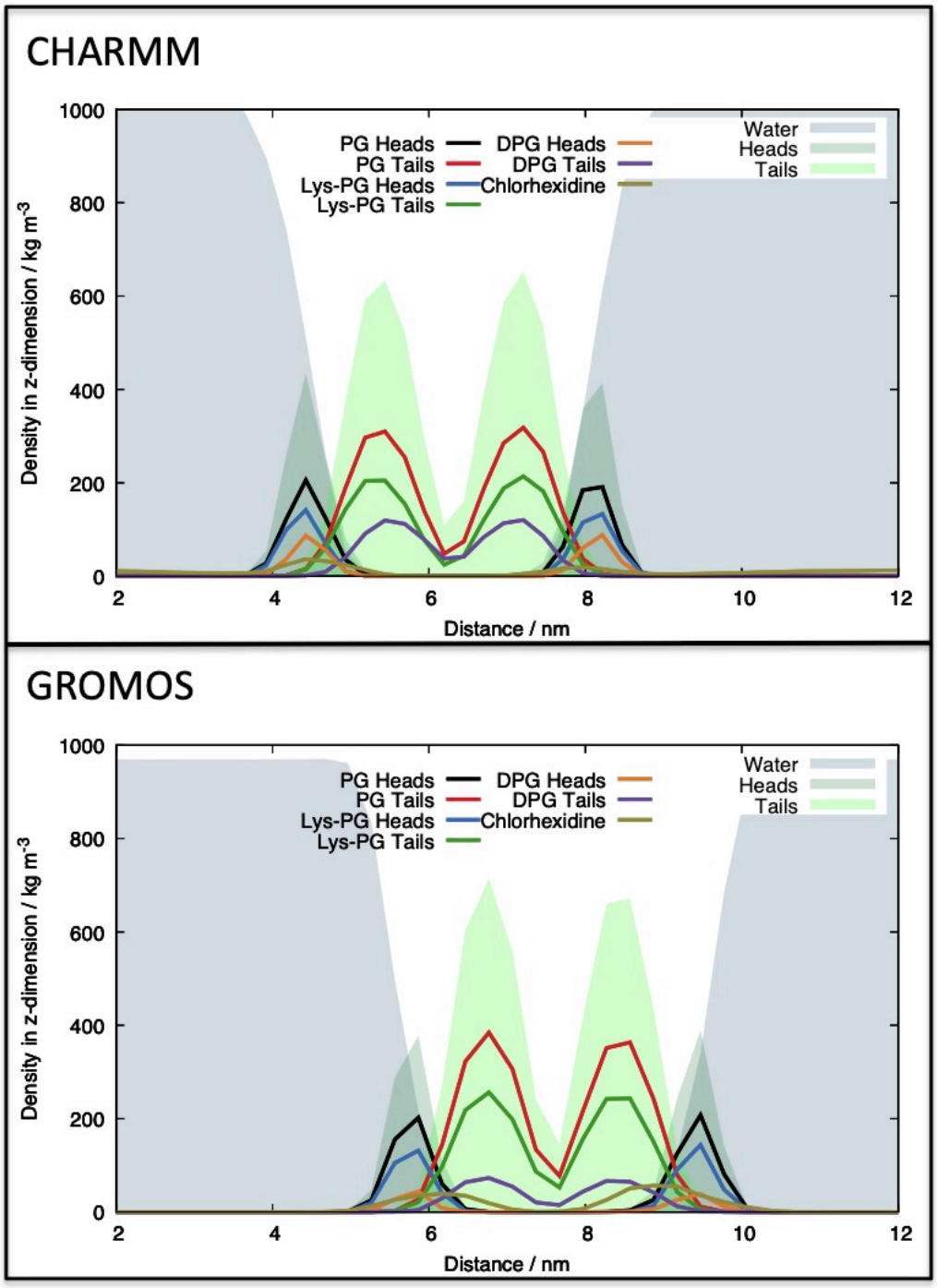

Figure 5.2: Densities of chlorhexidine, lipid head-groups and tails and solvent. This was calculated for the last 20 ns of the simulation. The force fields are shown above.

The membrane thicknesses from each simulation are shown in Figure 5.3. The GROMOS membrane thickness shows darker, thinner areas where chlorhexidine had entered the membrane. In contrast, the thickness of the CHARMM

membrane is similar throughout the membrane and did not show such concentrated thinner areas of the membrane. This supports the evidence from the density plots previously that chlorhexidine entered the membrane more fully in the GROMOS simulation.

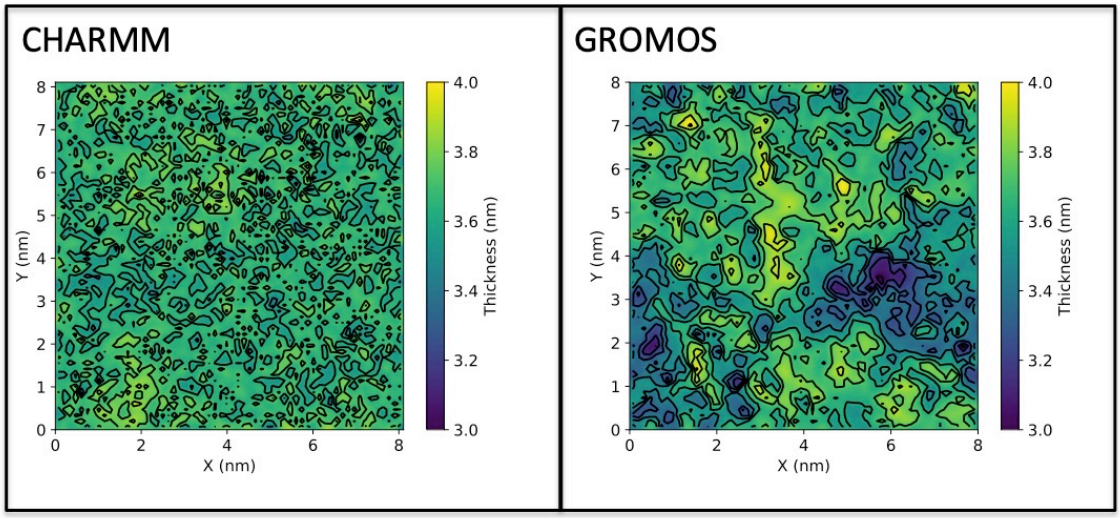

Figure 5.3: Membrane thickness of each simulation. The force fields are shown above.

The deuterium order parameters were measured for the acyl chains of the lipids in both membranes and shown in the Appendix, Figure A.2. This showed little difference between lipids within each force field. Overall, however, towards the end of chains, the GROMOS lipid tails were less organised than the CHARMM ones as they headed more steeply towards 0. This was inline with the previous analysis.

In addition to the thickness, the membrane density of the phosphates within the lipid head groups also showed greater disruption of the membrane in the GROMOS simulation, Figure 5.4. In this analysis, the phosphates were shown to be less tightly compacted and the density wider which suggested greater disruption to the membrane.

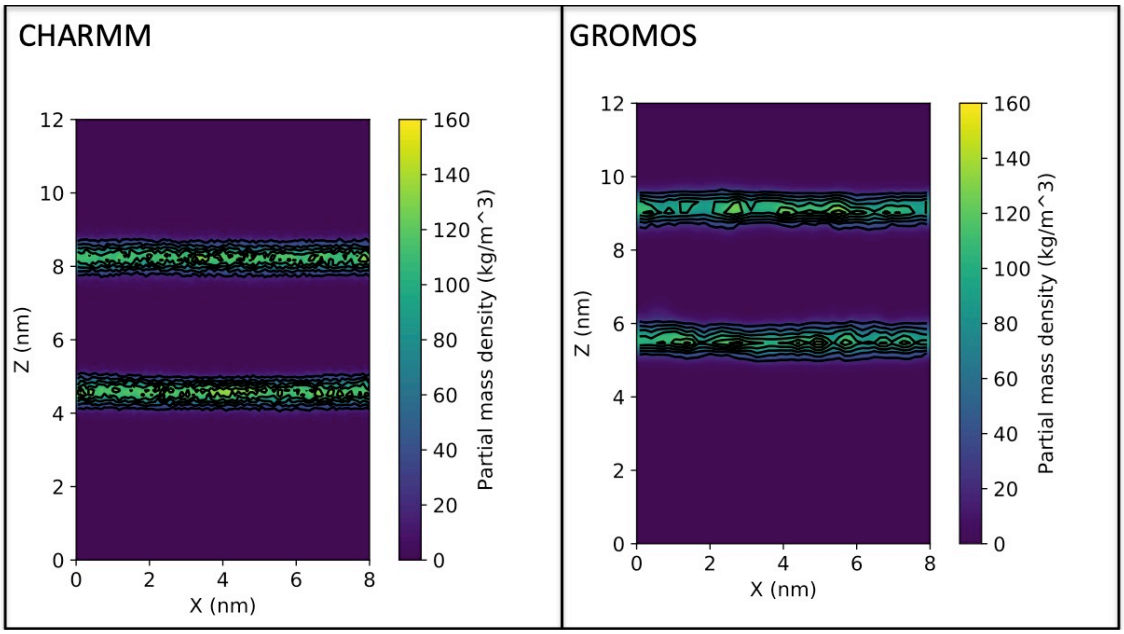

Figure 5.4: Phosphate density of lipid head-groups phosphates in Y-direction. The force fields are shown above.

The average number of contacts, less than 0.6 nm, between chlorhexidine and the lipids in the bilayer on average were measured, with the data being normalised to represent the differing lipid within the membrane, Figure 5.5. The aim of this was to see whether chlorhexidine showed a preference to contact a particular lipid type and whether this was consistent across the two force fields. Interestingly, there were more contacts between chlorhexidine and the lipids in the CHARMM simulation overall despite the evidence that chlorhexidine better enters the membrane in GROMOS force field simulations. However, these contacts were measured between chlorhexidine and lipid head groups meaning that chlorhexidine in GROMOS simulations are not contacting heads so frequently as they have inserted into the membrane.

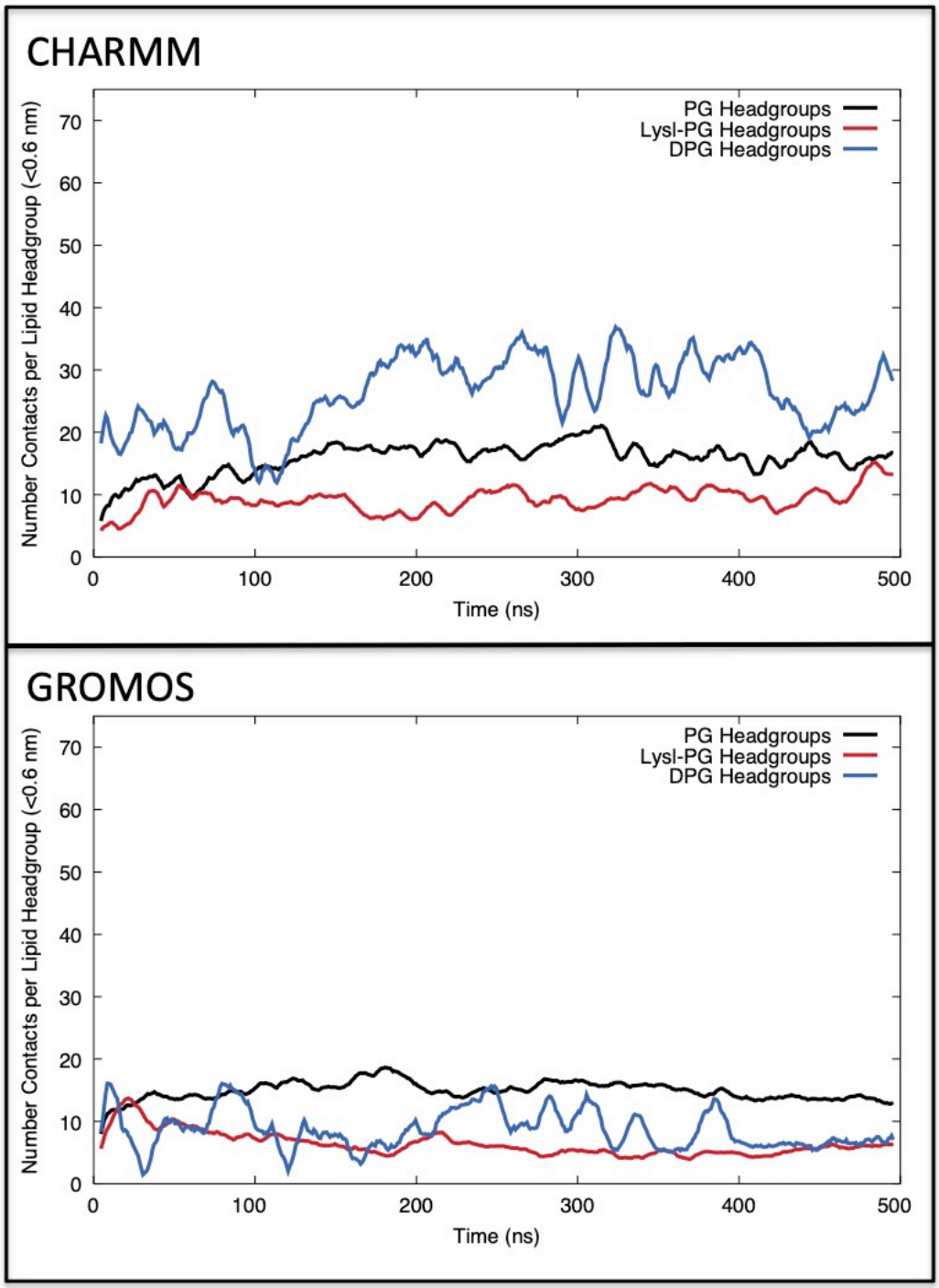

Figure 5.5: Average number contacts between chlorhexidine and different lipid head-groups, less than 0.6 nm, over time. This has been normalised to per lipid due to the differing numbers of each lipid type in the membrane. The force fields are shown above.

The lateral diffusion rates of the lipids in each bilayer were measured, Table 5.2. The lipids in the GROMOS simulation diffused across the membrane around 10 times slower than in CHARMM simulation. This may support suggestions that chlorhexidine is entering and crowding the lipids more when using the GROMOS force field than the CHARMM force field. This is based upon studies that have suggested lipids diffuse laterally more slowly in crowded bilayers[142].

Force field	PG Diffusion Rate (1e-5 cm^2/s)	Lysl-PG Diffusion Rate (1e-5 cm^2/s)	DPG Diffusion Rate (1e-5 cm^2/s)
CHARMM	0.0400 (±0.0433)	0.0277 (+/- 0.0295)	0.0417 (+/- 0.0417)
GROMOS	0.0013 (± 0.0003)	0.0014 (± 0.0008)	0.0013 (± 0.0008)

Table 5.2: The lipid diffusion rates of lipids throughout each simulation.

SASA was measured over time cumulatively of all chlorhexidine molecules in each system, Figure 5.6. There was very little difference between force fields of SASA throughout the simulations. This suggests that in both force fields that chlorhexidine was equally unable to interact with water in both force fields, which is indicative that chlorhexidine entered the membrane in both setup rather than of how disrupted the membrane or how far the chlorhexidine inserted in the bilayer.

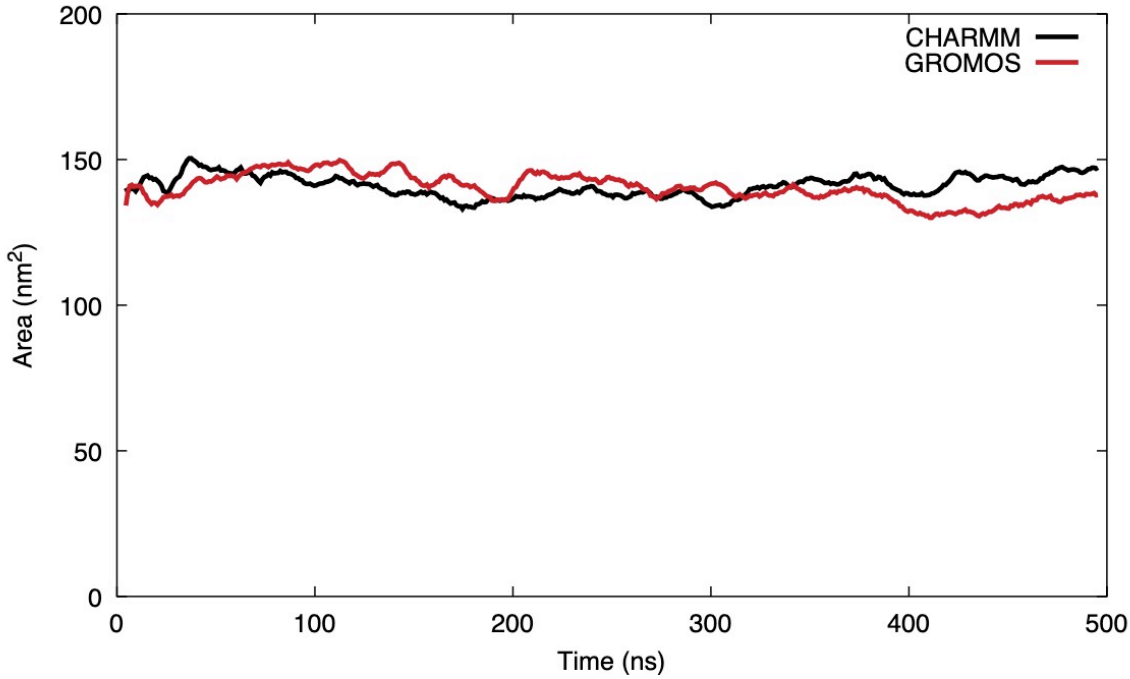

Figure 5.6: SASA of chlorhexidine over each simulation over time. The force fields are shown above.

In these simulations, APL began at around 0.65 nm^2 in the CHARMM system and 0.7 nm^2 in the GROMOS simulation, Figure 5.7. Interestingly, both the APL in both systems ended at a very similar point particularly in the last 200 ns of the simulations. As the method used for measure APL focused upon the lipid head groups, this may suggest that in both membranes chlorhexidine disrupted the upper region of the membrane similarly. Previous simulation work supports that this is the favoured location of chlorhexidine within the membrane, this suggests that both force fields are valid for displaying this aspect of the mode of action of chlorhexidine in an aqueous environment.

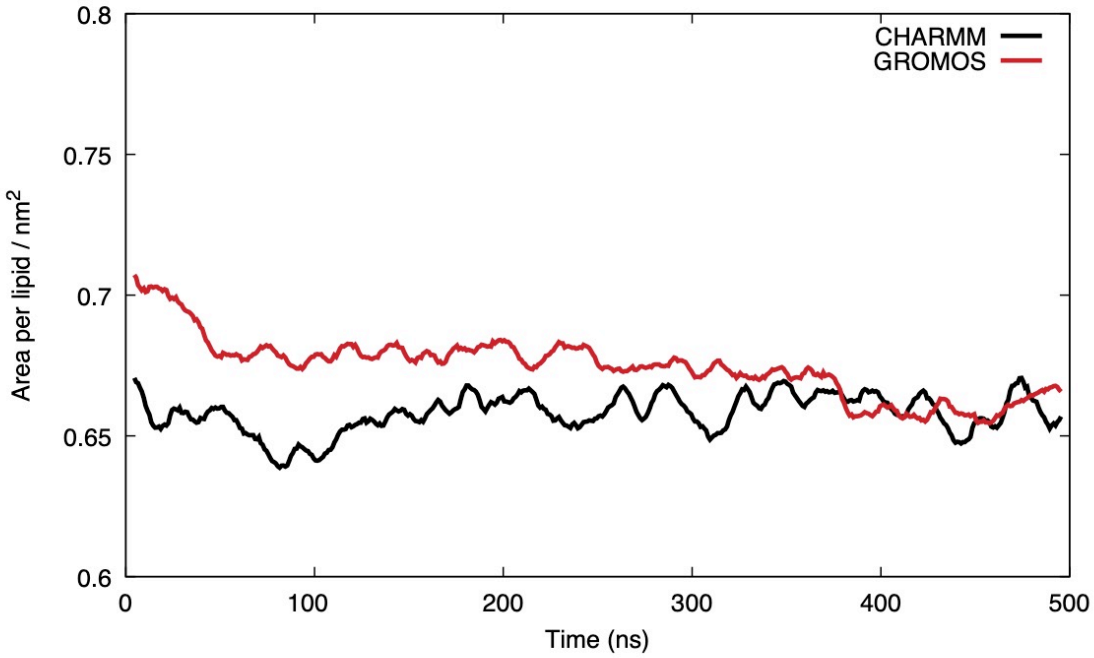

Figure 5.7: APL over each simulation over time. The force fields are shown above.

The number of hydrogen bonds between chlorhexidine and each lipid was measured over time (ns) with the donor acceptance distance was set at 3.0 A and the angle cut off was 20 degrees, Figure 5.8. The data was normalised to represent the different number of each lipid with the bilayers. As would be anticipated, both in CHARMM and GROMOS systems, chlorhexidine made the least hydrogen bonds with Lysl-PG, due to both chlorhexidine and this lipid being positively charged meaning this interaction would be unfavourable. In regards to PG, there are slightly more chlorhexidine hydrogen bonds with this lipid in the GROMOS simulation than the CHARMM. This is in line with the suggestion from contact number analysis; Figure 5.6 that suggested in GROMOS chlorhexidine favoured interacting PG over DPG. However, overall there was not a great difference between the numbers of hydrogen bonds formed with any lipid between force fields despite that generally there were more contacts between lipid head groups and chlorhexidine in the CHARMM force field simulation. As the data suggests that chlorhexidine enters further into the membrane in the GROMOS simulations, this may suggest that chlorhexidine is making hydrogen bonds with the lipid head groups from within the bilayer in

the GROMOS as this would account for the disparity between hydrogen bond numbers being similar between force fields yet the lipid head-chlorhexidine contacts being different. The similarity between the numbers of hydrogen bonds between force fields suggests that both force fields are appropriate for measuring this aspect of the membrane-chlorhexidine interaction.

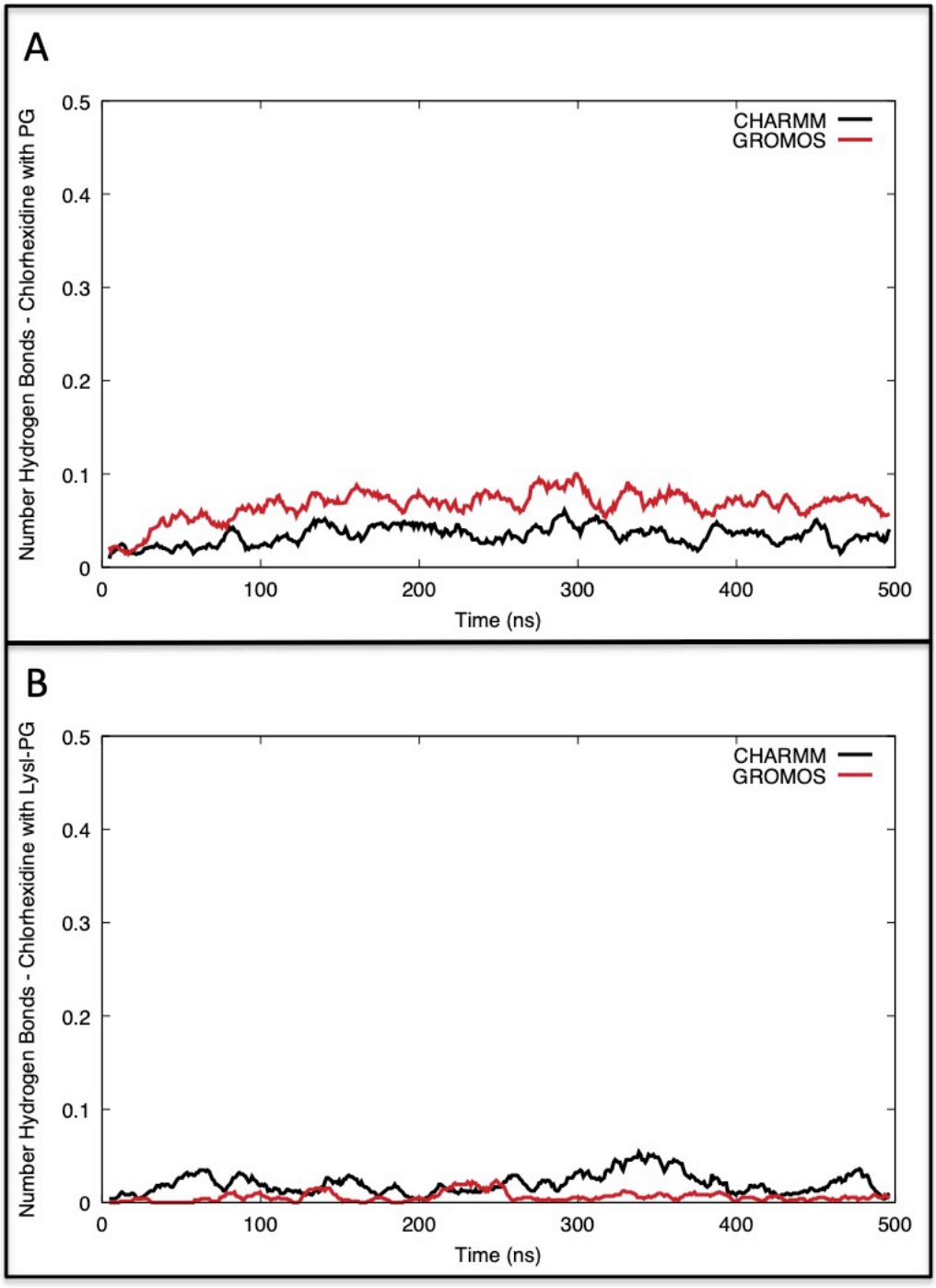

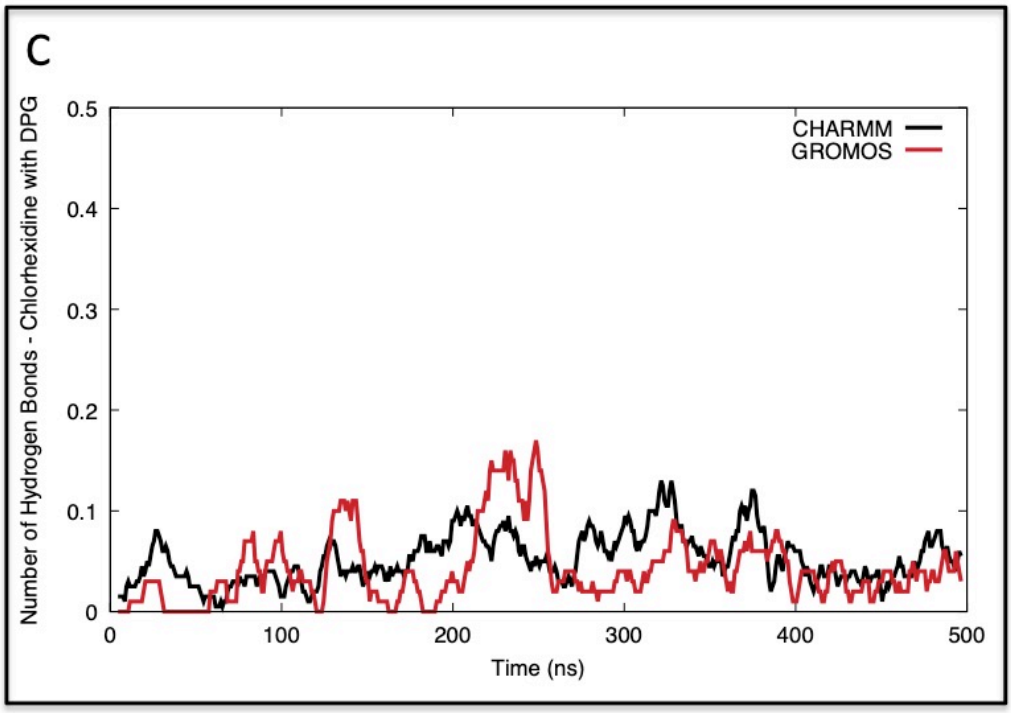

Figure 5.8: Hydrogen bonds between chlorhexidine and each A) PG B) Lysl-PG and B) DPG lipid on average over time. The donor acceptance distance was set to 3.0 A and the angle cut off 20 degrees.

It is important to understand the depth of insertion of chlorhexidine within the membrane, not only from the stand point of understanding the mode of action of chlorhexidine, but also whether seeing this mechanism is force field dependent. Therefore, the number of contacts between chlorhexidine and the lipid heads and tails less than 0.6 nm was measured over time (ns), Figure 5.9. The data was normalised due to there being more lipid tails than heads. Overall, the most contacts occured between the chlorhexidine and lipid heads in the CHARMM system whilst the least contacts happened between chlorhexidine and the lipid tail in the same force field. This shows that in the CHARMM simulation, chlorhexidine clearly sits comfortably within the head region of the bilayer but is not favourable or capable to enter any further. Notably, by the end of the simulation there were almost as many contacts between chlorhexidine and lipid tails in the GROMOS simulation as with head groups in the CHARMM simulation. Furthermore, there is a clear point in the GROMOS

simulation where the number contacts between chlorhexidine and the lipid tails over took the number of contacts with the lipid heads at around 300 ns. From this point the number of chlorhexidine head contacts dropped whilst the tail contacts continued to rise. This suggests that the GROMOS force field allows for chlorhexidine to penetrate deeper than can be seen in the CHARMM force field. However, it should be noted again that in neither force field did the chlorhexidine cross the membrane nor did it enter the centre of the bilayer.

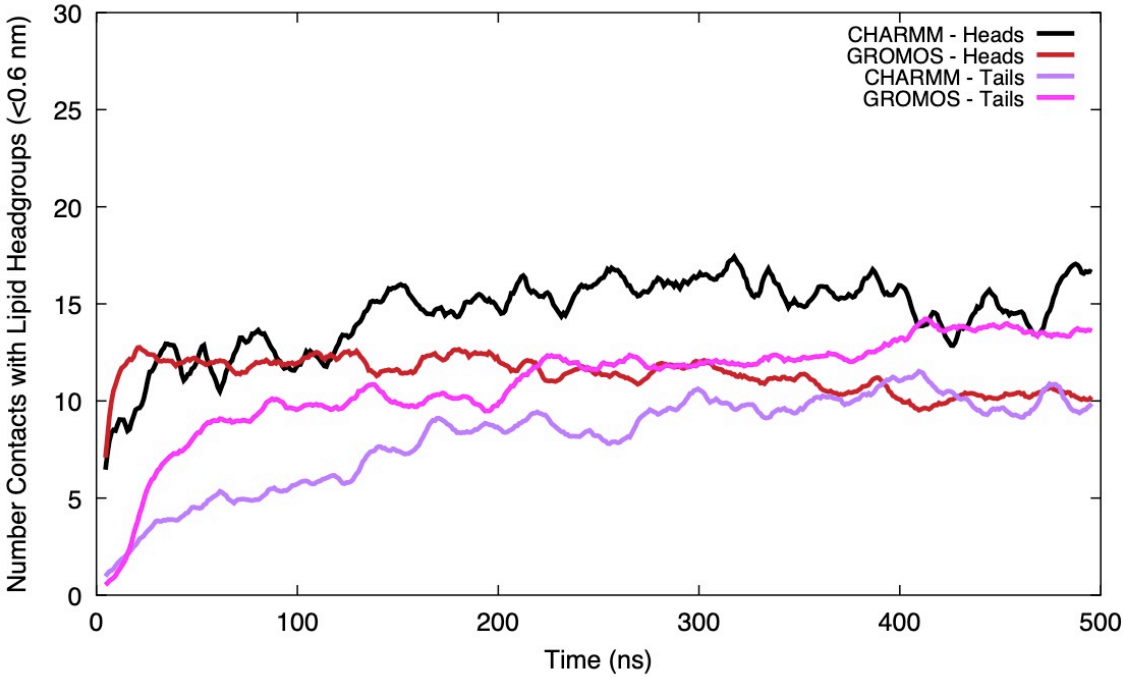

Figure 5.9: The average number of contacts less than 0.6 nm between chlorhexidine and lipid heads and tails over time. This was normalised due to the greater number of tails than heads. The force fields are shown above.

In addition to contacts with between chlorhexidine and components of the bilayer, the numbers of contacts less than 0.6 nm between chlorhexidine and Ca2+ in each system was measured, Figure 5.10. It would be expected that there would be few contacts between chlorhexidine and cations due to the cationic nature of chlorhexidine. However, comparing these contacts between the force fields shows that chlorhexidine comes into close contact more regularly with cations in the CHARMM force field than the GROMOS force field. The few contacts that occurred in the GROMOS were prior to the point of

insertion suggested previously, Figure 5.9. This may account for the similar SASA values being very similar between systems despite chlorhexidine clearly entering the membrane more deeply in the GROMOS simulation. It may be that the interactions seen in this analysis were reducing the SASA of chlorhexidine. Furthermore, as it would not be favourable for chlorhexidine to come into close contact with Ca^{2+} ions, GROMOS may better represent the charges involved in these systems; particularly as even when chlorhexidine is in solution at the beginning of the simulation there are less of these contacts in the GROMOS system than CHARMM.

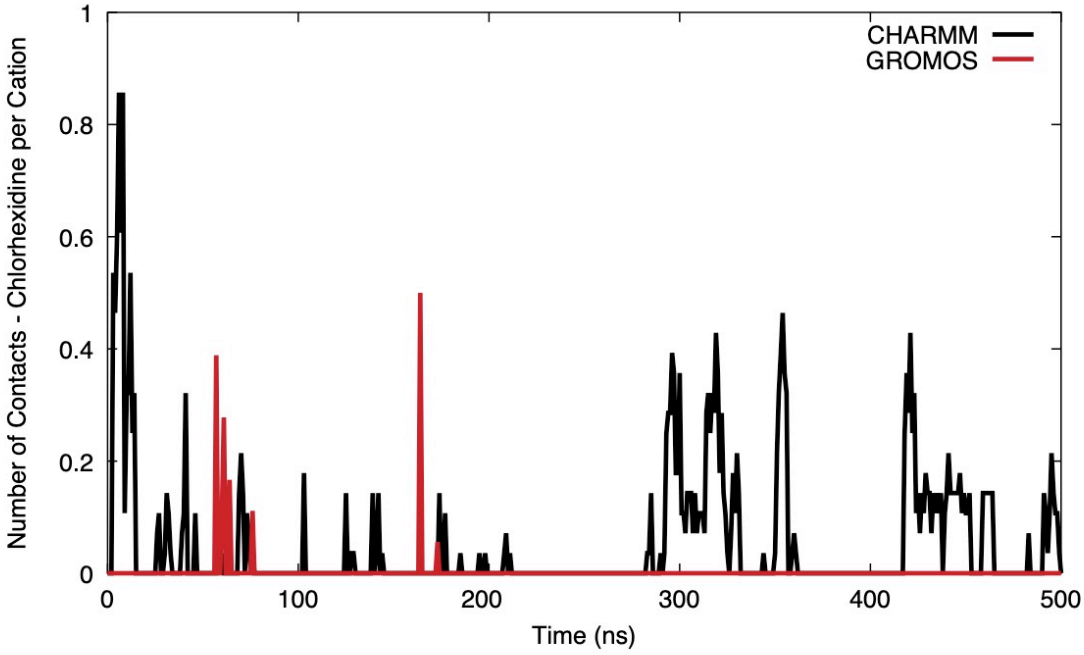

Figure 5.10: Average number of contacts between chlorhexidine and cations over time. This data was normalised to each chlorhexidine with an average ion due to the different availability of ions in each simulation. The force fields are shown above.

In order to better understand the conformation of chlorhexidine in each system throughout the simulation the distance between the chlorine atoms on the ends of each molecule was measured for each and averaged, Figure 5.11. Overall, past the 200 ns point of the simulations, at which chlorhexidine had at least entered the head group regions of the bilayer in both force fields, the chlorine atoms come into closer contact in the GROMOS simulation suggesting

that the chlorhexidine molecule is bent at the hexamethylene bridge which may be allowing the positively charged areas of the molecule to interact with the negatively charged. This conformation is supported by other simulation work[125]. The previous evidence has shown that chlorhexidine enters the membrane more thoroughly and causes greater disruption to the membrane in the GROMOS simulation, which may be an effect of the chlorhexidine taking this favourable conformation in this force field.

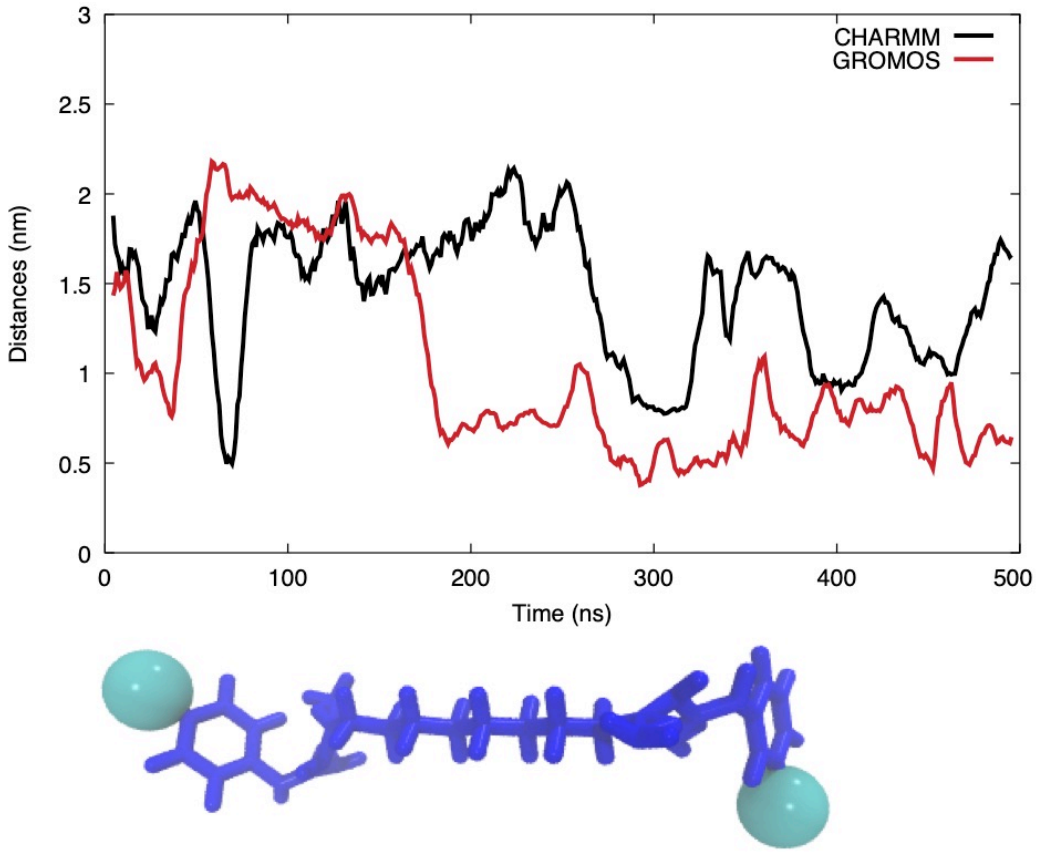

Figure 5.11: Average distance between chlorine atoms (cyan) on either end of each chlorhexidine (blue) in each simulation over time. The force fields are shown above.

The final analysis of this section involved tracking the Z-coordinates of four random chlorhexidine molecules in each system in relation to the Z-coordinates of the phosphates of the upper and lower leaflet over time, Figure 5.12. This aimed to show whether the depth of penetration was in fact different between force fields as suggested by the previous analysis. Note that the jumps across the membrane are due to periodic boundary effects rather than the chlorhexidine molecules crossing the membrane. From this it can be seen that the insertion depth of chlorhexidine is more in the GROMOS system than the CHARMM system. Furthermore, it appears in the GROMOS system that upon insertion of the molecules they stay within the membrane. Compared to the CHARMM molecule 4 which completely entered the head groups then comes out again, suggesting chlorhexidine is not stably inside the lipid heads as compared to GROMOS.

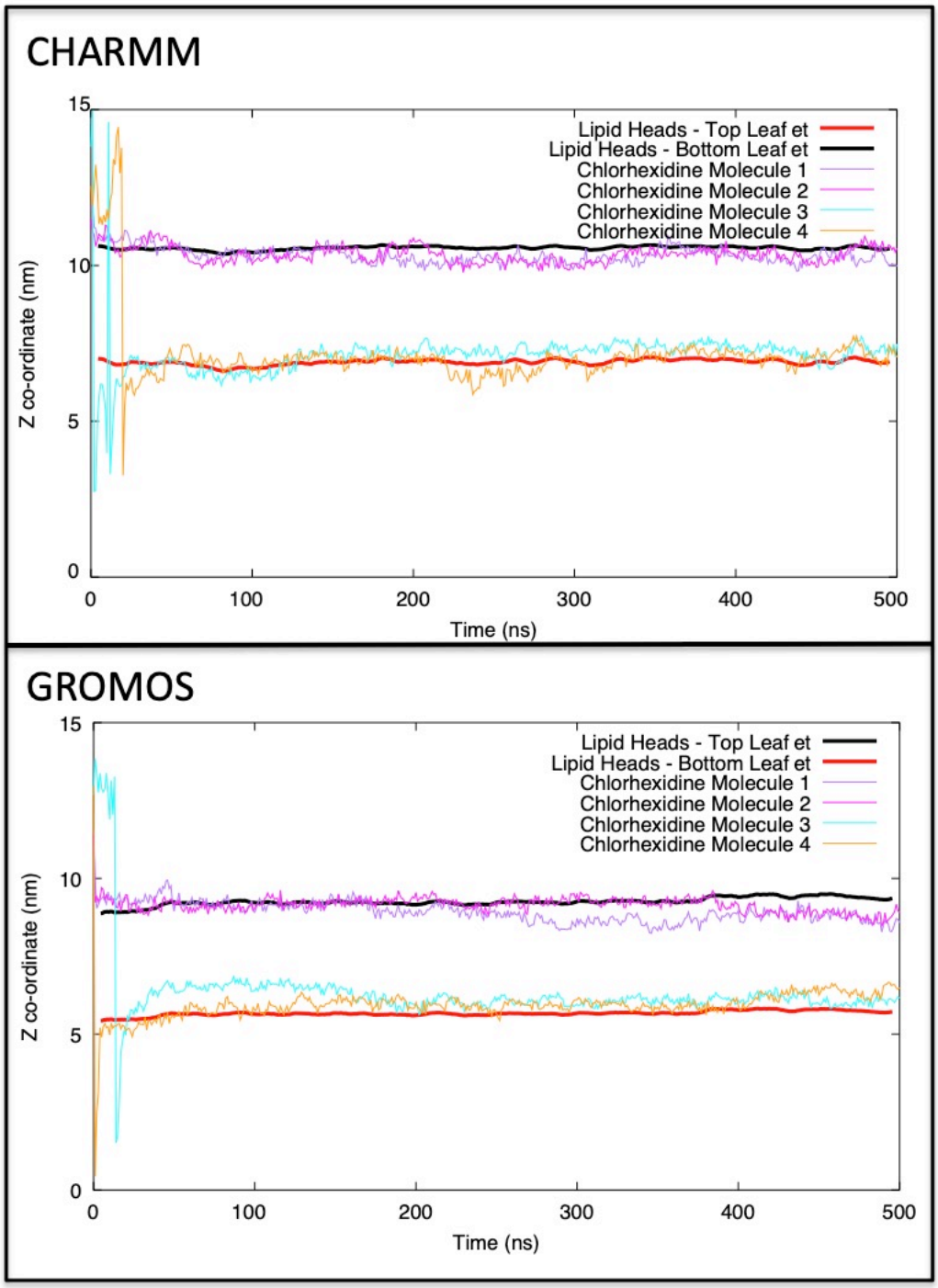

Figure 5.12: Z coordinates of 4 random chlorhexidine molecules in each force field system in relation to top and bottom leaflet or membrane over time. Note that the jumps across the membrane at the beginning of the simulation are a remnant of PBCs and chlorhexidine does not cross the membrane.

5.2.3 Conclusions

The effect of chlorhexidine on the lipid bilayer clearly was influenced by the force field used. Overall, it appeared that using the GROMOS force field showed chlorhexidine further entering and therefore disrupting the membrane more so than using the CHARMM force field. However, some of the expected behaviours of chlorhexidine were better demonstrated by the CHARMM force field: with particular reference to the preference of chlorhexidine to interact with DPG in this simulation. Unfortunately, there is little experimental data on whether chlorhexidine is known to have a preference for a particular lipid and the assumption that DPG should be the preference is based on the known aspects of the mode of action of chlorhexidine and the charges involved. In fact, overall there is little experimental data on the intricacies of exactly how chlorhexidine works on such a zoomed scale. Therefore it is difficult to say which force field exactly is displaying the true mechanisms of chlorhexidine and highlights the importance of molecular dynamics studies to be used in conjunction with experimental data. This difference between the two force fields also highlights that whilst GROMOS may be a better force field to show the exact mechanism of chlorhexidine it does not mean it is always the most appropriate force field to use.

Notably, at no point in any of the simulations using either force field did chlorhexidine fully enter the centre of the membrane. Whilst this is in line with other simulation data, it is unclear from experimental data as to whether this is an accurate depiction of how chlorhexidine actually behaves. Chlorhexidine entering only into the head region of the lipid bilayer may support how it has been shown to cause dents in the bacterial membrane. These deformations caused by chlorhexidine initially cause the cell to be unable to proliferate at low numbers but the cell to lyse at higher numbers. Therefore the evidence seen here may support that chlorhexidine does not fully enter the membrane and does not need to for the mechanism of bacteriostatic and bactericidal effects to work.

Despite this, it is important to consider the constraints of these simulations particularly in regards to the timescales that are achievable. It could be that chlorhexidine can enter the membrane fully using both force fields and it could be the favourable position of chlorhexidine. Therefore the next work involved using electroporation techniques in an attempt to have chlorhexidine fully enter the membrane and then from this position access the effect on the bilayer.

5.3 Chlorhexidine Electroporation Simulations

5.3.1 Electroporation Background and Aims

Electroporation is a technique used in simulations of membranes. Within the GROMACS code, a pulsed and oscillating electric field can be applied according to the following equation:

$$E(t)=E_0 \exp\left[-\frac{(t-t_o)}{2\sigma^2}\right]\cos\left[\omega(t-t_0)\right]$$

Equation 5.1: E_0 is the field strength, the angular frequency $\omega=2\pi c/\lambda$, t_0 is the time at of the peak in the field strength and σ is the width of the pulse[143].

Within the scope of studying lipid bilayers, adding an electric field can allow for a pore of solvent to be forced to form within the membrane. Pore formation can allow for proteins, peptides and other relevant molecules, that usually are important, to transport across the membrane[144]. Electroporation is one of the oldest techniques for manipulating the cell membrane and has been used extensively both experimentally and within simulation[145]. Applying a pulsating electric field to the membrane has been shown to enhance the membrane permeability of the cell membrane[146]. The technique is widely used within biomedicine and biotechnology for application including sRNA cell delivery to clinical electro-chemotherapy[147,148].

In addition to the use of electroporation *in vivo* and *in vitro*, extensive simulation work of these pores being formed have been studied to better understand the dynamics of the pores themselves and to try to allow molecules to cross the membrane.[20,149,150]

This work used electroporation in order to increase the cell permeability in order to allow chlorhexidine to transport further into the lipid bilayer.

5.3.2 Methods and Simulation Set-up

The simulations carried out for the electroporation work are listed in Table 5.3 and were all neutralised using Ca^{2+} ions.

Contents of Simulation	Force field	High V/nm simulation length (ps)	Low V/nm simulation length (ns)
10 chlorhexidine, *S. aureus* membrane, 22143 H_2O, 28 Ca^{2+}	CHARMM36	3 x 800	3 x 500 ns
10 chlorhexidine, *S. aureus* membrane, 22577 H2O, 28 Ca^{2+}	GROMOS54a7	3 x 800	3 x 500 ns

Table 5.3: List of simulations with differing force fields, electric fields and ion availability.

With the exception of the applying of the electric field, the simulation protocol for both force fields was the same as the previous section of work. The same analysis tools were also used. The electric field was applied in the Z-direction initially at a voltage of 0.40 V/nm^2 for 800 ps until a pore formed. This was then lowered to 0.04V/nm^2 still in the Z-direction, as the membrane would collapse if such a high electric field were maintained. This protocol is line with other simulation work[20]. The same chlorhexidine and *S. aureus* membrane model was used as for the previous work.

5.3.3 Results

The snapshots below, Figure 5.13, show the two electroporation systems at 800 ps, when pore formation occurred at the high electric field value (0.40 V/nm). At this point, there was clearly a larger pore in the GROMOS simulation than the CHARMM. Chlorhexidine was not pulled into the membrane by the pore formation in either simulation. The snapshots at the end point of the low electric field simulation (0.04 V/nm), Figure 5.14, shows the pore collapsed in both force fields and did not pull the chlorhexidine into the membrane at this stage either. However, chlorhexidine appears to have further entered the membrane again in the GROMOS simulation.

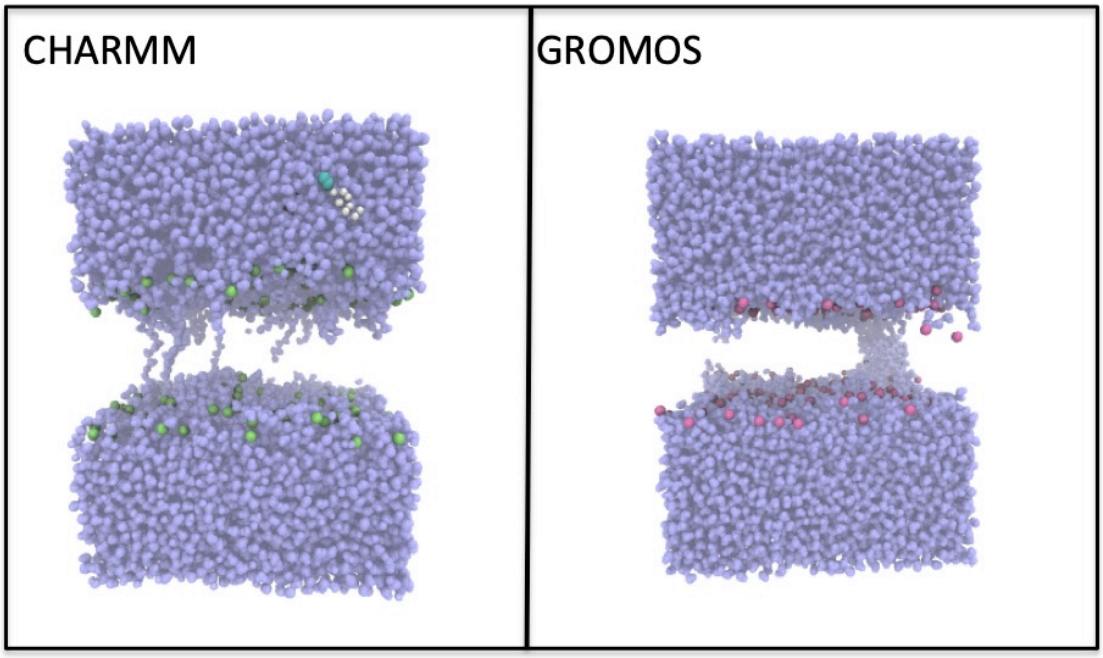

Figure 5.13: Snapshots of pore formation in electroporation simulations. The phosphate heads are shown in lime green and pink for CHARMM and GROMOS systems respectively, whilst chlorhexidine is in cyan, blue and white and water in lilac. Lipid tails have been omitted for clarity. The force fields are shown above.

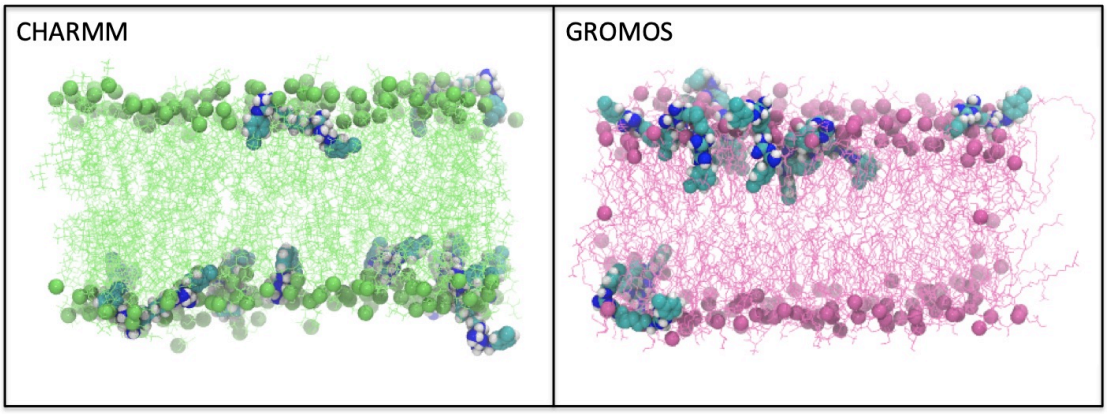

Figure 5.14: Snapshots of end point of low electric field simulations, 500 ns. Lipids are shown in lime green and pink for CHARMM and GROMOS systems respectively, whilst chlorhexidine is in cyan, blue and white. Water and ions have been omitted for clarity. The force fields are shown above.

The densities of the lipid components, chlorhexidine and solvent were again measured in the Z-dimension, Figure 5.15. In regards to the CHARMM simulation, chlorhexidine appears to have entered slightly further into the membrane in the electroporation than the equilibrium simulation. Whereas the position of chlorhexidine in the bilayer in the GROMOS simulation seems largely unchanged between the equilibrium and electroporation simulations.

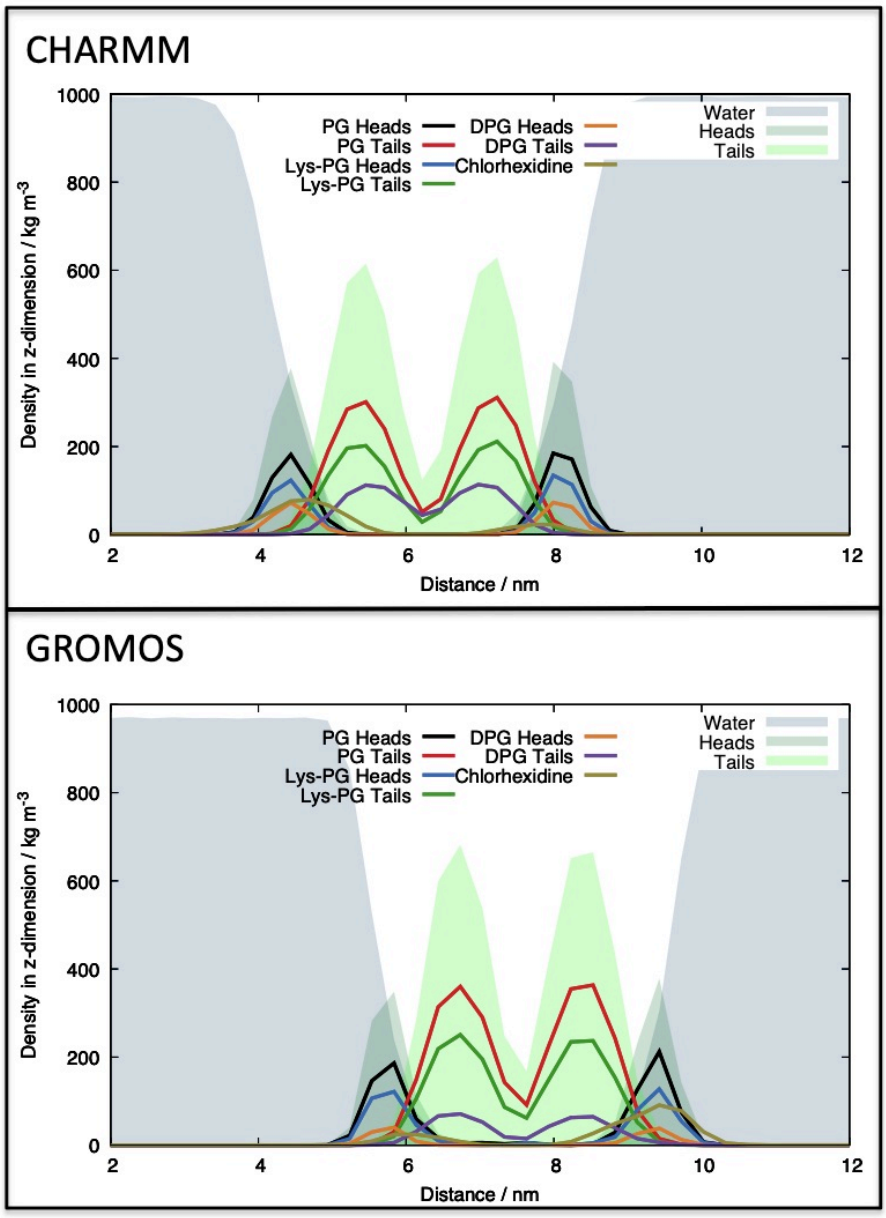

Figure 5.15: Densities of chlorhexidine, lipid head-groups and tails and solvent. This was calculated for the last 20 ns of the simulation. The force fields are shown above.

The membrane thickness was also measured for the electroporation systems, Figure 5.16. The GROMOS membrane had more darker, thin, patches within the membrane when an electric field had been applied. The CHARMM electroporated membrane seemed slightly darker and therefore thinner than the equilibrium membrane suggesting the electroporation is having an effect on the membrane. Further analysis was required to confirm how much this membrane thinning from the equilibrium simulations, particularly for the GROMOS simulation, was an effect of the electric field, the chlorhexidine molecules or a combination of the both with the electric field aiding in showing the mode of action of chlorhexidine.

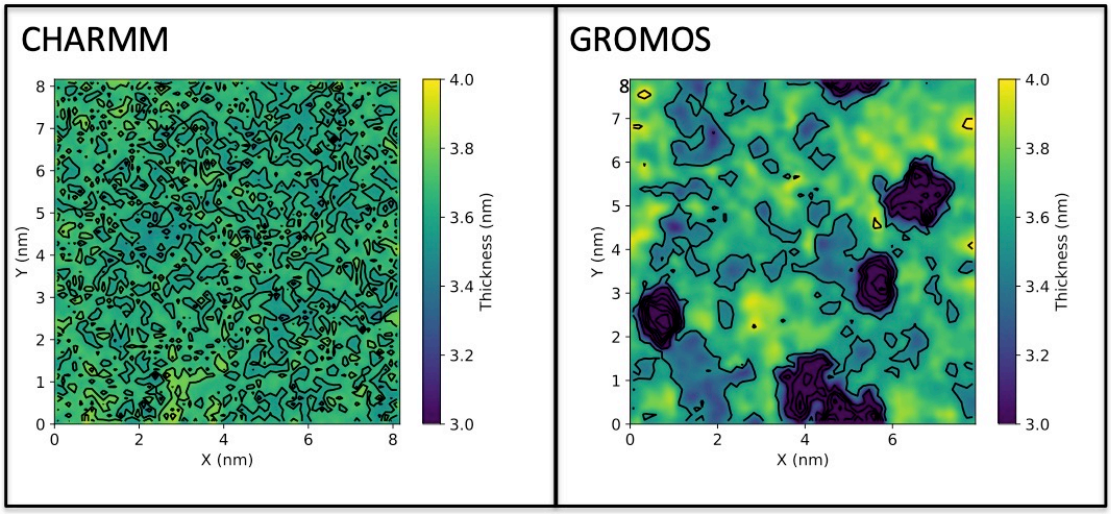

Figure 5.16: Membrane thickness of each electroporation simulation. The force fields are shown above.

The deuterium order parameters were measured for the acyl chains of the lipids in each membrane whilst being simulated with an electric field. This is shown in the Appendix, Figure A.3. This showed little difference compared to the systems at equilibrium, most probably due to the pores collapsing in both systems.

The density of the phosphates of the lipid head groups were again measured, Figure 5.17. There is a significant difference in the membranes from these figures with lipid head groups appearing to be pulled into the centre of the membrane in the GROMOS simulation. This effect was not seen in the CHARMM

simulation and may suggest that GROMOS further entered the membrane in this setup or that the electric field had a larger effect on the GROMOS simulation. However, this process of lipid heads flipping into the membrane whilst an electric field is in use was previously shown to happen using the GROMOS force field[20].

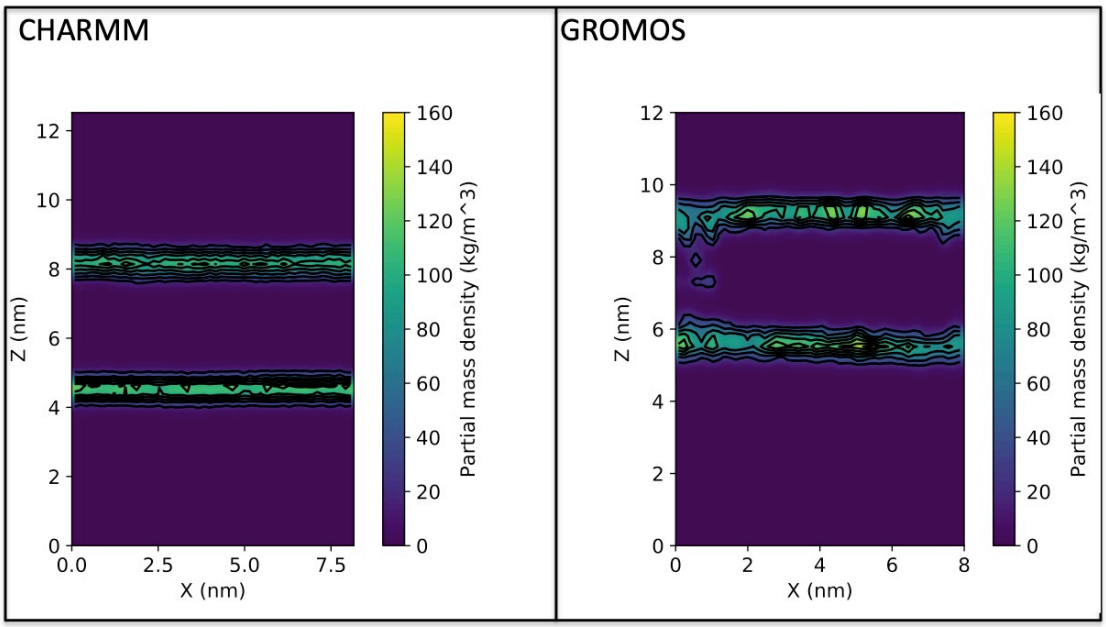

Figure 5.17: Phosphate density of lipid head groups' phosphates in y-direction in electroporation simulations. The force fields are shown above.

The number of average contacts between each lipid type and chlorhexidine less than 0.6 nm were measured over time, Figure 5.18. Collectively, chlorhexidine contacted lipid heads around the same amount for both force fields. The contacts between each lipid type and chlorhexidine remained largely similar in the GROMOS simulations between the equilibrium and electroporation simulations. However, the previously shown preference for chlorhexidine to heavily prefer contacts with DPG in the CHARMM force field was not shown here with there being little difference between the contacts with each lipid type. Whilst chlorhexidine in the GROMOS force field showed a clear preference to interact with PG and DPG as would be expected due to the charges.

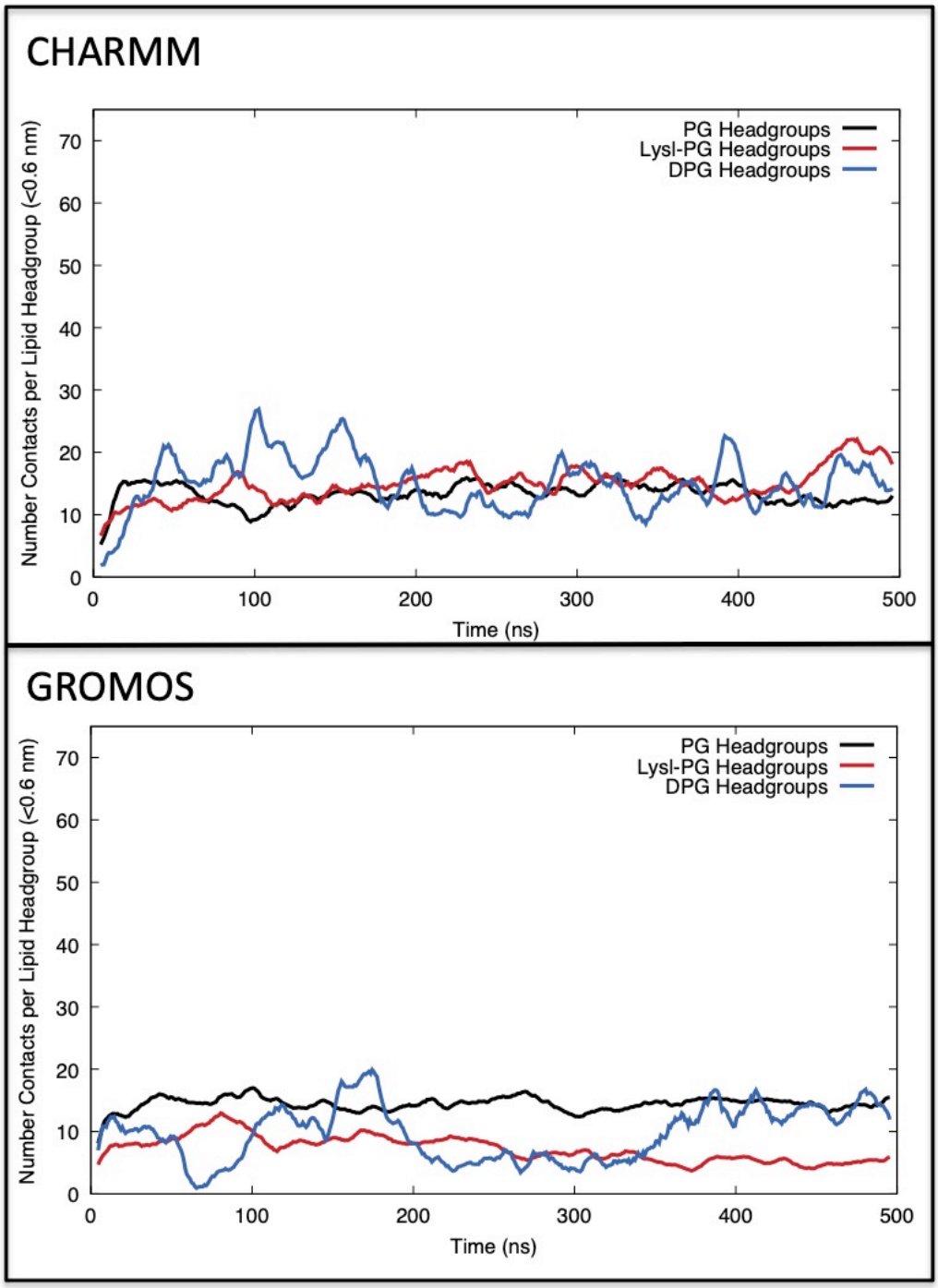

Figure 5.18: Average number contacts between chlorhexidine and different lipid head-groups over time. This has been normalised to per lipid due to the differing numbers of each lipid type in the membrane. The force fields are shown above.

The number of hydrogen bonds formed between chlorhexidine and each lipid type was measured over time (ns) for both force fields, Figure 5.19. This data was normalised to represent the different number of each lipid within the bilayer. Firstly, chlorhexidine using GROMOS made more hydrogen bonds with PG in comparison to when the CHARMM force field was was used. This would be expected based on the previous contact analysis. The hydrogen bonds between chlorhexidine and Lysl-PG was similar between force fields and over all occurred less than between chlorhexidine and PG and DPG. This would be anticipated due to the positive charge of chlorhexidine and Lysl-PG. The highest number of hydrogen bonds for both force fields occurred between chlorhexidine and DPG however it would be assumed these hydrogen bonds were short lived as the data has more spikes than with PG and Lysl-PG.

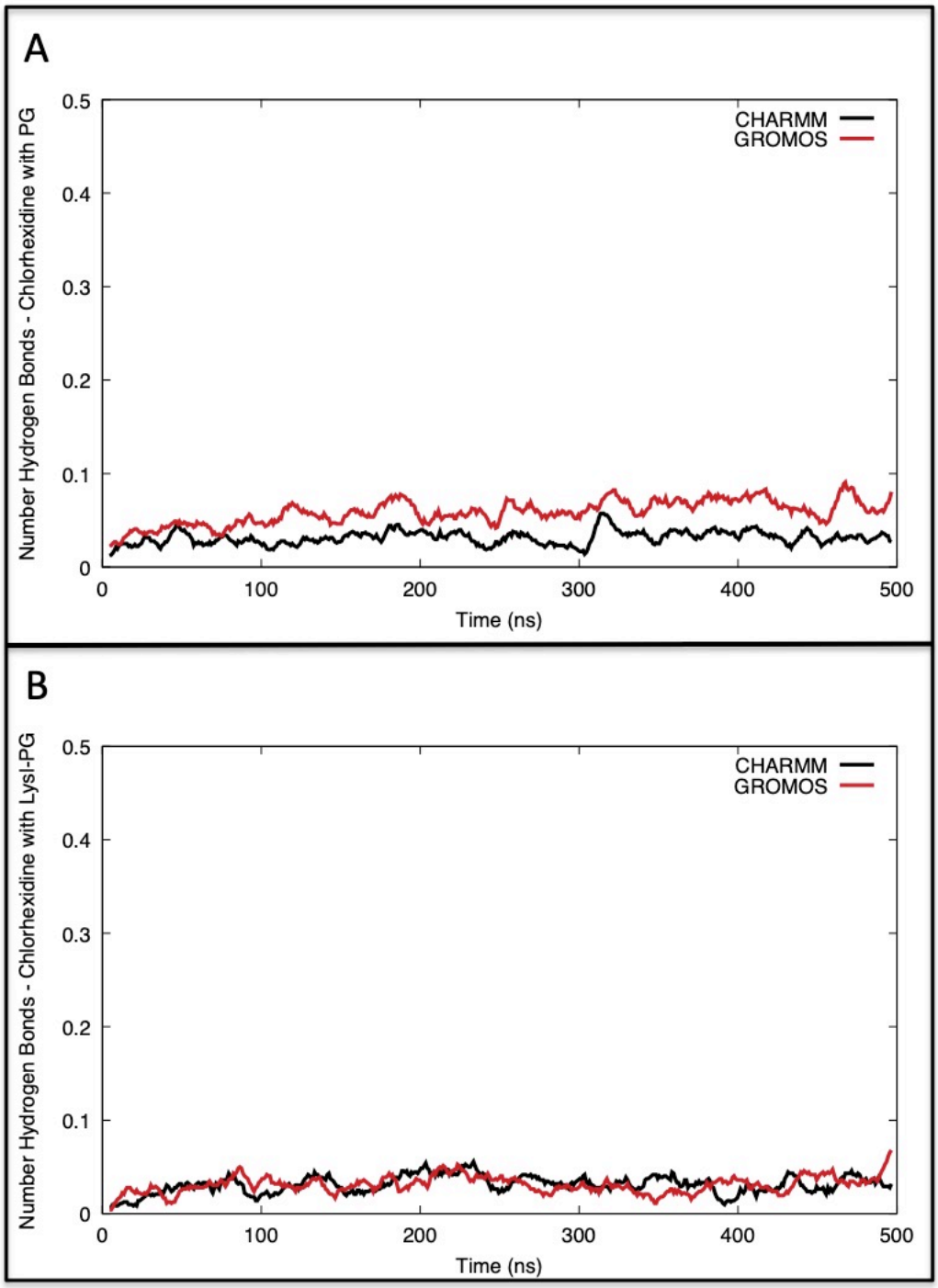
A
Number Hydrogen Bonds - Chlorhexidine with PG
0.5
0.4
0.3
0.2
0.1
0
0
100
200
300
400
500
Time (ns)
CHARMM
GROMOS
B
Number Hydrogen Bonds - Chlorhexidine with LysI-PG
0.5
0.4
0.3
0.2
0.1
0
0
100
200
300
400
500
Time (ns)
CHARMM
GROMOS

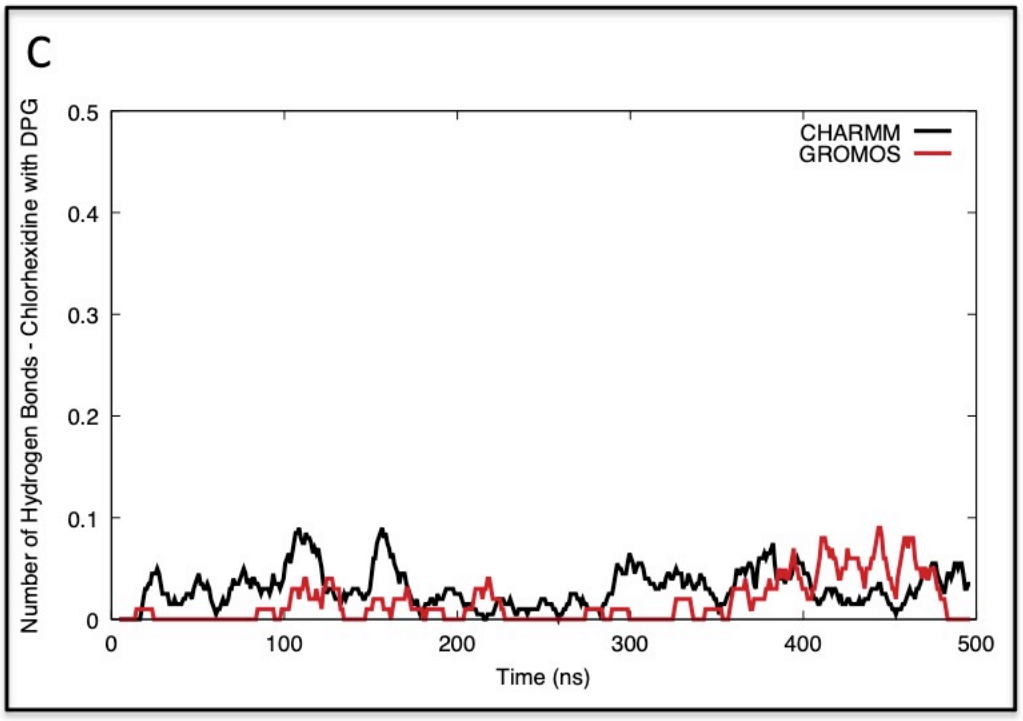

Figure 5.19: Number of hydrogen bonds between chlorhexidine and each A) PG B) Lysl-PG and C) DPG lipid on average over time. The data has been normalised to represent the different number of lipids available in each system. The donor acceptance distance was set to 3.0 A and the angle cut off 20 degrees.

The APL was measured over time, Figure 5.20. Between force fields there was little difference in the APL of the membranes, they both started higher and drop due the decrease in the electric field from 0.40 V/nm to 0.04 V/nm, causing the pore to collapse. After this point, the APL was broadly similar, at around 0.67 nm^2.

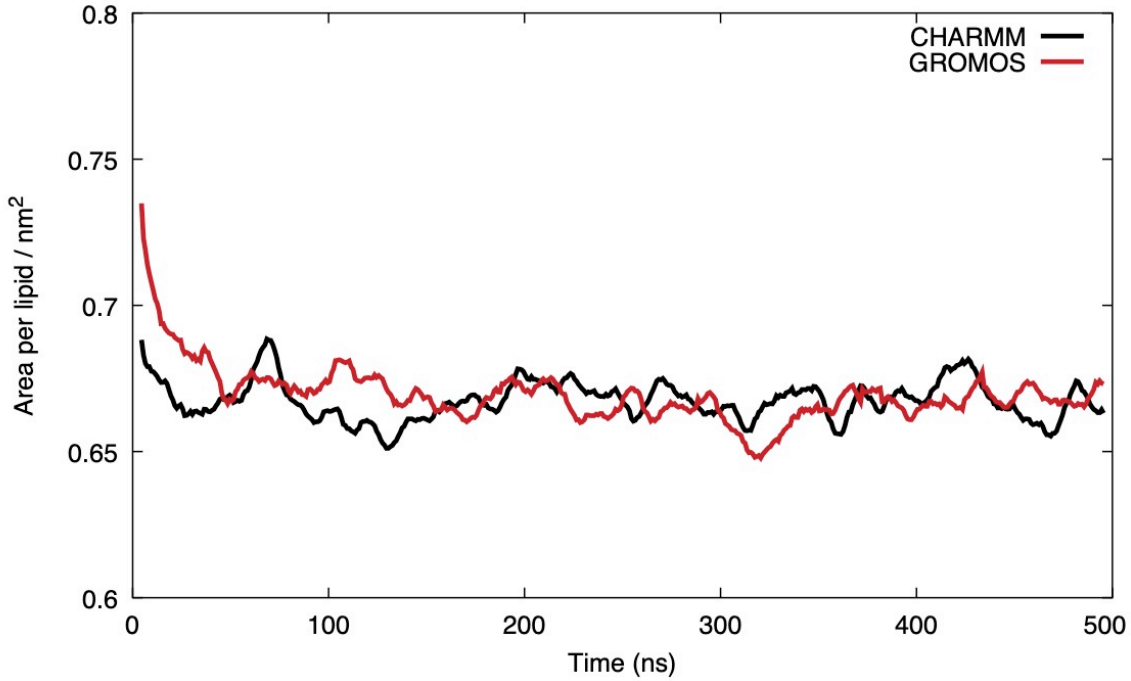

Figure 5.20: APL over each electroporation simulation over time. The force fields are shown above.

Furthermore, Figure 5.21 shows the SASA of chlorhexidine measured over time. The SASA was very stable and similar over the simulation for both systems. However, the SASA was less in the electroporation simulations than the equilibrium simulations suggesting that chlorhexidine is entering further into the membrane in both force fields using the electric field and may have caused the disruption previously discussed. Furthermore, as the SASA was very static throughout the simulations for both force fields, this would suggest that chlorhexidine entered the bilayer during the initial high electric field portion of the simulations. This may suggest that electroporation may speed up the entering of chlorhexidine.

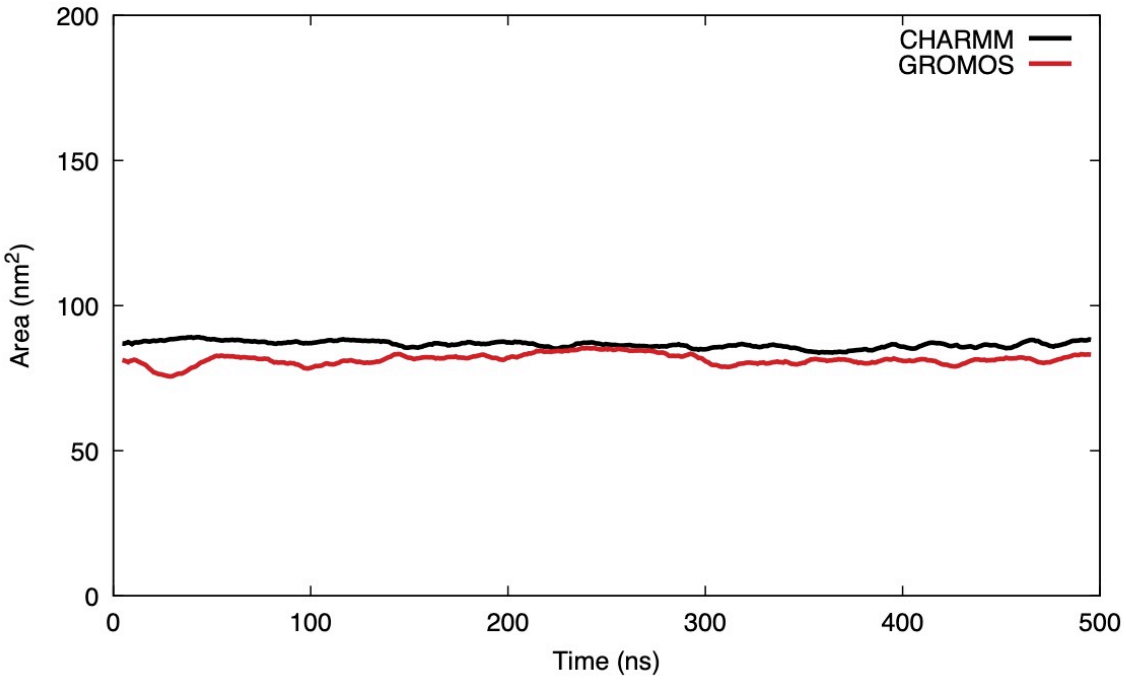

Figure 5.21: SASA of chlorhexidine over time in each electroporation simulation. The force fields are shown above.

In order to estimate the depth of insertion of chlorhexidine in these electric field simulation, the number of contacts <0.6 nm between chlorhexidine and the lipid heads and tails over time using each force field, Figure 5.22. Overall, this showed the most contacts between chlorhexidine and head groups in the CHARMM force field and with tails in the GROMOS force field. This suggests that GROMOS still allowed for chlorhexidine to enter the membrane more deeply into the bilayer than in CHARMM in both the equilibrium and electroporation setups. Overall, the contacts were similar for both the electroporation and equilibrium setups for both force fields suggesting that the electric field did not allow for chlorhexidine to further enter the membrane.

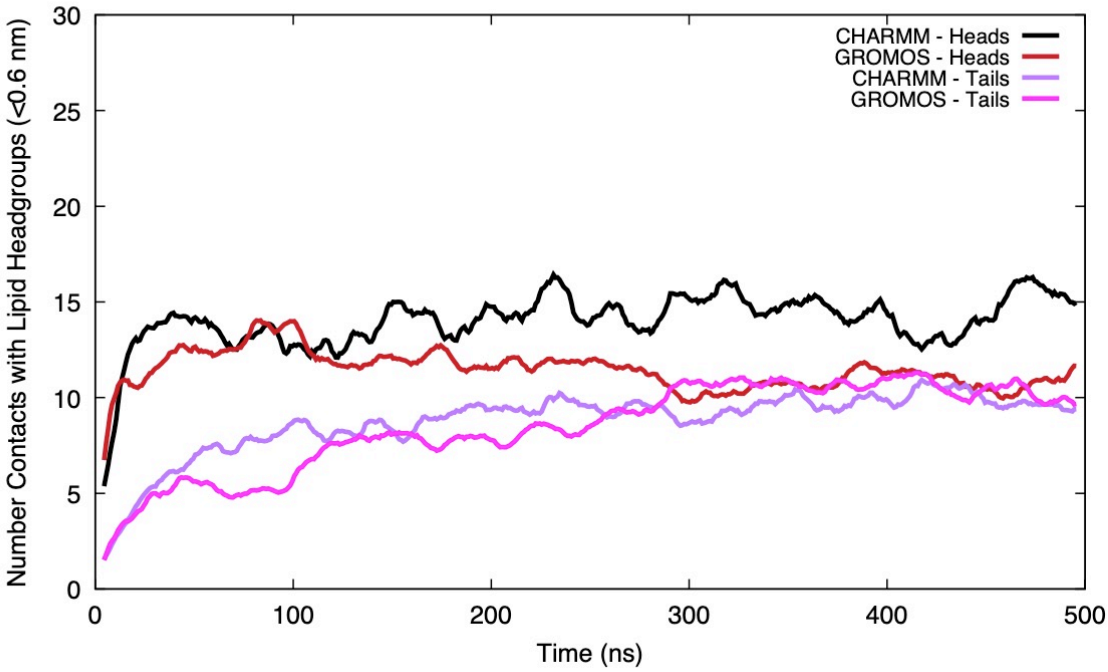

Figure 5.22: The average number of contacts less than 0.6 nm between chlorhexidine and lipid heads and tails over time. This was normalised due to the greater number of tails than heads. The force fields are shown above.

Finally again the Z-coordinates of four random chlorhexidine molecules in each system in relation to the Z-coordinates of the phosphates of the upper and lower leaflet over time were tracked, Figure 5.23. In both simulations, chlorhexidine only entered the head region of the bilayer as supported by previous analysis.

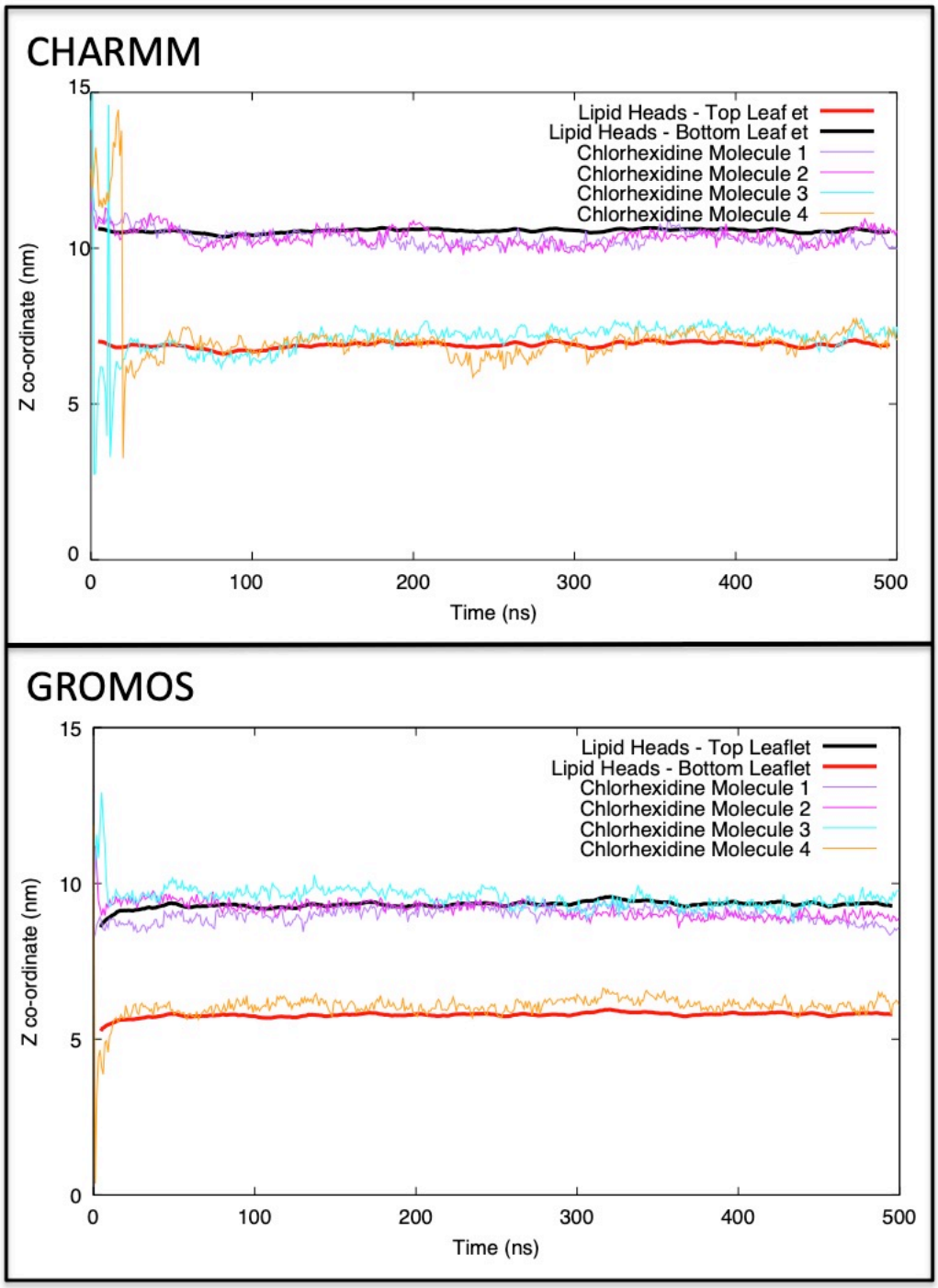

Figure 5.25: Z-coordinates (nm) of 4 random chlorhexidine molecules in each force field system in relation to top and bottom leaflet or membrane over time in electroporation simulations. Note that the jumps across the membrane at the beginning of the simulation are a remnant of PBCs and chlorhexidine does not cross the membrane.

5.3.4 Conclusions

Whilst there are differences between the force fields, in both, chlorhexidine never fully entered the bilayer, even when applying an electric field increased membrane permeability. As this is consistent between force fields, this may suggest that chlorhexidine does not need to fully enter the membrane in order to stop bacterial growth or kill bacteria. This could be why chlorhexidine has such broad efficacy against many microorganisms, not just bacteria, as phospholipid bilayers are quite similar between microorganisms.[114] It may also explain how chlorhexidine works so quickly as exposure does not need to be long if chlorhexidine need only sit in the lipid head area to cause an effect on the bacteria.

Finally, the differences between the force fields are difficult to untangle without further experimental work. There is little experimental work aimed at understanding molecular properties of realistic membranes like the membrane neither used here nor work with chlorhexidine studying similar parameters. Due to this it is difficult to say which force field is most accurate and shows the importance of force field development in conjunction with experimental data to allow for the most accurate simulation work to be conducted.

Chapter 6 - TCP Co-aggregation in Presence of Bacterial Products

6.1 Introduction

Regardless of the cause, all wounds are at risk of being contaminated by bacteria, which can result in an infection. It is therefore integral for the survival of the host to be able to counteract a bacterial infection and as such, hosts have developed defence systems. Upon initial bacterial infection, the host's innate immune response is engaged which causes the subsequent action of many proteins and peptides[151]. In humans, aspects of the innate immune system include neutrophil-derived alpha-defensins in addition to plasma proteins such as thrombin[152,153]. Toll-like receptors (TLRs) are responsible for recognising pathogen-associated molecule patterns (PAMPs) then recruiting adaptor proteins that in turn are responsible for the subsequent activation of other downstream cascades. This ultimately leads to the orchestration of inflammatory responses and other events such as cytokine production[154]. In the case of bacterial ligands being presented to TLRs, it can lead to the pathogen being phagocytosed, as well as its antigens presented to CD4+ T cells, which is important for the host developing an adaptive immune response[155].

There are many different types of PAMPs and these trigger different TLRs. Gram-negative component LPS triggers TLR4 whilst Gram-positive LTA triggers TLR2[156]. The TLR4 relay response to bacterial LPS is shown in Figure 6.1. It shows LPS binding to LPS binding protein (LBP). This is then transferred to CD14 then myeloid differentiation factor 2 (MD-2), a protein essential for this relay response. This in turns presents to TLR4 in complex with MD-2. TLR4 and MD-2 binding to the bacterial agonist signals the downstream immune responses[157]. CD14 has multi-purpose activity and can transfer other ligands to other TLRs, including lipopeptides like LTA to TLR2[158].

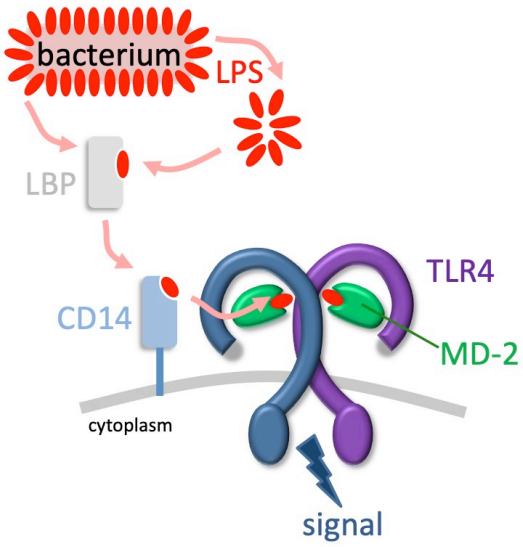

Figure 6.1: Schematic showing TLR relay for bacterial LPS recognition.

Although the sensing of bacteria and their products by TLRs is clearly critical for hosts mounting a sufficient innate and subsequent adaptive immune response, an excessive TLR response can also cause problems. Excessive TLR activation causes localised inflammation as seen in infected wounds but also severe systemic responses, which can result in sepsis[159]. Sepsis and septic shock are a significant mortality risk in intensive care units and cause around 8 million deaths per year[160]. Therefore, in addition to responding to bacterial infections, hosts must have a system to remove endotoxins to ensure a vigorous antibacterial response. Thrombin is an enzyme produced upon injury to the skin which helps coagulation of red blood cells to help seal the wound[34]. However beyond this role, thrombin is also proteolysed by human neutrophil elastase into thrombin-derived C-terminal peptides (TCPs) of differing sizes[35].

TCPs are found in wound fluids and have been shown to have antiendotoxic and antimicrobial functions. Previous work has shown 11 kDa TCPs scan aggregate LPS and *E. coli* bacteria, leading to bacterial death and consequential phagocytosis[35]. Furthermore, a recombinant 96-amino acid TCP (TCP96) has been shown to aggregate both Gram-positive and Gram-negative bacterial

envelope products including LPS and LTA[161]. This aggregation reduces inflammatory signalling caused by such components therefore downgrading the immune response. It is thought that this host mechanism is to prevent the side effects of an immune over-response such as sepsis[162].

6.2 Initial TCP Co-aggregation Simulations

This work aimed to show the molecular mechanisms of TCP96 co-aggregation in the presence of *P. aeruginosa* and *E. coli* LPS and *S. aureus* LTA and whether TCP96 aggregates in the presence of peptidoglycan (PGN) that has not been shown experimentally and therefore acted as a negative control.

6.2.1 Methods and Simulation Set-up

The CG models of TCP96 and *E. coli* LPS were taken from previously published work, with the closely related *P. aeruginosa* LPS model derived from that reported in previously[35]. This involved switching the GL0 and GL5 beads in the original *E. coli* LPS CG model and shortening the lengths of the carbon lipid tails[163]. The initial CG model for *S. aureus* LTA was initially constructed based on an atomic model kindly provided by Dr. T. J. Piggott. This model did not include the extended glycerol-phosphate units but was restricted to the hydrophobic diacylglycerol component and carbon lipid tails, which anchor LTA to the cell membrane, and are likely to be key in the aggregation of the molecule, as well as interacting with the hydrophobic TLR2 ligand-binding pocket[158]. The PGN was modelled from a PGN atomistic monomer from previous in-house work.

The contents of each simulation are shown in Table 6.1. In all systems, the proteins and microbial products were randomly placed and solvated with standard, non-polarizable Martini water particles, antifreeze (WF) and neutralizing Na^+ and Cl^- particles. The simulations were run using the Martini 2.2 bforce field at 313 K and 1 bar, which was kept constant using the Berendsen algorithms[70,133]. All simulations and analyses were carried out using GROMACS 2018, whereas rendering was performed using VMD[96,108]. BitClust was used for conformational cluster analysis; with a cut-off of 0.1 nm used to define a cluster[104].

Contents	Solvent	Length
8 x TCP molecules	10786 H_2O, 1264 WF, 16 Cl^-	5 x 1 μs
8 x TCP molecules 8 x *P. aeruginosa* LPS	10559 H_2O, 1263 WF, 16 Na^+	5 x 1 μs
8 x TCP molecules 8 x *E. coli* LPS	10693 H_2O, 1261 WF, 16 Na^+	5 x 1 μs
8 x TCP molecules 8 x *S. aureus* LTA	10694 H_2O, 1263 WF	5 x 1 μs
8 x TCP molecules 8 x PGN	10662 H_2O, 1251 WF	5 x 1 μs

Table 6.1: Contents, solvent and length of simulations conducted.

6.2.2 Results

Visualisation of the progression of the simulations is shown in Figure 6.2. From this it can be seen that TCP alone aggregates the least as evident from the largely separated TCP molecules. Whereas, the TCP simulated with both *P. aeruginosa* and *E. coli* LPS appeared to have aggregated together more closely with the LPS than TCP-only control. The simulation with *S. aureus* LTA and TCP did demonstrate aggregation, but not as tightly as seen with the LPS and TCP systems, showing two different aggregates. The system with TCP and *S. aureus* PGN did also show aggregation formation, but was more similar to the TCP only system and looked less tightly packed compared to the TCP and LPS systems. This would be in line with the experimental suggestion that PGN does not cause TCP to aggregate.

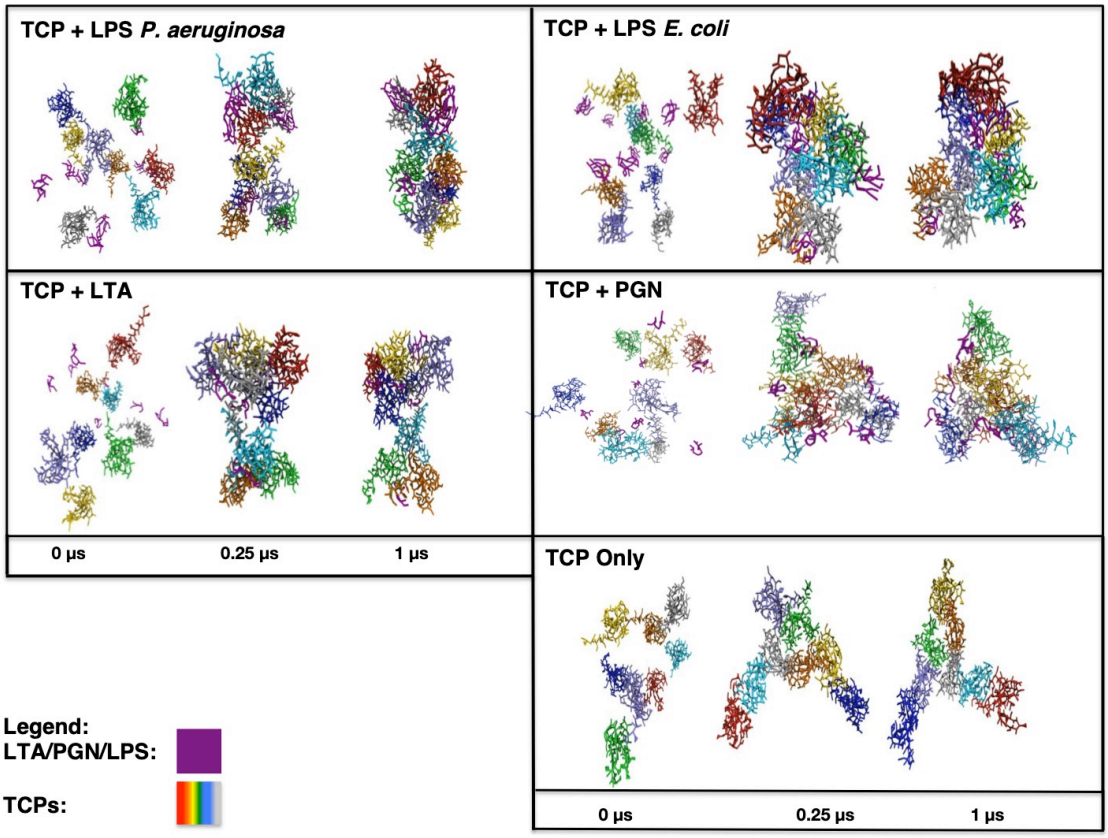

Figure 6.2: Snapshots showing progress of simulations showing point of aggregation at 0.25 µs and the end point of 1 µs. LTA, PGN and LPS are shown in purple with the TCP shown in various other colours.

Based on the visualisations, further analysis was conducted to better understand the interactions between the bacterial envelope components and TCP. The mean pair-wise intermolecular distances between TCP fragments in the presence and absence of the microbial components are shown in Figure 6.3. The TCP only system matrix seems to have overall larger distances than the others suggesting that the TCP fragments did not come into as close contact in the absence of bacterial components. Overall, the rest of the systems seem fairly comparable in patterns of colour therefore suggesting the TCP came into similar proximity in these systems.

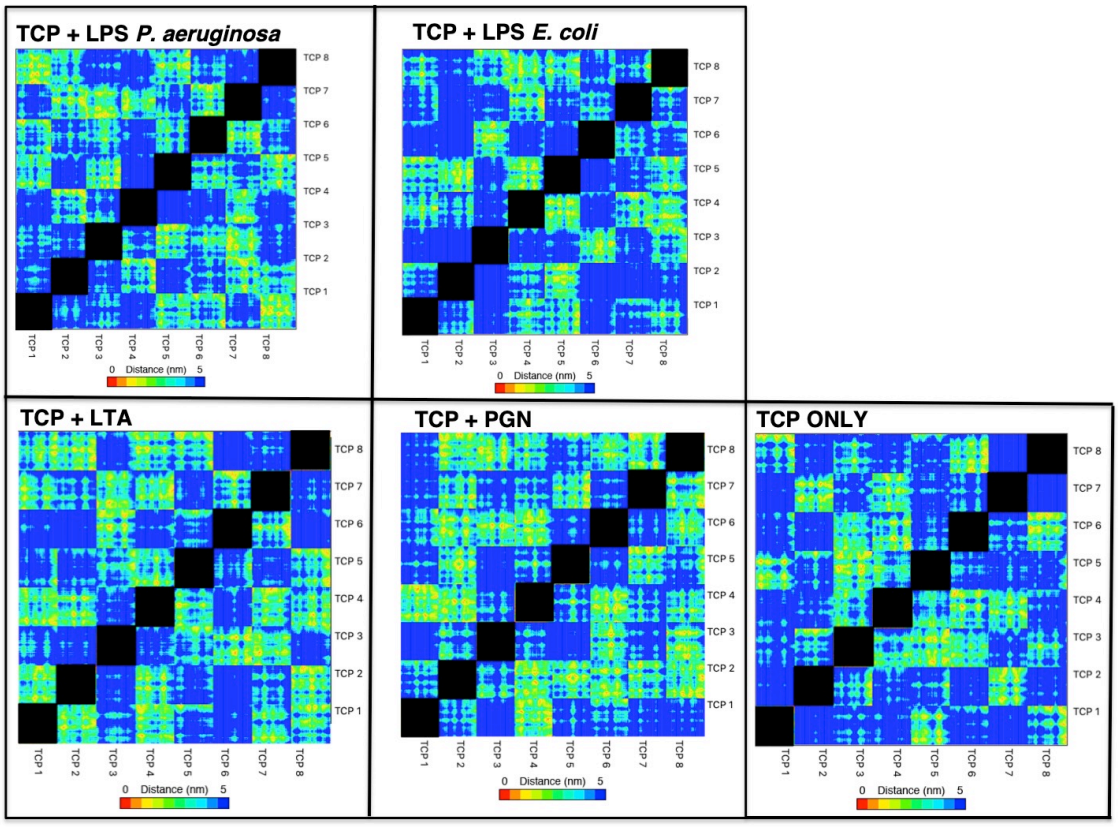

Figure 6.3: Mean intermolecular distance between TCP96 fragments following co-aggregation simulations in the presence/absence of the microbial products. The black boxes in the centre of each matrix were to omit self-contact.

The RDF was measured for the probability of TCP molecules to come within a certain distance of other TCP molecules, Figure 6.4. The control TCP-TCP interaction for the system in the absence of any microbial products is shown in each figure for comparison. For this the first peak is primarily considered

therefore TCP was likely to come into closer contact when in the presence of *P. aeruginosa* LPS and *S. aureus* PGN. Whilst the former would be expected the latter was surprising based on experimental data and it was unclear at this point the implications of this. TCP molecules were less likely to come into as close contact in the presence of *E. coli* LPS and *S. aureus* LTA than TCP alone. This analysis was measured over the total of the simulation therefore it could have been that the behaviour of the simulations was disguising the endpoint aggregation of TCP molecules as suggested by the previous analysis.

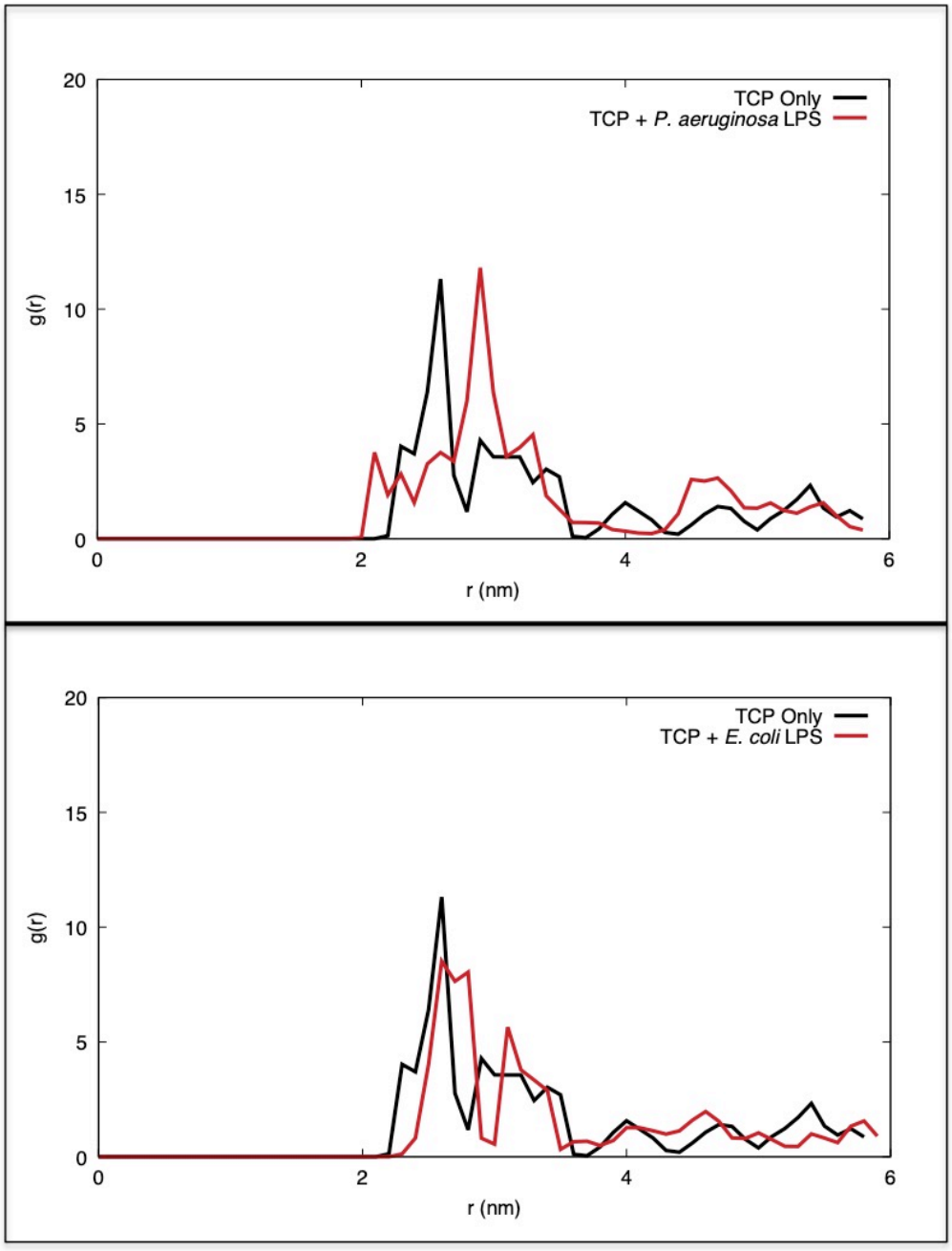

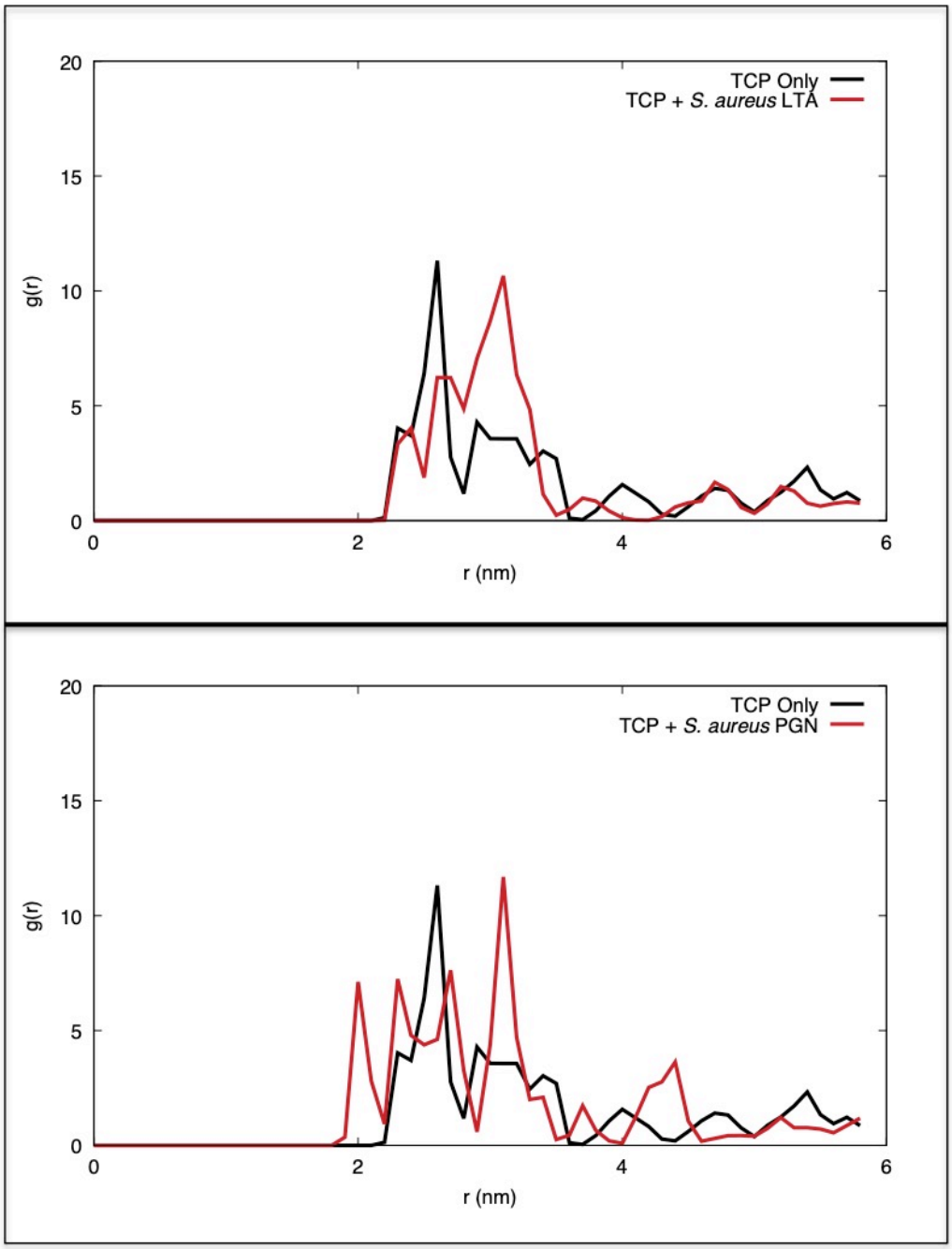

Figure 6.4: The RDF measuring the probability of TCP96 distances with other TCP96 molecules.

Based on the previous analysis, the probable distances between TCP molecules in each system were measured over 200 ns sections of the simulation and the average taken, Figure 6.5, with the standard deviation used for error bars and the P-value made in comparison to the TCP only value. This suggested that TCP came into closer contact with other TCP molecules when in the presence of *P.*

aeruginosa and *E. coli* LPS than in the absence of these products. Interestingly, this data suggested TCP aggregated in the presence of *S. aureus* PGN which was not as hypothesised. Contrastingly, TCP with *S. aureus* LTA did not aggregate as anticipated.

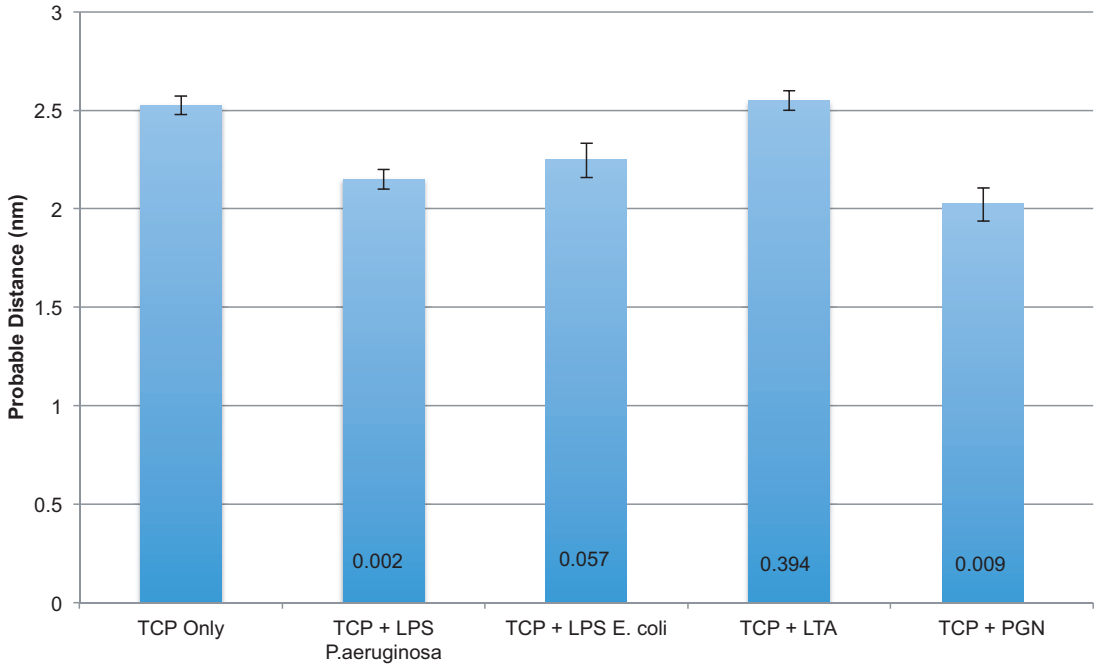

Figure 6.5: The probable average distance between TCP96 molecules in each system. This was measured for each 200 ns section of the simulation with the average shown. The P-value in reference to the TCP only probable distance shows they are all significantly different from the control. The error bars are the standard deviation taken from the averages.

Cluster analysis of the TCP conformations within in each system are shown in Figure 6.6. Notably, the most frequent clusters and RMSD distributions throughout the simulations were most similar in the TCP only system and the TCP and *S. aureus* LTA, which was previously shown to come into a similarly close contact as the control setup, with the most frequent cluster occurring in the middle of the simulation. The most frequent clusters of TCP in the systems in the presence of both LPS species both occurred towards the end of the simulation. This suggests both LPS species caused TCP to behave similarly.

Interestingly, the mean RMSD amongst clusters for TCP was within a very tight band in all setups and the common clusters generally all occurred within distinct sections of each simulation.

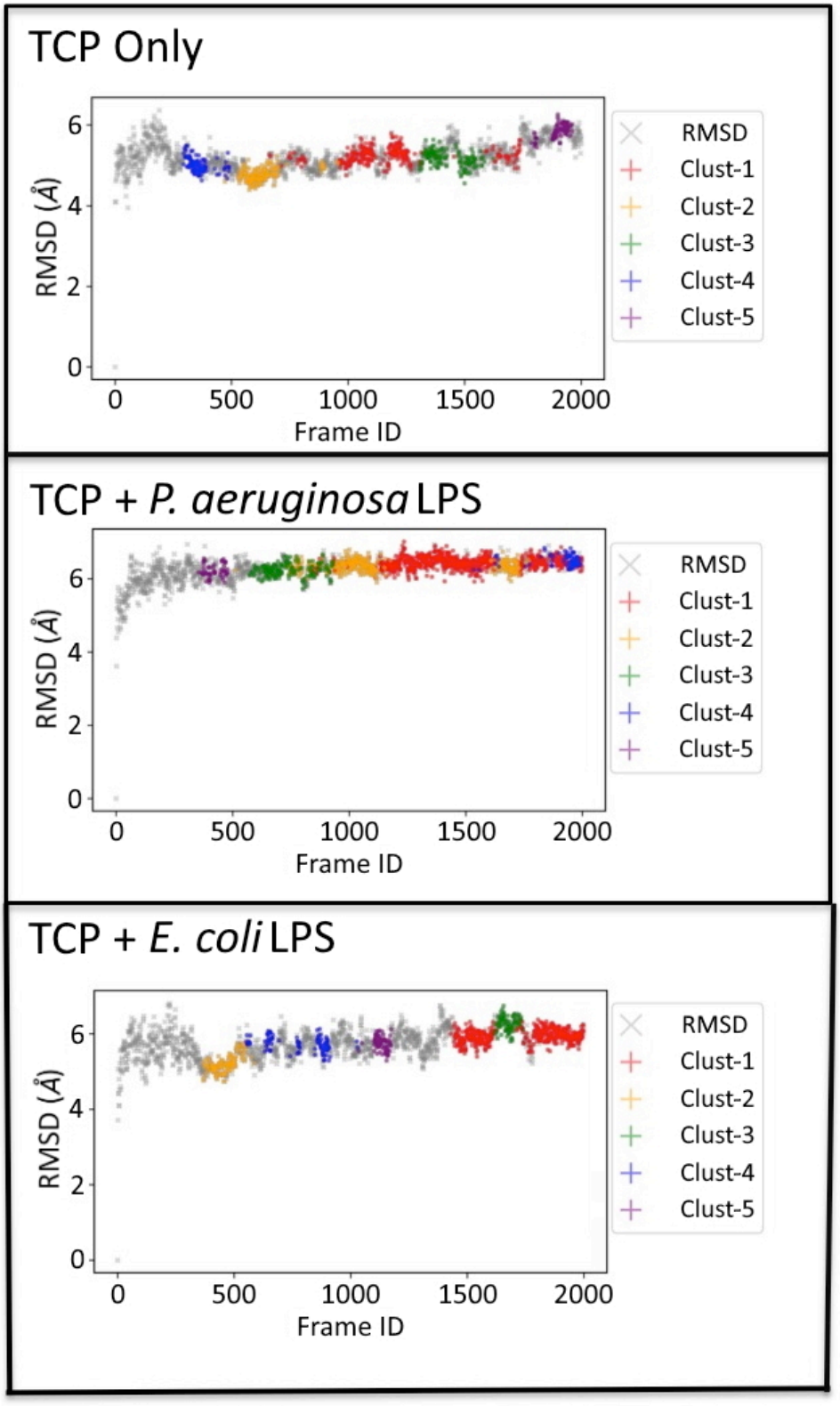

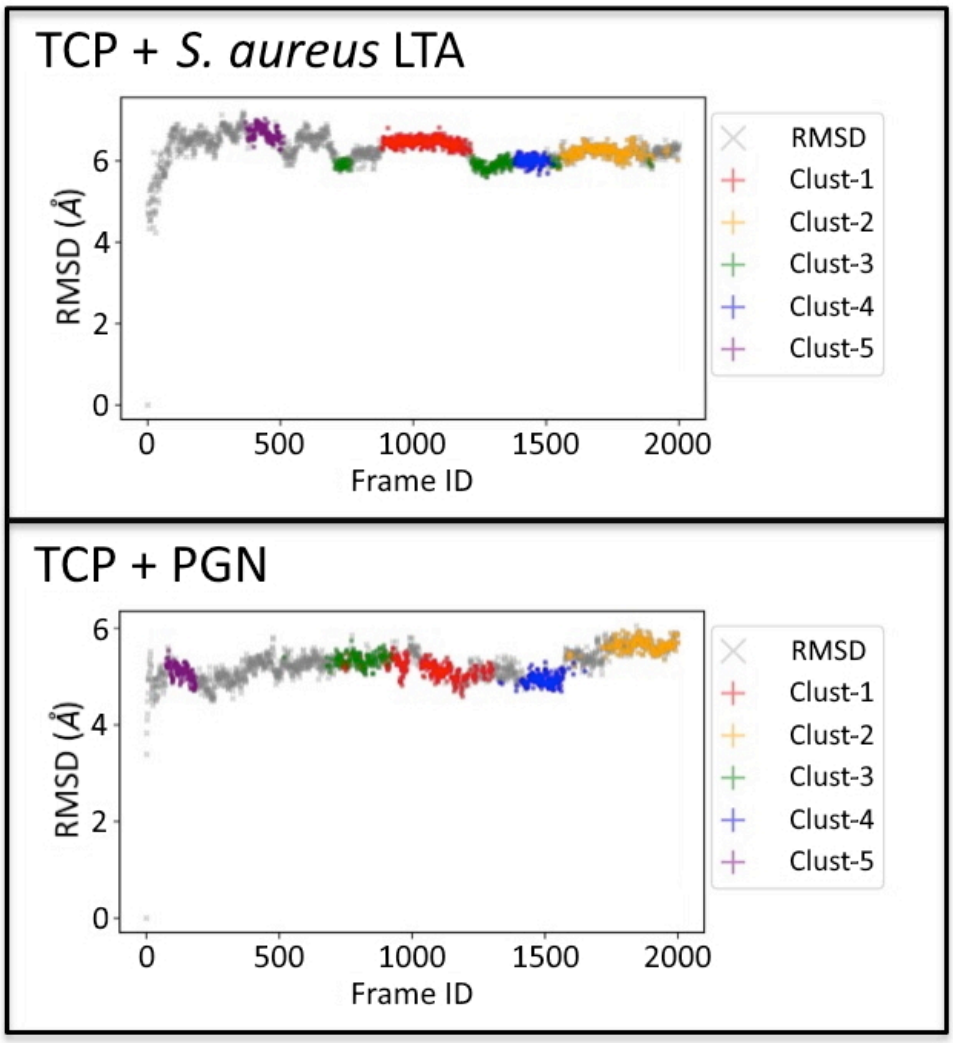

Figure 6.6: Superposition of the first five clusters onto RMSD of all frames to show the frequency of those conformations of TCP96 in the presence and absence of microbial products.

The cluster sizes of TCP in the presence and absence of the microbial products are shown in Figure 6.7. The largest cluster sizes were in the simulations with TCP and both LPS species, as supported by the previous data. However, TCP in the presence of *P. aeruginosa* LPS had fewer conformations that did not fall into a cluster than TCP in the presence of *E. coli* LPS. The largest clusters were largely similar in size in the remaining systems whilst the unclustered conformations were similar between the TCP in the presence of LTA and PGN. The similarity between the cluster analysis of the systems with LTA and PGN may suggest that TCP aggregated similarly in these systems, which would not be anticipated. It

would be anticipated TCP in the presence of LTA behaved more closely to the TCP in the presence of LPS. This showed little difference of the conformations of TCP in the presence of microbial products but was different when TCP was simulated alone. The 5 most common clusters of TCP from this work are shown in the Appendix, Figure A.4. This showed little difference of the conformations of TCP in the presence of microbial products but was different when TCP was simulated alone.

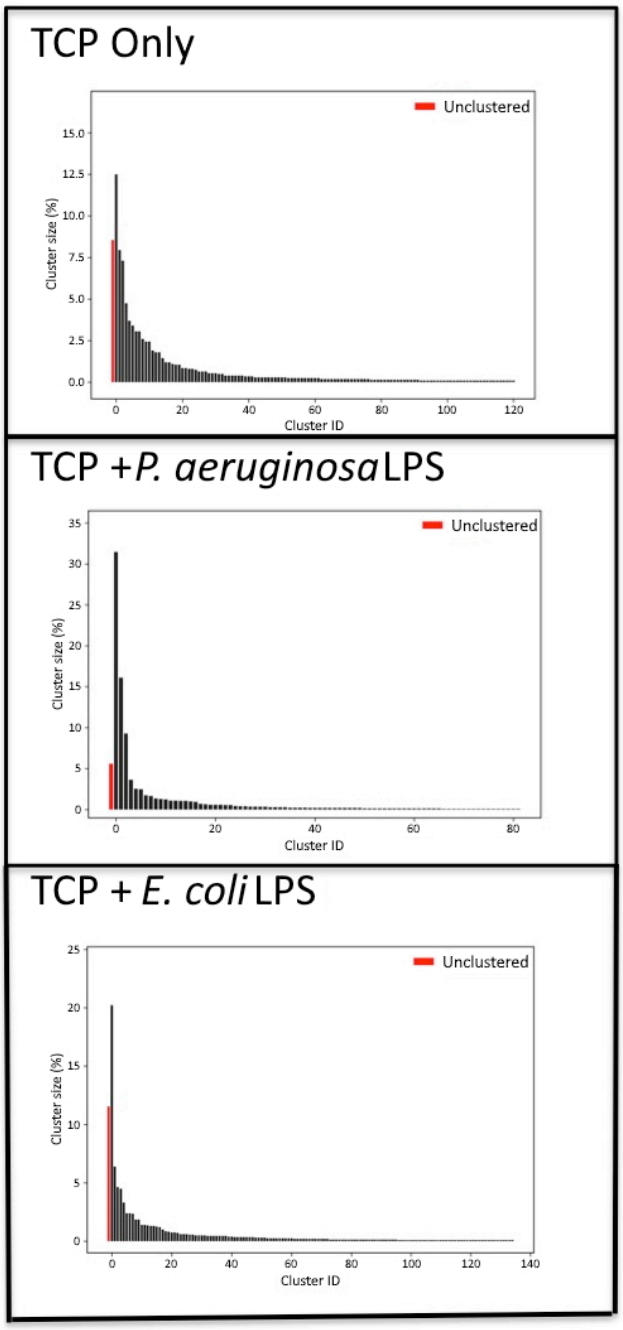

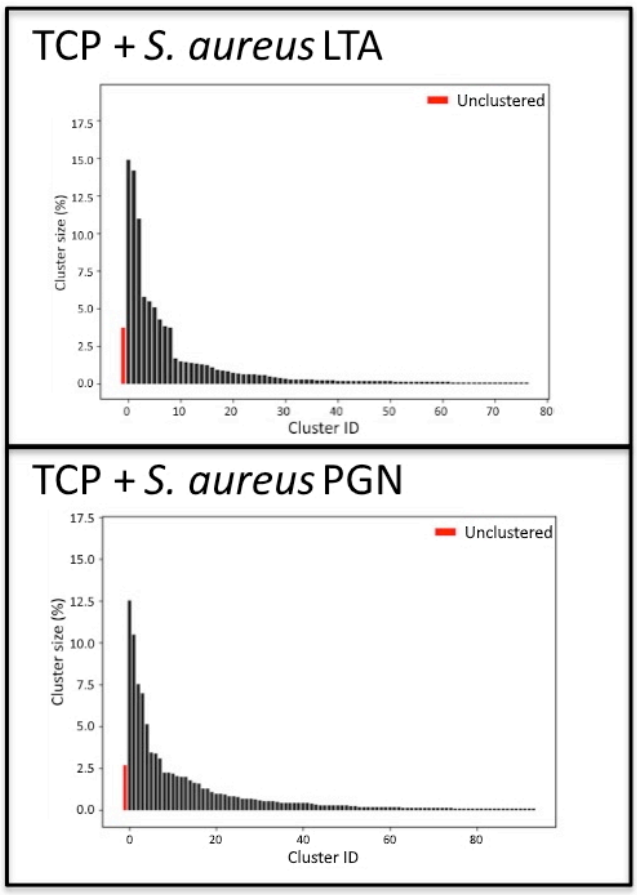

Figure 6.7: Cluster sizes of TCP96 conformations in the presence and absence of microbial products that fall into a cluster as well as the outliers from any cluster in red.

The number of contacts <0.6 nm were measured between TCP and the microbial components. Figure 6.8. This showed TCP having the most contacts with both LPS species throughout the simulations, especially *E.coli* LPS. Interestingly, a similar number of contacts occurred between TCP and LTA and *P. aeruginosa* LPS. Contacts between LTA and TCP occurred more than between TCP and PGN, which suggested that LTA did come into contact with TCP despite not causing TCP aggregation.

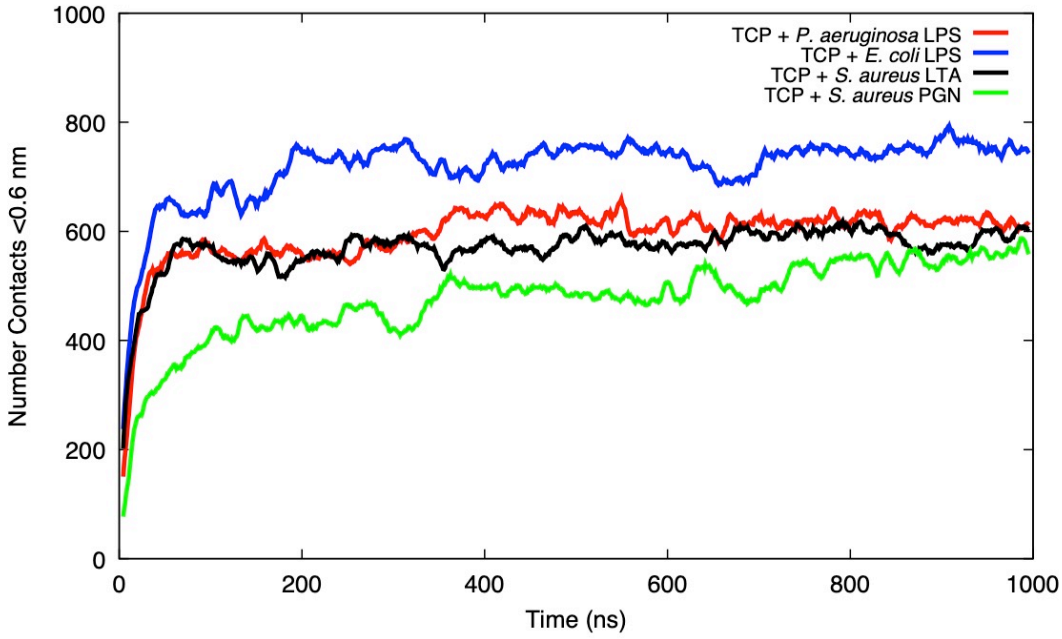

Figure 6.8: Number of contacts <0.6 nm between TCP96 and antimicrobial products over time.

The minimum distance between TCP and antimicrobial products was also measured over time, Figure 6.9. The distance between TCP and the bacterial components were broadly similar for all systems.

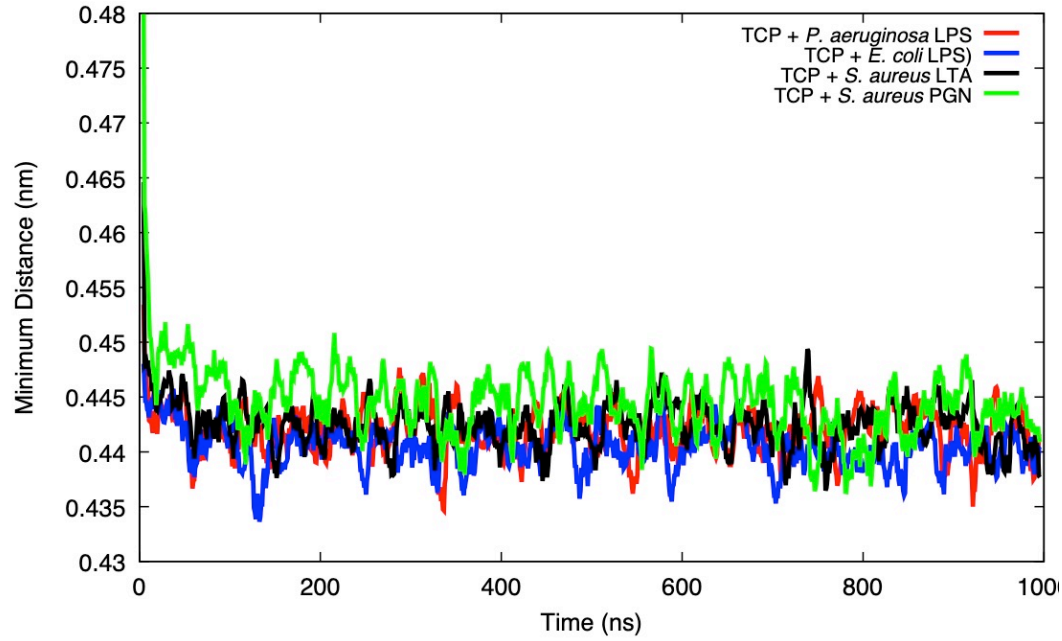

Figure 6.9: Minimum distance between TCP96 and microbial products over time.

The R(g) of TCP molecules in the presence and absence of microbial products was measured over time (ns), Figure 6.10. The R(g) was overall slightly less in the simulations with only TCP and when simulated with PGN. On the other hand, the R(g) was slightly higher in the simulations with both LPS species and LTA, which could suggest that both LPS and LTA cause similar behaviour of TCP aggregating despite LTA not causing aggregation of TCP molecules.

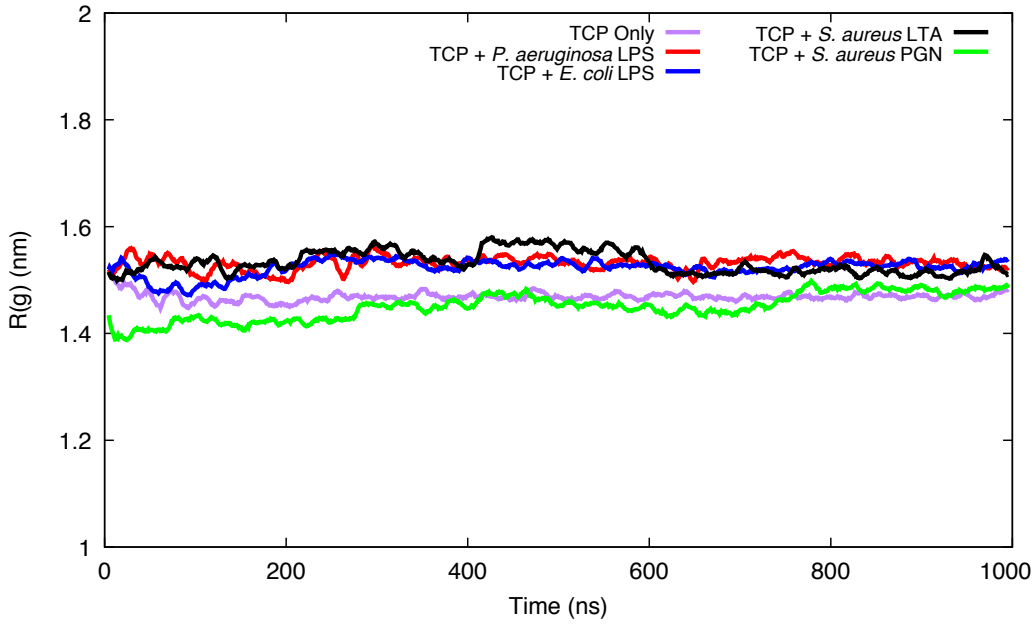

Figure 6.10: R(g) of TCP96 molecules over time in the presence and absence of microbial products.

6.2.3 Initial Conclusions

The evidence from this initial section of this study showed an increased proclivity for TCP aggregation in the presence of both LPS species, however this effect appeared to be slightly heightened by the *P. aeruginosa* LPS than the *E. coli* LPS. Surprisingly, PGN showed a slight aggregation effect but less aggregation effect than with TCP and LPS. LTA did not cause aggregation, as we would have expected from the experimental data.

6.3 Increasing LTA and PGN Ratio to TCP

It was hypothesised that the reason LTA did not cause TCP co-aggregation was due to its size. The LTA and PGN CG models were composed of around half the number of beads than the LPS model, and therefore, this means more LTA molecules may be needed to observe the aggregation mechanism. This section aimed to study whether a larger number of LTA molecules were required for TCP aggregation.

6.3.1 Methods and Simulation Set-up

Further simulations were therefore run with a 1:2 ratio of TCP:LTA/PGN, using the same simulation protocol as previously described. The results were then compared to the TCP only and 1:1 ratio of TCP:LTA/PGN from the previous section. The exact contents of these simulations are described in Table 6.2.

Contents	**Solvent**	**Length**
8 x TCP molecules	10786 H_2O, 1264 WF, 16 Cl^-	5 x 1 μs
8 x TCP molecules 8 x *S. aureus* LTA	10694 H_2O, 1263 WF	5 x 1 μs
8 x TCP molecules 16 x *S. aureus* LTA	10547 H_2O, 1243 WF, 16 Na^+	5 x 1 μs
8 x TCP molecules 8 x PGN	10662 H_2O, 1251 WF	5 x 1 μs
8 x TCP molecules 16 x PGN	10583 H_2O, 1275 WF, 16 Na^+	5 x 1 μs

Table 6.2: Contents, solvent and length of simulations conducted, varying the ratio of LTA/PGN to TCP.

6.3.2 Results

The visualisations of TCP with LTA and PGN at 1:1 and 1:2 ratios throughout the simulations are shown in Figure 6.11. The TCP was observed to aggregate more when at a 1:2 ratio with LTA than with 1:1 suggesting that a higher ratio of LTA is required to trigger LTA aggregation most probably due to the smaller LTA size. In the TCP:LTA 1:2 system, there was 1 cluster compared to the TCP:LTA 1:1 system that had 2 clusters. In contrast, TCP does not appear to have aggregated any more when there were more PGN molecules present in the system. This data thus supports experimental evidence that PGN does not cause significant TCP aggregation.

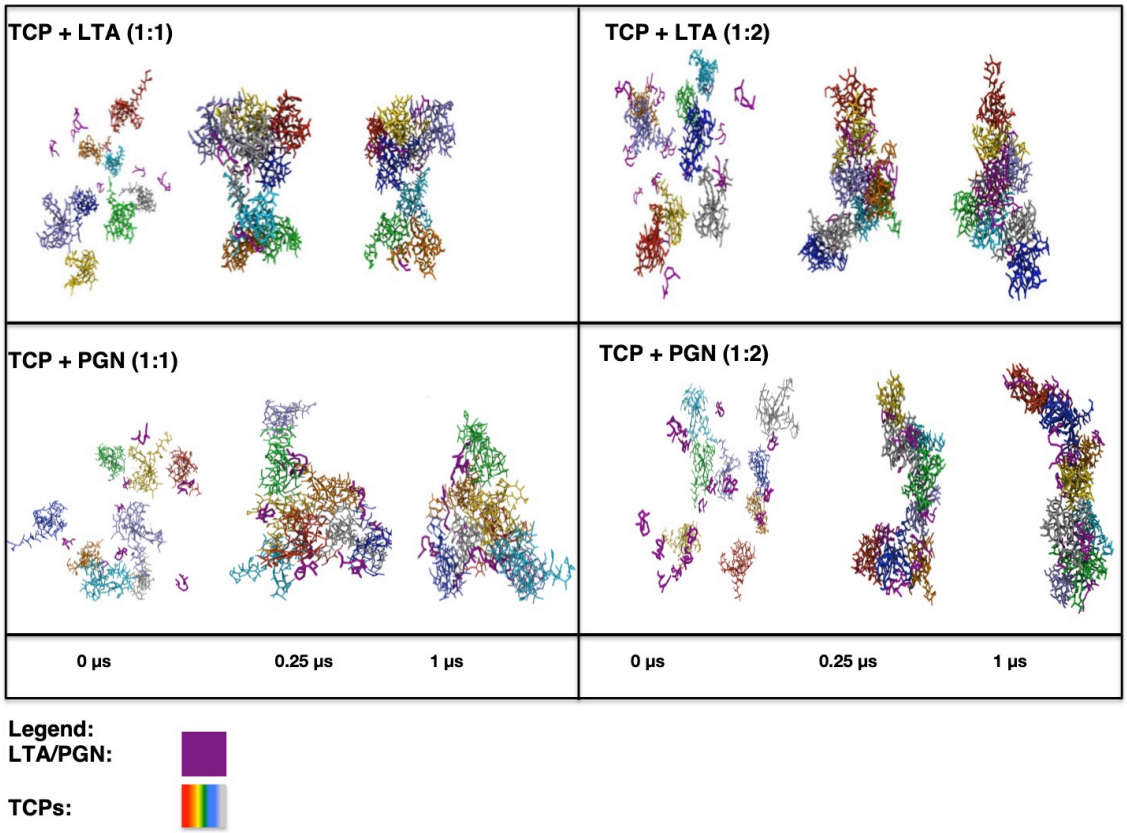

Figure 6.11: Snapshots showing progress of simulations showing point of aggregation at 0.25 µs and the end point of 1 µs. LTA and PGN are shown in purple with the TCP shown in various other colours.

The mean intermolecular distance between TCP fragments with differing ratios of LTA and PGN are shown in Figure 6.12. The TCP:LTA 1:2 matrix appeared to show TCP molecules coming into slightly closer contact than did the TCP:LTA 1:1

matrix, particularly focusing around the centre of the plot. This supports the previous suggestion that a higher number of LTA molecules do cause TCP to aggregate. Conversely, TCP molecules seem to not come into as close contact in the TCP:PGN 1:2 matrix than the TCP:PGN 1:1 system. This suggests that higher concentrations of PGN interfere with TCP aggregation.

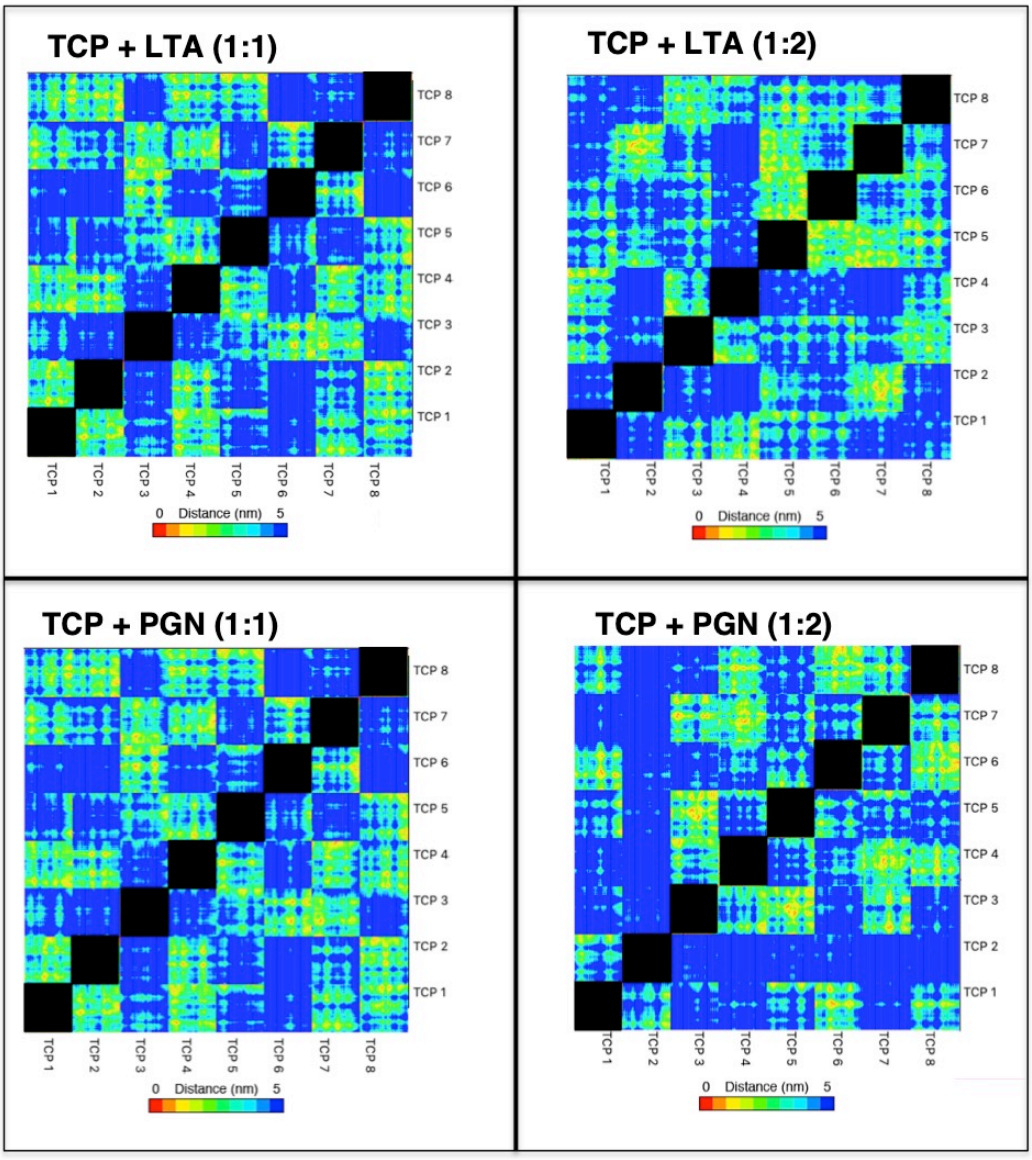

Figure 6.12: Mean intermolecular distance between TCP96 fragments following co-aggregation simulations in the presence/absence of the microbial products. The black boxes in the centre of each matrix were to omit self-contact.

The RDF was again calculated to measure the probable distances between TCP molecules in the presence and absence of LTA and PGN at differing ratios, Figure 6.13. This revealed that TCP molecules would come into closer contact in the TCP:LTA 1:2 system than the corresponding system at a 1:1 ratio. This supports the previous analysis. Meanwhile, the first peak of the TCP:PGN 1:2 ratio indicated that TCP molecules cannot come into quite such close contact as in the TCP:PGN 1:1 system.

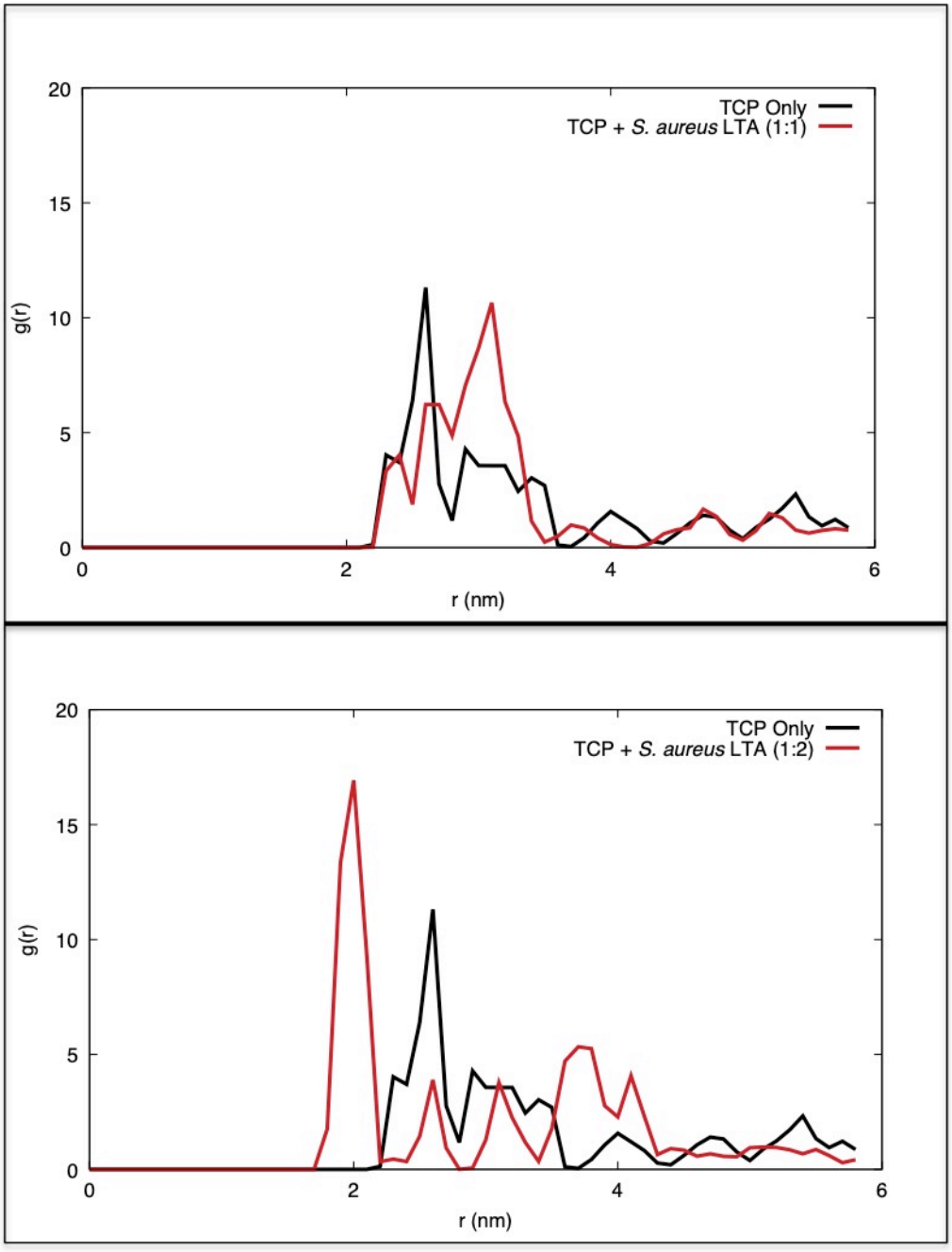

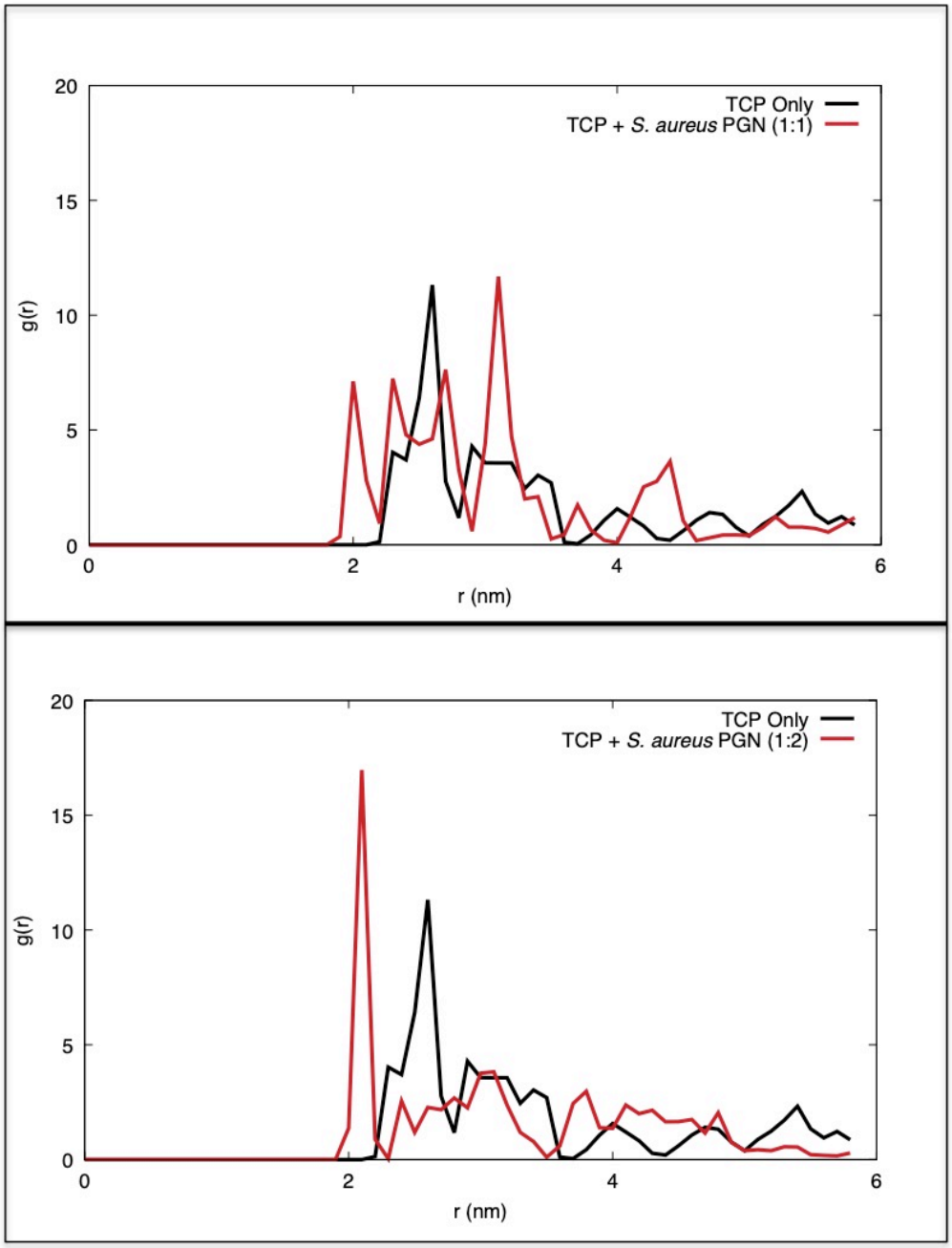

Figure 6.13: The RDF measuring the probability of TCP96 distances with other TCP96 molecules with differing ratios of TCP:LTA/PGN.

The probable average distances of TCP molecules in each system are shown in Figure 6.14. This shows TCP molecules coming into a considerably closer contact in the TCP:LTA 1:2 system, with an extremely low P-value suggesting this difference is significant. In contrast, there did not seem to be a larger difference between TCP molecules distances in the PGN systems, and furthermore the P-value comparing the 1:1 and 1:2 data was less significantly different.

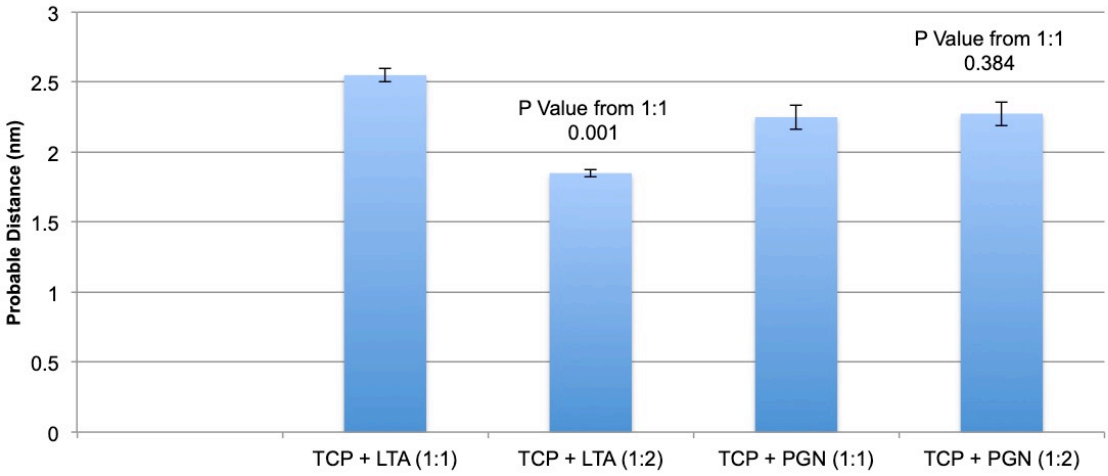

Figure 6.14: The probable average distance between TCP96 molecules in each system. This was measured for each 200 ns section of the simulation with the average shown. The P-value in reference to the probable distance in the 1:1 ratio simulation shows they are all significantly different from the control. The error bars are the standard deviation taken from the averages.

Cluster analysis of TCP conformations were again measured, Figure 6.15. The distribution of the cluster in reference to the RMSD was very similar between the two PGN systems with the two most common clusters occurring at very similar points of the simulations. This suggests that increasing the PGN ratio to TCP did not particularly affect the conformations adopted by TCP. In contrast, the TCP:LTA 1:2 system showed more similar clustering to that which is seen in the TCP systems in the presence of both LPS. As LPS molecules were shown to aggregate TCP, the increased LTA molecules likely caused TCP to aggregate also.

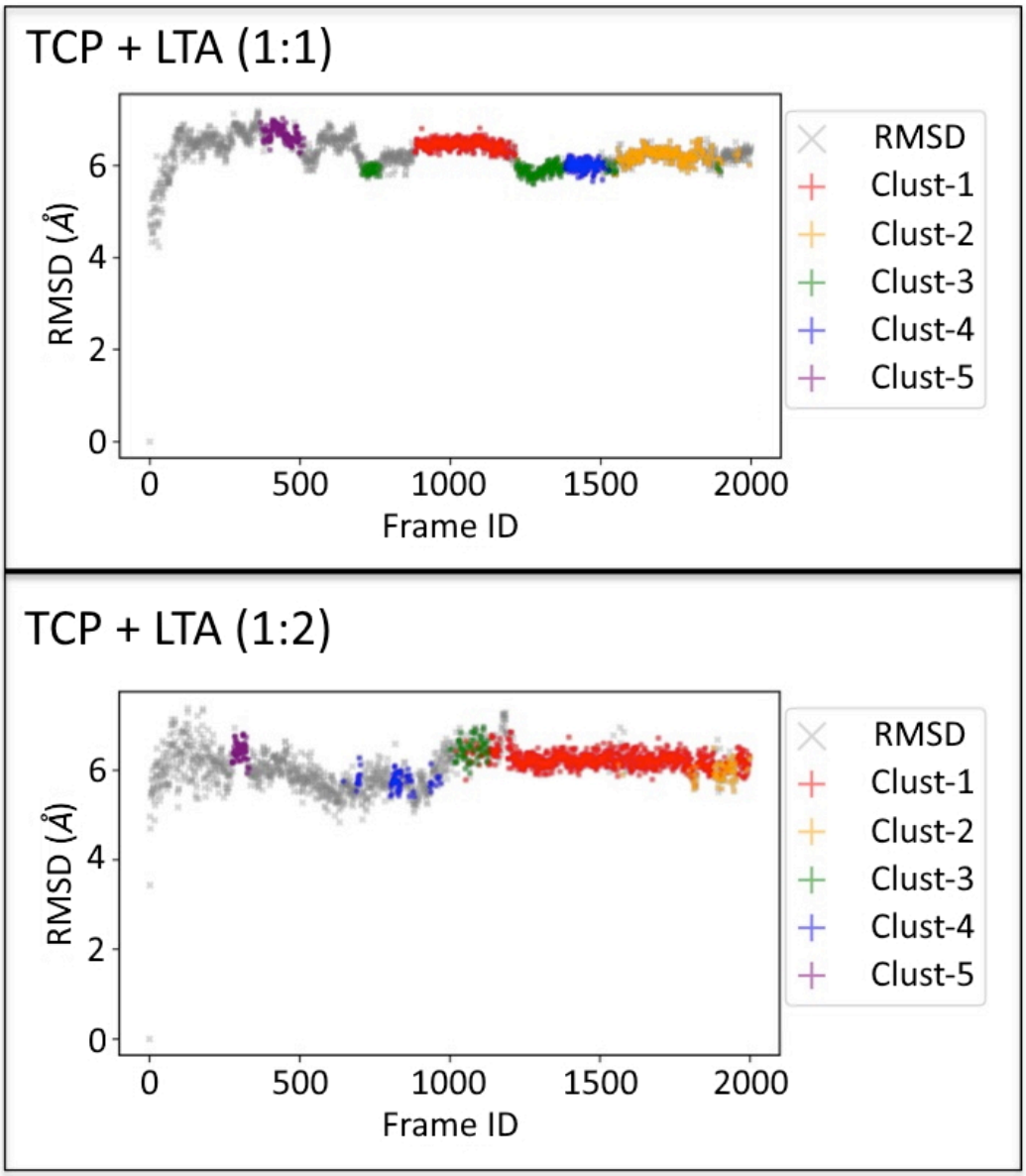
TCP + LTA (1:1)
RMSD (Å)
0
2
4
6
0
500
1000
1500
2000
Frame ID
RMSD
Clust-1
Clust-2
Clust-3
Clust-4
Clust-5
TCP + LTA (1:2)
RMSD (Å)
0
2
4
6
0
500
1000
1500
2000
Frame ID
RMSD
Clust-1
Clust-2
Clust-3
Clust-4
Clust-5

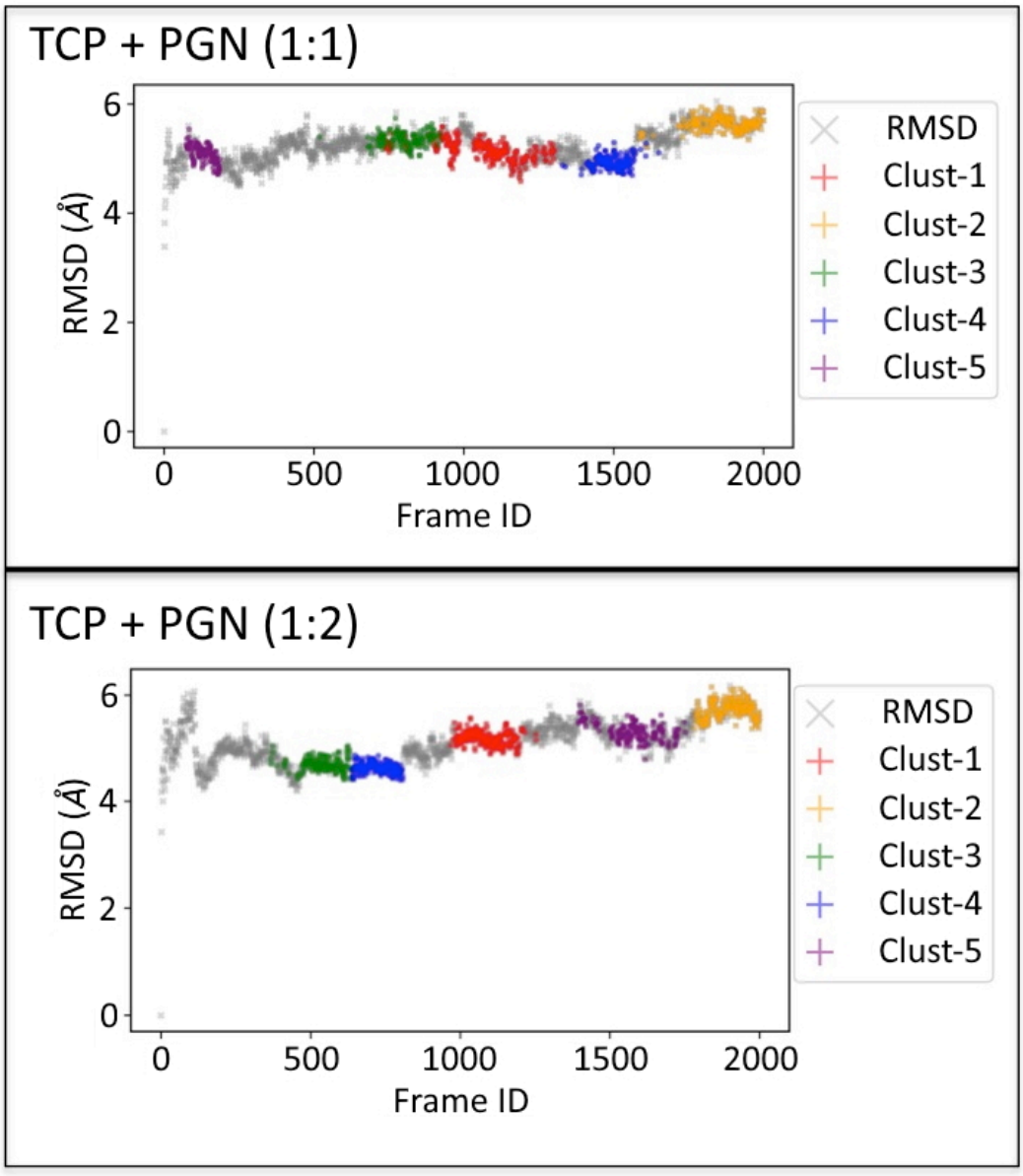

Figure 6.15: Superposition of the first five clusters onto RMSD of all frames to show the frequency of those conformations of TCP96 in the presence and absence of microbial products.

The cluster sizes of TCP in these simulations are shown in Figure 6.16. This supports the previous analysis in that TCP in the LTA:TCP 1:2 system had a similar number of clusters to the TCP in the presence of LPS. Whereas, there was not a large difference between the two PGN systems. The 5 most common clusters of TCP are also shown in the Appendix, Figure A.5. There was little difference between the most common conformations between simulations.

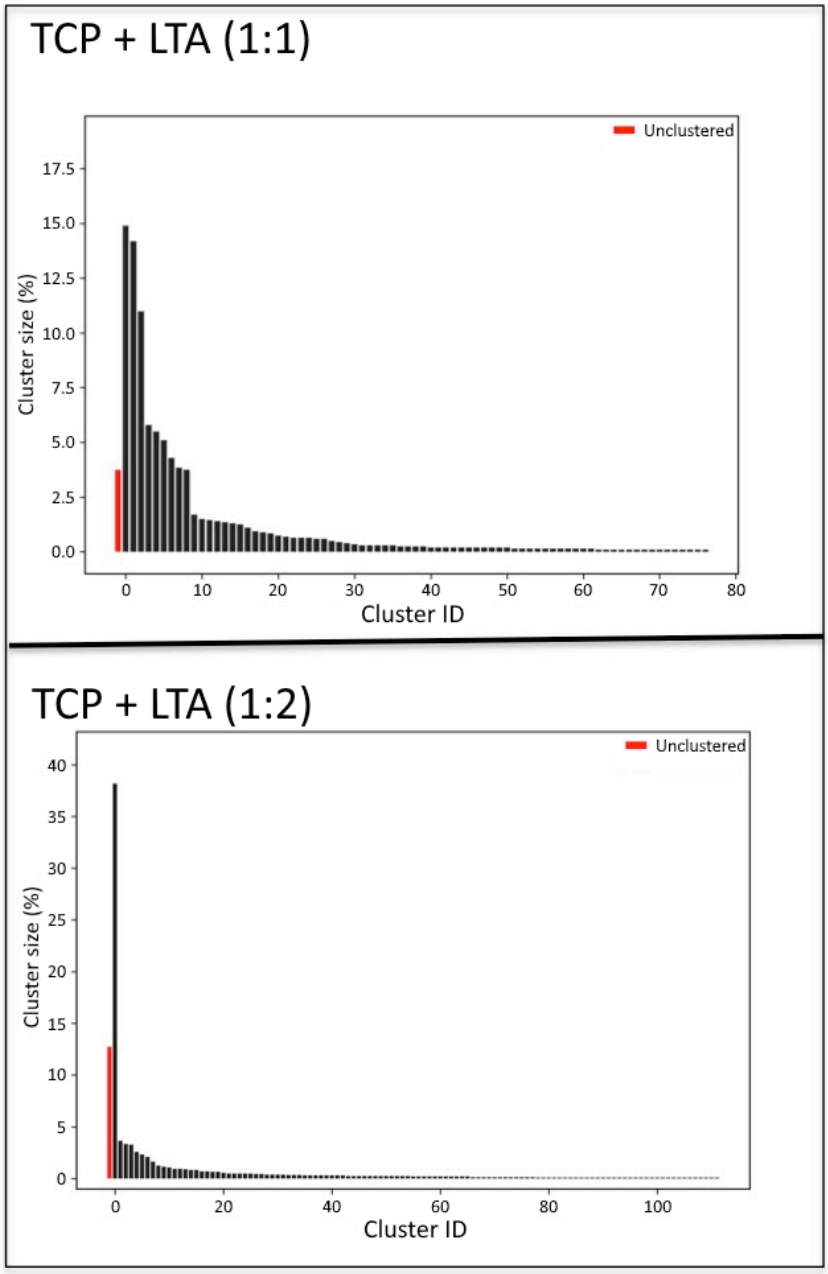

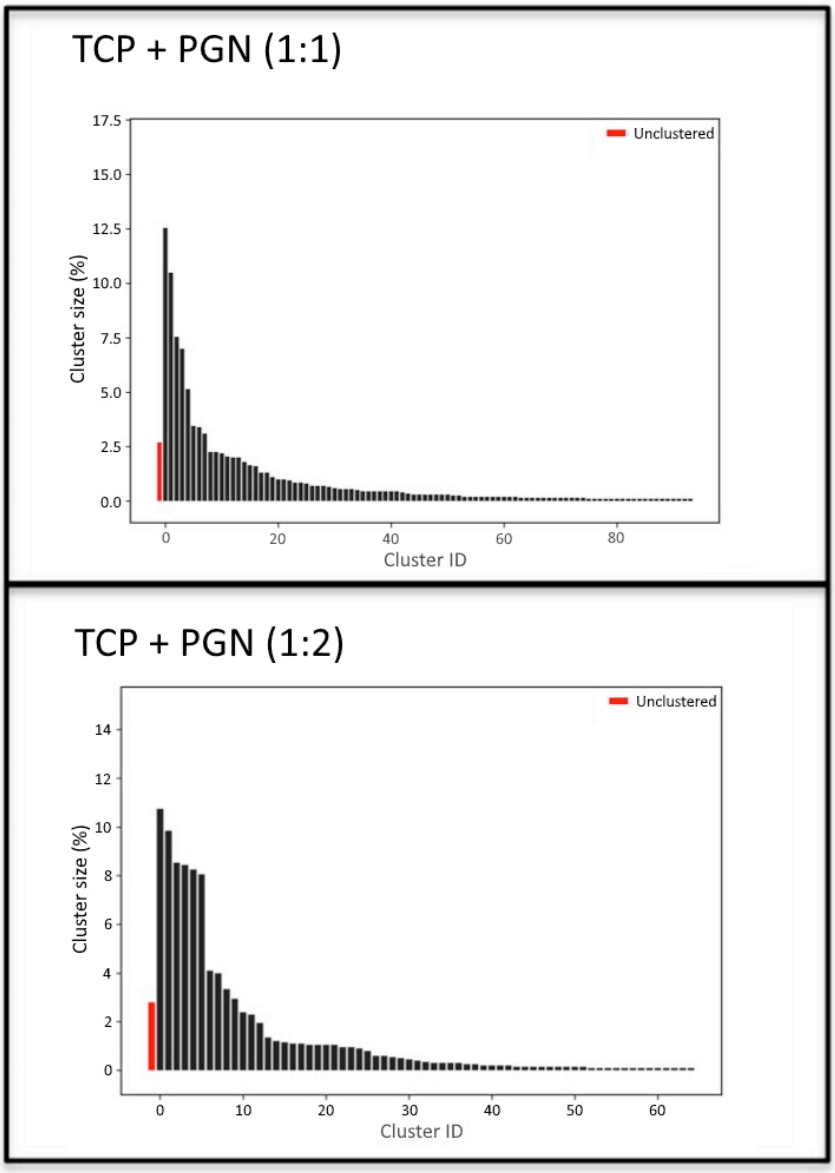

Figure 6.16: Cluster sizes of TCP96 conformations in the presence and absence of microbial products that fall into a cluster as well as the outliers from any cluster in red.

The SASA of TCP molecules in each system were measured over time, Figure 6.17. This showed that the SASA of TCP molecules was slightly larger in the TCP:PGN 1:2 ratio than the 1:1 system. This further suggests a larger concentration of PGN interferes with TCP aggregation.

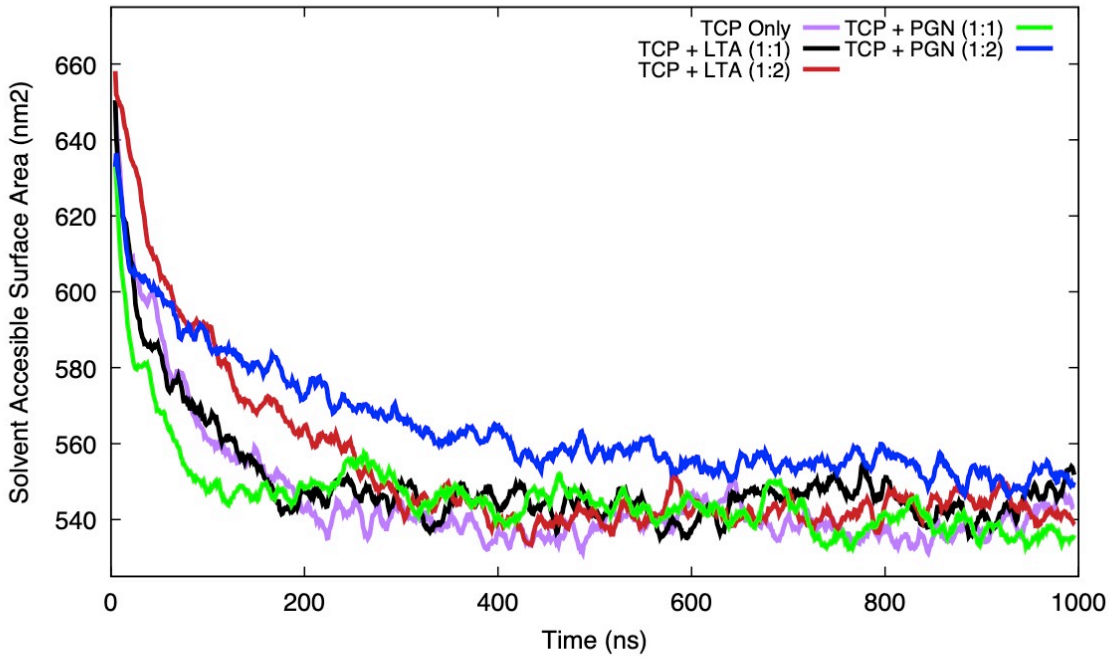

Figure 6.17: SASA of TCP96 molecules in the presence and absence of LTA and PGN at differing ratios.

The minimum distance between TCP and LTA/PGN was measured over time, Figure 6.18. As with the previous figure of this analysis, this did not show a significant difference between the distance between TCP and the microbial components. This could be due to the large size of the TCP molecules in comparison to the microbial products making it difficult for the microbial products.

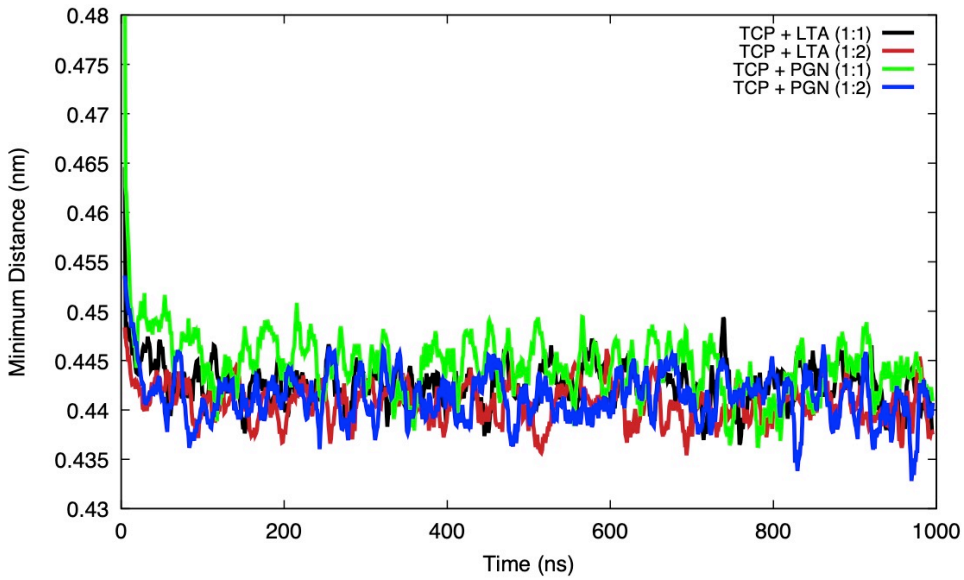

Figure 6.18: Minimum distance between TCP96 and different ratios of LTA and PGN over time.

The R(g) values of TCP molecules in the presence and absence of LTA and PGN at differing ratios were measured over time, Figure 6.19. There was little difference between the R(g) of TCP molecules in each system. However the R(g) of TCP in the presence of PGN was slightly larger over time, particularly in the TCP:PGN 1:2 system.

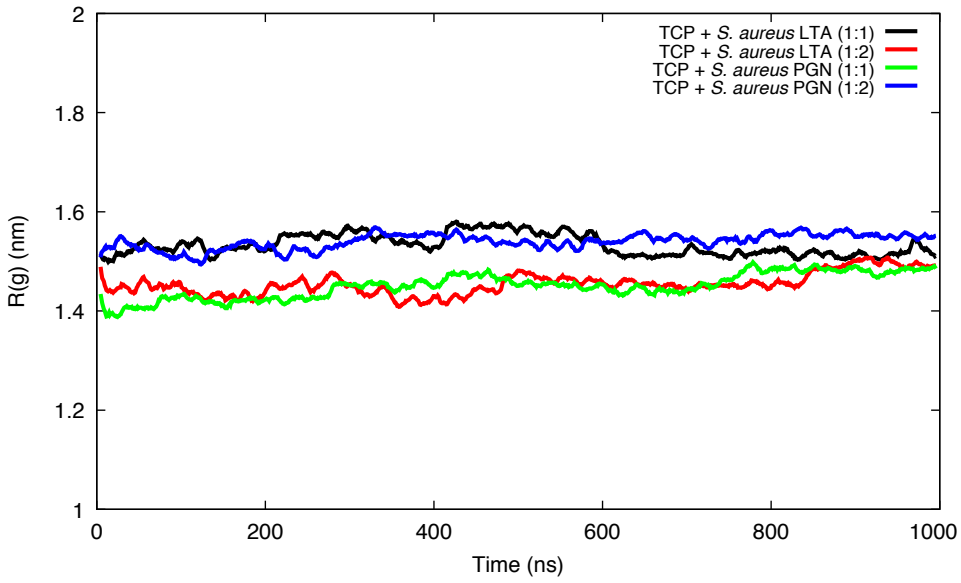

Figure 6.19: R(g) (nm) of TCP96 molecules over time (ns) in the presence LTA and PGN at differing ratios.

The R(g) was also measured for the last 20 ns section of LTA and PGN in the presence of TCP at differing ratios, Figure 6.20. This showed a clear difference between the R(g) of LTA at the different ratios, with LTA in the 1:2 ratio having a smaller R(g) than the 1:1 ratio. This suggested that LTA at a higher ratio with TCP had a smaller R(g) due to the molecules being aggregated amongst the TCP molecules. Whereas, the R(g) of PGN in the TCP:PGN 1:2 simulation was very stable in the last section of the simulation and more similar to the R(g) of PGN in the 1:1 simulation. Indeed, by the end of the simulation the R(g) of PGN in the TCP:PGN 1:1 was slightly larger than the 1:2 ratio. This could suggest that a higher ratio of PGN to TCP does not increase TCP aggregation and could perhaps slightly inhibit this behaviour.

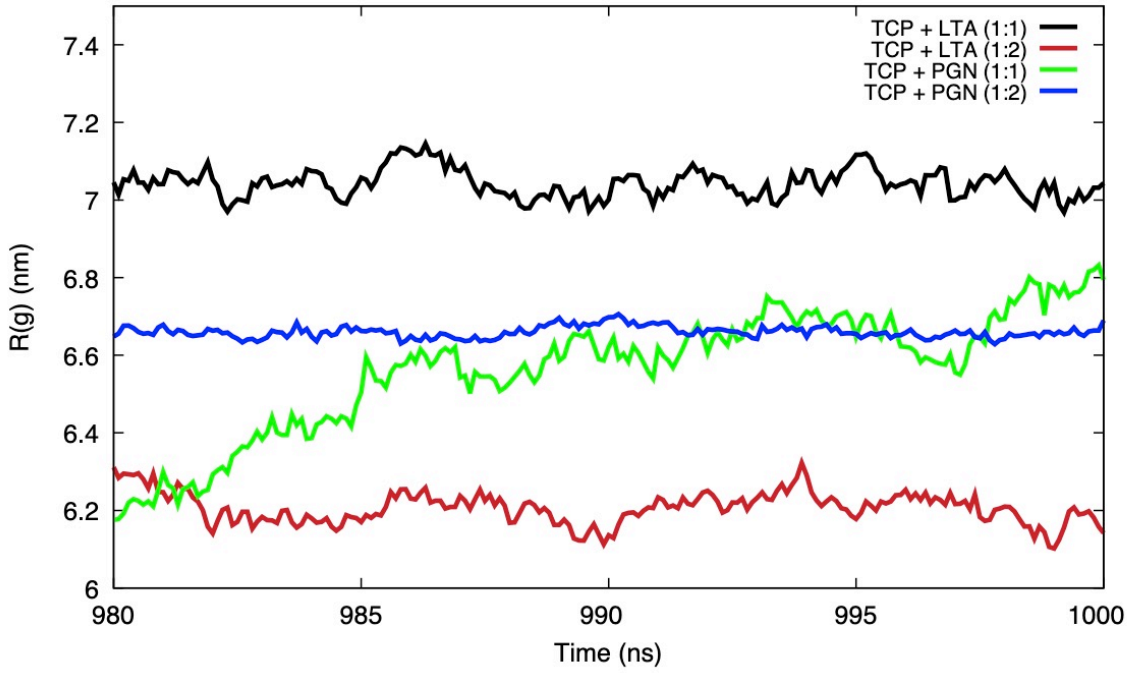

Figure 6.20: R(g) of LTA and PGN in the presence of TCP96 at differing ratios over time.

6.3.3 Conclusions

This data lent additional support to the observation that a higher concentration of LTA is required compared with LPS for efficient TCP96 aggregation. Meanwhile, increasing the PGN concentration caused no increase of TCP aggregation and by some measures of the analysis increased PGN resulted in decreased TCP aggregation. Thus, at the relevant concentration of microbial components, the simulations support the experimental data.

Overall this study shows that bacterial envelope components cause the aggregation of TCP96. The activities of TCP96 in the presence of LPS and LTA present an endogenous method by which aggregation-prone TCPs facilitate and control inflammation. From the hosts' standpoint, this behaviour is beneficial for localising and controlling inflammation. This observation is of interest as this suggests that outcomes such as sepsis and septic shock can be avoided. Furthermore, improving our understanding of these mechanisms and perhaps manipulating them further to the benefit of the host, may reduce our dependence on antibiotics and relieve some of the strain and concern in regards to antimicrobial resistance.

Appendix

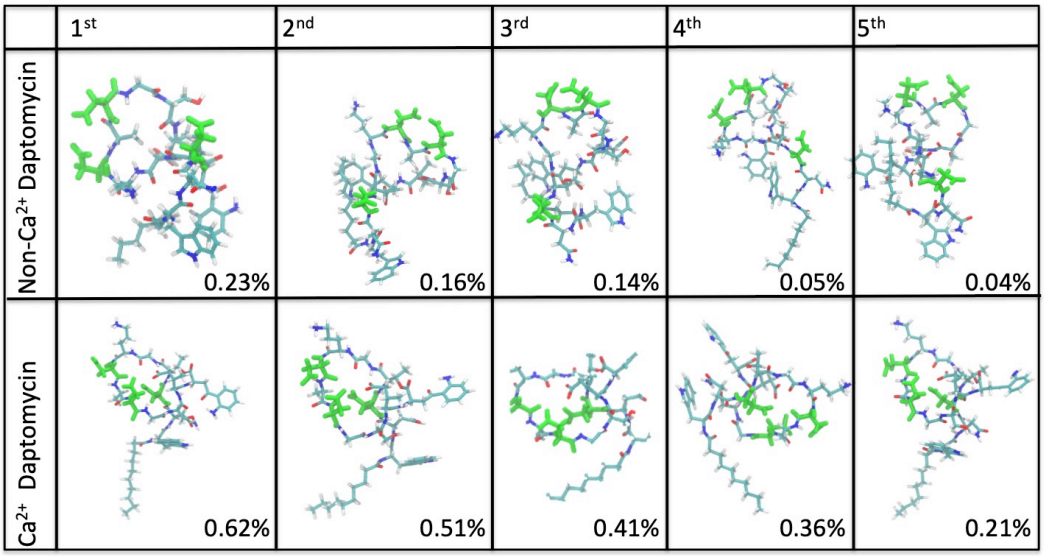

A.1: The 5 most common conformations of daptomycin models within each system based on conformational cluster analysis in systems with 15 daptomycin molecules and *S. aureus* membrane. The molecules are shown in cyan, red blue & white, with the exception of the aspartates shown in green. The percentage each cluster represents is shown in the bottom right corner of each cluster.

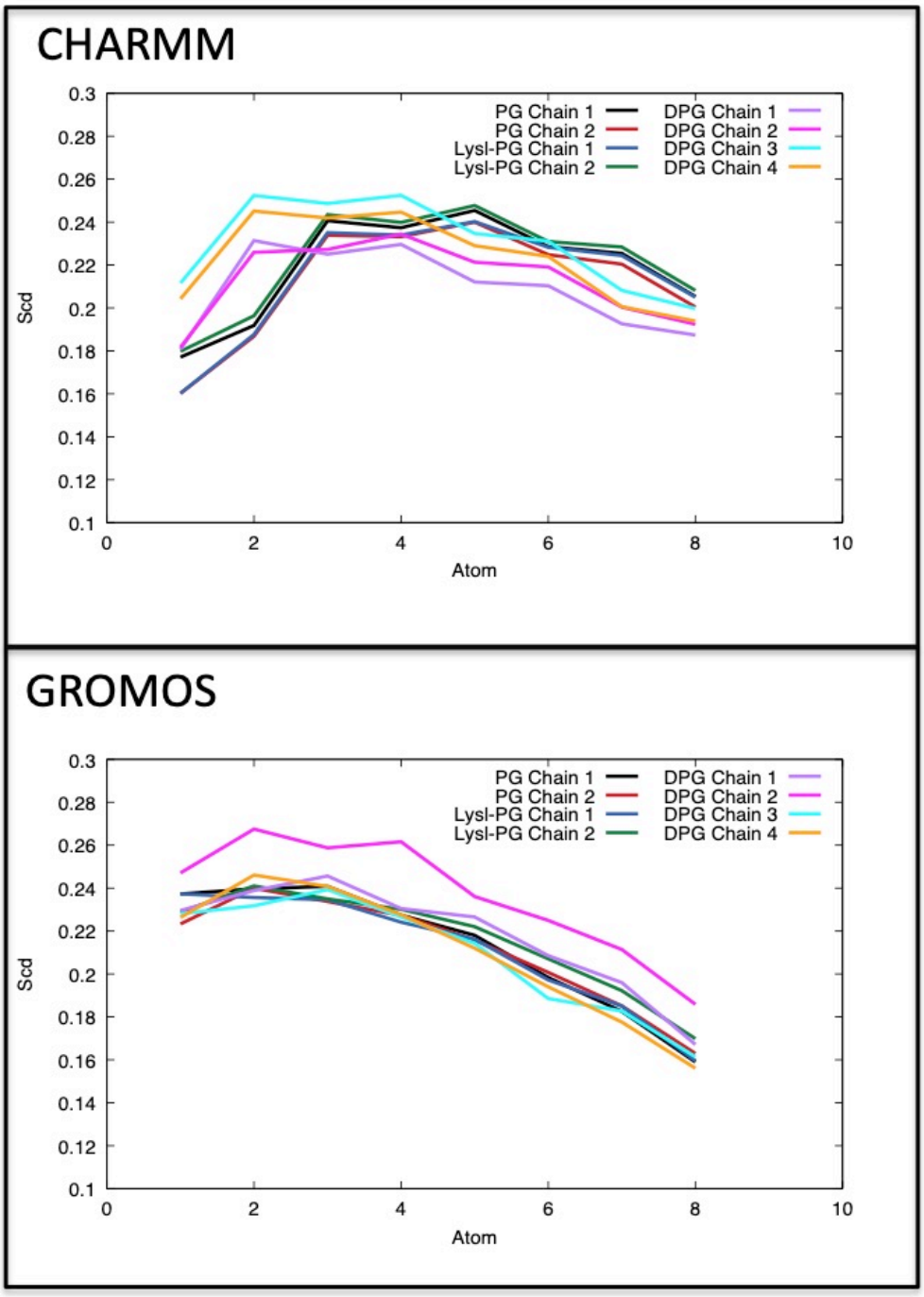

Figure A.2: Deuterium order parameters (Scd per atom) of each lipid tail chain calculated over the simulations at equilibrium. The force fields are shown above.

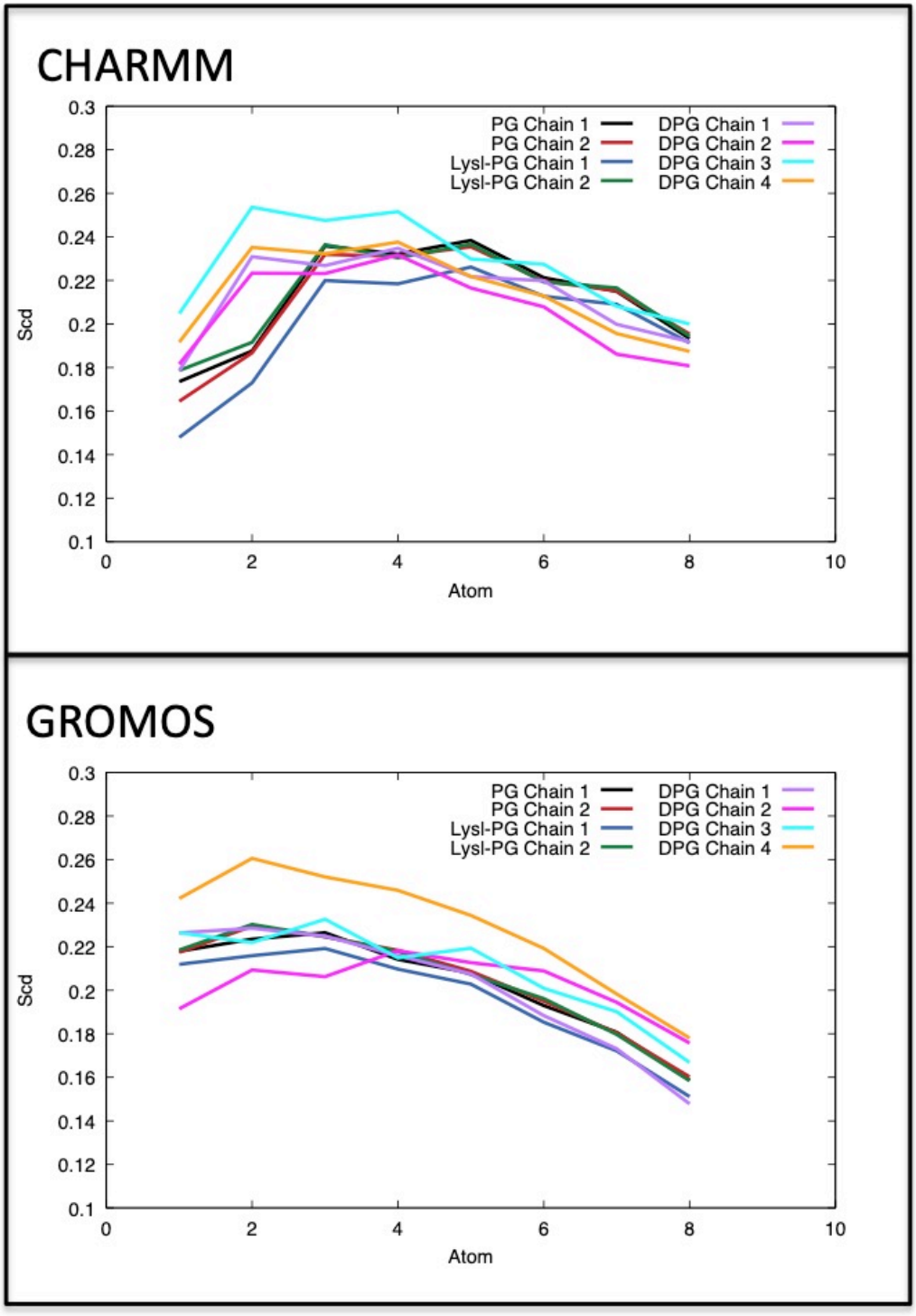

Figure A.3: Deuterium order parameters (Scd per atom) of each lipid tail chain calculated over the electroporation simulations. The force fields are shown above.

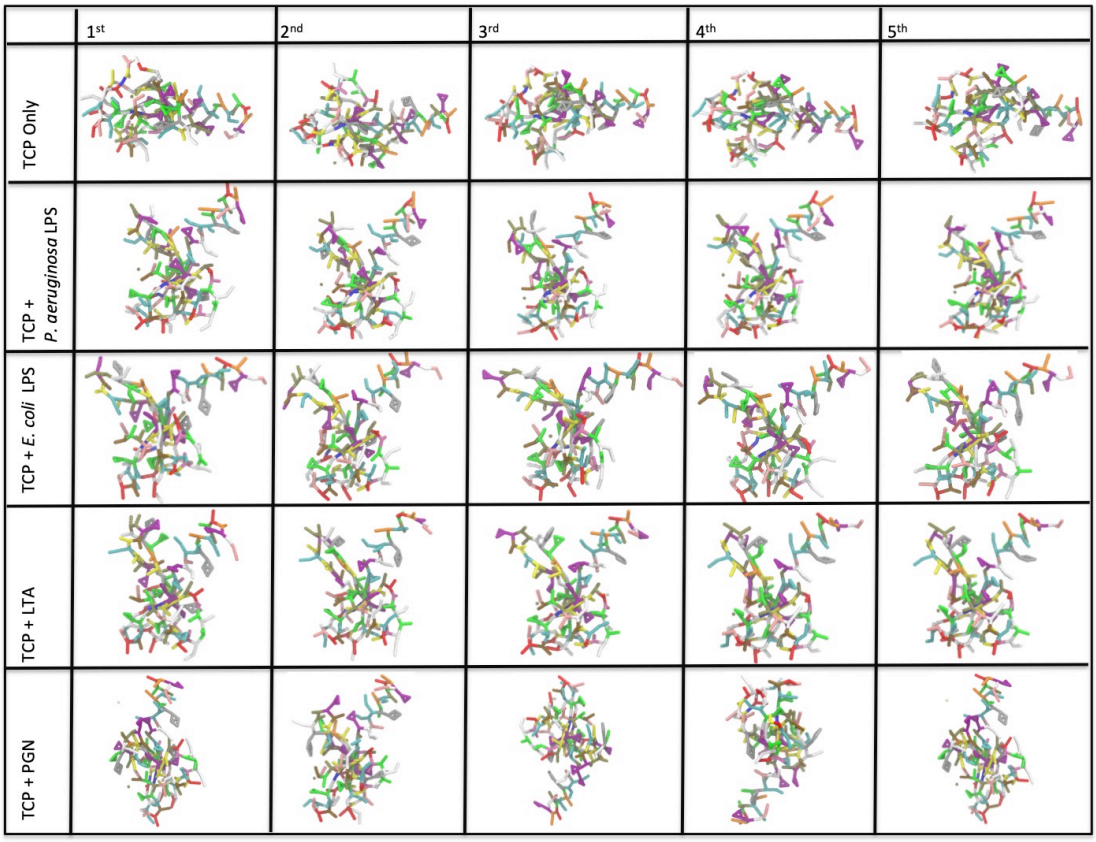

Figure A.4: The conformations of TCP96 in the 5 most common clusters in each simulation in the presence of different bacterial products.

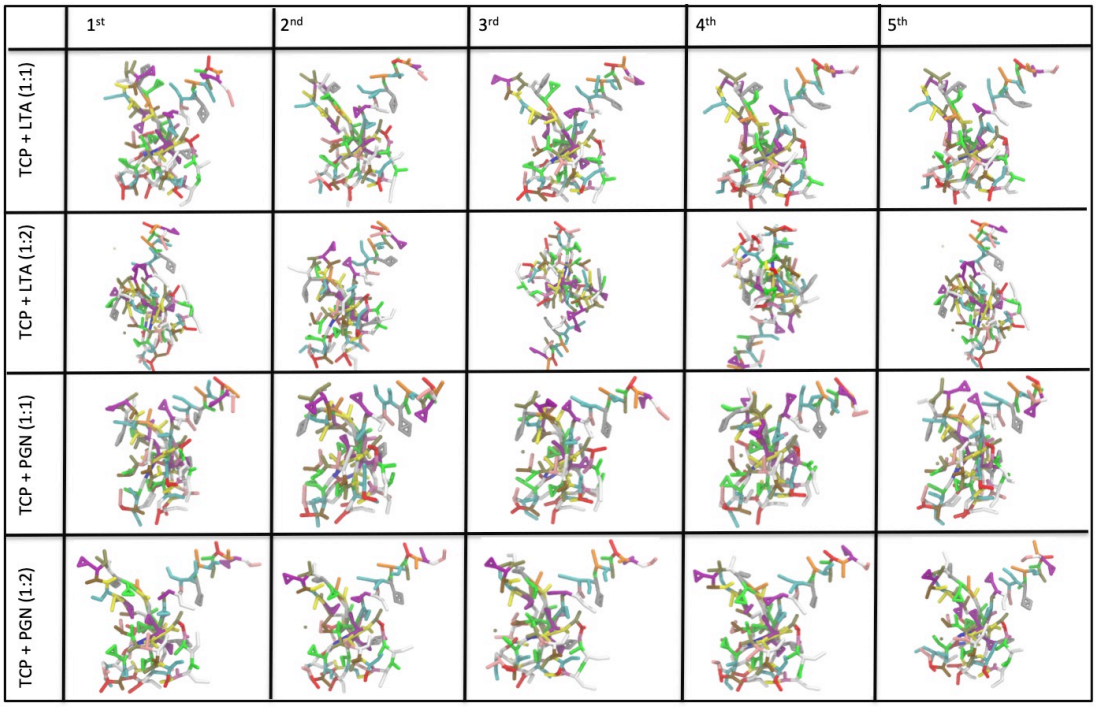

Figure A.5: The conformations of TCP96 in the 5 most common clusters in each simulation with 1:2 ratio of TCP:/LTA.

Bibliography

1. Young, K. D. The Selective Value of Bacterial Shape. *Microbiol. Mol. Biol. Rev.* (2006). doi:10.1128/mmbr.00001-06
2. Moyes, R. B., Reynolds, J. & Breakwell, D. P. Differential staining of bacteria: Gram stain. *Current Protocols in Microbiology* (2009). doi:10.1002/9780471729259.mca03cs15
3. Beveridge, T. J. Structures of gram-negative cell walls and their derived membrane vesicles. *Journal of Bacteriology* (1999). doi:10.1128/jb.181.16.4725-4733.1999
4. Raetz, C. R. H. & Whitfield, C. Lipopolysaccharide endotoxins. *Annual Review of Biochemistry* (2002). doi:10.1146/annurev.biochem.71.110601.135414
5. Hancock, R. E. W. & Bell, A. Antibiotic uptake into gram-negative bacteria. in *Current Topics in Infectious Diseases and Clinical Microbiology* (1989). doi:10.1007/978-3-322-86064-4_5
6. Vollmer, W., Blanot, D. & De Pedro, M. A. Peptidoglycan structure and architecture. *FEMS Microbiology Reviews* (2008). doi:10.1111/j.1574-6976.2007.00094.x
7. Braun, V. Covalent lipoprotein from the outer membrane of escherichia coli. *BBA - Reviews on Biomembranes* (1975). doi:10.1016/0304-4157(75)90013-1
8. Bogdanov, M. *et al.* Phospholipid distribution in the cytoplasmic membrane of Gram-negative bacteria is highly asymmetric, dynamic, and cell shape-dependent. *Sci. Adv.* (2020). doi:10.1126/sciadv.aaz6333
9. Raetz, C. R. H. & Dowhan, W. Biosynthesis and function of phospholipids in Escherichia coli. *Journal of Biological Chemistry* (1990).
10. Neuhaus, F. C. & Baddiley, J. A Continuum of Anionic Charge: Structures and Functions of d-Alanyl-Teichoic Acids in Gram-Positive Bacteria. *Microbiol. Mol. Biol. Rev.* (2003). doi:10.1128/mmbr.67.4.686-723.2003
11. Silhavy, T., Kahne, D. & Walker, S. The bacterial cell envelope. *Cold Spring Harbor perspectives in biology* **2**, 1–16 (2010).

12. Kuehnert, M. J. *et al.* Prevalence of Staphylococcus aureus nasal colonization in the United States, 2001-2002. *J. Infect. Dis.* **193**, 172–9 (2006).
13. Boucher, H., Miller, L. G. & Razonable, R. R. Serious Infections Caused by Methicillin-Resistant *Staphylococcus aureus*. *Clin. Infect. Dis.* **51**, S183–S197 (2010).
14. Fowler, V. G. *et al.* Daptomycin versus standard therapy for bacteremia and endocarditis caused by Staphylococcus aureus. *N. Engl. J. Med.* **355**, 653–665 (2006).
15. Kollef, M. H. Limitations of vancomycin in the management of resistant staphylococcal infections. *Clin. Infect. Dis.* **45 Suppl 3**, S191–S195 (2007).
16. Shockman, G. D. & Barrett, J. F. Structure, function, and assembly of cell walls of gram-positive bacteria. *Annu Rev Microbiol* **37**, 501–527 (1983).
17. Brown, L., Wolf, J. M., Prados-Rosales, R. & Casadevall, A. Through the wall: extracellular vesicles in Gram-positive bacteria, mycobacteria and fungi. *Nat. Rev. Microbiol.* **13**, 620–30 (2015).
18. Ton-That, H., Marraffini, L. A. & Schneewind, O. Protein sorting to the cell wall envelope of Gram-positive bacteria. *Biochimica et Biophysica Acta - Molecular Cell Research* **1694**, 269–278 (2004).
19. McGillivray, D. J. *et al.* Structure of functional Staphylococcus aureus ??-hemolysin channels in tethered bilayer lipid membranes. *Biophys. J.* **96**, 1547–1553 (2009).
20. Piggot, T. J., Holdbrook, D. a & Khalid, S. Electroporation of the *E. coli* and *S. Aureus* Membranes: Molecular Dynamics Simulations of Complex Bacterial Membranes. *J. Phys. Chem. B* **115**, 13381–13388 (2011).
21. Peschel, A. *et al. Staphylococcus aureus* Resistance to Human Defensins and Evasion of Neutrophil Killing via the Novel Virulence Factor Mprf Is Based on Modification of Membrane Lipids with l-Lysine. *J. Exp. Med.* **193**, 1067–1076 (2001).
22. Kapoor, G., Saigal, S. & Elongavan, A. Action and resistance mechanisms of antibiotics: A guide for clinicians. *J. Anaesthesiol. Clin. Pharmacol.* **33**, 300 (2017).

23. Kanoh, S. & Rubin, B. K. Mechanisms of action and clinical application of macrolides as immunomodulatory medications. *Clinical Microbiology Reviews* (2010). doi:10.1128/CMR.00078-09
24. Vannuffel, P. & Cocito, C. Mechanism of action of streptogramins and macrolides. *Drugs* (1996). doi:10.2165/00003495-199600511-00006
25. Cué Brugueras, M., Morejón García, M. & Salup Díaz, R. Present situation of quinolones. *Rev. Cuba. Farm.* (2005).
26. Wehrli, W. Rifampin: Mechanisms of action and resistance. *Rev. Infect. Dis.* (1983). doi:10.1093/clinids/5.Supplement_3.S407
27. Yoneyama, H. & Katsumata, R. Antibiotic resistance in bacteria and its future for novel antibiotic development. *Bioscience, Biotechnology and Biochemistry* (2006). doi:10.1271/bbb.70.1060
28. Bermingham, A. & Derrick, J. P. The folic acid biosynthesis pathway in bacteria: Evaluation of potential for antibacterial drug discovery. *BioEssays* (2002). doi:10.1002/bies.10114
29. Waxman, D. J. & Strominger, J. L. Penicillin-binding proteins and the mechanism of action of β-lactam antibiotics. *Annu. Rev. Biochem.* (1983). doi:10.1146/annurev.bi.52.070183.004141
30. Cho, H., Uehara, T. & Bernhardt, T. G. Beta-lactam antibiotics induce a lethal malfunctioning of the bacterial cell wall synthesis machinery. *Cell* (2014). doi:10.1016/j.cell.2014.11.017
31. Grundmann, H., Aires-de-Sousa, M., Boyce, J. & Tiemersma, E. Emergence and resurgence of meticillin-resistant Staphylococcus aureus as a public-health threat. *Lancet* (2006). doi:10.1016/S0140-6736(06)68853-3
32. Velkov, T., Roberts, K. D., Nation, R. L., Thompson, P. E. & Li, J. Pharmacology of polymyxins: New insights into an 'old class of antibiotics. *Future Microbiol.* (2013). doi:10.2217/fmb.13.39
33. Pogliano, J., Pogliano, N. & Silverman, J. A. Daptomycin-mediated reorganization of membrane architecture causes mislocalization of essential cell division proteins. *J. Bacteriol.* (2012). doi:10.1128/JB.00011-12
34. Andreatta, R. H., Liem, R. K. & Scheraga, H. A. Mechanism of action of

thrombin on fibrinogen. I. Synthesis of fibrinogen-like peptides, and their proteolysis by thrombin and trypsin. *Proc. Natl. Acad. Sci. U. S. A.* (1971). doi:10.1073/pnas.68.2.253

35. Petrlova, J. *et al.* Aggregation of thrombin-derived C-terminal fragments as a previously undisclosed host defense mechanism. *Proc. Natl. Acad. Sci. U. S. A.* (2017). doi:10.1073/pnas.1619609114
36. Papareddy, P. *et al.* Proteolysis of human thrombin generates novel host defense peptides. *PLoS Pathog.* (2010). doi:10.1371/journal.ppat.1000857
37. Litsky, W. DISINFECTION, STERILIZATION, AND PRESERVATION. *Am. J. Public Heal. Nations Heal.* (1968). doi:10.2105/ajph.58.11.2175-b
38. Williamson, D. A., Carter, G. P. & Howden, B. P. Current and emerging topical antibacterials and antiseptics: Agents, action, and resistance patterns. *Clinical Microbiology Reviews* (2017). doi:10.1128/CMR.00112-16
39. Russell, A. D. Mechanisms of antimicrobial action of antiseptics and disinfectants: An increasingly important area of investigation. *J. Antimicrob. Chemother.* (2002). doi:10.1093/jac/49.4.597
40. Reid, C. J., Alcock, M. & Penn, D. Hydrogen peroxide - A party trick from the past? *Anaesthesia and Intensive Care* (2011). doi:10.1177/0310057x1103900604
41. Tezvergil-Mutluay, A. *et al.* The anti-MMP activity of benzalkonium chloride. *J. Dent.* (2011). doi:10.1016/j.jdent.2010.10.003
42. Challacombe, S. J., Kirk-Bayley, J., Sunkaraneni, V. S. & Combes, J. Povidone iodine. *British Dental Journal* (2020). doi:10.1038/s41415-020-1589-4
43. Sidhwa, F. & Itani, K. M. F. Skin Preparation Before Surgery: Options and Evidence. *Surg. Infect. (Larchmt).* (2015). doi:10.1089/sur.2015.010
44. Darouiche, R. O. *et al.* Chlorhexidine-alcohol versus povidone-iodine for surgical-site antisepsis. *N. Engl. J. Med.* **362**, 18–26 (2010).
45. Solderer, A. *et al.* Efficacy of chlorhexidine rinses after periodontal or implant surgery: a systematic review. *Clinical Oral Investigations* (2019).

doi:10.1007/s00784-018-2761-y

46. Maris, P. Modes of action of disinfectants. *Rev. Sci. Tech.* **14**, 47–55 (1995).

47. Houari, A. & Di Martino, P. Effect of chlorhexidine and benzalkonium chloride on bacterial biofilm formation. *Lett. Appl. Microbiol.* (2007). doi:10.1111/j.1472-765X.2007.02249.x

48. WHO. WHO model formulary 2008. *Pharm. J.* (2009).

49. Alkharashi, M., Lindsley, K., Law, H. A. & Sikder, S. Medical interventions for acanthamoeba keratitis. *Cochrane Database of Systematic Reviews* (2015). doi:10.1002/14651858.CD010792.pub2

50. Jones, C. G. Chlorhexidine: is it still the gold standard? *Periodontol. 2000* **15**, 55–62 (1997).

51. Dodds, D. R. Antibiotic resistance: A current epilogue. *Biochemical Pharmacology* (2017). doi:10.1016/j.bcp.2016.12.005

52. Džidić, S., Šušković, J. & Kos, B. Antibiotic resistance mechanisms in bacteria: Biochemical and genetic aspects. *Food Technol. Biotechnol.* (2008).

53. Yeaman, M. R. & Yount, N. Y. Mechanisms of antimicrobial peptide action and resistance. *Pharmacological Reviews* (2003). doi:10.1124/pr.55.1.2

54. Lambert, P. A. Mechanisms of antibiotic resistance in Pseudomonas aeruginosa. in *Journal of the Royal Society of Medicine, Supplement* (2002).

55. Hiramatsu, K., Cui, L., Kuroda, M. & Ito, T. The emergence and evolution of methicillin-resistant Staphylococcus aureus. *Trends in Microbiology* (2001). doi:10.1016/S0966-842X(01)02175-8

56. Goering, R. V *et al.* Attacking the enemy: antimicrobial agents and chemotherapy. in *Mims' Medical Microbiology* (2008). doi:10.1016/b978-0-323-04475-2.50037-6

57. Ferreira, C. M., Ferreira, W. A., Almeida, N. C. O. da S., Naveca, F. G. & das Graças Vale Barbosa Barbosa, M. Extended-spectrum beta-lactamase-producing bacteria isolated from hematologic patients in manaus, state of Amazonas, Brazil. *Brazilian J. Microbiol.* (2011). doi:10.1590/S1517-

83822011000300028

58. Hockney, R. W., Goel, S. P. & Eastwood, J. W. A 10000 particle molecular dynamics model with long range forces. *Chem. Phys. Lett.* (1973). doi:10.1016/0009-2614(73)80315-X

59. Verlet, L. Computer 'experiments' on classical fluids. I. Thermodynamical properties of Lennard-Jones molecules. *Phys. Rev.* (1967). doi:10.1103/PhysRev.159.98

60. Hess, B., Bekker, H., Berendsen, H. J. C. & Fraaije, J. G. E. M. LINCS: A Linear Constraint Solver for molecular simulations. *J. Comput. Chem.* (1997). doi:10.1002/(SICI)1096-987X(199709)18:12<1463::AID-JCC4>3.0.CO;2-H

61. Berendsen, H. J. C., Postma, J. P. M., van Gunsteren, W. F., DiNola, A. & Haak, J. R. Molecular dynamics with coupling to an external bath. *J. Chem. Phys.* **81**, 3684–3690 (1984).

62. Hoover, W. G. Canonical dynamics: Equilibrium phase-space distributions. *Phys. Rev. A* (1985). doi:10.1103/PhysRevA.31.1695

63. Berendsen, H. J. C., Postma, J. P. M., Gunsteren, W. F. Van & Hermans, J. Interaction models for water in relation to protein hydration. *Intermol. Forces* 331–342 (1981). doi:10.1007/978-94-015-7658-1_21

64. Nosé, S. & Klein, M. L. Constant pressure molecular dynamics for molecular systems. *Mol. Phys.* **50**, 1055–1076 (1983).

65. Darden, T., York, D. & Pedersen, L. Particle mesh Ewald: An N·log(N) method for Ewald sums in large systems. *J. Chem. Phys.* (1993). doi:10.1063/1.464397

66. Essmann, U. *et al.* A smooth particle mesh Ewald method. *J Chem Phys* **103**, 8577–8593 (1995).

67. Schmid, N. *et al.* Definition and testing of the GROMOS force-field versions 54A7 and 54B7. *Eur. Biophys. J.* (2011). doi:10.1007/s00249-011-0700-9

68. Huang, J. & Mackerell, A. D. CHARMM36 all-atom additive protein force field: Validation based on comparison to NMR data. *J. Comput. Chem.* (2013). doi:10.1002/jcc.23354

69. Marrink, S. J., Risselada, H. J., Yefimov, S., Tieleman, D. P. & De Vries, A. H. The MARTINI force field: Coarse grained model for biomolecular simulations. *J. Phys. Chem. B* (2007). doi:10.1021/jp071097f

70. Jelger Risselada, H., Fuhrmans, M., Periole, X. & Marrink, S. The MARTINI Force Field. in *Coarse-Graining of Condensed Phase and Biomolecular Systems* 5–19 (2008). doi:10.1201/9781420059564.ch2

71. De Jong, D. H., Baoukina, S., Ingólfsson, H. I. & Marrink, S. J. Martini straight: Boosting performance using a shorter cutoff and GPUs. *Comput. Phys. Commun.* (2016). doi:10.1016/j.cpc.2015.09.014

72. Periole, X., Cavalli, M., Marrink, S. J. & Ceruso, M. ELNEDYN: Keep your proteins stable. *J. Chem. Th. Comp.* (2009).

73. Debono, M. *et al.* A21978C, a complex of new acidic peptide antibiotics: Isolation, chemistry, and mass spectral structure elucidation. *J. Antibiot. (Tokyo).* (1987). doi:10.7164/antibiotics.40.761

74. Eliopoulos, G. M. *et al.* In vitro and in vivo activity of LY 146032, a new cyclic lipopeptide antibiotic. *Antimicrob. Agents Chemother.* (1986). doi:10.1128/AAC.30.4.532

75. Sauermann, R., Rothenburger, M., Graninger, W. & Joukhadar, C. Daptomycin: A review 4 years after first approval. *Pharmacology* (2008). doi:10.1159/000109868

76. Buehlmann, M. *et al.* Highly effective regimen for decolonization of methicillin-resistant Staphylococcus aureus carriers. *Infect. Control Hosp. Epidemiol.* **29**, 510–516 (2008).

77. Brown, S. *et al.* Methicillin resistance in <i>Staphylococcus aureus<i/> requires glycosylated wall teichoic acids. *Proc. Natl. Acad. Sci. U. S. A.* **109**, 18909–14 (2012).

78. Baltz, R. H., Brian, P., Miao, V. & Wrigley, S. K. Combinatorial biosynthesis of lipopeptide antibiotics in Streptomyces roseosporus. in *Journal of Industrial Microbiology and Biotechnology* **33**, 66–74 (2006).

79. Grünewald, J., Sieber, S. A., Mahlert, C., Linne, U. & Marahiel, M. A. Synthesis and derivatization of daptomycin: A chemoenzymatic route to acidic lipopeptide antibiotics. *J. Am. Chem. Soc.* (2004).

doi:10.1021/ja045455t

80. Chen, Y. F., Sun, T. L., Sun, Y. & Huang, H. W. Interaction of daptomycin with lipid bilayers: A lipid extracting effect. *Biochemistry* (2014). doi:10.1021/bi500779g

81. Muraih, J. K., Pearson, A., Silverman, J. & Palmer, M. Oligomerization of daptomycin on membranes. *Biochim. Biophys. Acta - Biomembr.* **1808**, 1154–1160 (2011).

82. Lee, M. T. *et al.* Molecular State of the Membrane-Active Antibiotic Daptomycin. *Biophys. J.* (2017). doi:10.1016/j.bpj.2017.05.025

83. Gray, D. A. & Wenzel, M. More than a pore: A current perspective on the in vivo mode of action of the lipopeptide antibiotic daptomycin. *Antibiotics* (2020). doi:10.3390/antibiotics9010017

84. Scott, W. R. P., Baek, S. Bin, Jung, D., Hancock, R. E. W. & Straus, S. K. NMR structural studies of the antibiotic lipopeptide daptomycin in DHPC micelles. *Biochimica et Biophysica Acta - Biomembranes* **1768**, 3116–3126 (2007).

85. Kirkham, S. *et al.* Self-Assembly of the Cyclic Lipopeptide Daptomycin: Spherical Micelle Formation Does Not Depend on the Presence of Calcium Chloride. *ChemPhysChem* (2016). doi:10.1002/cphc.201600308

86. Jung, D., Rozek, A., Okon, M. & Hancock, R. E. W. Structural transitions as determinants of the action of the calcium-dependent antibiotic daptomycin. *Chem. Biol.* (2004). doi:10.1016/j.chembiol.2004.04.020

87. Baltz, R. H., Miao, V. & Wrigley, S. K. Natural products to drugs: Daptomycin and related lipopeptide antibiotics. *Natural Product Reports* (2005). doi:10.1039/b416648p

88. Bunkóczi, G., Vértesy, L. & Sheldrick, G. M. Structure of the lipopeptide antibiotic tsushimycin. *Acta Crystallogr. Sect. D Biol. Crystallogr.* (2005). doi:10.1107/S0907444905017270

89. Muraih, J. K., Harris, J., Taylor, S. D. & Palmer, M. Characterization of daptomycin oligomerization with perylene excimer fluorescence: Stoichiometric binding of phosphatidylglycerol triggers oligomer formation. *Biochim. Biophys. Acta - Biomembr.* (2012).

doi:10.1016/j.bbamem.2011.10.027

90. Kreutzberger, M. A., Pokorny, A. & Almeida, P. F. Daptomycin-Phosphatidylglycerol Domains in Lipid Membranes. *Langmuir* (2017). doi:10.1021/acs.langmuir.7b01841

91. Xie, Y. & Yang, L. Calcium and Magnesium Ions Are Membrane-Active against Stationary-Phase Staphylococcus aureus with High Specificity. *Sci. Rep.* (2016). doi:10.1038/srep20628

92. Hachmann, A. B., Angert, E. R. & Helmann, J. D. Genetic analysis of factors affecting susceptibility of bacillus subtilis to daptomycinvt. *Antimicrob. Agents Chemother.* (2009). doi:10.1128/AAC.01329-08

93. Randall, C. P., Mariner, K. R., Chopra, I. & O'Neill, A. J. The target of daptomycin is absent from Escherichia coli and other gram-negative pathogens. *Antimicrob. Agents Chemother.* (2013). doi:10.1128/AAC.02005-12

94. Müller, A. *et al.* Daptomycin inhibits cell envelope synthesis by interfering with fluid membrane microdomains. *Proc. Natl. Acad. Sci. U. S. A.* (2016). doi:10.1073/pnas.1611173113

95. Hamoen, L. W. & Wenzel, M. Editorial: Antimicrobial Peptides - Interaction with Membrane Lipids and Proteins. *Front. Cell Dev. Biol.* (2017). doi:10.3389/fcell.2017.00004

96. Priyatham, T. & Bauri, R. *Gromacs 2018*. *Materials Characterization* (2010). doi:10.1016/j.matchar.2009.10.005

97. Jorgensen, W. L., Chandrasekhar, J., Madura, J. D., Impey, R. W. & Klein, M. L. Comparison of simple potential functions for simulating liquid water. *J. Chem. Phys.* (1983). doi:10.1063/1.445869

98. Parrinello, M. Polymorphic transitions in single crystals: A new molecular dynamics method. *J. Appl. Phys.* **52**, 7182 (1981).

99. Hayami, masaaki, Okabe, A., Kariyama, R., Abe, M. & Kanemasa, Y. Lipid Composition of Staphylococcus aureus and Its Derived L-forms. *Microbiol. Immunol.* (1979). doi:10.1111/j.1348-0421.1979.tb00483.x

100. Mishra, N. N. & Bayer, A. S. Correlation of cell membrane lipid profiles with daptomycin resistance in methicillin-resistant staphylococcus

aureus. *Antimicrob. Agents Chemother.* (2013). doi:10.1128/AAC.02182-12

101. Yu, W., He, X., Vanommeslaeghe, K. & MacKerell, A. D. Extension of the CHARMM general force field to sulfonyl-containing compounds and its utility in biomolecular simulations. *J. Comput. Chem.* (2012). doi:10.1002/jcc.23067
102. Vanommeslaeghe, K. & MacKerell, A. D. Automation of the CHARMM general force field (CGenFF) I: Bond perception and atom typing. *J. Chem. Inf. Model.* (2012). doi:10.1021/ci300363c
103. Bazan-Krzywosza?ska, A., Mr?wczy?ska, M., Skiba, M. & ??czak, A. Economic conditions for the development of energy efficient civil engineering using RES in the policy of cohesion of the European Union (2014?2020). Case study: The town of Zielona Gora. *Energy Build.* **118**, 170–180 (2016).
104. González-Alemán, R. *et al.* BitClust: Fast Geometrical Clustering of Long Molecular Dynamics Simulations. *J. Chem. Inf. Model.* (2020). doi:10.1021/acs.jcim.9b00828
105. Buchoux, S. FATSLiM: A fast and robust software to analyze MD simulations of membranes. *Bioinformatics* (2017). doi:10.1093/bioinformatics/btw563
106. Pronk, S. *et al.* GROMACS 4.5: A high-throughput and highly parallel open source molecular simulation toolkit. *Bioinformatics* **29**, 845–854 (2013).
107. Castillo, N., Monticelli, L., Barnoud, J. & Tieleman, D. P. Free energy of WALP23 dimer association in DMPC, DPPC, and DOPC bilayers. *Chem. Phys. Lipids* **169**, 95–105 (2013).
108. Stone, J. Using VMD. *Main* **Chapter 5**, Unit 5.7 (2011).
109. Carvalho, C. N. *et al.* Ions release and pH of calcium hydroxide–, chlorhexidine– and bioactive glass–based endodontic medicaments. *Braz. Dent. J.* **27**, 325–331 (2016).
110. Gomes, A. & Cunha, S. Bismuth-Catalyzed Synthesis of Macrocyle Bisguanidines. in (2013). doi:10.5151/chempro-14bmos-r0333-2
111. Ferguson, D. B., Marley, J. T. & Hartwell, G. R. The effect of chlorhexidine

gluconate as an endodontic irrigant on the apical seal: long-term results. *J. Endod.* **29**, 91–94 (2003).

112. Cattaneo, D., Mccormick, L. J., Cordes, D. B., Slawin, A. M. Z. & Morris, R. E. Crystal structure resolution of two different chlorhexidine salts. *J. Mol. Struct.* **1121**, 70–73 (2016).
113. HUGO, W. B. & LONGWORTH, A. R. Some aspects of the mode of action of chlorhexidine. *J. Pharm. Pharmacol.* (1964). doi:10.1111/j.2042-7158.1964.tb07384.x
114. Kuyyakanond, T. & Quesnel, L. B. The mechanism of action of chlorhexidine. *FEMS Microbiol. Lett.* (1992). doi:10.1016/0378-1097(92)90211-6
115. Samanth, S. A. & Varghese, S. S. The most effective concentration of chlorhexidine as a mouthwash- systematic review. *Journal of Pharmaceutical Sciences and Research* (2017).
116. Cheung, H. Y. *et al.* Differential actions of chlorhexidine on the cell wall of bacillus subtilis and escherichia coli. *PLoS One* (2012). doi:10.1371/journal.pone.0036659
117. Cheung, H.-Y. *et al.* Differential actions of chlorhexidine on the cell wall of *Bacillus subtilis* and *Escherichia coli*. *PLoS ONE* **7**, (2012).
118. Rosenberg, A., Alatary, S. D. & Peterson, A. F. Safety and efficacy of the antiseptic chlorhexidine gluconate. *Surg. Gynecol. Obstet.* (1976).
119. Komljenović, I., Marquardt, D., Harroun, T. A. & Sternin, E. Location of chlorhexidine in DMPC model membranes: A neutron diffraction study. *Chem. Phys. Lipids* (2010). doi:10.1016/j.chemphyslip.2010.03.007
120. Fraud, S., Campigotto, A. J., Chen, Z. & Poole, K. MexCD-OprJ multidrug efflux system of Pseudomonas aeruginosa: Involvement in chlorhexidine resistance and induction by membrane-damaging agents dependent upon the AlgU stress response sigma factor. *Antimicrob. Agents Chemother.* (2008). doi:10.1128/AAC.01072-08
121. Lode, H. M. Clinical impact of antibiotic-resistant Gram-positive pathogens. *Clinical Microbiology and Infection* **15**, 212–217 (2009).
122. Wang, Y., Schlamadinger, D. E., Kim, J. E. & McCammon, J. A.

Comparative molecular dynamics simulations of the antimicrobial peptide CM15 in model lipid bilayers. *Biochim. Biophys. Acta - Biomembr.* (2012). doi:10.1016/j.bbamem.2012.02.017

123. Zhao, L. *et al.* Molecular dynamics simulations of human antimicrobial peptide LL-37 in model POPC and POPG lipid bilayers. *Int. J. Mol. Sci.* (2018). doi:10.3390/ijms19041186
124. Petkov, P., Lilkova, E., Ilieva, N. & Litov, L. Self-association of antimicrobial peptides: A molecular dynamics simulation study on bombinin. *Int. J. Mol. Sci.* (2019). doi:10.3390/ijms20215450
125. Van Oosten, B. *et al.* Small molecule interaction with lipid bilayers: A molecular dynamics study of chlorhexidine. *J. Mol. Graph. Model.* (2014). doi:10.1016/j.jmgm.2013.12.007
126. Balagopal, S. & Arjunkumar, R. Chlorhexidine: The gold standard antiplaque agent. *J. Pharm. Sci. Res.* **5**, 270–274 (2013).
127. Bhardwaj, P., Hans, A., Ruikar, K., Guan, Z. & Palmer, K. L. Reduced chlorhexidine and daptomycin susceptibility in vancomycin-resistant Enterococcus faecium after serial chlorhexidine exposure. *Antimicrob. Agents Chemother.* (2018). doi:10.1128/AAC.01235-17
128. Frenkel, D. & Smit, B. *Understanding molecular simulation: From algorithms to applications*. *Understanding molecular simulation: From algorithms to applications* (1996).
129. Vanommeslaeghe, K. *et al.* CHARMM general force field: A force field for drug-like molecules compatible with the CHARMM all-atom additive biological force fields. *J. Comput. Chem.* (2010). doi:10.1002/jcc.21367
130. Warshel, A. & Levitt, M. Theoretical studies of enzymic reactions: Dielectric, electrostatic and steric stabilization of the carbonium ion in the reaction of lysozyme. *J. Mol. Biol.* (1976). doi:10.1016/0022-2836(76)90311-9
131. McCammon, J. A., Gelin, B. R. & Karplus, M. Dynamics of folded proteins. *Nature* (1977). doi:10.1038/267585a0
132. Brooks, B. R. *et al.* CHARMM: A program for macromolecular energy, minimization, and dynamics calculations. *J. Comput. Chem.* (1983).

doi:10.1002/jcc.540040211

133. BERENDSEN, H. J. C., VAN GUNSTEREN, W. F., ZWINDERMAN, H. R. J. & GEURTSEN, R. G. Simulations of Proteins in Water. *Ann. N. Y. Acad. Sci.* (1986). doi:10.1111/j.1749-6632.1986.tb20961.x

134. Bayly, C. I. *et al.* A Second Generation Force Field for the Simulation of Proteins, Nucleic Acids, and Organic Molecules. *J. Am. Chem. Soc.* (1995). doi:10.1021/ja00124a002

135. Pastor, R. W. & MacKerell, A. D. Development of the CHARMM force field for lipids. *Journal of Physical Chemistry Letters* (2011). doi:10.1021/jz200167q

136. Reif, M. M., Winger, M. & Oostenbrink, C. Testing of the GROMOS force-field parameter set 54A8: Structural properties of electrolyte solutions, lipid bilayers, and proteins. *J. Chem. Theory Comput.* (2013). doi:10.1021/ct300874c

137. Piggot, T. J., Piñeiro, Á. & Khalid, S. Molecular dynamics simulations of phosphatidylcholine membranes: A comparative force field study. *J. Chem. Theory Comput.* (2012). doi:10.1021/ct3003157

138. Poger, D. & Mark, A. E. Lipid bilayers: The effect of force field on ordering and dynamics. *J. Chem. Theory Comput.* (2012). doi:10.1021/ct300675z

139. Sandoval-Perez, A., Pluhackova, K. & Böckmann, R. A. Critical Comparison of Biomembrane Force Fields: Protein-Lipid Interactions at the Membrane Interface. *J. Chem. Theory Comput.* (2017). doi:10.1021/acs.jctc.7b00001

140. Wang, Y. *et al.* How reliable are molecular dynamics simulations of membrane active antimicrobial peptides? *Biochim. Biophys. Acta - Biomembr.* (2014). doi:10.1016/j.bbamem.2014.04.009

141. Koziara, K. B., Stroet, M., Malde, A. K. & Mark, A. E. Testing and validation of the Automated Topology Builder (ATB) version 2.0: Prediction of hydration free enthalpies. *J. Comput. Aided. Mol. Des.* (2014). doi:10.1007/s10822-014-9713-7

142. Guigas, G. & Weiss, M. Effects of protein crowding on membrane systems. *Biochim. Biophys. Acta - Biomembr.* (2016).

doi:10.1016/j.bbamem.2015.12.021

143. Kutzner, C., Grubmüller, H., De Groot, B. L. & Zachariae, U. Computational electrophysiology: The molecular dynamics of ion channel permeation and selectivity in atomistic detail. *Biophys. J.* (2011). doi:10.1016/j.bpj.2011.06.010

144. Delemotte, L. & Tarek, M. Molecular dynamics simulations of lipid membrane electroporation. *J. Membr. Biol.* (2012). doi:10.1007/s00232-012-9434-6

145. Zhang, L. Electroporation and Electrofusion in Cell Biology. *Bioelectrochemistry Bioenerg.* (1991). doi:10.1016/0302-4598(91)80050-d

146. Chen, C., Smye, S. W., Robinson, M. P. & Evans, J. A. Membrane electroporation theories: A review. *Medical and Biological Engineering and Computing* (2006). doi:10.1007/s11517-005-0020-2

147. Villemejane, J. & Mir, L. M. Physical methods of nucleic acid transfer: General concepts and applications. *British Journal of Pharmacology* (2009). doi:10.1111/j.1476-5381.2009.00032.x

148. Cadossi, R., Ronchetti, M. & Cadossi, M. Locally enhanced chemotherapy by electroporation: Clinical experiences and perspective of use of electrochemotherapy. *Future Oncology* (2014). doi:10.2217/fon.13.235

149. Böckmann, R. A., De Groot, B. L., Kakorin, S., Neumann, E. & Grubmüller, H. Kinetics, statistics, and energetics of lipid membrane electroporation studied by molecular dynamics simulations. *Biophys. J.* **95**, 1837–1850 (2008).

150. Polak, A. *et al.* Electroporation of archaeal lipid membranes using MD simulations. *Bioelectrochemistry* **100**, 18–26 (2014).

151. Zasloff, M. Antimicrobial peptides of multicellular organisms. *Nature* (2002). doi:10.1038/415389a

152. Ganz, T. Defensins: Antimicrobial peptides of innate immunity. *Nature Reviews Immunology* (2003). doi:10.1038/nri1180

153. Bode, W. The structure of thrombin: A Janus-headed proteinase. *Seminars in Thrombosis and Hemostasis* (2006). doi:10.1055/s-2006-

939551

154. Medzhitov, R., Preston-Hurlburt, P. & Janeway, C. A. A human homologue of the Drosophila toll protein signals activation of adaptive immunity. *Nature* (1997). doi:10.1038/41131

155. Los, F. C. O., Randis, T. M., Aroian, R. V & Ratner, A. J. Role of pore-forming toxins in bacterial infectious diseases. *Microbiol. Mol. Biol. Rev.* **77**, 173–207 (2013).

156. Takeuchi, O. *et al.* Differential roles of TLR2 and TLR4 in recognition of gram-negative and gram-positive bacterial cell wall components. *Immunity* (1999). doi:10.1016/S1074-7613(00)80119-3

157. Park, B. S. *et al.* The structural basis of lipopolysaccharide recognition by the TLR4-MD-2 complex. *Nature* (2009). doi:10.1038/nature07830

158. Jin, M. S. *et al.* Crystal Structure of the TLR1-TLR2 Heterodimer Induced by Binding of a Tri-Acylated Lipopeptide. *Cell* (2007). doi:10.1016/j.cell.2007.09.008

159. Tsujimoto, H. *et al.* Role of toll-like receptors in the development of sepsis. *Shock* (2008). doi:10.1097/SHK.0b013e318157ee55

160. Martin, G. S., Mannino, D. M., Eaton, S. & Moss, M. The epidemiology of sepsis in the United States from 1979 through 2000. *N. Engl. J. Med.* (2003). doi:10.1056/NEJMoa022139

161. Papareddy, P. *et al.* C-terminal peptides of tissue factor pathway inhibitor are novel host defense molecules. *J. Biol. Chem.* (2010). doi:10.1074/jbc.M110.127019

162. Saravanan, R. *et al.* Structural basis for endotoxin neutralisation and anti-inflammatory activity of thrombin-derived C-terminal peptides. *Nat. Commun.* (2018). doi:10.1038/s41467-018-05242-0

163. Huber, R. G. *et al.* A Thermodynamic Funnel Drives Bacterial Lipopolysaccharide Transfer in the TLR4 Pathway. *Structure* **26**, 1151-1161.e4 (2018).